UNIVERSITY OF CALIFORNIA,
IRVINE

# Filamentous Bacteriophage as a Functional Biomaterial for Biomarker-Based Diagnostics

DISSERTATION

submitted in partial satisfaction of the requirements
for the degree of

DOCTOR OF PHILOSOPHY

in Chemistry

by

Emily Caitlin Sanders

Dissertation Committee:
Professor Gregory A. Weiss, Chair
Professor Reginald M. Penner
Professor Jennifer A. Prescher

2021

## Dedication

To Darrik, Datura, and Stormageddon

*UNLESS someone like you cares a whole awful lot,*
*nothing is going to get better.*
*It's not.*

Dr. Seuss
*The Lorax*

*When we stand together there is nothing,*
*nothing,*
*nothing*
*we cannot accomplish.*

Senator Bernie Sanders

# Table of Contents

# List of Figures

# List of Tables

# List of Equations

## Acknowledgements

I would like to thank the American Society for Microbiology for permission to include chapter 4 in my dissertation, which was originally published in *mSphere* (doi: 10.1128/mSphere.00203-21). I want to thank the American Chemical Society for permission to include chapters 6, 7, and 8 in my dissertation. Portions of chapter 6 were originally published in *Analytical Chemistry* (doi: 10.1021/acs.analchem.0c00534), portions of chapter 7 were originally published in *Accounts of Chemical Research* (doi: 10.1021/acs.accounts.0c00474), and portions of chapter 8 were originally published in *ACS Applied Materials and Interfaces* (doi: 10.1021/acsami.8b16071).

I would like to thank my co-authors and collaborators, without whom this body of work would not be in its presented form. A portion of chapter 2 was co-authored with Alicia M. Santos, Eugene Nguyen, Aidan A. Gelston, Sudipta Majumdar, and Gregory A. Weiss. A portion of chapter 3 was co-authored with Sanjana R. Sen, Aidan A. Gelston, Alicia M. Santos, Xuan Luo, Keertna Bhuvan, Derek Y. Tang, Colin L. Raston, and Gregory A. Weiss. A portion of chapter 4 was co-authored with Sanjana R. Sen, Kristin N. Gabriel, Brian M. Miller, Hariny M. Isoda, Gabriela S. Salcedo, Jason E. Garrido, Rebekah P. Dyer, Rie Nakajima, Aarti Jain, Ana-Maria Caldaruse, Alicia M. Santos, Keertna Bhuvan, Delia F. Tifrea, Joni L. Ricks-Oddie, Philip L. Felgner, Robert A. Edwards, Sudipta Majumdar, and Gregory A. Weiss. A portion of chapter 5 was co-authored with Sanjana R. Sen, Alicia M. Santos, Keertna Bhuvan, Derek Y. Tang, Aidan A. Gelston, Joni L. Ricks-Oddie, and Gregory A. Weiss. A portion of chapter 6 was co-authored with Apurva Bhasin, Joshua M. Ziegler, Jeffrey S. Briggs, Nicholas P. Drago, Aisha M. Attar, Alicia M. Santos, Marie Y. True, Alana F. Ogata, Debora V. Yoon, Sudipta Majumdar, Andrew J. Wheat, Shae V. Patterson, Gregory A. Weiss, and Reginald M. Penner. A portion of

chapter 7 was co-authored with Apurva Bhasin, Nicholas P. Drago, Sudipta Majumdar, Gregory A. Weiss, and Reginald M. Penner. A portion of chapter 8 was co-authored with Aisha M. Attar, Mark B. Richardson, Gaetano Speciale, Sudipta Majumdar, Rebekah P. Dyer, Reginald M. Penner, and Gregory A. Weiss.

I would like to express my deepest gratitude and admiration for my committee chair, Professor Gregory A. Weiss. At a time when all felt lost, Greg was there to catch me and lift me up. When I lost faith in my abilities, Greg was there to remind me I **can** and **will** accomplish my goals. Greg would not let me accept anything but the best for myself. I would not be the scientist or human I am today without his guidance and mentorship.

To my committee members, Prof. Reg Penner and Prof. Jenn Prescher, thank you for your assistance and kind words through the years. Reg has been my co-mentor on a number of the projects presented in this dissertation and has always respected my thoughts and contributions to our collaborations. Jenn was my committee chair for both my second year written and oral examinations, and offered me much needed guidance, support, and tissues during the unique challenges I faced in my first year.

To my mentors, of which I have many, thank you for everything you have done to help me get to this point. This acknowledgement is not exhaustive, but there are a few mentors I would like to highlight. First, Prof. Amanda Murphy, my undergraduate research advisor, thank you for your unwavering support and belief in me! I graduated from WWU five years ago and you are still happy to offer me guidance, advice, and connections. Next, Dr. Sudipta Majumdar, a former Weiss lab researcher, thank you for your years of support and direction. Lastly, to the vast network of folks associated with ChemTwitter, who connected me to a larger community and helped me find my postdoc!

To my labmates, thank you for all of the laughs, movie nights, off-key birthday songs, stale leftover group meeting popcorn, and support. I wish we could have spent more time together in the last year, but even with shift schedules and remote meetings, we had a good time. Particularly, I want to give a shout out to Sanjana Sen and Kristin Gabriel: we have worked together for FOUR years, co-authored a paper together, and we still like each other! Also, thank you to Aidan Gelston, Alicia Santos, Arjun Sunil Pamidi, Brian Miller, Rachel Rubenstein, Vy Pham, and Wyatt Swift-Ramirez, who proofread portions of this dissertation.

To my undergraduate research mentees, thank you for giving me the immense honor of mentoring you. Thank you for putting your trust in me, and I cannot wait to see what is in store for you all. Never forget I am always here for you as a mentor, a friend, and your biggest cheerleader. Alicia Santos, I am beyond proud of what you have accomplished and I know you will find success in your PhD and beyond. Aidan Gelston, in less than a year you became an author on three manuscripts. Be proud of yourself, because I am. Eugene Nguyen, I know you will find success wherever your path takes you.

To the Division of Teaching in Excellence and Innovation, particularly Dr. Daniel Mann, thank you for the incredible opportunity to engage in pedagogy in a way I would not otherwise be able to. Similarly, I would like to thank Prof. Renee Link, who allowed me to assist her in transforming peer mentorship in the Chemistry department from nonexistent to gold standard.

To my family, thank you for comforting me during the hard times, and celebrating with me during the good. My grandparents – Steve and Janice – thank you for loving me unconditionally since the day I was born and making sure I always knew it. My mom, Susan, thank you for being my best friend and the person I want to share all of my news with. My

dad, Dave, thank you for being the father who chose me. My siblings, Joel and Chelsea, thank you for your support and love. My niblings, Becca, Ethan, Sam, Rachel, Zeke, Bodie, and Chloe, thank you for being a constant source of laughter and joy. My in-laws, Tammie, D, and Kade, thank you for welcoming me into the family with open arms. I hope I make you all proud, and someday you will understand what it is that I do for a living.

Last, but not least, thank you to my husband, Darrik. It is hard to believe that a little over 5 years ago we made the decision to move to California together after only a few months of dating. Now we are on our fourth year of marriage and on our way to our next big adventure abroad! Thank you for loving me and supporting me.

## Curriculum Vitae

EMILY SANDERS

EDUCATION

**University of California, Irvine, CA**
Ph.D. Chemistry **2021**

**Western Washington University, Bellingham, WA**
B.S. Biochemistry **2016**

AWARDS AND HONORS

| | |
|---|---|
| UCI Chemistry Dissertation Fellowship | **Spring 2021** |
| UC Irvine Pedagogical Fellow | **2020-2021** |
| DTEI Graduate Fellowship | **2020** |
| Outstanding Poster Award | **2016** |
| Oscar Edwin Olson Sciences Endowment (Awarded twice) | **2014 – 2016** |
| NSF-REU Fellowship Recipient | **2015** |

RESEARCH EXPERIENCE

**University of California, Irvine, CA**
Research Assistant: Prof. Gregory Weiss **2017 – present**
*Project 1: Developed method to directly select for sandwich ELISA pairs via phage display. Project 2: Designed and tested SARS-CoV-2 epitopes to identify markers for COVID-19 disease severity. Project 3: Developed a platform technology to perform immunoblot assay in less than 5 minutes. Project 4: Provided phage display and molecular biology support to the development of the Virus BioResistor.*

Research Assistant: Prof. Aaron Esser-Kahn **2016 – 2017**
*Developed novel step-growth polymerization by in situ Cu(II) reduction and subsequent click chemistry.*

**Western Washington University, Bellingham, WA**
Undergraduate Research Assistant: Prof. Amanda Murphy **2015 – 2016**
*Engineered 3D silk fibroin structures*

TEACHING EXPERIENCE

**University of California, Irvine, CA**
**Graduate Teaching Assistant** **2016 – present**

Organized and taught undergraduate and graduate level chemistry lectures and labs, graded lab reports, papers, and exams.

**Western Washington University, Bellingham, WA**
**Undergraduate Laboratory Assistant** **2014 – 2015**
Assisted professor with laboratory oversight, maintaining safety, and grading student notebooks.

## MENTORSHIP EXPERIENCE

**Research Mentorship**
*I have directly mentored 3 undergraduate researchers.*
*Alicia M. Santos, whom I have mentored since June 2018, will begin her PhD at Dartmouth in Fall 2021. Alicia will graduate as a co-author on five manuscripts, has presented at a national ACS conference, and has received several merit-based fellowships and scholarships.*

**Pedagogical Mentorship**
*I have mentored over 50 graduate students as a TA mentor for the Chemistry Department at UC Irvine as well as a Pedagogical Fellow for UCI's Division of Teaching Excellence and Innovation.*

## PUBLICATIONS

Bhasin, A.†; Choi, E.J.†; Drago, N.P.†; Garrido, J.E.; **Sanders, E.C.;** Shin, J.; Andoni, I.; Kim, D.-H.; Fang, L.; Weiss, G.A.; Penner, R.M. Enhancing the Sensitivity of the Virus BioResistor by Over-Oxidation: Detecting IgG Antibodies. *Submitted.* † = co-equal contributors

Sen, S.; **Sanders, E.C.;** Santos, A.M.; Bhuvan, K.; Tang, D.; Gelston, A.A.; Weiss, G.A. Evidence for Deleterious Original Antigenic Sin in SARS-CoV-2 Immune Response. *Submitted.*

**Sanders, E.C.;** Gelston, A.A.; Sen, S.; Santos, A.M.; Bhuvan, K.; Tang, D.; Luo, X.; Raston, C.L.; Weiss, G.A. Under 5 Minute Immunoblot Assays by Vortex Fluidic Device Acceleration. *In Review.*

Sen, S.†; **Sanders, E.C.†**; Gabriel, K.N.†; Miller, B.M.; Isoda, H.M.; Salcedo, G.S.; Garrido, J.E.; Dyer, R.P.; Nakajima, R.; Jain, A.; Caldaruse, A.-M.; Santos, A.M.; Bhuvan, K.; Tifrea, D.F.; Ricks-Oddie, J.L.; Felgner, P.L.; Edwards, R.A.; Majumdar, S.; Weiss, G.A. Predicting COVID-19 Severity with a Specific Nucleocapsid Antibody plus Disease Risk Factory Score. *mSphere.* **2021**, *6*(2), 1-13.
**† = co-equal contributors**

Bhasin, A.; Dragon, N.P.; Majumdar, S.; **Sanders, E.C.;** Weiss, G.A.; Penner, R.M. Viruses Masquerading as Antibodies in Biosensors: The Development of The Virus BioResistor. *Acc. Chem. Res.* **2020**, *52*(10), 2384-2394.

Bhasin, A.; **Sanders, E.C.**; Ziegler, J.M.; Briggs, J.S.; Drago, N.P.; Attar, A.M.; Santos, A.M.; True, M.Y.; Ogata, A.F.; Yoon, D.V.; Majumdar, S.; Wheat, A.J.; Patterson, S.V.; Weiss, G.A.; Penner, R.M. A Virus BioResistor (VBR) for the Detection of the Bladder Cancer Marker DJ-1 in Urine at 10 pM in One Minute. *Anal. Chem.* **2020**, *92*(9), 6654-6666.

Attar, A.M.; Richardson, M.B.; Speciale, G.; Majumdar, S.; Dyer, R.P.; **Sanders, E.C.**; Penner, R.M.; Weiss, G.A. Electrochemical quantification of glycated and non-glycated human serum albumin in synthetic urine. *ACS Appl. Mater. Interfaces.* **2019,** *11*(5), 4757-4765.

Mohapatra, H.; Ayarza, J.; **Sanders, E.C.**; Scheuermann A.M.; Griffin, P.J.; Esser-Kahn, A.P. Ultrasound Promoted Step-Growth Polymerization and Polymer Crosslinking Via Copper Catalyzed Azide-Alkyne 'Click' (CuAAC) Reaction. *Angew. Chem.* **2018**, *57*, 11208-11212.

## MANUSCRIPTS IN PREPARATION

**Sanders, E.C.;** Santos, A.M.; Nguyen, E.; Gelston, A.A.; Majumdar, S.; Weiss, G.A. Phage vs Phage: Direct Selections of Compatible Binding Pairs for Sensitive Biomarker Detection.

## PRESENTATIONS

**ACS National Meeting: San Diego, CA**
*Oral: "Electrochemical quantification of bladder cancer biomarkers with a sandwich phage-based bioresistor."*
**Sanders, E.C.;** Santos, A.M.; Majumdar, S.; Penner, R.M.; Weiss, G.A. **2019**

**ACS National Meeting: San Francisco, CA**
*Oral: "Crosslinking acrylate-containing polymers by downstream piezoelectric reduction."*
**Sanders, E.C.;** Mohapatra, H.; Esser-Kahn, A.P. **2017**

**ACS National Meeting: San Diego, CA**
*Oral: "Electrically conductive silk fibroin scaffolds for use as nerve conduits."*
**Sanders, E.C.**; Severt, S.Y.; Murphy, A.M. **2016**

## Abstract of the Dissertation

Filamentous Bacteriophage as a Functional Biomaterial for Biomarker-Based Diagnostics

by

Emily Caitlin Sanders

Doctor of Philosophy in Chemistry

University of California, Irvine, 2021

Professor Gregory A. Weiss, Chair

Filamentous bacteriophage have proven to be a powerful biotechnology tool. A direct genotype-to-phenotype relationship makes phage easily genetically modified to display peptide or proteins on their solvent-facing surface. Thus, phage can function as pseudo-antibodies with similar binding affinity and target specificity. Furthermore, rational design of peptide or protein libraries allows for discovery of new target-binders via biopanning. Additionally, phage are increasingly gaining traction as a biomaterial due to an inherent monodispersity and ease of chemical modification (Chapter 1).

In this dissertation, I will present how I have used phage display to validate a new immunoblot assay technique (Chapter 3), to identify a COVID-19 antibody that correlates with disease severity and investigate the origin of this antibody (Chapter 4, Chapter 5), and to detect valuable biomarkers with novel biosensing platforms (Chapter 6, Chapter 7, Chapter 8). Additionally, I have contributed new knowledge to the field of phage display by developing a novel method to directly select for noncompetitive binding peptides and antibody fragments for the more sensitive and specific sandwich ELISA (Chapter 2).

# CHAPTER 1

## Functionalization of Materials with Filamentous Phage Beyond Phage Display

### 1.1 Abstract

Bacteriophage technology has given rise to a multitude of tools to benefit human health and livelihood. However, the vast majority of these tools revolve around phage display rather than the intrinsic properties of phage. As a material, phage have several robust properties that are useful for materials applications, including ease of chemical modification, low isoelectric point, flexibility, and monodispersity. This review will present and critically analyze how these properties inherent to phage have been exploited to create hybrid materials for drug conjugation, biosensing, drug delivery, and ordering quantum dots.

## 1.2 Introduction

Functional materials are valuable for a variety of applications with direct benefits to human health and progress. Traditionally, functionalization of materials is done via chemical modifications of the material itself.[1–3] In contrast, biological approaches to create functional materials may constitute a greener and more platform approach. In principle, a genetically modifiable component of a functional material affords greater control and generalizability.

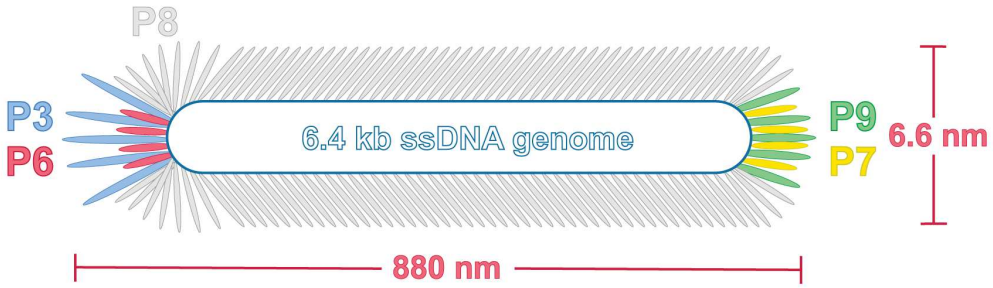


**Figure 1-1. Schematic representation of filamentous phage.** The ssDNA phage genome (6.4 kb) is encapsulated by phage coat proteins, P3, P6, P7, P8, and P9. The capsid is typically about 880 nm long and 6.6 nm wide (not to scale).

Filamentous bacteriophage (from here on referred to as just phage) are viruses that infect *Escherichia coli* (*E. coli*) displaying an F pilus protein.[4–9] Discovered in the 1960s, these filamentous viral particles are about 880 nm long and 6.6 nm wide (**Fig. 1-1**).[10,11] The 6.4 kb[12] ssDNA phage genome is protected by a capsid comprised of five major proteins. The P8 structural protein forms most of the capsid at an abundance of about 2700 copies (~88% of viral mass)[13] along the length of the virus and gives rise to the capsid's α-helical shape.[14–16] The less abundant capsid proteins, P3, P6, P7, and P9 are found on the ends of the capsid.

Phage have a number of inherent properties capable of conferring additional functionality to a variety of materials. There are several reported methods to manufacture hybrid materials with phage. A rather obvious method will be covered briefly in section 1.4; affinity immobilization via phage display. However, this method has been extensively reviewed,[17–19] thus this review will center on the less commonly considered methods to

create phage hybrid materials. Specifically, the review will focus on phage hybrid materials formed via inherent properties of the phage such as ease of chemical modification, isoelectric point (pI), flexibility, and monodispersity (**Fig. 1-2**).

### 1.3 History of Phage in Biotechnology

Phage emerged as a biotechnology tool in 1985, when Nobel laureate George P. Smith first described how phenotypic phage variants could be created by inserting foreign DNAs into the viral genome.[20] Specifically, Smith demonstrated an antigen could be propagated on phage capsid as a fusion to P3. The success of the cloning was evidenced by both a restriction digest and an immunosorbent assay. Furthermore, the modified phage remained infectious. Smith astutely predicted that this method would be a breakthrough in molecular recognition screening.

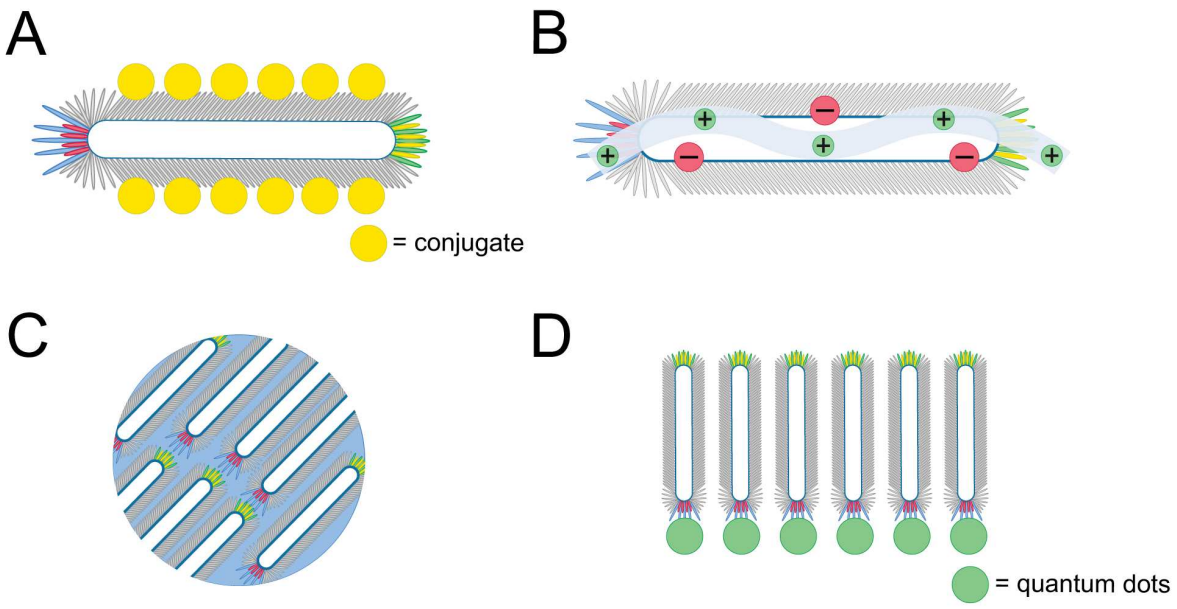


**Figure 1-2. Phage hybrid materials generated through intrinsic phage properties. A)** Phage can be modified to introduce a multitude of conjugates and linkages to larger materials. **B)** Anionic phage form strong electrostatic interactions with cationic polymers. **C)** The flexibility of filamentous phage provides a surfactant to form drug delivery vehicles. **D)** Phage's inherent monodispersity and anisotropy gives rise to liquid crystalline structures that can be used to order quantum dots.

Smith's vision of phage display as a biopanning technique was swiftly investigated. In 1988, Smith and Stephen F. Parmley reported proof-of-concept work for "biopanning", a proposed process in which phage libraries bearing randomized epitopes are screened against an antigen of interest (**Fig. 1-3**).[21] This biopanning goal was realized in a follow up paper in 1990 in *Science* by Smith and Jamie K. Scott. The researchers triumphantly reported their success constructing and screening phage-displayed hexapeptide epitope libraries against the monoclonal antibodies (mAbs) A2 and M33.[22]

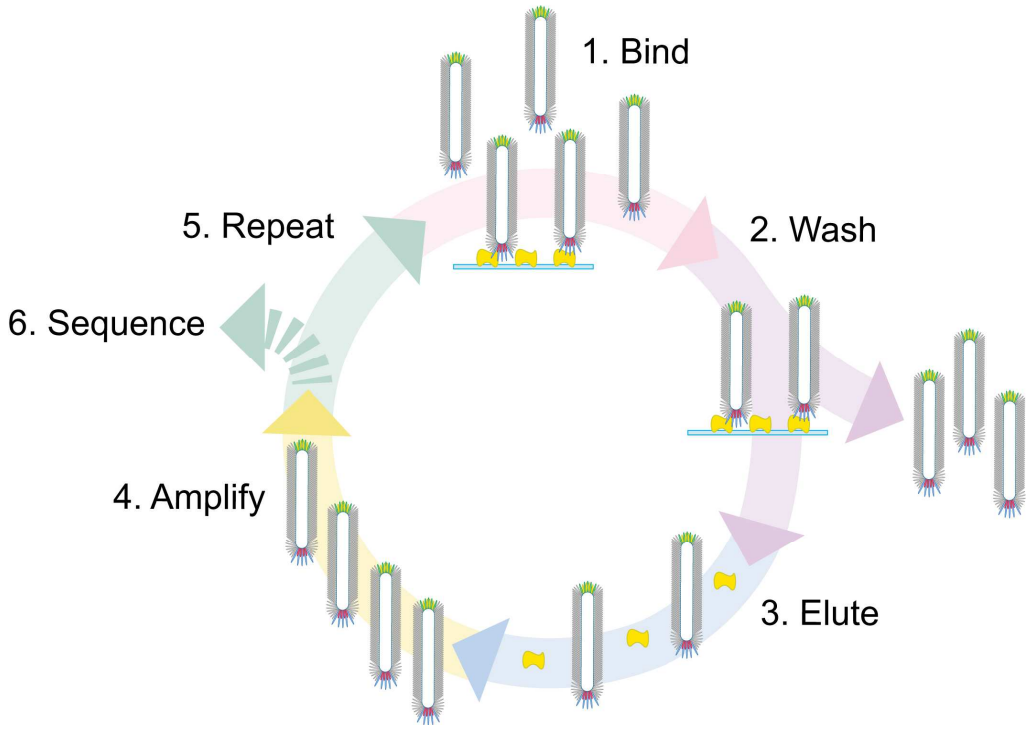


**Figure 1-3. Phage biopanning. 1)** The target antigen is adsorbed to a solid support and exposed to a phage library. **2)** Nonbinding phage are removed by washing. **3)** Binding assemblies are eluted from the microtiter plate. **4)** The phage are used to infect *E. coli* and amplified. **5)** The process is repeated with the amplified selectants as the phage library for the next round of selection. **6)** After several rounds of selections, the selectants are identified by DNA sequencing.

Following Smith's seminal work, fellow Nobel laureate Sir Gregory P. Winter won the race to display antibody fragments on phage.[23,24] Specifically, Winter and associates successfully displayed P3-fused single-chain variable fragments (scFvs) and biopanned for binding to hen egg white lysozyme (HEWL). By enzyme-linked immunosorbent assay

(ELISA), the researchers demonstrated anti-HEWL scFv phage undeniably bound its target, even over the "essentially identical" turkey egg white lysozyme.[25] The consequences of the above body of work are profound and far-reaching. Phage display technology has delivered 9 FDA-approved human antibody drugs (**Table 1-1**).[26–30]

**Table 1-1. Current FDA approved human antibody drugs discovered by phage display.**

| Antibody | Target | Approval |
|---|---|---|
| Adalimumab[31] | TNFα | 2002 |
| Belimumab[32] | BCAF | 2011 |
| Ramucirumab[33] | VEGFR2 | 2014 |
| Necitumumab[34] | EGFR | 2015 |
| Atezolizumab[35] | PD-L1 | 2016 |
| Avelumab[36] | PD-L1 | 2017 |
| Guselkumab[37] | IL-23 | 2017 |
| Emapalumab[38] | IFNγ | 2018 |
| Moxetumomab pasudodox[39] | CD22 | 2018 |

While all the capsid proteins can be used for phage display,[40] the primary targets are P8, for its high copy number, and P3, for its ubiquity and tolerance of larger polypeptides.[10,41] These display strategies generally revolve around two types of binding modes: targeting and functionalization. Targeting binders are characterized by high affinity to a target antigen, typically for detection purposes. In contrast, functional binders modify their targets and can be used as bioconjugation tools.[42] Both of these binding modes, as well as the previously mentioned properties inherent to all filamentous phage, are routinely used to generate and functionalize phage hybrid materials.

### 1.4 Chemical Modification of Phage

The protein capsid of phage presents a multitude of functionalization opportunities to form new hybrid materials (**Fig. 1-4**).[43] As phage can detect antigens with antibody-level affinity, there are several clear avenues for phage hybrid materials in place of antibodies. For example, consider antibody drug conjugates (ADCs). ADC therapy is a revolutionary oncological treatment in which the targeting capability of antibodies is paired with a cytotoxic payload to destroy cancer cells.[44] However, long-term antibody production relies on hybridoma cell lines, which can be arduous and time-consuming to produce. Thus, phage drug conjugates (PDCs) present a lucrative substitute.

Iftach Yacoby *et al.* first presented phage conjugates as a viable alternative to ADCs in 2006.[45] Phage were modified with a cytotoxic drug via a N-hydroxysuccinimide (NHS) reaction. As verified later by Kai Li *et al.*, this strategy, when implemented with rhodamine-NHS can result in 1600 ± 280 P8 modifications (**Fig. 1-4**).[43] However, the researchers also noted a loss in rhodamine signal above 400 modifications, indicating crowding. With final modification totals ± 17% in phage, NHS chemistry is notoriously challenging to control and preferable for applications that do not require particularly careful labeling.

In contrast to NHS chemistry, activation of carboxylates with 1-ethyl-3-(3-dimethylaminopropyl) (EDC) chemistry can result in 150 ± 18 modifications per phage, according to Kai Li *et al* (**Fig. 1-4**).[43] This offers greater control and a lesser risk of conjugate crowding. Hagit Bar *et al.* exploited this modification strategy to link hygromycin and doxorubicin to phage.[46] However, the researchers calculated ~10,000 modifications per phage, which they credit to the enhanced solubility afforded by the aminoglycoside antibiotic of choice, rather than the previously tested chloramphenicol (~3,000 modifications).[47]

Therefore, consistent phage modification with EDC can be challenging due to its dependency on the hydrophobicity of the payload.

Kai Li *et al.* demonstrated that the two tyrosine residues on phage (Tyr 21 and Tyr 22) can both be modified via diazonium coupling chemistry (**Fig. 1-4**).[43] Despite the known promiscuity of this reaction with histidine and lysine residues, mass spectrometry analysis revealed strong selectivity for tyrosine modification. With 400 ± 40 modifications per phage, this conjugation method was the most specific and most controlled. Thus, it is this author's opinion that the diazonium coupling reaction provides clear benefits over NHS and EDC chemistries to form PDCs and other phage hybrid materials.

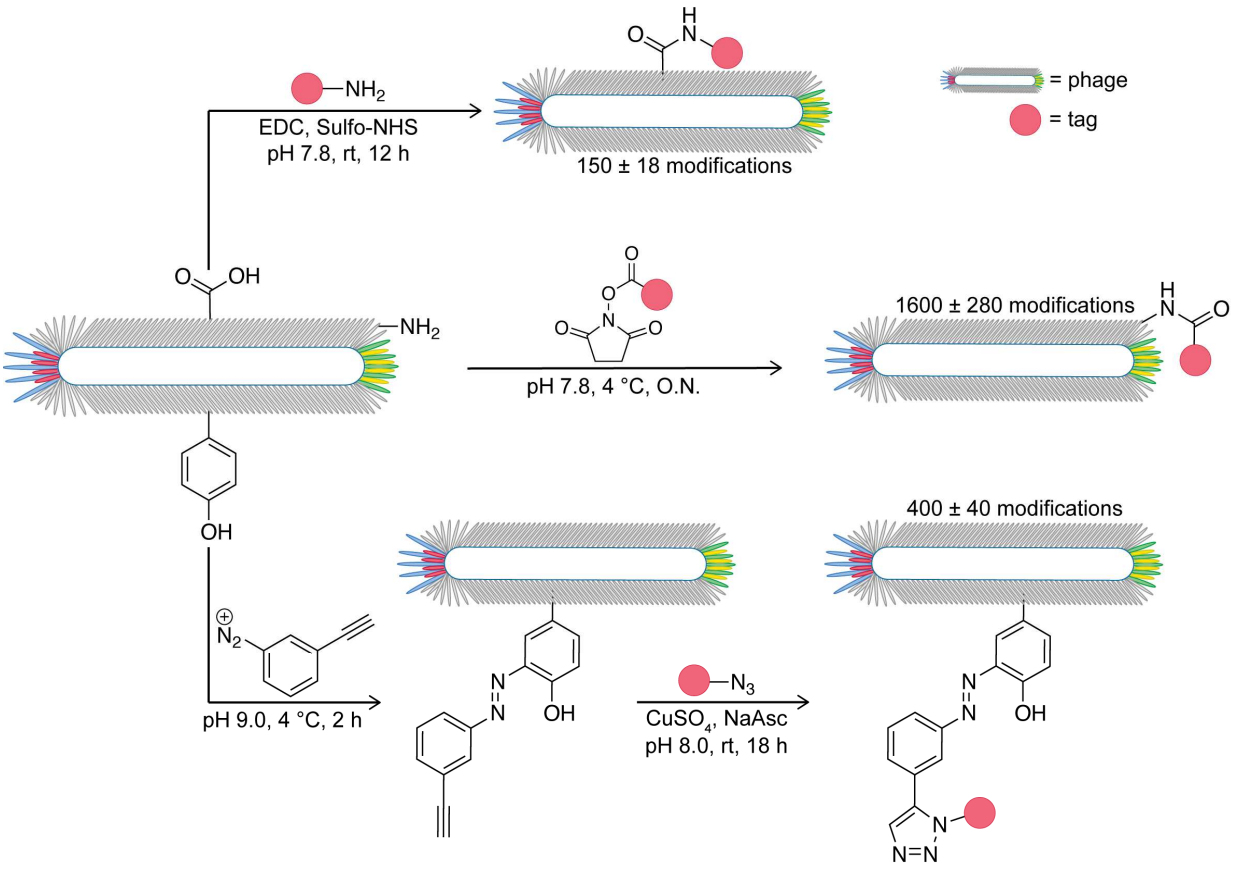


**Figure 1-4. Common modifications of phage.** The protein capsid of phage can be modified via NHS, EDC, and diazonium coupling chemistry for conjugation to small molecules for drug delivery.

## 1.5 Phage Immobilization via Intermolecular Forces

*Isoelectric point.* Phage are overall electronegative, with an experimentally determined pI of 4.2.[48] Thus, phage is anionic at neutral pH and can be electrostatically entrapped or "wrapped" in cationic polymers.[49,50] Jessica Arter *et al.* took advantage of this intrinsic property of phage to electrochemically synthesize phage poly(3,4-ethylenedioxythiophene) (PEDOT) nanowires for the detection of prostate specific membrane antigen (PSMA).[51,52]

Later, the Penner and Weiss labs expanded this method to copolymerize virus-PEDOT films for electrochemical impedance spectroscopy (EIS) detection of antibodies, PSMA, and HSA.[53–56] While these biosensors provided excellent proof-of-concept, they were cumbersome and not ready for clinical applications.[57] Thus, in 2017, the virus bioresistor (VBR) was born.[58] This new technology ultimately enabled detection of 10 pM protein deglycase 1 (DJ-1) via phage deposition reliant on electrostatic interactions.[59]

*Flexibility. A* common motivation to create functional biomaterials is for the delivery of drugs that cannot reach their target before degradation. Drug delivery vehicles should be non-cytotoxic, resilient to fluctuating biological conditions, and ultimately, capable of releasing their payloads.[60] The laboratory of Qian Wang first reported creating 3D phage hybrid assemblies through a simple method.[61] Briefly, aqueous phage suspensions were combined with poly(4-vinylpyridine) (P4VP) suspended in DMF at room temperature. After dialysis, spherical colloids were observed via transmission electron microscopy. The researchers hypothesized this assembly method worked due to the flexibility of filamentous phage.[62] These initial findings led to an additional report in which the same assembly method

yielded doxorubicin-releasing nanoparticles.[63] Thus, the inherent properties of phage allow for the formation of drug delivery vehicles.

### 1.6 Phage: A Liquid Crystalline Material

Phage's rod-like shape and inherent monodispersity unlocks lyotropic liquid crystalline (LC) phases as their concentration increases (**Fig. 1-5**).[64,65] Liquid crystals are highly valuable for optical devices, biosensors, and biomimicry.[66] From 10 to 20 mg/mL, phage become sterically packed together and align vertically with one another in the nematic phase. Next, from 20 to 80 mg/mL, phage enter the cholesteric phase, in which they are stacked in highly ordered layers.[65,67–69] Finally, at 100 mg/mL and above, phage becomes smectic, ordered both positionally and orientationally.[70,71] All these phases have been exploited to give rise to higher order structures.[72]

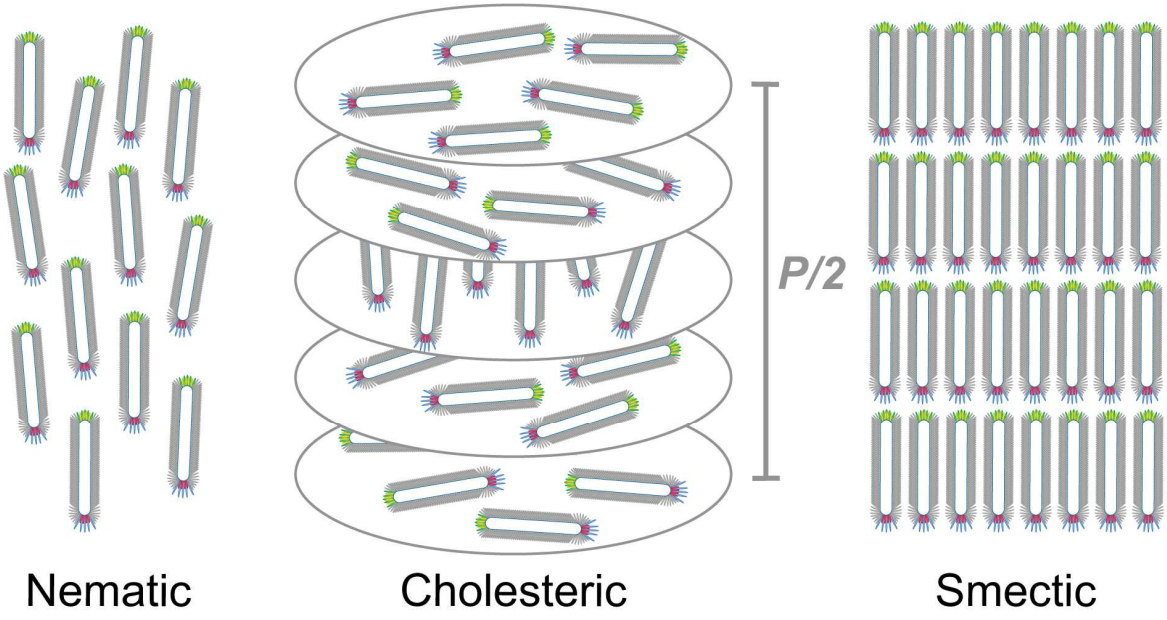


**Figure 1-5. Liquid crystalline structures of filamentous phage.** These structures are observed in a concentration-dependent manner and can give rise to higher order structures.

The laboratory of Angela M. Belcher explored the functionality of LC phage by first selecting P3-displayed peptides for a variety of semiconducting crystals.[73] In a subsequent study, Belcher and associates then suspended the A7 phage with ZnS quantum dots, resulting

in a liquid crystal hybrid material that could be observed at the nematic, cholesteric, and smectic phases.[72] As described in a 2003 communication from the Belcher lab, the phage were selected to bind streptavidin.[74] Streptavidin binds to biotin with high affinity. Thus, biotinylated streptavidin-binding phage can be used to align a variety of nanomaterials in a liquid crystalline phase.

Jun Cao *et al*. further elucidated the potential applications of LC phage.[75] The surfaces of phage were modified through N-hydroxysuccinimide chemistry to install pH-sensitive phenylboronic acid (PBA). Despite sharing physical properties with the unmodified phage, the modified phage could switch between chiral nematic and pure nematic LC phases in a pH-dependent manner. Furthermore, the anionic boronic acids decorating the phage surface conferred an additional phase change in response to diols. Thus, PBA-modified phage could be used for detection of either pH or the presence of diols.

Owing to its liquid crystalline behavior, phage have inherent piezoelectric properties.[76] Briefly, piezoelectric materials release electrons when stretched or compressed. Piezoelectric materials are an attractive option for bioimplants due to their ability to harvest energy without external input.[77–79] Byung Yang Lee *et al.* first used a simple drop-cast method to create self-assembled phage-based electric energy generators.[80] In 2019, Ju-Hyuck Lee *et al*. vertically aligned phage on a gold film via a hexahistidine-$Ni^{2+}$ affinity interaction, resulting in 100 times more piezoelectric power when compared to the drop-cast method.[81] At the time of publication, the piezoelectric energy output from this device was the highest ever reported for a biomaterial.

Humans are not the only organisms to take advantage of phage's liquid crystalline structure.[82] *Pseudomonas aeruginosa* (*P. aeruginosa*) is an opportunistic pathogen that can

result in multidrug-resistant (MDR) viral pneumonia, especially in immunocompromised patients.[83,84] The laboratory of E. Peter Greenberg reported 11 out of 14 filamentous phage gene products within the *P. aeruginosa* genome were upregulated in the protective biofilm.[85,86] The researchers hypothesized the phage had a role in gene transfer or toxicity. However, in 2015, Secor *et al.* shared a new insight: the phage form a liquid crystalline biofilm matrix that protects the *P. aeruginosa* from desiccation and antibiotics.[87,88] Thus, fundamental understanding of the liquid crystalline properties of phage could lead to advanced treatments for deadly MDR *P. aeruginosa* infection and other phage-microbe interactions we have yet to discover.

## 1.7 Conclusion

In conclusion, the inherent properties of phage are as valuable to functionalize hybrid materials as those exploited through phage display. Phage are readily propagated through typical molecular biology techniques, easily chemically modified, and monodisperse by nature. Additionally, phage can access liquid crystalline phases useful for alignment of quantum dots and piezoelectric energy generation. This review has presented the journey of phage biotechnology from Smith's seminal phage display work to a key component in a variety of hybrid materials.

## 1.8 References


(1) Kamran, U.; Heo, Y. J.; Lee, J. W.; Park, S. J. Functionalized Carbon Materials for Electronic Devices: A Review. *Micromachines* **2019**, *10* (4), 1-25. https://doi.org/10.3390/mi10040234.

(2) Zhang, Y.; Tamijani, A. A.; Taylor, M. E.; Zhi, B.; Haynes, C. L.; Mason, S. E.; Hamers, R. J. Molecular Surface Functionalization of Carbon Materials via Radical-Induced Grafting of Terminal Alkenes. *J. Am. Chem. Soc.* **2020**, *141* (20), 8277–8288. https://doi.org/10.1021/jacs.9b02369.

(3) Williamson, J. B.; Lewis, S. E.; Johnson, R. R.; Manning, I. M.; Leibfarth, F. A. C–H Functionalization of Commodity Polymers. *Angew. Chemie - Int. Ed.* **2019**, *58* (26), 8654–8668. https://doi.org/10.1002/anie.201810970.

(4) Bayer, M. E.; Bayer, M. H. Effects of Bacteriophage Fd Infection on Escherichia Coli HB11 Envelope: A Morphological and Biochemical Study. *J. Virol.* **1986**, *57* (1), 258–266. https://doi.org/10.1128/jvi.57.1.258-266.1986.

(5) Hofschneider, V. P. H. Untersuchungen Über "kleine“ E. Coli K12 Bakteriophagen. *Verlag der Zeitschrift für Naturforsch.* **1963**, *18* (3), 203–210.
(6) Marvin, D. A.; Hoffmann-Berling, H. Physical and Chemical Properties of Two New Small Bacteriophages. *Nature* **1963**, *197* (4866), 517–518. https://doi.org/10.1038/197517b0.
(7) Marvin, D. A.; Hoffmann-Berling, H. A Fibrous DNA Phage (Fd) and a Spherical RNA Phage (Fr) Specific for Male Strains of E. Coli: *Zeitschrift fur Naturforsch. B* **1963**, *18* (11), 884–893. https://doi.org/10.1515/znb-1963-1106.
(8) Loeb, T.; Zinder, N. D. A Bacteriophage Containing RNA. *Proc. Natl. Acad. Sci. U. S. A.* **1961**, *47*, 282–289. https://doi.org/10.1073/pnas.47.3.282.
(9) Zinder, N. D. Single-Stranded DNA-Containing Bacteriophages. *Bio Essays* **1986**, *5* (2), 84–87.
(10) Smith, G. P.; Petrenko, V. A. Phage Display. *Chem. Rev.* **1997**, *97* (2), 391–410. https://doi.org/10.1021/cr960065d.
(11) Bradley, D. E. The Structure of Some Bacteriophages Associated With Male Strains Of. *J. Gen. Microbiol.* **1964**, *35*, 471–482. https://doi.org/10.1099/00221287-35-3-471.
(12) Beck, E.; Sommer, R.; Auerswald, E. A.; Kurz, C.; Zink, B.; Osterburg, G.; Schaller, H.; Sugimoto, K.; Sugisaki, H.; Okamoto, T.; Takanami, M. Nucleotide Sequences of Bacteriophage Fd DNA. *Nucleic Acids Res.* **1978**, *5* (12), 4495–4504.
(13) Bayer, R.; Feigenson, G. W. Reconstitution of M13 Bacteriophage Coat Protein. A New Strategy to Analyze Configuration of the Protein in the Membrane. *BBA - Biomembr.* **1985**, *815* (3), 369–379. https://doi.org/10.1016/0005-2736(85)90363-3.
(14) Marvin, D. A.; Hale, R. D.; Nave, C.; Citterich, M. H. Molecular Models and Structural Comparisons of Native and Mutant Class I Filamentous Bacteriophages: Ff (Fd, F1, M13) If1 and IKe. *J. Mol. Biol.* **1994**, *235* (1), 260–286. https://doi.org/10.1016/S0022-2836(05)80032-4.
(15) Pratt, D.; Tzagoloff, H.; Beaudoin, J. Conditional Lethal Mutants of the Small Filamentous Coliphage M13. II. Two Genes for Coat Proteins. *Virology* **1969**, *39* (1), 42–53. https://doi.org/10.1016/0042-6822(69)90346-8.
(16) Thomas, G. J.; Murphy, P. Structure of Coat Proteins in Pfl and Fd Virions by Laser Raman Spectroscopy. *Science (80-. ).* **1975**, *188* (4194), 1205–1207. https://doi.org/10.1126/science.1170637.
(17) Günay, K. A.; Klok, H.-A. Identification of Soft Matter Binding Peptide Ligands Using Phage Display. *Bioconjug. Chem.* **2015**, *26* (10), 2012–2015. https://doi.org/10.1021/acs.bioconjchem.5b00377.
(18) Seker, U. O. S.; Demir, H. V. Material Binding Peptides for Nanotechnology. *Molecules* **2011**, *16* (2), 1426–1451. https://doi.org/10.3390/molecules16021426.
(19) Cao, B.; Yang, M.; Mao, C. Phage as a Genetically Modifiable Supramacromolecule in Chemistry, Materials and Medicine. *Acc. Chem. Res.* **2016**, *49* (6), 1111–1120. https://doi.org/10.1021/acs.accounts.5b00557.
(20) Smith, G. P. Filamentous Fusion Phage: Novel Expression Vectors That Display Cloned Antigens on the Virion Surface. *Science (80-. ).* **1985**, *228* (4705), 1315–1317. https://doi.org/10.1126/science.4001944.
(21) Parmley, S. F.; Smith, G. P. Antibody-Selectable Filamentous Fd Phage Vectors: Affinity Purification of Target Genes. *Gene* **1988**, *73* (2), 305–318. https://doi.org/10.1016/0378-1119(88)90495-7.
(22) Scott, J. K.; Smith, G. P. Searching for Peptide Ligands with an Epitope Library. *Science (80-. ).* **1990**, *249* (4967), 386–390. https://doi.org/10.1126/science.1696028.
(23) McCafferty, J.; Griffiths, A. D.; Winter, G.; Chiswell, D. J. Phage Antibodies Filamentous Phage Displaying Antibody Variable Domains. *Nature* **1990**, *348* (6301), 552.
(24) Barderas, R.; Benito-Peña, E. The 2018 Nobel Prize in Chemistry: Phage Display of Peptides and Antibodies. *Anal. Bioanal. Chem.* **2019**, *411* (12), 2475–2479. https://doi.org/10.1007/s00216-019-01714-4.
(25) Bartik, K.; Dobson, C. M.; Redfield, C. 1H-NMR Analysis of Turkey Egg-white Lysozyme and Comparison with Hen Egg-white Lysozyme. *Eur. J. Biochem.* **1993**, *215* (2), 255–266. https://doi.org/10.1111/j.1432-1033.1993.tb18030.x.
(26) Lu, R. M.; Hwang, Y. C.; Liu, I. J.; Lee, C. C.; Tsai, H. Z.; Li, H. J.; Wu, H. C. Development of Therapeutic Antibodies for the Treatment of Diseases. *J. Biomed. Sci.* **2020**, *27* (1), 1–30. https://doi.org/10.1186/s12929-019-0592-z.
(27) Barbas, C. F.; Kang, A. S.; Lerner, R. A.; Benkovic, S. J. Assembly of Combinatorial Antibody Libraries on Phage Surfaces: The Gene III Site. *Proc. Natl. Acad. Sci. U. S. A.* **1991**, *88* (18), 7978–7982.

https://doi.org/10.1073/pnas.88.18.7978.
(28) Kaplon, H.; Reichert, J. M. Antibodies to Watch in 2019. *MAbs* **2019**, *11* (2), 219–238. https://doi.org/10.1080/19420862.2018.1556465.
(29) Hoogenboom, H. R. Overview of Antibody Phage-Display Technology and Its Applications. *Methods Mol. Biol.* **2002**, *178*, 1–37. https://doi.org/10.1385/1-59259-240-6:001.
(30) Chen, G.; Sidhu, S. S. Design and Generation of Synthetic Antibody Libraries for Phage Display. *Methods Mol. Biol.* **2014**, *1131*, 113–131. https://doi.org/10.1007/978-1-62703-992-5_8.
(31) Den Broeder, A.; Van de Putte, L. B. A.; Rau, R.; Schattenkirchner, M.; Van Riel, P. L. C. M.; Sander, O.; Binder, C.; Fenner, H.; Bankmann, Y.; Velagapudi, R.; Kempeni, J.; Kupper, H. A Single Dose, Placebo Controlled Study of the Fully Human Anti-Tumor Necrosis Factor-α Antibody Adalimumab (D2E7) in Patients with Rheumatoid Arthritis. *J. Rheumatol.* **2002**, *29* (11), 2288–2298.
(32) Ding, C. Belimumab, an Anti-BLyS Human Monoclonal Antibody for Potential Treatment of Inflammatory Autoimmune Diseases. *Expert Opin. Biol. Ther.* **2008**, *8* (11), 1805–1814. https://doi.org/10.1517/14712598.8.11.1805.
(33) Krupitskaya, Y.; Wakelee, H. A. Ramucirumab, a Fully Human MAb to the Transmembrane Signaling Tyrosine Kinase VEGFR-2 for the Potential Treatment of Cancer. *Curr. Opin. Investig. Drugs* **2009**, *10* (6), 597–605.
(34) Kuenen, B.; Witteveen, P. O.; Ruijter, R.; Giaccone, G.; Dontabhaktuni, A.; Fox, F.; Katz, T.; Youssoufian, H.; Zhu, J.; Rowinsky, E. K.; Voest, E. E. A Phase I Pharmacologic Study of Necitumumab (IMC-11F8), a Fully Human IgG1 Monoclonal Antibody Directed against EGFR in Patients with Advanced Solid Malignancies. *Clin. Cancer Res.* **2010**, *16* (6), 1915–1923. https://doi.org/10.1158/1078-0432.CCR-09-2425.
(35) McDermott, D. F.; Sosman, J. A.; Sznol, M.; Massard, C.; Gordon, M. S.; Hamid, O.; Powderly, J. D.; Infante, J. R.; Fassò, M.; Wang, Y. V.; Zou, W.; Hegde, P. S.; Fine, G. D.; Powles, T. Atezolizumab, an Anti-Programmed Death-Ligand 1 Antibody, in Metastatic Renal Cell Carcinoma: Long-Term Safety, Clinical Activity, and Immune Correlates from a Phase Ia Study. *J. Clin. Oncol.* **2016**, *34* (8), 833–842. https://doi.org/10.1200/JCO.2015.63.7421.
(36) Boyerinas, B.; Jochems, C.; Fantini, M.; Heery, C. R.; Gulley, J. L.; Tsang, K. Y.; Schlom, J. Antibody-Dependent Cellular Cytotoxicity Activity of a Novel Anti–PD-L1 Antibody Avelumab (MSB0010718C) on Human Tumor Cells. *Cancer Immunol. Res.* **2015**, *3* (10), 1148–1157. https://doi.org/10.1158/2326-6066.CIR-15-0059.
(37) Sofen, H.; Smith, S.; Matheson, R. T.; Leonardi, C. L.; Calderon, C.; Brodmerkel, C.; Li, K.; Campbell, K.; Marciniak, S. J.; Wasfi, Y.; Wang, Y.; Szapary, P.; Krueger, J. G. Guselkumab (an IL-23-Specific MAb) Demonstrates Clinical and Molecular Response in Patients with Moderate-to-Severe Psoriasis. *J. Allergy Clin. Immunol.* **2014**, *133* (4), 1032–1040. https://doi.org/10.1016/j.jaci.2014.01.025.
(38) Al-Salama, Z. T. Emapalumab: First Global Approval. *Drugs* **2019**, *79* (1), 99–103. https://doi.org/10.1007/s40265-018-1046-8.
(39) Kreitman, R. J.; Dearden, C.; Zinzani, P. L.; Delgado, J.; Karlin, L.; Robak, T.; Gladstone, D. E.; le Coutre, P.; Dietrich, S.; Gotic, M.; Larratt, L.; Offner, F.; Schiller, G.; Swords, R.; Bacon, L.; Bocchia, M.; Bouabdallah, K.; Breems, D. A.; Cortelezzi, A.; Dinner, S.; Doubek, M.; Gjertsen, B. T.; Gobbi, M.; Hellmann, A.; Lepretre, S.; Maloisel, F.; Ravandi, F.; Rousselot, P.; Rummel, M.; Siddiqi, T.; Tadmor, T.; Troussard, X.; Yi, C. A.; Saglio, G.; Roboz, G. J.; Balic, K.; Standifer, N.; He, P.; Marshall, S.; Wilson, W.; Pastan, I.; Yao, N. S.; Giles, F. Moxetumomab Pasudotox in Relapsed/Refractory Hairy Cell Leukemia. *Leukemia* **2018**, *32* (8), 1768–1777. https://doi.org/10.1038/s41375-018-0210-1.
(40) Bass, S.; Greene, R.; Wells, J. A. Hormone Phage: An Enrichment Method for Variant Proteins with Altered Binding Properties. *Proteins Struct. Funct. Bioinforma.* **1990**, *8* (4), 309–314. https://doi.org/10.1002/prot.340080405.
(41) Barbas, C. F. I.; Burton, D. R.; Scott, J. K.; Silverman, G. J. *Phage Display: A Laboratory Manual*; Cold Spring Harbor Laboratory Press, 2001.
(42) Davidson, T. A.; McGoldrick, S. J.; Kohn, D. H. Phage Display to Augment Biomaterial Function. *Int. J. Mol. Sci.* **2020**, *21* (17), 1–17. https://doi.org/10.3390/ijms21175994.
(43) Li, K.; Chen, Y.; Li, S.; Nguyen, H. G.; Niu, Z.; You, S.; Mello, C. M.; Lu, X.; Wang, Q. Chemical Modification of M13 Bacteriophage and Its Application in Cancer Cell Imaging. *Bioconjug. Chem.* **2010**, *21* (7), 1369–1377. https://doi.org/10.1021/bc900405q.
(44) Drago, J. Z.; Modi, S.; Chandarlapaty, S. Unlocking the Potential of Antibody–Drug Conjugates for Cancer

Therapy. *Nat. Rev. Clin. Oncol.* **2021**, *0123456789*, 1–18. https://doi.org/10.1038/s41571-021-00470-8.

(45) Yacoby, I.; Bar, H.; Benhar, I. Targeted Drug-Carrying Bacteriophages as Antibacterial Nanomedicines. *Antimicrob. Agents Chemother.* **2007**, *51* (6), 2156–2163. https://doi.org/10.1128/AAC.00163-07.

(46) Bar, H.; Yacoby, I.; Benhar, I. Killing Cancer Cells by Targeted Drug-Carrying Phage Nanomedicines. *BMC Biotechnol.* **2008**, *8*, 1–14. https://doi.org/10.1186/1472-6750-8-37.

(47) Yacoby, I.; Shamis, M.; Bar, H.; Shabat, D.; Benhar, I. Targeting Antibacterial Agents by Using Drug-Carrying Filamentous Bacteriophages. *Antimicrob. Agents Chemother.* **2006**, *50* (6), 2087–2097. https://doi.org/10.1128/AAC.00169-06.

(48) Zimmermann, K.; Hagedorn, H.; Heuck, C. C.; Hinrichsen, M.; Ludwig, H. The Ionic Properties of the Filamentous Bacteriophages Pf1 and Fd. *J. Biol. Chem.* **1986**, *261* (4), 1653–1655. https://doi.org/10.1016/s0021-9258(17)35990-2.

(49) Lamboy, J. A.; Arter, J. A.; Knopp, K. A.; Der, D.; Overstreet, C. M.; Palermo, E. F.; Urakami, H.; Yu, T. Bin; Tezgel, O.; Tew, G. N.; Guan, Z.; Kuroda, K.; Weiss, G. A. Phage Wrapping with Cationic Polymers Eliminates Nonspecific Binding between M13 Phage and High PI Target Proteins. *J. Am. Chem. Soc.* **2009**, *131* (45), 16454–16460. https://doi.org/10.1021/ja9050873.

(50) Lamboy, J. A.; Tam, P. Y.; Lee, L. S.; Jackson, P. J.; Avrantinis, S. K.; Lee, H. J.; Corn, R. M.; Weiss, G. A. Chemical and Genetic Wrappers for Improved Phage and RNA Display. *Chembiochem* **2008**, *9* (17), 2846–2852. https://doi.org/10.1002/cbic.200800366.Chemical.

(51) Arter, J. A.; Taggart, D. K.; McIntire, T. M.; Penner, R. M.; Weiss, G. A. Virus-PEDOT Nanowires for Biosensing. *Nano Lett.* **2010**, *10* (12), 4858–4862. https://doi.org/10.1021/nl1025826.

(52) Arter, J. A.; Diaz, J. E.; Donavan, K. C.; Yuan, T.; Penner, R. M.; Weiss, G. A. Virus-Polymer Hybrid Nanowires Tailored to Detect Prostate-Specific Membrane Antigen. *Anal. Chem.* **2012**, *84* (6), 2776–2783. https://doi.org/10.1021/ac203143y.

(53) Donavan, K. C.; Arter, J. A.; Pilolli, R.; Cio, N.; Weiss, G. A.; Penner, R. M.; Chimica, D.; Aldo, B. Virus - Poly(3,4-Ethylenedioxythiophene) Composite Films for Impedance-Based Biosensing. *Anal. Chem.* **2011**, *83*, 2420–2424.

(54) Ogata, A. F.; Edgar, J. M.; Majumdar, S.; Briggs, J. S.; Patterson, S. V.; Tan, M. X.; Kudlacek, S. T.; Schneider, C. A.; Weiss, G. A.; Penner, R. M. Virus-Enabled Biosensor for Human Serum Albumin. *Anal. Chem.* **2017**, *89* (2), 1373–1381. https://doi.org/10.1021/acs.analchem.6b04840.

(55) Diaz, J. E.; Yang, L. C.; Lamboy, J. A.; Penner, R. M.; Weiss, G. A. *Synthesis of a Virus Electrode for Measurement of Prostate Specific Membrane Antigen*; Rasooly, A., Herold, K. E., Eds.; Humana Press, 2009; Vol. 504. https://doi.org/10.1007/978-1-60327-569-9.

(56) Mohan, K.; Donavan, K. C.; Arter, J. A.; Penner, R. M.; Weiss, G. A. Sub-Nanomolar Detection of Prostate-Specific Membrane Antigen in Synthetic Urine by Synergistic, Dual-Ligand Phage. *J. Am. Chem. Soc.* **2013**, *135* (20), 7761–7767. https://doi.org/10.1021/ja4028082.

(57) Bhasin, A.; Drago, N. P.; Majumdar, S.; Sanders, E. C.; Weiss, G. A.; Penner, R. M. Viruses Masquerading as Antibodies in Biosensors: The Development of the Virus BioResistor. *Acc. Chem. Res.* **2020**. https://doi.org/10.1021/acs.accounts.0c00474.

(58) Bhasin, A.; Ogata, A. F.; Briggs, J. S.; Tam, P. Y.; Tan, M. X.; Weiss, G. A.; Penner, R. M. The Virus Bioresistor: Wiring Virus Particles for the Direct, Label-Free Detection of Target Proteins. *Nano Lett.* **2018**, *18* (6), 3623–3629. https://doi.org/10.1021/acs.nanolett.8b00723.

(59) Bhasin, A.; Sanders, E. C.; Ziegler, J. M.; Briggs, J. S.; Drago, N. P.; Attar, A. M.; Santos, A. M.; True, M. Y.; Ogata, A. F.; Yoon, D. V.; Majumdar, S.; Wheat, A. J.; Patterson, S. V.; Weiss, G. A.; Penner, R. M. Virus Bioresistor (VBR) for Detection of Bladder Cancer Marker DJ-1 in Urine at 10 PM in One Minute. *Anal. Chem.* **2020**, *92* (9), 6654–6666. https://doi.org/10.1021/acs.analchem.0c00534.

(60) Patra, J. K.; Das, G.; Fraceto, L. F.; Campos, E. V. R.; Rodriguez-Torres, M. D. P.; Acosta-Torres, L. S.; Diaz-Torres, L. A.; Grillo, R.; Swamy, M. K.; Sharma, S.; Habtemariam, S.; Shin, H. S. Nano Based Drug Delivery Systems: Recent Developments and Future Prospects. *J. Nanobiotechnology* **2018**, *16* (1), 1–33. https://doi.org/10.1186/s12951-018-0392-8.

(61) Li, T.; Wu, L.; Suthiwangcharoen, N.; Bruckman, M. A.; Cash, D.; Hudson, J. S.; Ghoshroy, S.; Wang, Q. Controlled Assembly of Rodlike Viruses with Polymers. *Chem. Commun.* **2009**, No. 20, 2869–2871. https://doi.org/10.1039/b901995b.

(62) Nam, K. T.; Reelle, B. R.; Lee, S. W.; Belcher, A. M. Genetically Driven Assembly of Nanorings Based on the M13 Virus. *Nano Lett.* **2004**, *4* (1), 23–27. https://doi.org/10.1021/nl0347536.

(63) Suthiwangcharoen, N.; Li, T.; Li, K.; Thompson, P.; You, S.; Wang, Q. M13 Bacteriophage-Polymer Nanoassemblies as Drug Delivery Vehicles. *Nano Res.* **2011**, *4* (5), 483–493. https://doi.org/10.1007/s12274-011-0104-2.
(64) Purdy, K. R.; Fraden, S. Isotropic-Cholesteric Phase Transition of Filamentous Virus Suspensions as a Function of Rod Length and Charge. *Phys. Rev. E - Stat. Physics, Plasmas, Fluids, Relat. Interdiscip. Top.* **2004**, *70* (6), 8. https://doi.org/10.1103/PhysRevE.70.061703.
(65) Dogic, Z.; Fraden, S. Ordered Phases of Filamentous Viruses. *Curr. Opin. Colloid Interface Sci.* **2006**, *11* (1), 47–55. https://doi.org/10.1016/j.cocis.2005.10.004.
(66) Woltman, S. J.; Jay, G. D.; Crawford, G. P. Liquid-Crystal Materials Find a New Order in Biomedical Applications. *Nat. Mater.* **2007**, *6* (12), 929–938. https://doi.org/10.1038/nmat2010.
(67) Dogic, Z.; Fraden, S. Cholesteric Phase in Virus Suspensions. *Langmuir* **2000**, *16* (20), 7820–7824. https://doi.org/10.1021/la000446t.
(68) Lapointe, J.; Marvin, D. A. Filamentous Bacterial Viruses VIII. Liquid Crystals of Fd. *Mol. Cryst. Liq. Cryst.* **1973**, *19* (3–4), 269–278. https://doi.org/10.1080/15421407308084657.
(69) Grelet, E.; Fraden, S. What Is the Origin of Chirality in the Cholesteric Phase of Virus Suspensions? *Phys. Rev. Lett.* **2003**, *90* (19), 4. https://doi.org/10.1103/PhysRevLett.90.198302.
(70) Dogic, Z.; Fraden, S. Smectic Phase in a Colloidal Suspension of Semiflexible Virus Particles. *Phys. Rev. Lett.* **1997**, *78* (12), 1–4.
(71) Lee, S. W.; Wood, B. M.; Belcher, A. M. Chiral Smectic C Structures of Virus-Based Films. *Langmuir* **2003**, *19* (5), 1592–1598. https://doi.org/10.1021/la026387w.
(72) Lee, S.-W. Ordering of Quantum Dots Using Genetically Engineered Viruses. *Science (80-. ).* **2002**, *296* (5569), 892–895. https://doi.org/10.1126/science.1068054.
(73) Whaley, S. R.; English, D. S.; Hu, E. L.; Barbara, P. F.; Belcher, A. M. Selection of Peptides with Semiconductor Binding Specificity for Directed Nanocrystal Assembly. *Nature* **2000**, *405* (6787), 665–668. https://doi.org/10.1038/35015043.
(74) Lee, S. W.; Lee, S. K.; Belcher, A. M. Virus-Based Alignment of Inorganic, Organic, and Biological Nanosized Materials. *Adv. Mater.* **2003**, *15* (9), 689–692. https://doi.org/10.1002/adma.200304818.
(75) Cao, J.; Liu, S.; Xiong, J.; Chen, Y.; Zhang, Z. Stimuli Responsive Chiral Liquid Crystal Phases of Phenylboronic Acid Functionalized Rodlike Viruses and Their Interaction with Biologically Important Diols. *Chem. Commun.* **2014**, *50* (72), 10402–10405. https://doi.org/10.1039/c4cc04639k.
(76) Park, I. W.; Kim, K. W.; Hong, Y.; Yoon, H. J.; Lee, Y.; Gwak, D.; Heo, K. Recent Developments and Prospects of M13-Bacteriophage Based Piezoelectric Energy Harvesting Devices. *Nanomaterials* **2020**, *10* (1). https://doi.org/10.3390/nano10010093.
(77) Ali, F.; Raza, W.; Li, X.; Gul, H.; Kim, K. H. Piezoelectric Energy Harvesters for Biomedical Applications. *Nano Energy* **2019**, *57*, 879–902. https://doi.org/10.1016/j.nanoen.2019.01.012.
(78) Zhou, Q.; Lau, S.; Wu, D.; Kirk Shung, K. Piezoelectric Films for High Frequency Ultrasonic Transducers in Biomedical Applications. *Prog. Mater. Sci.* **2011**, *56* (2), 139–174. https://doi.org/10.1016/j.pmatsci.2010.09.001.
(79) Hwang, G. T.; Byun, M.; Jeong, C. K.; Lee, K. J. Flexible Piezoelectric Thin-Film Energy Harvesters and Nanosensors for Biomedical Applications. *Adv. Healthc. Mater.* **2015**, *4* (5), 646–658. https://doi.org/10.1002/adhm.201400642.
(80) Lee, B. Y.; Zhang, J.; Zueger, C.; Chung, W. J.; Yoo, S. Y.; Wang, E.; Meyer, J.; Ramesh, R.; Lee, S. W. Virus-Based Piezoelectric Energy Generation. *Nat. Nanotechnol.* **2012**, *7* (6), 351–356. https://doi.org/10.1038/nnano.2012.69.
(81) Lee, J. H.; Lee, J. H.; Xiao, J.; Desai, M. S.; Zhang, X.; Lee, S. W. Vertical Self-Assembly of Polarized Phage Nanostructure for Energy Harvesting. *Nano Lett.* **2019**, *19* (4), 2661–2667. https://doi.org/10.1021/acs.nanolett.9b00569.
(82) Hay, I. D.; Lithgow, T. Filamentous Phages: Masters of a Microbial Sharing Economy. *EMBO Rep.* **2019**, *20* (6), 1–24. https://doi.org/10.15252/embr.201847427.
(83) Barbier, F.; Andremont, A.; Wolff, M.; Bouadma, L. Hospital-Acquired Pneumonia and Ventilator-Associated Pneumonia: Recent Advances in Epidemiology and Management. *Curr. Opin. Pulm. Med.* **2013**, *19* (3), 216–228. https://doi.org/10.1097/MCP.0b013e32835f27be.
(84) Sadikot, R. T.; Blackwell, T. S.; Christman, J. W.; Prince, A. S. Pathogen-Host Interactions in Pseudomonas Aeruginosa Pneumonia. *Am. J. Respir. Crit. Care Med.* **2005**, *171* (11), 1209–1223. https://doi.org/10.1164/rccm.200408-1044SO.

(85) Greenberg, E. P.; Whiteley, M.; Bangera, M. G.; Bumgarner, R. E.; Parsek, M. R.; Teitzel, G. M.; Lory, S. Gene Expression in Pseudomonas Aeruginosa Biofilms. *Nature* **2001**, *413*, 860–864.
(86) Knezevic, P.; Voet, M.; Lavigne, R. Prevalence of Pf1-like (pro)Phage Genetic Elements among Pseudomonas Aeruginosa Isolates. *Virology* **2015**, *483*, 64–71. https://doi.org/10.1016/j.virol.2015.04.008.
(87) Secor, P. R.; Sweere, J. M.; Michaels, L. A.; Malkovskiy, A. V.; Lazzareschi, D.; Katznelson, E.; Rajadas, J.; Birnbaum, M. E.; Arrigoni, A.; Braun, K. R.; Evanko, S. P.; Stevens, D. A.; Kaminsky, W.; Singh, P. K.; Parks, W. C.; Bollyky, P. L. Filamentous Bacteriophage Promote Biofilm Assembly and Function. *Cell Host Microbe* **2015**, *18* (5), 549–559. https://doi.org/10.1016/j.chom.2015.10.013.Filamentous.
(88) Chang, Y. W. Bacteria Suit up with Virus Armor. *Proc. Natl. Acad. Sci. U. S. A.* **2020**, *117* (12), 6297–6299. https://doi.org/10.1073/pnas.2001931117.

# CHAPTER 2

## Phage vs. Phage: Direct Selections of Sandwich Binding Pairs for Improved Biomarker Detection

### 2.1 Abstract

The sandwich immunoassay format is generally more sensitive and specific than other common formats such as direct, indirect, and competitive. A sandwich assay necessitates two separate target-binders, typically antibodies or antibody fragments (Fabs), that do not compete with each other. However, the most common method to identify sandwich binding pairs is via guess-and-check with a panel of candidates, which can be cumbersome and expensive. Additionally, sandwich assays that rely on commercial antibodies can suffer from quality loss outside of researchers' control. This report presents a reimagined phage display selection protocol that directly identifies sandwich binding peptides and Fabs. This modified protocol yielded a novel peptide and Fab that can sandwich the bladder cancer biomarker DJ-1 in concert with a previously selected DJ-1 binding peptide. Furthermore, the sandwich assays resulted in apparent affinity similar to that observed for a previously reported peptide/antibody sandwich. The results reported here could guide the discovery of new sandwich binding partners to develop novel clinical biomarker assays.

## 2.2 Introduction

Advances in precision medicine are paving the future of patient care with tailored diagnostics and treatments. This personalized medical approach could benefit from sensitive, accurate, biomarker-based diagnostics to detect diseases early and monitor treatment response.[1,2] Because this approach requires frequent testing, the ideal sample should be collected noninvasively in a "liquid biopsy" (e.g. blood, urine, or saliva).[3–6] However, these fluids can vary considerably in composition and biomarker concentrations, which are typically low.[7–11] Thus, precision medicine necessitates platforms for sensitive and selective biomarker detection in complex physiological fluids.

The sandwich-format assay can address the dual challenges of sensitivity and selectivity.[12–17] However, this assay format requires two compatible binding partners to noncompetitively target the same antigen. The most prominent example of a sandwich-format assay is the at-home pregnancy test, which can detect the early pregnancy hormone human chorionic gonadotropin.[18] This assay system has also been applied to countless detection platforms for ailments such as bladder cancer[19], severe skeletal injury[20], and heart failure[21], among many others. The requirement for the target binding to both antibodies addresses the specificity challenge inherent in biological assays. Additionally, an improvement in sensitivity is often observed.

However, identification of antibody pairs is often cumbersome and costly. Typically, a collection of commercial antibodies is acquired and systematically screened to test each antibody pair. As the number of testable antibodies increases, however, the required assays increases combinatorially. Once a sandwich pair is found, product discontinuation or genetic drift of the hybridoma cell line could result in the loss of an effective assay.[22,23]

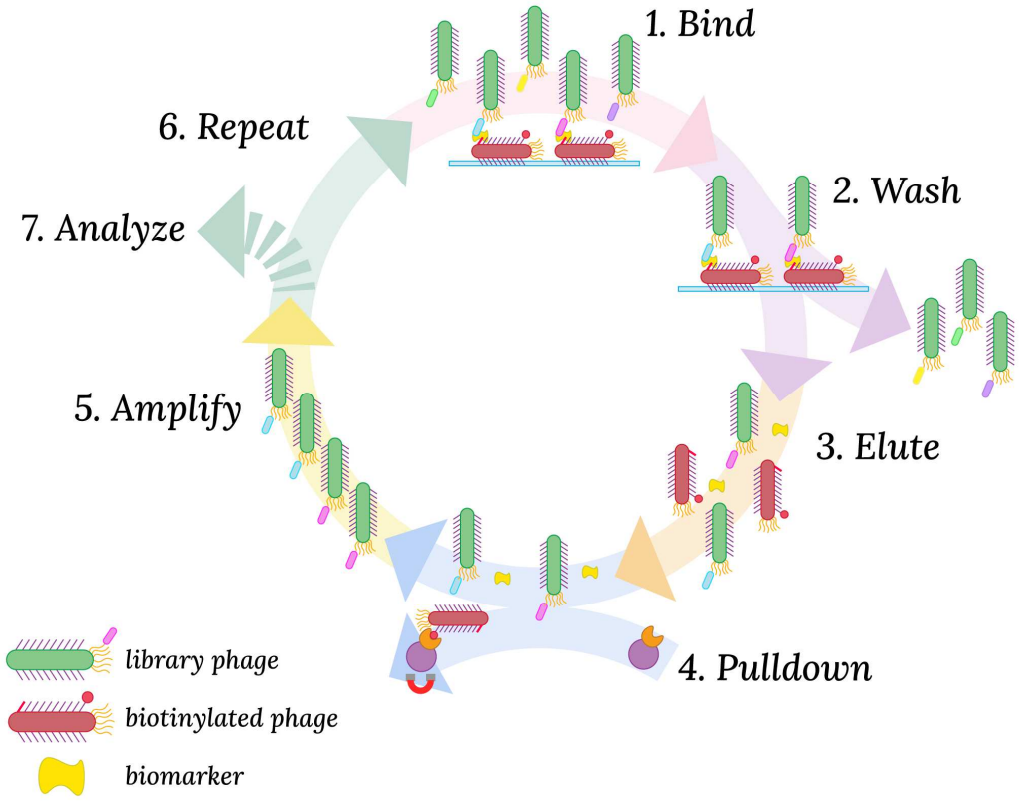


**Figure 2-1. Phage vs. phage selection strategy.** **1)** The bDL1Φ is adsorbed to a microtiter plate and exposed to DJ-1. Next, the phage library is added and allowed to bind. **2)** Nonbinding phage are removed by washing. **3)** Sandwich assemblies are eluted from the microtiter plate by the addition of acid with sonication. **4)** The suspended bDL1Φ are removed from solution with magnetic streptavidin beads. **5)** The sandwich binding phage are used to infect *E. coli* and amplified. **6)** The process is repeated with the amplified selectants as the phage library for the next round of selection. **7)** After 3-4 rounds of selections, the selectants are identified by DNA sequencing.

To address these issues, a number of reports describe methods for improved sandwich pair discovery. For example, Ki *et al.* immobilized cetuximab, a commercially available antibody, on a microtiter plate and performed antibody phage display selections.[24] While this technique successfully identified a sandwich pair, the method still requires a commercial antibody in a solid support binding mode. Gorman *et al.* demonstrated a powerful phage-display technique for the direct selection of monobody sandwich pairs, Megaprimer Shuffling for Tandem Affinity Reagents (MegaSTAR). With MegaSTAR, the researchers identified a multitude of highly sensitive nanobody sandwich pairs.[25] However, this approach requires lengthy and technically challenging subcloning steps to generate a

tandem phage library for each target. Therefore, a stream-lined and facile approach to discovering sandwich binding pairs could find many applications.

Here we address this challenge with a simple, expedient, and generalizable method, termed phage vs. phage (PvP) selection. Using PvP, non-overlapping phage-displayed binders specific for protein deglycase 1 (DJ-1), a multi-functional biomarker for several cancers and Parkinson's disease,[26–32] are identified from both peptide and antibody fragment (Fab) libraries. Enzyme-linked immunosorbent assays (ELISA) demonstrate the specific and sensitive sandwich binding pairs generated by the method.

### 2.3 Results and Discussion

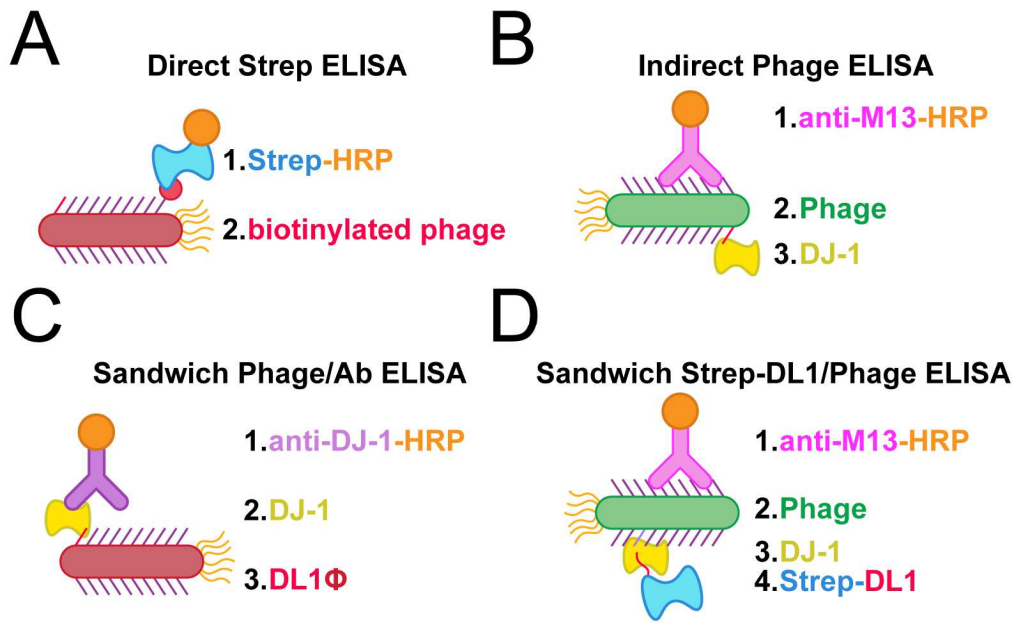


**Figure 2-2. Schematics of ELISA formats presented. A)** The direct strep-HRP ELISA detects biotinylated phage with peroxidase-conjugated streptavidin (Strep-HRP). **B)** DJ-1 is detected via phage-displayed binders and peroxidase-conjugated anti-M13 antibody (anti-M13-HRP). **C)** DJ-1 is sandwiched between DL1Φ and an anti-DJ-1 antibody. **D)** DJ-1 is sandwiched between DL1-conjugated streptavidin (Strep-DL1) and phage-displayed binders. The sandwich assembly is detected with anti-M13-HRP.

*Sandwich Phage Selections.* The method reported here builds on conventional phage display. First, conventional selections are used to identify an effective binder for one half of the sandwich assembly. This known binding partner must be exhaustively culled from

solution during the selection for the second half of the sandwich interaction. Such exhaustive removal avoided amplifyication of the known ligand. Biotinylation and subtraction with streptavidin magnetic beads insures only noncompetitive phage display ligands are selected for amplification. We termed this approach phage vs. phage (PvP) selection (**Fig. 2-1**).

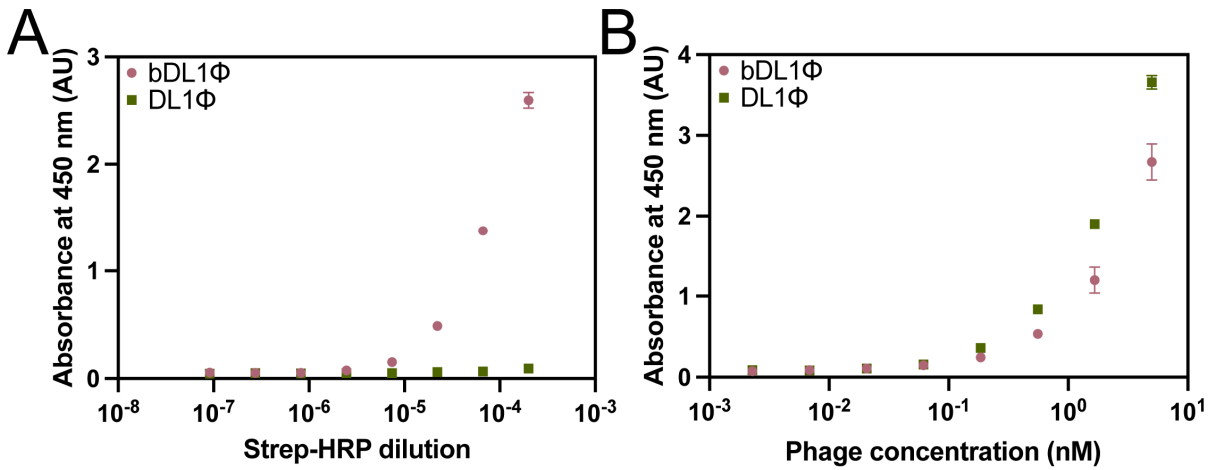


**Figure 2-3. Analysis of phage biotinylation and target-binding effects.** **A)** Biotinylation of phage was confirmed via direct detection with peroxidase-conjugated streptavidin. **B)** A direct ELISA with DJ-1 verified that biotinylated phage could still bind the target antigen. ELISA data were fit to a four-parameter logistic curve. Error is represented as SEM (n = 3).

For PvP selection, biotinylated DJ-1 Ligand 1 Phage (bDL1Φ) were adsorbed to a microtiter plate rather than the target antigen. In PvP, DL1Φ's target antigen, DJ-1, is added after blocking nonspecific interactions. Next, the addition of phage library allows binding to the DL1Φ/DJ-1 complex. In theory, only noncompetitive sandwich binding partners should be selected. However, due to DL1Φ's overwhelming abundance compared to any selectant in the library, removal of DL1Φ from the sandwich assembly was required to avoid suppression of selectants from each round.

Removing DL1Φ was inspired by a streptavidin-biotin pulldown assay. First, DL1Φ and negative control phage (NegΦ) were biotinylated via N-hydroxysuccinimide (NHS) chemistry to yield bDL1Φ and bNegΦ. The efficiency of the biotinylation reactions were confirmed via a direct strep ELISA (**Fig. 2-2A**) detection with peroxidase-conjugated

streptavidin (**Fig. 2-3A**). Additionally, an indirect phage ELISA (**Fig. 2-2B)** demonstrated biotinylation did not prevent DL1Φ from binding DJ-1 (**Fig. 2-3B**). For PvP to function, streptavidin magnetic beads must completely remove bDL1Φ from solution. A pull-down assay titrating the concentration of magnetic beads provided proof-of-concept for PvP selections.

*Characterization of Sandwich Peptide Selectants.* The PvP selection strategy was first performed with a P8-display mega-random peptide library[33] (**Table 2-1**). The method yielded three peptides amenable to further characterization (**Table 2-2**). A phage indirect ELISA with DJ-1 and the selectants (DL2Φ, DL3Φ, and DL4Φ) produced sigmoidal curves characteristic of dose-dependent binding in an indirect phage ELISA (**Fig. 2-4A**). All selectants demonstrated sub-micromolar phage $EC_{50}$ values, about one order of magnitude higher in apparent affinity than the previously reported $EC_{50}$ for DL1Φ (14 pM).[34] This loss in apparent affinity could result from the DL1 peptide blocking the most thermodynamically productive binding sites on DJ-1. Supporting this hypothesis, the PvP selectants are not homologous to DL1 (**Table 2**). Additionally, the selectants have an average theoretical isoelectric point (pI) of 4.47 ± 1.11, compared to 8.01 for DL1, which suggests noncompetitive binding with DJ-1.

**Table 2-1. Titers, blocking agents, and stringency for PvP peptide selections.**

| | Titers | Blocking | Washes |
|---|---|---|---|
| Round 1 | $7.9 \times 10^8$ | Nonfat Milk | 3 |
| Round 2 | $3.4 \times 10^5$ | Bovine serum albumin | 6 |
| Round 3 | $2.4 \times 10^5$ | Human serum albumin | 6 |
| Round 4 | $\sim 1.0 \times 10^6$ | Pierce blocking | 6 |

**Table 2-2. Comparison of DL1 peptide with PvP selectants.**

| Peptide | Amino Acid Sequence | Theoretical pI |
|---|---|---|
| DL1 | KYRYVCHDVGGTLYCIRDWV | 8.03 |
| DL2 | TSYQCHDCGSSLCCVVLPEI | 4.35 |
| DL3 | TEIWYLVL | 4.00 |
| DL4 | SRVFVISCEGPLCTLHTFIA | 6.46 |
| DL5 | CMKEAMCPV | 5.99 |
| DL6 | SLCWNTWFFVCME | 4.00 |
| DL7 | DGSYCEYGPVQDACWTNY | 3.49 |
| DL8 | PGSYCQYGPMQDACCTNY | 3.80 |
| DL9 | ALTYCYSGPETWVCGQDS | 3.67 |

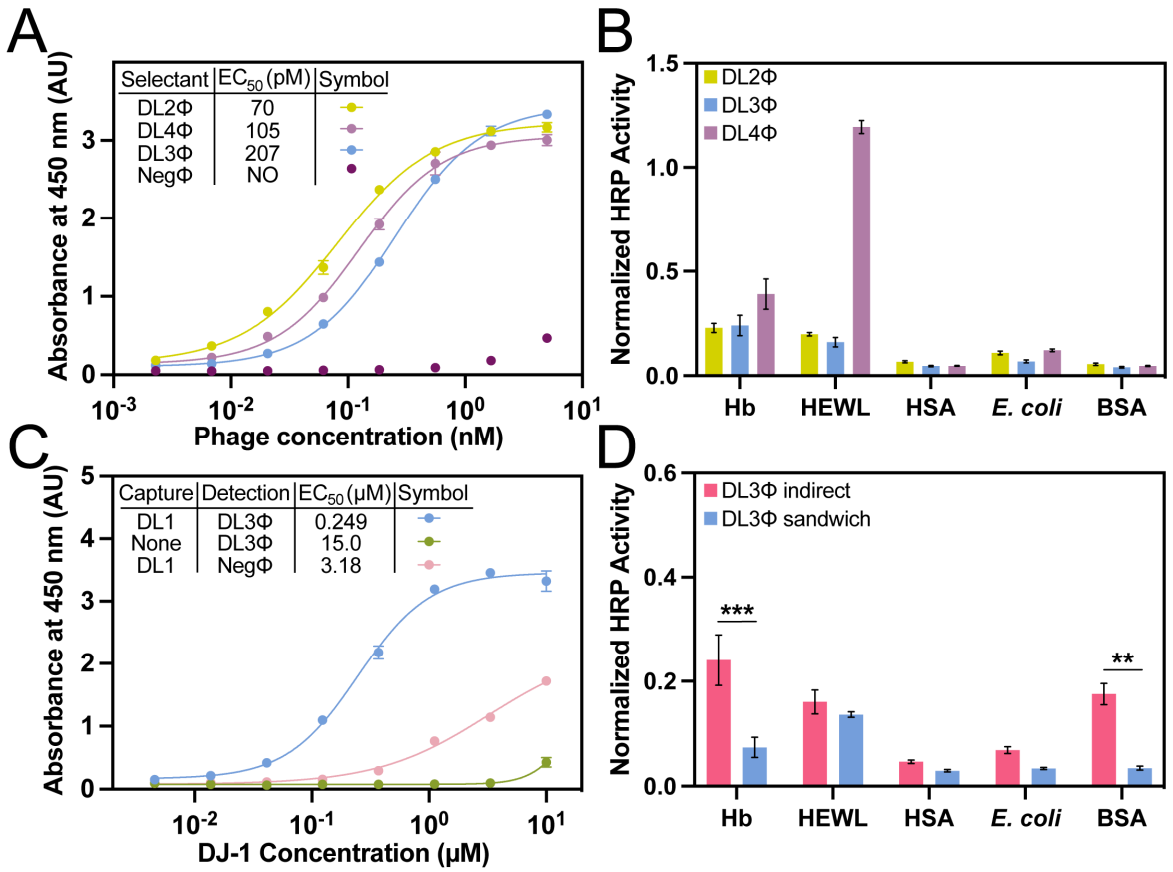


**Figure 2-4. Sensitivity and specificity determination of sandwich peptide selectants.** **A)** A dose-dependent direct phage assay with sandwich peptide selectants. Sub-micromolar phage $EC_{50}$ values were observed. NO = not observed. **B)** A indirect phage assay with DJ-1, Hb, HEWL, HSA, *E. coli* lysate, and BSA determined the specificity of the sandwich selectants. Data are normalized to DJ-1 signal. **C)** Streptavidin-bound DL1 peptide sandwiched DJ-1 with DL3Φ. The resultant dose-dependent response yielded a DJ-1 $EC_{50}$ of 249 pM. **D)** The DL1-DL3Φ sandwich also demonstrated improved selectivity for DJ-1. ANOVA with Sidak's multiple comparisons yielded P values of <0.01 (**) and <0.001 (***). ELISA data were fit to a four-parameter logistic curve. Error bars represent SEM (n = 3).

The relative specificity of each selectant was determined by indirect phage ELISA with a profile of competing antigens (**Table 2-3, Fig. 2-4B**). Hemoglobin (Hb), human serum albumin (HSA), and F$^-$ *E. coli* lysate are potential interfering substances in biofluids. The high-pI hen egg white lysozyme (HEWL) was chosen to assess the nonspecificity binding to the anionic phage. Due to its ubiquity as a blocking agent in assays, bovine serum albumin (BSA) was also included. Compared to the other selectants, DL9Φ displayed a lack of specificity for DJ-1 over HEWL. However, all selectants were further assessed due to an expected improvement in both sensitivity and specificity from the sandwich binding interaction.

**Table 2-3. Panel of antigens in specifcity assays.**

| Protein | Native Species | Molecular Weight (kDa) | pI |
|---|---|---|---|
| DJ-1 | *Homo sapiens* | 20.7 | 6.7 |
| HSA | *Homo sapiens* | 66.5 | 4.7 |
| Hb | *Homo sapiens* | 64 | 6.8 |
| HEWL | *Gallus domesticus* | 14.4 | 11.3 |
| *E. coli* | *Escherichia coli* | Varies | Varies |

*Sandwich ELISAs with Peptide Selectants.* Despite extensive efforts, a sandwich ELISA with two phage binding partners failed repeatedly (data not shown). This necessitated an alternative strategy, the sandwich strep-DL1/phage ELISA (**Fig. 2-2D**). Non-phage-displayed, biotinylated DL1 peptides were immobilized on a streptavidin-coated microtiter plate and exposed to serial dilutions of DJ-1. Next, phage peptide selectants completed the sandwich assembly, followed by a peroxidase-conjugated anti-phage antibody to detect the binding interaction (**Fig. 2-3C**). The DL2Φ and DL9Φ sandwich ELISAs were unsuccessful. However, the DL3Φ sandwich ELISA returned a sigmoidal binding curve and a DJ-1 $EC_{50}$ comparable to a previously reported sandwich phage/antibody ELISA (**Fig. 2-2C**) with a commercial anti-DJ-1 antibody (206 nM).[34] At higher concentrations nonspecificity with

NegΦ is observed; however, these concentrations are not biologically relevant and the background signal significantly decreases with lower DJ-1 concentrations.

The sandwich strep-DL1/phage ELISA described above with the same panel of interfering antigens (Hb, HEWL, HSA, *E. coli* lysate, and BSA) evaluated the specificity improvements with the sandwich assembly (**Fig. 2-4D**). The raw assay data are challenging to accurately compare, as the assay formats (indirect vs. sandwich) are not analogous. Thus, the data were normalized to the DJ-1 signal for each assay format. Statistical analysis of these normalized data revealed an enhancement of specificity. Specifically, the Hb and BSA signal dropped significantly in the sandwich format, with P values of $<0.001$ and $<0.01$, respectively. These data, when considered with the dose-dependent sandwich ELISA data, indicate that the PvP selection strategy is capable of yielding sandwich binding pairs. Furthermore, these pairs can rival a sandwich assay with a commercial antibody in sensitivity and improve selectivity compared to the phage indirect assay.

*PvP Selections with Fab Phage-Displayed Library.* An additional selection protocol with a different phage library demonstrated the generality of the PvP method. The procedure was performed exactly as described above with a P3 Fab phage-displayed library in place of MRPL (**Table 2-4**).[35] Three rounds of PvP selections identified a DJ-1 binding phage-displayed Fab (DFab1Φ) (**Table 2-5**). An indirect phage ELISA with immobilized DJ-1 revealed a DFab1Φ $EC_{50}$ of 393 pM, a similar affinity to the peptide selectants (**Fig. 2-5A**). Similarly, DFab1Φ demonstrated high selectivity for DJ-1 over the panel of interfering antigens (**Fig. 2-5B**)

**Table 2-4. Titers, blocking agents, and stringency for PvP Fab selections.**

| | Titers | Blocking | Washes |
|---|---|---|---|
| Round 1 | $6.7 \times 10^8$ | Nonfat Milk | 3 |
| Round 2 | $3.3 \times 10^5$ | Bovine serum albumin | 3 |
| Round 3 | $6.7 \times 10^5$ | Pierce blocking | 6 |

**Table 2-5. DFab1Φ variable regions.**

| Fab Site | Amino Acid Sequence |
|---|---|
| CDRL3 | FYYYSGYLF |
| CDRH1 | DFTGDS |
| CDRH2 | SISASGGDTD |
| CDRH3 | WAPHYYAF |

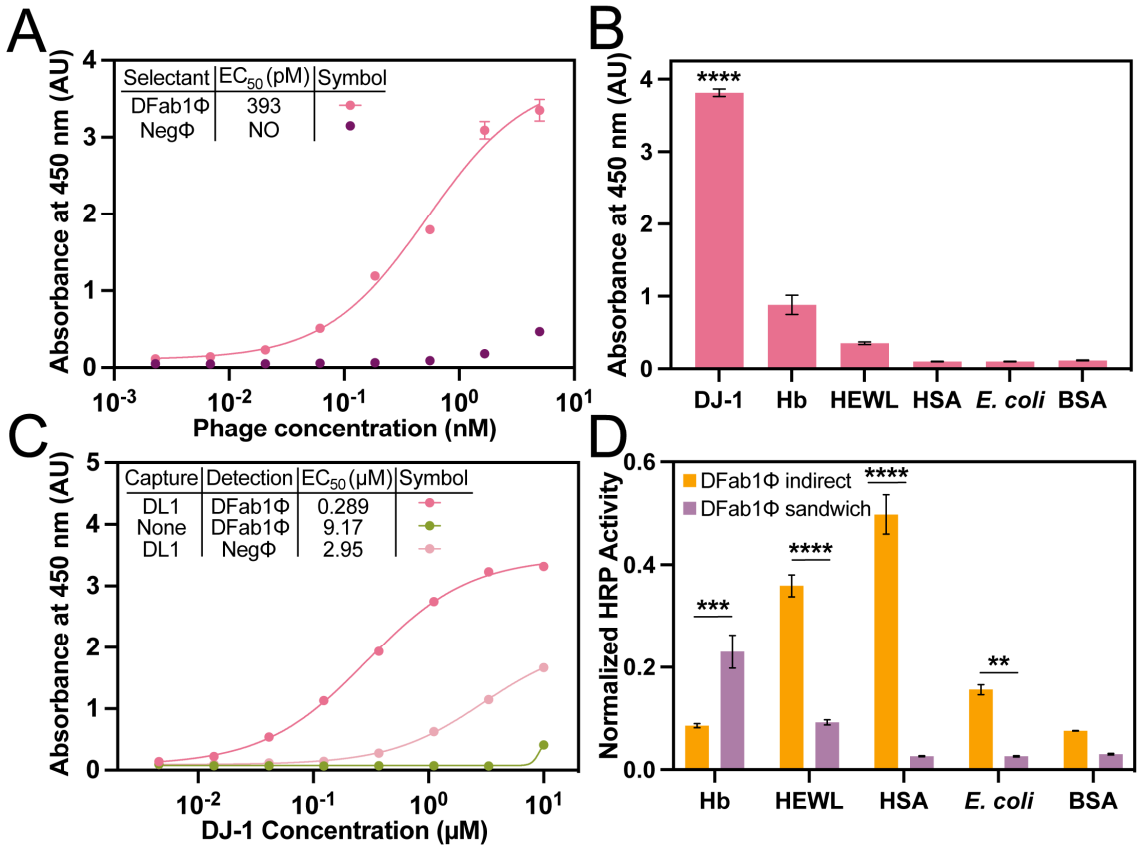


**Figure 2-5. Sensitivity and specificity determination of DFab1. A)** A dose-dependent direct phage assay with DFab1Φ and NegΦ. Data were fit to a four-parameter logistic curve and yielded sub-picomolar phage $EC_{50}$ values. Error is represented as SEM (n = 3). **B)** An indirect phage assay with DJ-1, Hb, HEWL, HSA, *E. coli* lysate, and BSA determined the specificity of the sandwich selectants. Data are normalized DJ-1. ANOVA with Tukey's multiple comparisons yielded P values of <0.0001 (****). **C)** A similar dose-dependent response with an $EC_{50}$ of 1.53 μM was observed in an identical sandwich ELISA with DFab1Φ. **D)** The DL1-DFab1Φ also demonstrated strong selectivity for DJ-1. ELISA data were fit to a four-parameter logistic curve. Error is represented as SEM. NO = not observed. ANOVA with Tukey's multiple comparisons yielded P values of <0.01 (**). <0.001 (***), <0.0001 (****).

A sandwich strep-DL1/phage ELISA like described above revealed a DJ-1 $EC_{50}$ of 289 nM (**Fig. 2-5C**). This value is also comparable to the DL3Φ sandwich strep-DL1/phage ELISA. Finally, the DL1/DFab1Φ sandwich assembly demonstrated improved specificity over DJ-1 compared to the indirect phage ELISA for HEWL, HSA, and *E. coli*, with P values of <0.0001, <0.0001, and <0.01, respectively. Interestingly, a decrease in specificity over DJ-1 for Hb was also observed, with a P value of <0.001 (**Fig. 2-5D**). Homology searching in sequence data bases did not reveal any significant homology between DJ-1 and either subunit of Hb. Thus, it is challenging to comment on the origin of this perceived non-specificity.

## 2.4 Conclusions

The sandwich ELISA format is commonly used in human health applications due to its higher sensitivity and specificity, but determination of noncompetitive sandwich binding pairs beyond a "guess-and-check" method remains elusive. Furthermore, even when a sandwich assay is established with a commercial antibody, the assay's efficacy can be compromised by uncontrollable circumstances. This report presents a modified phage display protocol that directly selects for peptides and Fabs that bind to DJ-1 in concert with the well-established DL1 peptide. Furthermore, these assays demonstrated apparent affinity comparable to a similar sandwich assay with a commercial antibody and improved specificity over the corresponding indirect phage ELISA. Additionally, PvP selections are comparatively simpler than other reported direct sandwich selection methods and can be implemented into any research space currently performing traditional phage display selections. Thus, the PvP selection method could provide the basis for more sandwich assays to be brought to clinical settings.

## 2.5 Materials and Methods

*Phage Propagation and Purification.* The phagemid DNA was transformed into SS320 competent *E. coli*, and cells were plated on a LB agar plate supplemented with 50 μg/mL carbenicillin and incubated overnight at 37 °C. A single colony was selected to inoculate 25 mL of 2YT (16 g tryptone, 5 g NaCl, 10 g yeast extract in 1 L autoclaved water) supplemented with 50 μg/mL carbenicillin and 2.5 μg/mL tetracycline. The culture was shaken at 37 °C until $OD_{600}$ reached 0.5; then, 30 μM IPTG and sufficient M13KO7 to achieve a multiplicity of infection of 4.6 was added. After an additional 45 min incubation, 8 mL of the culture was used to inoculate 150 mL of 2YT supplemented with carbenicillin (50 μg/mL), kanamycin (20 μg/mL), and IPTG (30 μM). This culture was incubated at 30 °C with shaking at 225 rpm for 18 h.

The cultures were centrifuged at 10 krpm (15300 x g) for 10 min. The supernatant was transferred to a centrifuge tube containing 1/5 the volume of PEG8000 (20%, w/v) and NaCl (2.5 M). The tube was mixed by inversion 5 times and stored on ice for 30 min. The solution was centrifuged at 10 krpm (15300 x g) for 15 min. The supernatant was decanted, and the tubes were centrifuged for an additional 4 min at 4 krpm (2429 x g) with the pellets facing out. The pellets were resuspended in PBS and the precipitation steps were repeated. Phage concentrations were quantified by measuring absorbance at 268 nm. Finally, the phage were diluted to 60 nM, flash frozen with glycerol (10%, v/v), and stored at -80 °C.

*NHS-Biotin Modification of Phage.* M13 bacteriophage displaying was diluted to 1 mg/mL. The diluted phage (1 mL) and EZ-Link NHS-biotin (ThermoFisher, 33 mM in DMSO) were combined and incubated overnight at room temperature. After incubation, the solution was added to a 3000 MWCO membrane and dialyzed with stirring in 1000x the volume of 1X

PBS. After 4 h, the 1X PBS was replaced with fresh solution and the dialysis was continued overnight.

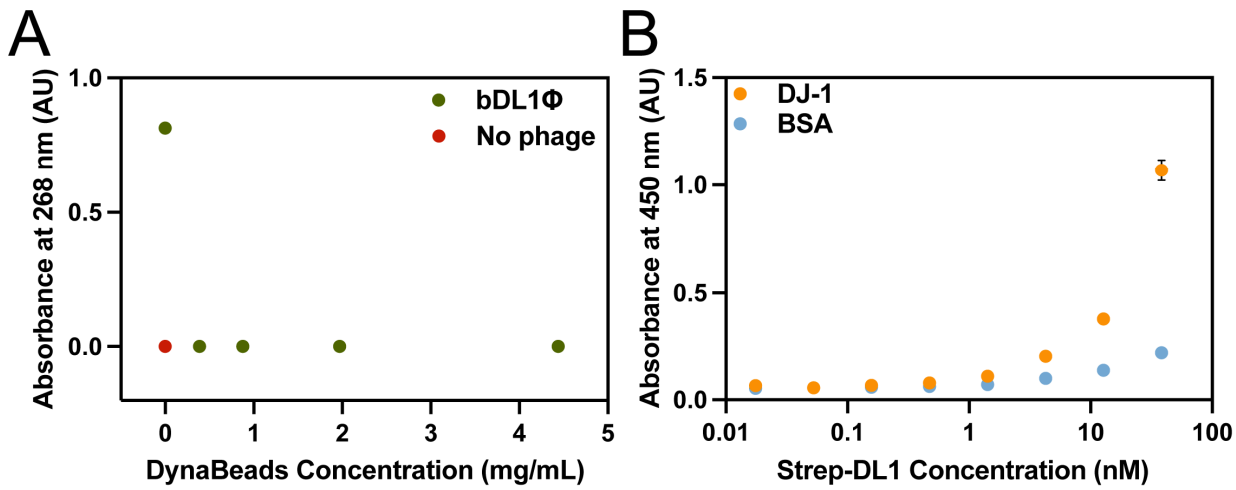


**Figure 2-6. Additional Assays for PvP Selections and Strep-DL1 Binding. A)** DynaBeads titration ELISA determined concentration of DynaBeads required for complete pulldown of bDL1Φ. **B)** The strep-DL1 complex can bind DJ-1 in a dose-dependent manner.

*Direct Strep-HRP ELISA.* Unless otherwise specified, all incubation steps were performed at 150 rpm and room temperature. A 96-well Maxisorp plate was coated with 100 µL/well of phage (1 nM in 50 mM $Na_2CO_3$) and incubated overnight at 4 °C. The coating solution was discarded, and the wells were blocked with 400 µL of blocking buffer (0.2% BSA in PBS) for 30 min. The blocking solution was removed, and the wells were washed three times with PBS-T (0.05% Tween-20 in PBS) followed by incubation for 1 h with serially diluted HRP-Conjugated Streptavidin (ThermoFisher) in PBT (0.2% BSA, 0.05% Tween-20 in PBS). The solution was again discarded, and the wells were washed five additional times with PBS-T and one final time with PBS. 1-Step Ultra TMB-ELISA Substrate Solution (Thermo Scientific, 100 µL per well) was added to each well, followed by 2 M $H_2SO_4$ (100 µL) after sufficient color had developed. The absorbance at 450 nm was measured with an Epoch Microplate Spectrophotometer (BioTek) and the resulting data were analyzed and fitted with GraphPad Prism 9.

*Dynabeads Titration.* Dynabeads M-270 Streptavidin (Invitrogen) were serially diluted in PBS from 4.44 to 0.389 mg/mL. Solutions of phage were added to the Dynabead dilutions such that the final phage concentration was 17 nM. The solutions were incubated with shaking at 150 rpm for 10 min. A magnet was used to pull down the Dynabeads and the supernatant was pipetted into a new container. Negative control solutions with no phage were also performed side-by-side. Final phage concentration was determined by absorbance at 268 nm (**Fig. 2-6A**).

*Indirect Phage Affinity ELISA.* A 96-well Nunc Maxisorp plate was coated with 10 μg/mL DJ-1 in coating buffer (100 μL/well, 50 mM $Na_2CO_3$) and incubated overnight at 4 °C. The coating solution was discarded, and the plate was blocked and washed as previously described. The plate was incubated with serially diluted phage in PBT for 1 h. The solution was removed, and 100 μL of 1:5000 Anti-M13 Monoclonal Antibody, HRP (Creative Diagnostics) diluted in PBT were added to each well. The plate was incubated for another 30 min, the antibody solution was discarded, and the wells were washed five times with PBS-T and once with PBS. From this point, the plate was treated exactly as described above.

*Phage vs. Phage Selections.* All incubation steps were performed on an orbital shaker at 150 rpm and room temperature. Biotinylated DL1Φ (bDL1Φ) was diluted to 1 nM in coating buffer and incubated on a Nunc MaxiSorp plate overnight (100 μL/well). The solution was discarded, and the wells were blocked for 30 min with 400 μL of either casein, BSA, HSA (0.2%), or Pierce Protein-Free Blocking Buffer. Next, the wells were washed with 100 μL PBS-T three times and incubated with 100 μL DJ-1 (3 μM in PBS with 0.05% Tween-20 and 0.2% corresponding blocking agent, or in Piece Protein-Free Blocking Buffer) for 1 h. The wells were again washed three times and incubated with the prepared phage library (60

nM in blocking buffer, 100 µL per well) for 90 min. The wells were washed again three times to remove nonspecific phage ligands.

The sandwich assemblies were eluted from the plate with HCl (0.1 M, 100 µL per well) and sonication in a water bath for 10 min. The eluted solutions were combined and neutralized with 1/3 the volume of Tris-HCl (1 M, pH 8.0). Dynabeads M-270 Streptavidin were added (2 mg/mL) and the solution incubated at 4 °C with shaking at 150 rpm for 30 min. The magnetic beads were pulled down with a magnet and the supernatant was collected. The eluted phage solution was used to infect log phase *E. coli* XL-1 Blue cells (20 mL, supplemented with 5 µg/mL tetracycline). The culture was incubated with shaking at 225 rpm at 37 °C for 1 h. Next, M13KO7 helper phage (NEB) was added to reach a multiplicity of infection of 4.6 and the culture was incubated with shaking at 225 rpm 37 °C for 45 min. The culture was transferred to 200 mL of 2YT supplemented with 50 µg/mL carbenicillin and 20 µg/mL kanamycin) and incubated at 37 °C with shaking at 225 rpm for 18 h. The phage were precipitated as described above, and the resulting phage pellets were resuspended in 1X PBS-T with glycerol (10%, v/v), separated into 1 mL aliquots, flash frozen with liquid nitrogen, and stored at -80 °C. As required, the phage solution was thawed on ice and precipitated a second time.

After 3 or 4 rounds of selections, spot assays were performed on 96 selectants. Briefly, individual phage colonies were amplified in 96 deep well plates as before. After centrifugation at 3 krpm (1462 x g), the supernatants were assayed by phage-based ELISA to assess binding to either DJ-1 or the blocking agent, BSA. From these screens, potential DJ-1 binders were isolated and evaluated by Sanger sequencing (**Fig. 2-7**).

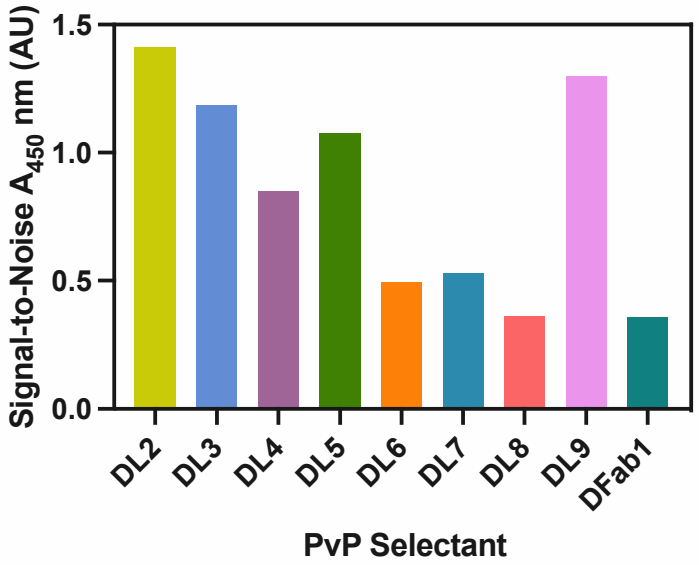


**Figure 2-7 PvP selectant spot assay results.** Data are normalized to signal for BSA.

*Indirect Phage Specificity ELISA.* A 96-well Nunc Maxisorp plate was coated with 10 µg/mL of either BSA, HSA, hemoglobin, lysozyme, or *E. coli* supernatant in coating buffer (100 µL/well) and incubated overnight at 4 °C. From this point, the plate was treated identically to that described in *Indirect Phage Affinity ELISA*.

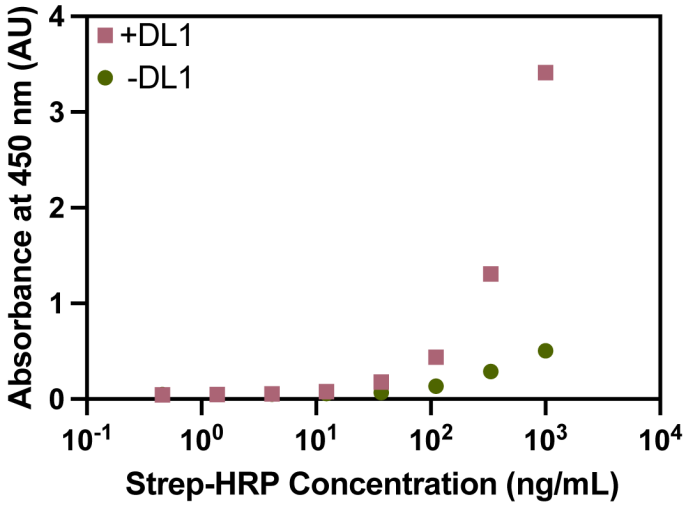


**Figure 2-8. ELISA to confirm strep-DL1 remains specific for DJ-1.**

*Direct Strep-DL1-HRP and DJ-1 ELISA.* The wells of a 96-well Nunc Maxisorp plate were coated with 10 ug/mL DJ-1 in coating buffer (100 µL) and incubated at 4 °C with shaking at 150 rpm overnight. The coating solution was discarded, and blocking buffer (400

μL) was added to each well. The plate was incubated for 1 h at room temperature with shaking at 150 rpm. Next, a prepared strep-HRP:DL1 peptide solution (1:24 molar ratio, 230 nM peptide) was serially diluted by a factor of 3 in PBT. The dilutions were added to the appropriate wells (100 μL) and incubated at room temperature with shaking at 150 rpm for 1 h. From this point, the plate was treated identically to that described above (**Fig. 2-8**).

*Sandwich Strep-DL1/Phage Affinity ELISA.* A 96-well Nunc Maxisorp plate was coated with 1:24 molar ratio of strep-DL1 in coating buffer (100 μL) and incubated at 4 °C with shaking at 150 rpm overnight. This solution was discarded and blocking buffer was added to each well (400 μL) for 1 h at room temperature with shaking at 150 rpm. DJ-1 was serially diluted by a factor of 3 in PBT starting at 10 μM. The dilutions were added to each well (100 μL) and the plate was incubated at room temperature for 1 h with shaking at 150 rpm. The plate was washed three times and 1 nM of phage selectants were added to each well (100 μL in PBT). The plate was incubated at room temperature for 1 h with shaking at 150 rpm, followed by an additional three washes. Next, 1:5,000 anti-M13-HRP was added to each well (100 μL in PBT) and the plate was incubated at room temperature for 30 min with shaking at 150 rpm. From this point, the plate was treated identically to that described above.

*Sandwich Strep-DL1/Phage Specificity ELISA.* A 96-well Nunc Maxisorp plate was coated with 1:24 molar ratio of strep-DL1 in coating buffer (100 μL) and incubated at 4 °C with shaking at 150 rpm overnight. This solution was discarded and blocking buffer was added to each well (400 μL) for 1 h at room temperature with shaking at 150 rpm. BSA, HSA, hemoglobin, lysozyme, (10 μM, 100 μL/well) or *E. coli* supernatant in PBT and incubated 1 h at 4 °C. From this point, the plate was treated identically to that described in *Sandwich Strep-DL1/Phage Affinity ELISA.*

*Data Analysis.* All data and statistics (mean, SEM, P values) were analyzed with GraphPad Prism 9.0. Specificity ELISA data were normalized by division of the DJ-1 signal for each assay type. Analysis of variance (ANOVA) with Sidak's multiple comparisons was performed to determine significance between DL3Φ indirect and DL3Φ sandwich ELISAs. ANOVA with Dunnett's multiple comparisons was performed to determine significance between DFab1Φ indirect and DFab1Φ sandwich ELISAs.

## 2.6 References


(1) Califf, R. M. Biomarker Definitions and Their Applications. *Exp. Biol. Med.* **2018**, *243*, 213–221. https://doi.org/10.1177/1535370217750088.

(2) Vargas, A. J.; Harris, C. C. Biomarker Development in the Precision Medicine Era: Lung Cancer as a Case Study. **2016**, *16* (8), 525–537. https://doi.org/10.1038/nrc.2016.56.Biomarker.

(3) Li, G.; Hu, J.; Hu, G. Biomarker Studies in Early Detection and Prognosis of Breast Cancer. *Adv. Exp. Med. Biol.* **2017**, *1026*, 27–39. https://doi.org/10.1007/978-981-10-6020-5_2.

(4) Anastasiu, C. V.; Moga, M. A.; Neculau, A. E.; Bălan, A.; Scârneciu, I.; Dragomir, R. M.; Dull, A. M.; Chicea, L. M. Biomarkers for the Noninvasive Diagnosis of Endometriosis: State of the Art and Future Perspectives. *Int. J. Mol. Sci.* **2020**, *21* (5), 1–24. https://doi.org/10.3390/ijms21051750.

(5) Burton, C.; Ma, Y. Current Trends in Cancer Biomarker Discovery Using Urinary Metabolomics: Achievements and New Challenges. *Curr. Med. Chem.* **2018**, *26* (1), 5–28. https://doi.org/10.2174/0929867324666170914102236.

(6) Poulet, G.; Massias, J.; Taly, V. Liquid Biopsy: General Concepts. *Acta Cytol.* **2019**, *63* (6), 449–455. https://doi.org/10.1159/000499337.

(7) Murphy, S.; Zweyer, M.; Mundegar, R. R.; Swandulla, D.; Ohlendieck, K. Proteomic Serum Biomarkers for Neuromuscular Diseases. *Expert Rev. Proteomics* **2018**, *15* (3), 277–291. https://doi.org/10.1080/14789450.2018.1429923.

(8) Rosado, M.; Silva, R.; Bexiga, M. G.; Jones, J. G.; Manadas, B.; Anjo, S. I. Advances in Biomarker Detection: Alternative Approaches for Blood-Based Biomarker Detection. *Adv. Clin. Chem.* **2019**, *92*, 141–199.

(9) Weaver, V. M.; Kotchmar, D. J.; Fadrowski, J. J.; Silbergeld, E. K. Challenges for Environmental Epidemiology Research: Are Biomarker Concentrations Altered by Kidney Function or Urine Concentration Adjustment? *J. Expo. Sci. Environ. Epidemiol.* **2016**, *26* (1), 1–8. https://doi.org/10.1038/jes.2015.8.

(10) Steckl, A. J.; Ray, P. Stress Biomarkers in Biological Fluids and Their Point-of-Use Detection. *ACS Sensors* **2018**, *3* (10), 2025–2044. https://doi.org/10.1021/acssensors.8b00726.

(11) Finamore, A.; Peluso, I.; Cauli, O. Salivary Stress/Immunological Markers in Crohn's Disease and Ulcerative Colitis. *Int. J. Mol. Sci.* **2020**, *21* (22), 1–17. https://doi.org/10.3390/ijms21228562.

(12) Aydin, S. A Short History, Principles, and Types of ELISA, and Our Laboratory Experience with Peptide/Protein Analyses Using ELISA. *Peptides* **2015**, *72*, 4–15. https://doi.org/10.1016/j.peptides.2015.04.012.

(13) Uotila, M.; Ruoslahti, E.; Engvall, E. Two-Site Sandwich Enzyme Immunoassay with Monoclonal Antibodies to Human Alpha-Fetoprotein. *J. Immunol. Methods* **1981**, *42*, 11–15.

(14) Kato, K.; Hamaguchi, Y.; Okawa, S.; Ishikawa, E.; Kobayashi, K. Use of Rabbit Antibody IgG Bound onto Plain and Aminoalkylsilyl Glass Surface for the Enzyme-Linked Sandwich Immunoassay. *J. Biochem.* **1977**, *82* (1), 261–266. https://doi.org/10.1093/oxfordjournals.jbchem.a131678.

(15) Koulouris, S.; Lekatsas, I.; Karabinos, I.; Ioannidis, G.; Katostaras, T.; Kranidis, A.; Triantafillou, K.; Thalassinos, N.; Anthopoulos, L. Microalbuminuria: A Strong Predictor of 3-Year Adverse Prognosis in Nondiabetic Patients with Acute Myocardial Infarction. *Am. Heart J.* **2005**, *149* (5), 840–845.

https://doi.org/10.1016/j.ahj.2004.07.031.
(16) Cox, K. L.; Devanaryan, V.; Kriauciunas, A.; Manetta, J.; Montrose, C.; Sittampalam, S. Immunoassay Methods. In *Assay Guidance Manual*; Eli Lilly & Company and the National Center for Advancing Translational Sciences, 2011; pp 1–38.
(17) Schmidt, S. D.; Mazzella, M. J.; Nixon, R. A.; Mathews, P. M. Aβ Measurement by Enzyme-Linked Immunosorbent Assay. *Methods Mol. Biol.* **2012**, *849*, 507–527. https://doi.org/10.1007/978-1-61779-551-0_34.
(18) Gnoth, C.; Johnson, S. Strips of Hope: Accuracy of Home Pregnancy Tests and New Developments. *Geburtshilfe Frauenheilkd.* **2014**, *74* (7), 661–669. https://doi.org/10.1055/s-0034-1368589.
(19) Van Rhijn, B. W. G.; Van Der Poel, H. G.; Van Der Kwast, T. H. Urine Markers for Bladder Cancer Surveillance: A Systematic Review. *Eur. Urol.* **2005**, *47* (6), 736–748. https://doi.org/10.1016/j.eururo.2005.03.014.
(20) Muller-Bardorff, M.; Hallermayer, K.; Schroder, A.; Ebert, C.; Borgya, A.; Gerhardt, W.; Remppis, A.; Zehelein, J.; Katus, H. A. Improved Troponin T ELISA Specific for Cardiac Troponin T Isoform: Assay Development and Analytical and Clinical Validation. *Clin. Chem.* **1997**, *43* (3), 458–466.
(21) Liew, O. W.; Yandle, T. G.; Chong, J. P. C.; Ng, Y. X.; Frampton, C. M.; Ng, T. P.; Lam, C. S. P.; Richards, A. M. High-Sensitivity Sandwich ELISA for Plasma NT-ProUcn2: Plasma Concentrations and Relationship to Mortality in Heart Failure. *Clin. Chem.* **2016**, *62* (6), 856–865. https://doi.org/10.1373/clinchem.2015.252932.
(22) Voskuil, J. Commercial Antibodies and Their Validation. *F1000Research* **2014**, *3* (232), 1–12. https://doi.org/10.12688/f1000research.4966.1.
(23) Couchman, J. R. Commercial Antibodies: The Good, Bad, and Really Ugly. *J. Histochem. Cytochem.* **2009**, *57* (1), 7–8. https://doi.org/10.1369/jhc.2008.952820.
(24) Ki, M. K.; Kang, K. J.; Shim, H. Phage Display Selection of EGFR-Specific Antibodies by Capture-Sandwich Panning. *Biotechnol. Bioprocess Eng.* **2010**, *15* (1), 152–156. https://doi.org/10.1007/s12257-009-3080-6.
(25) Gorman, K. T.; Roby, L. C.; Giuffre, A.; Huang, R.; Kay, B. K. Tandem Phage-Display for the Identification of Non-Overlapping Binding Pairs of Recombinant Affinity Reagents. *Nucleic Acids Res.* **2017**, *45* (18), 1–9. https://doi.org/10.1093/nar/gkx688.
(26) Repici, M.; Giorgini, F. DJ-1 in Parkinson's Disease: Clinical Insights and Therapeutic Perspectives. *J. Clin. Med.* **2019**, *8* (9), 1377. https://doi.org/10.3390/jcm8091377.
(27) Kawate, T.; Tsuchiya, B.; Iwaya, K. Expression of DJ-1 in Cancer Cells: Its Correlation with Clinical Significance. *Adv. Exp. Med. Biol.* **2017**, *1037*, 45–59. https://doi.org/10.1007/978-981-10-6583-5_4.
(28) Kumar, P.; Nandi, S.; Tan, T. Z.; Ler, S. G.; Chia, K. S.; Lim, W.-Y.; Bütow, Z.; Vordos, D.; De laTaille, A.; Al-Haddawi, M.; Raida, M.; Beyer, B.; Ricci, E.; Colombel, M.; Chong, T. W.; Chiong, E.; Soo, R.; Park, M. K.; Ha, H. K.; Gunaratne, J.; Thiery, J. P. Highly Sensitive and Specific Novel Biomarkers for the Diagnosis of Transitional Bladder Carcinoma Prashant. *Oncotarget* **2015**, *6* (15), 13539–13549. https://doi.org/3.
(29) Chen, Y.; Kang, M.; Lu, W.; Guo, Q.; Zhang, B.; Xie, Q.; Wu, Y. DJ-1, a Novel Biomarker and a Selected Target Gene for Overcoming Chemoresistance in Pancreatic Cancer. *J. Cancer Res. Clin. Oncol.* **2012**, *138* (9), 1463–1474. https://doi.org/10.1007/s00432-012-1205-3.
(30) Bai, J.; Guo, C.; Sun, W.; Li, M.; Meng, X.; Yu, Y.; Jin, Y.; Tong, D.; Geng, J.; Huang, Q.; Qi, J.; Fu, S. DJ-1 May Contribute to Metastasis of Non-Small Cell Lung Cancer. *Mol. Biol. Rep.* **2012**, *39* (3), 2697–2703. https://doi.org/10.1007/s11033-011-1024-7.
(31) Davidson, B.; Hadar, R.; Schlossberg, A.; Sternlicht, T.; Slipicevic, A.; Skrede, M.; Risberg, B.; Flørenes, V. A.; Kopolovic, J.; Reich, R. Expression and Clinical Role of DJ-1, a Negative Regulator of PTEN, in Ovarian Carcinoma. *Hum. Pathol.* **2008**, *39* (1), 87–95. https://doi.org/10.1016/j.humpath.2007.05.014.
(32) Fan, J.; Yu, H.; Lv, Y.; Yin, L. Diagnostic and Prognostic Value of Serum Thioredoxin and DJ-1 in Non-Small Cell Lung Carcinoma Patients. *Tumor Biol.* **2016**, *37* (2), 1949–1958. https://doi.org/10.1007/s13277-015-3994-x.
(33) Bhasin, A.; Ogata, A. F.; Briggs, J. S.; Tam, P. Y.; Tan, M. X.; Weiss, G. A.; Penner, R. M. The Virus Bioresistor: Wiring Virus Particles for the Direct, Label-Free Detection of Target Proteins. *Nano Lett.* **2018**, *18* (6), 3623–3629. https://doi.org/10.1021/acs.nanolett.8b00723.
(34) Bhasin, A.; Sanders, E. C.; Ziegler, J. M.; Briggs, J. S.; Drago, N. P.; Attar, A. M.; Santos, A. M.; True, M. Y.; Ogata, A. F.; Yoon, D. V.; Majumdar, S.; Wheat, A. J.; Patterson, S. V.; Weiss, G. A.; Penner, R. M. Virus Bioresistor (VBR) for Detection of Bladder Cancer Marker DJ-1 in Urine at 10 PM in One Minute. *Anal.*

*Chem.* **2020**, *92* (9), 6654–6666. https://doi.org/10.1021/acs.analchem.0c00534.
(35) Persson, H.; Ye, W.; Wernimont, A.; Adams, J. J.; Koide, A.; Koide, S.; Lam, R.; Sidhu, S. S. CDR-H3 Diversity Is Not Required for Antigen Recognition by Synthetic Antibodies. *J. Mol. Biol.* **2013**, *425* (4), 803–811. https://doi.org/10.1016/j.jmb.2012.11.037.

# CHAPTER 3

## Under 5 Minute Immunoblot Assays by Vortex Fluidic Device Acceleration

### 3.1 Abstract

Unlocking the potential of personalized medicine in point-of-care settings requires a new generation of biomarker and proteomic assays. Ideally, assays could inexpensively perform hundreds of quantitative protein measurements in parallel at the bedsides of patients. This goal greatly exceeds current capabilities. Furthermore, biomarker assays are often challenging to translate from benchtop to clinic due to difficulties achieving the necessary selectivity, sensitivity, and reproducibility. To address these challenges, we developed an efficient (<5 min), robust (low CoVs), and inexpensive (decreasing reagent use and cost by >70%) immunoassay method. Specifically, the immunoblot membrane is dotted with the sample and then developed in a vortex fluidic device (VFD) reactor. All assay steps – blocking, binding, and washing – leverage the unique thin-film microfluidics of the VFD. The approach can accelerate direct, indirect, and sandwich immunoblot assays. The applications demonstrated include assays relevant to both the laboratory and the clinic.

## 3.2 Introduction

The promises of personalized medicine require efficient, inexpensive testing for the presence and concentration of biomarkers. Low-cost diagnostics for broad deployment of precision medicine also represent a health justice issue, as high-tech medical devices often neglect resource-limited areas.[1] The extreme disparity between technologically lagging and advanced settings directly impacts disease mortality and morbidity, particularly for infectious diseases.[2] Thus, a clear need exists for a simple, cost-effective platform technology to advance precision medicine worldwide.

Point-of-care (PoC) tests have revolutionized diagnostics and patient care. For example, the rapid Strep A test has reduced unnecessary antibiotic treatments with clear benefits to public health.[3] Similarly, PoC influenza tests can allow early antiviral intervention, if conducted within 72 hours post-symptom onset.[4,5] The pregnancy test for chorionic gonadotropin has changed women's reproductive health and has emerged as both the most common at-home and PoC diagnostic test.[6] Despite these successful examples, a clear gap exists between the thousands of evidence-based biomarkers reported and their validation in the clinic.[7] Thus, technology allowing PoC biomarker validation and widespread deployment is required to close this gap.

Already used extensively for biomarker-based tests, immunoblot assays (IAs) offer a low-tech, but highly effective disease diagnostic. For example, an IA was developed as a cost-effective tool for detection of Dengue, a rampant ailment in countries lacking medical infrastructure for more complicated testing.[8] Similarly, IAs have been developed for the diagnosis of myofibrillar myopathies.[9] Most prominently, an IA is used in concert with an

enzyme-linked immunosorbent assay (ELISA) to diagnose human immunodeficiency virus.[10,11]

However, IAs typically incur high costs and have complex protocols and low sensitivity.[12,13] Despite these limitations, IAs in laboratories are often used to optimize conditions for the more experimentally demanding and time-consuming Western blot. A conventional IA typically requires >2 hr and consumes significant amounts of expensive reagents (e.g., primary and secondary antibodies).[14] Kurien *et al.* previously described a shortened, >40 min IA protocol reliant on processing the blot with reagents pre-warmed to 37 °C, which suggests thermally driving equilibration is one approach to accelerating IAs.[15] An alternative, especially for temperature sensitive applications, the Vitrozm Zoom Blot Plate, a single-use apparatus, can perform a multiplexed IA in 60 min.[16]

Eliminating the IA's background is key to improving its sensitivity. Wu *et al.* determined that inefficient washing is the main contributor to high background in IAs.[17] We envisioned applying the mechanical energy of a vortex fluidic device (VFD) to provide stringent washes, accelerated equilibration, and decrease IA background. Previously, the VFD has been used to drive protein purification and tethering[18], recovery of DNA from formalin-preserved tissue[19], protein folding[20], and embedding active enzyme in xerogels.[21] Here, we report using the easily-deployed VFD to improve IA sensitivity and reduce processing time to <5 min.

### 3.3 Results and Discussion

To access the unique microfluidics of the VFD, IAs were performed entirely inside a VFD quartz reactor. Briefly, antigens were dotted on a nitrocellulose membrane that was sandwiched between two sheets of filter paper. The paper assembly was rolled into a

cylinder and placed concentrically within the VFD reactor. All subsequent blocking, binding, and washing steps then took place inside the spinning VFD.

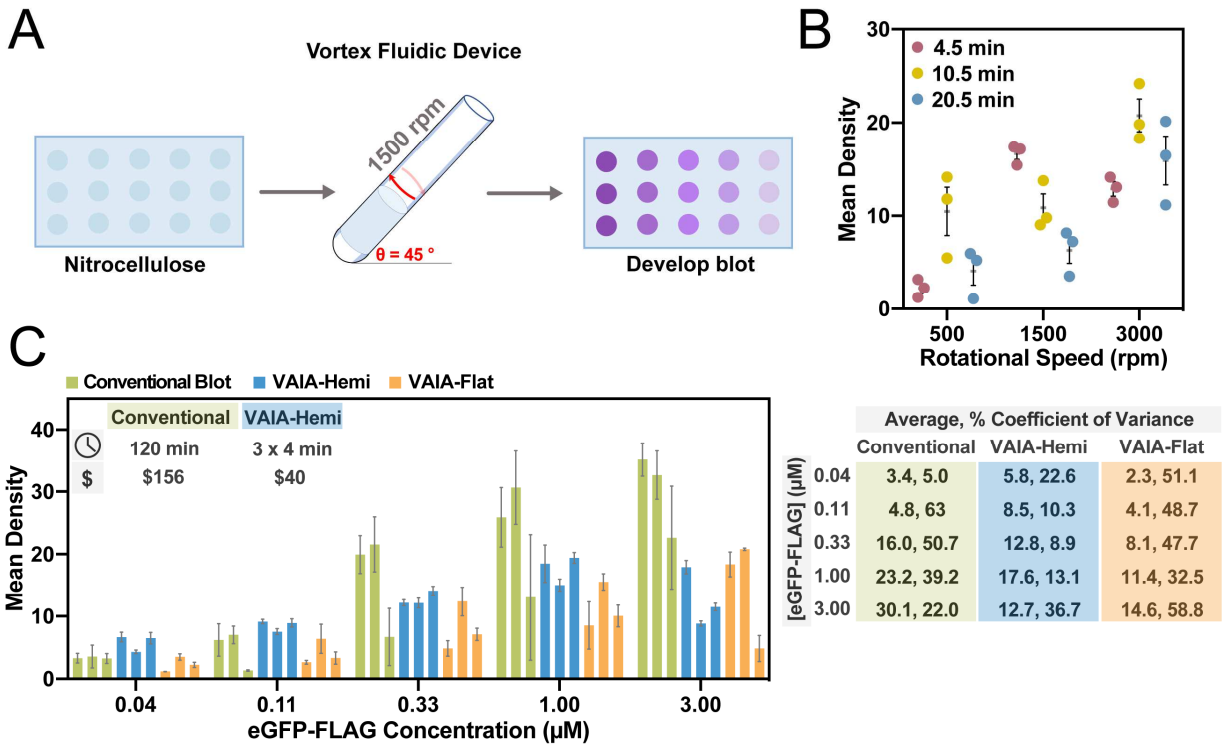


**Figure 3-1. Optimization of the VAIA method.** **A)** Nitrocellulose membranes dotted with target antigens are concentrically placed in a VFD reactor. The VFD reactor is tilted at 45° and rotated at 1500 rpm throughout the assay steps. Membranes are removed from the VFD reactor and the assay dots are visualized with a colorimetric reagent. **B)** An indirect phage IA was used to optimize VAIA rotational speed and assay time. Systematic screening of 9 combinations of these parameters revealed 1500 rpm and a 4.5 min assay time yielded the highest signal-to-noise ratios and lowest error. Error bars represent SEM (n = 3). **C)** A direct eGFP-FLAG detection IA was used to compare quantitation with VAIA to the conventional IA method. VAIA was faster, more robust, and more sensitive than the conventional method. The fluid flow was examined by performing VAIA with either hemispherical-bottom VFD reactors or flat-bottom VFD reactors. Error bars represent SEM for each group of dots on each immunoblot (n = 3). Coefficients of variance indicate variation between separate immunoblots (n = 3).

The initial optimization of the VFD-accelerated IA (VAIA) was performed with a previously described, robust assay format.[22] The dotted HSA antigen was captured by addition of a small quantity (2 mL of 1 nM phage) of a phage-displayed HSA binding ligand and visualized by colorimetric activity of a peroxidase-conjugated, phage-specific antibody (2 mL of 1:10,000 diluted antibody in PBS) (**Fig. 3-1A**). The VFD conditions, including rotational speed and time, were subject to optimization. Ultimately, 1500 rpm and 4.5 min

total of blocking (1 min), phage binding (2 min), antibody binding (1 min), and washing (2 x 15 s) steps yielded the greatest signal-to-noise ratios and the lowest levels of non-specific background binding (**Fig. 3-1B**).

Next, a direct assay further demonstrated the generality of the technique and revealed the effects of fluid flow on VAIA (**Fig. 3-1C**). The model protein, enhanced green fluorescent protein with a C-terminal FLAG-tag (eGFP-FLAG)[23], was detected with an anti-eGFP peroxidase-conjugated antibody. The assay was performed in either a hemispherical quartz VFD tube (VAIA-Hemi) or a flat-bottom quartz VFD tube (VAIA-Flat). At the optimal speed, the curved hemispherical base of the tube and the curved wall of the tube are expected to create a Coriolis fluid flow impacting the inner surface of the tube. Overall, the fluid flow afforded by the VAIA-Hemi resulted in more sensitivity and lower variability, where the rapid processing arises from the Coriolis fluid flow inducing high mass transfer into and out of the membrane.

The multifunctional eGFP-FLAG fusion protein provided a useful model to demonstrate a multitude of classic IA methods. The FLAG-tag was used as the antigen in both indirect (4.5 min) and direct (3.25 min) IA formats (**Fig. 3-2A**). Both formats delivered a dose-dependent response and the expected binding patterns (i.e., one format has higher sensitivity due to stronger binding affinity). Specifically, the direct FLAG immunoblot has drastically reduced signal below 0.33 μM. However, the indirect FLAG immunoblot maintains a detectable signal to concentrations of eGFP-FLAG as low as 0.04 μM. These data are

consistent with the finding that indirect immunoassays are generally more sensitive due to signal amplification by the secondary antibody.[26]

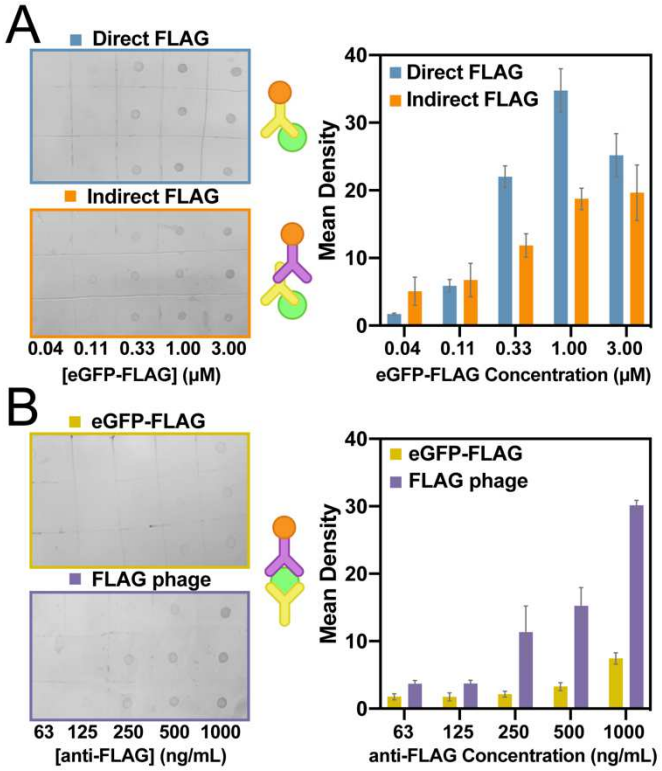


**Figure 3-2. Generalization of VAIA to three common immunoassay formats. A)** Both an indirect and direct anti-FLAG VAIA allowed dose-dependent quantification of eGFP-FLAG. The different binding modes cause the data to vary in both sensitivity and saturation limit. **B)** Anti-FLAG antibodies captured either FLAG phage or eGFP-FLAG for sandwich VAIAs. Detection of FLAG phage was more sensitive, but both methods resulted in useful signal. A schematic for each assay format is provided (middle). Error bars represent SEM (n = 3).

Another common IA, the sandwich-format, features an antigen entrapped between two noncompetitive antibodies. VAIA enabled two different sandwich-format assays to be performed with each requiring <5 min (**Fig. 3-2B**). An anti-FLAG antibody was dotted on the membrane and captured either eGFP-FLAG or FLAG-tagged M13 bacteriophage (FLAG phage). The eGFP-FLAG fusion was sandwiched with anti-eGFP-HRP; the FLAG phage was sandwiched with anti-M13-HRP. Both immunoblots demonstrated dose-dependent binding; however, the FLAG phage signal was significantly more intense and sensitive. Taken as a whole, the wide variety of IA formats demonstrate the generality and robustness of VAIA.

The previously described assays were all performed with a commercial blocking agent, ChonBlock (CB). However, researchers typically block with solutions of bovine serum albumin (BSA), non-fat milk (NFM), or high concentrations of the non-ionic detergent Tween-20. Therefore, the eGFP-FLAG direct detection with anti-eGFP-HRP was repeated with these more common blocking conditions (**Fig. 3-2**). All four blocking conditions resulted in a robust signal; however, 5% CB had the best signal-to-noise and therefore the best sensitivity. The experiments illustrate the adaptability of the VAIA platform for application to a variety of IA conditions and reagents.

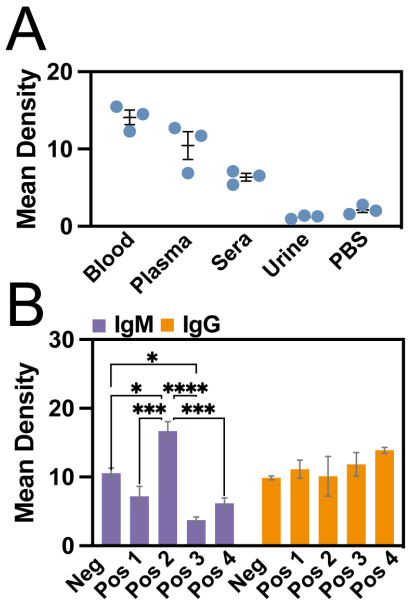


**Figure 3-3. Clinical potential of VAIAs with biofluids.** A) An indirect HSA immunoassay in plasma, sera, urine, blood, and PBS demonstrated VAIA applicability to a variety of biofluids. B) IgM and IgG levels in plasma from healthy and COVID-19 patients were assayed with VAIA. Error bars represent SEM (n = 3). ANOVA with Tukey's multiple comparisons yields p-values of *<0.05, ***<0.001, ****<0.0001.

VAIA also works well for potential clinical applications. In clinical samples, endogenous proteins can be challenging to detect due to the complex composition of the biofluid, including interfering substances. Human serum albumin (HSA) levels in the body are a biomarker for malnutrition, cirrhosis, and kidney disease.[24,25] Here, detection of

endogenous HSA in diluted plasma, sera, urine, and blood from human patients validated testing of biofluids with VAIA (**Fig. 3-3A**). HSA levels were the highest in blood, followed by plasma, then sera. In urine, the measured HSA levels were undetectable (i.e., comparable to the negative control). This result is predictable, as urine from healthy donors should be relatively HSA-free.[26]

Several diseases can be diagnosed through the assessment of immunoglobulin levels in biofluids.[27–29] However, the current state-of-the-art immunoglobulin assays are lengthy and complicated. Here, pooled plasma from healthy donors and COVID-19 patients further characterized the clinical potential of VAIA (**Fig. 3-3B**). Interestingly, immunoglobulin G (IgG) levels were consistent amongst the pooled plasma (no significance by ANOVA), and immunoglobulin M (IgM) levels varied drastically from one another. This data agrees with previous measurements from our laboratory.[23] In summary, the strong wash conditions of VAIA can overcome interfering substances during IAs with clinical samples.

The approach described here could find use in many chemical processes requiring the interactions of solid and liquid states. In diagnostics, for example, molecular recognition often requires molecules in liquid-phase to bind to a target affixed to solid support. The VFD-driven rapid equilibration could accelerate equilibration of otherwise slow binding events. Furthermore, the >10-fold acceleration, combined with decreased cost, and simplified execution suggests the work reported here could advance IAs in academic, industrial, and clinical spaces.

We conclude by noting that VAIA satisfies the requirements for bringing proteomic assays to PoC settings. VAIA is robust, rapid, and technically simple to execute, unlike conventional IAs. This conclusion was verified by an independent operator who replicated

the Materials and Methods. Additionally, the large number of assay formats in this report demonstrates VAIA's adaptability to a variety of established immunoassay formats. The approach can be readily scaled to examine hundreds to potentially thousands of proteins in one assay using a <5 min, inexpensive sandwich format assay. Most importantly, the data are unambiguous, digitizable with a cell phone camera, and robust. Therefore, VAIA could address the gap between development and implementation of biomarker-based precision medicine.

### 3.4 Materials and Methods

*Propagation and Purification of M13 Phage-Displayed Peptide Ligands.* The HSA-binding- or FLAG-phagemid was transformed into SS320 Escherichia coli (*E. coli*) competent cells and heat-shocked at 42 °C for 40 s. The cells were plated onto a pre-warmed LB-carbenicillin plate at 37 °C overnight. Near a flame, a 20 mL primary culture of 2YT (16 g tryptone, 10 g yeast extract, 5 g NaCl in 1 L autoclaved, nanopure water) with carbenicillin (50 mg/mL) and tetracycline (5 mg/mL) was inoculated with a single colony and incubated with shaking at 225 rpm and 37 °C until an $OD_{600}$ of 0.5 to 0.7 was reached. Next, the primary culture was induced by addition of isopropyl β-D thiogalactopyranoside (IPTG, 30 μM) and M13KO7 helper phage (8 nM, 5 μL). After incubation for 45 min at 37 °C with shaking at 225 rpm, 8 mL of the primary culture was transferred to 150 mL of 2YT supplemented with carbenicillin (50 μg/mL), kanamycin (20 μg/mL), and IPTG (30 μM) and incubated for 18 h at 30 °C with shaking at 225 rpm.

To harvest the phage, the expression culture was centrifuged at 10 krpm (15300 x g) for 10 min at 4 °C. The supernatant was transferred to a 250 mL centrifuge bottle with 30 mL of 20% (w/v) PEG-8000/2.5 M NaCl and inverted three times. After incubation on ice for

45 min, an additional centrifugation was done at 10 krpm (15300 x g) for 30 min at 4 °C. Without disturbing the pellets, the supernatant was decanted, and the centrifuge bottles were centrifuged with pellets facing away from the central axis of the rotor at 4 krpm (2,500 x g) for 4 min at 4 °C. The pellets were resuspended in 1X PBS (10 mM phosphate, 137 mM NaCl, pH 7.2) supplemented with TWEEN-20 (0.05%, v/v) and glycerol (10%, v/v), aliquoted into 1.5 mL Eppendorf tubes, flash frozen with liquid nitrogen, and stored at -80 °C. As required, the phage were thawed on ice. One-fifth of the total volume of 20% (w/v) PEG-8000/2.5 M NaCl was added, and the phage was incubated on ice for 45 min. Next, the phage were centrifuged at 10 krpm (15300 x g) for 30 min at 4 °C. The supernatant was decanted, and the pellets were resuspended in 1X PBS. The phage were centrifuged a final time at 10 krpm (15300 x g) for 10 min and decanted into a clean tube. The phage concentration was determined by measuring the absorbance at 268 nm, multiplying the $A_{268}$ value by a factor of 8.14, and correcting for the dilution factor.

*Expression and IMAC Purification of eGFP-FLAG.* A pET28c plasmid containing eGFP-FLAG fused to an N-terminal His-tag was transformed into BL21 DE3* E. coli heat-shock, competent cells. Cells were plated on a carbenicillin-supplemented (50 μg/mL) LB-agar plate and incubated at 37 °C overnight. A single colony was transferred to an overnight culture of 25 mL LB media (10 g tryptone, 10 g NaCl, 5 g yeast extract in 1 L autoclaved nanopure water) supplemented with carbenicillin (50 μg/mL) and incubated at 37 °C for 18 h. An expression culture of 500 mL LB supplemented with carbenicillin (50 μg/mL) was inoculated with 5 mL of the seed culture before incubation at 37 °C with shaking at 225 rpm until an $OD_{600}$ ~0.5 was reached. The cultures were induced by addition of 0.5 mM IPTG and incubated for 18 h at 25 °C. To harvest the protein, the culture was centrifuged (9632 x g)

for 20 min, resuspended in lysis buffer (20 mM Tris-HCl, 250 mM NaCl, pH 8), and sonicated. The lysate was centrifuged (26,892 rcf, 45 min, 4 °C), and the supernatant was incubated with charged $Ni^{2+}$-charge IMAC (Profinity™) resin overnight on a rotary shaker (150 rpm at 4 °C). The resin-bound protein was purified by gravity column, first by washing with lysis buffer containing 20 mM imidazole and then eluted with lysis buffer containing 250 mM imidazole. The eluted fractions were visualized using a 12% SDS-PAGE (Bio-rad Mini-PROTEAN Tetra electrophoresis system) stained with Coomassie brilliant blue dye (**Fig. 3-4**). The eluted fractions containing the purified eGFP-FLAG were pooled, and the buffer exchanged for 3 column volumes (20 mL) with lysis buffer without imidazole using a 10 kDa cutoff microconcentrator (Vivaspin, Fisher Scientific). The protein concentration was determined by Bradford assay using the estimated MW.

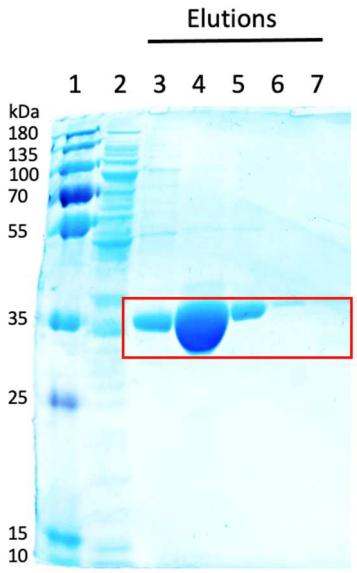


**Figure 3-4. SDS-PAGE analysis of eGFP-FLAG expression and purification.** The fusion protein had an expected molecular weight of ~32 kDa, as indicated with a red box. From left to right, the lanes are the following: 1) PageRuler Plus Prestained Protein Ladder, 2) Flowthrough, 3) Wash, 4) Elution 1, 5) Elution 2, 6) Elution 3, 7) Elution 4.

*Optimization of VAIA Rotational Speed and Assay Time.* The general process of arraying samples for testing is as follows. The nitrocellulose membrane was trimmed to fit

the inner circumference of the VFD reactor (5 cm) and marked with a pencil to create a 1 x 1 cm square for each sample. The negative control (1 µL of PBS) or experimental antigen (1 µL of 50 mg/mL HSA in PBS) was applied as a dot directly to the membrane, which was allowed to dry as usual. Next, the membrane was sandwiched between two pieces of filter paper cut to the size of the membrane; this assembly prevents damage to the membrane during processing. The filter paper membrane sandwich was shaped into a cylinder and placed concentrically within the glass VFD reactor for assay.

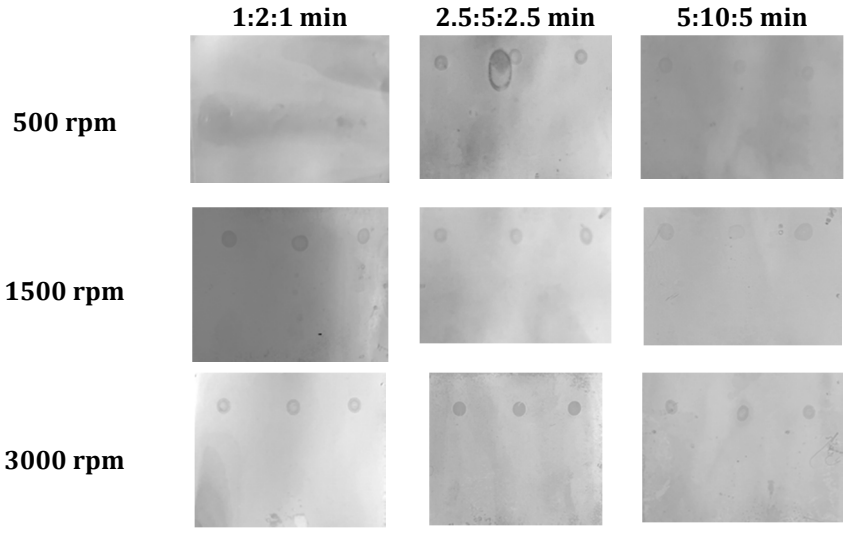


**Figure 3-5. Images of HSA-phage VAIAs with varying speeds and assay times.** For each blot, the top row is dotted with HSA, the bottom row is dotted with PBS. Images were taken under a light table with an iPhone 12 mini camera and imported into ImageJ for further analysis. For images shown in this manuscript, an additional adjustment of contrast was performed.

VAIA speed and assay time were optimized through an indirect phage assay. These assays consisted of three distinct steps performed with different times in 1:2:1 ratios (blocking : phage binding : antibody binding) (**Fig. 3-5**). Different rotational speeds were also explored for each ratio. First, each membrane was blocked with 3 mL 5X Chonblock (Chondrex Inc.) in PBS (blocking buffer) at the indicated speeds and times, and the solution was discarded. Next, 3 mL of HSA-binding phage (HSA-L3) diluted in blocking buffer was

added to the VFD reactor for processing at the indicated speeds and times. The solution was discarded, and 3 mL of 1X PBS with 0.05% (v/v) Tween-20 (PBS-T) was added to the reactor to wash the membrane for 15 s before discarding the solution. Next, the HSA/HSA-L3 binding interaction was detected through addition of 3 mL anti-M13-HRP (Creative Diagnostics) diluted in blocking buffer (1:10,000) before VFD processing at the indicated speeds and times. Finally, this solution was discarded, and the membrane sandwich was washed once more as previously described.

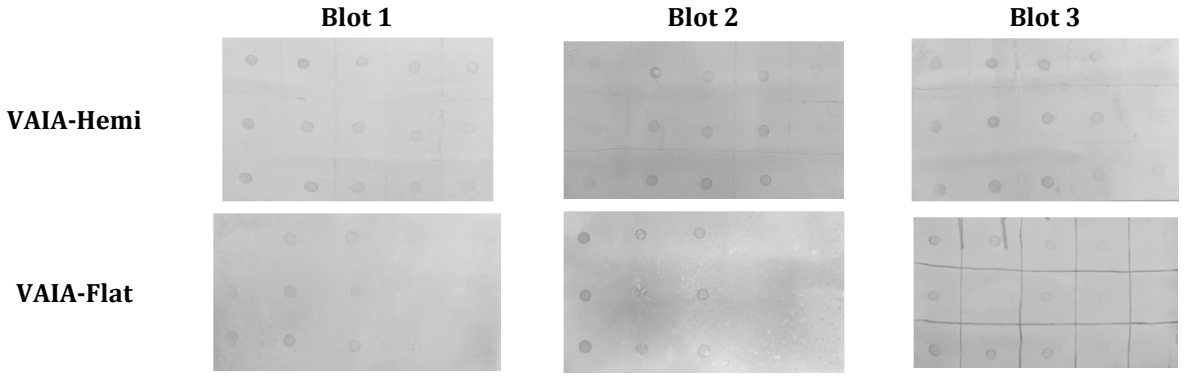


**Figure 3-6. Images of eGFP-FLAG VAIAs.** From left to right on each blot, the eGFP-FLAG concentrations are: 3.00 µM, 1.00 µM, 0.33 µM, 0.11 µM, 0.04 µM. Images were acquired under a light table with an iPhone 12 mini camera and imported into ImageJ for further analysis. For images shown in this manuscript, an additional adjustment of contrast was performed.

After each assay was complete, the membrane was removed from the VFD reactor through gentle tapping and placed on a clean paper towel. Sufficient TMB solution was added to cover the membrane surface. After sufficient time passed for color to develop (1 to 5 min), each membrane was rinsed with water and imaged after drying. All membranes were imaged using top-down lighting by a light table with an iPhone 12 Mini camera (**Fig. 3-6**). The images were transferred into Image-J and converted to 8-bit grayscale format, as directed by the software. Next, the background was subtracted with a 50.0 rolling ball radius and light-dark inverted. The mean density of each assay dot was measured and imported into Prism 9.0 for further analysis.

*Direct Detection of eGFP-FLAG with Conventional Dot Blot.* The membranes were prepared as described above. These assays were performed in separate plastic containers. To prevent non-specific binding, 10 mL of blocking buffer were added to each container, shaken at 150 rpm for 30 min, then discarded. Next, 10 mL of 1:1,000 anti-eGFP-HRP in blocking buffer were added to each container, shaken at 150 rpm for 60 min, then discarded. Each membrane was washed with 10 mL PBS-T with shaking at 150 rpm for 10 min three times. The membranes were developed, and the data were processed as described above (**Fig. 3-7**).

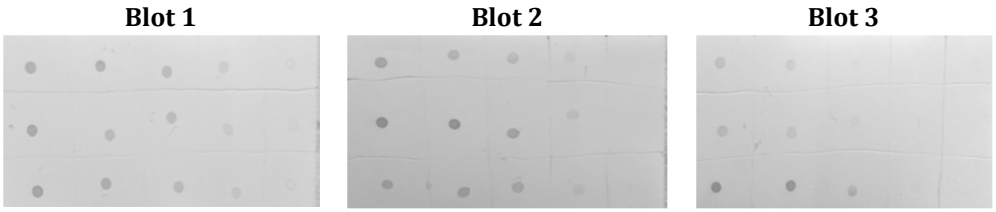


**Figure 3-7. Images of conventional eGFP-FLAG IAs.** From left to right for each blot, the eGFP-FLAG concentrations are: 3.00 μM, 1.00 μM, 0.33 μM, 0.11 μM, 0.04 μM. Images were acquired under a light table with an iPhone 12 mini camera and imported into ImageJ for further analysis. For images shown in this manuscript, an additional adjustment of contrast was performed after data analysis.

*Direct VAIA Detection of eGFP-FLAG with anti-FLAG-HRP.* The membranes were prepared and blocked as previously described. Next, 2 mL of 1:1,000 anti-FLAG-HRP (Sigma-Aldrich) in blocking buffer were added to the tube and spun at 1500 rpm for 2 min. The solution was then discarded, and the membranes were washed and processed as described above.

*Indirect VAIA Detection of eGFP-HRP with anti-FLAG and anti-mouse-HRP.* The membranes were prepared and blocked as previously described. The solution was then discarded. Next, 2 mL of 1:1,000 anti-FLAG (Sigma-Aldrich) in blocking buffer were added to the tube and spun at 1500 rpm for 2 min. The solution was discarded, and the membrane was washed by adding 2 mL of PBS-T and spinning at 1500 rpm for 15 s. After discarding the

wash solution, 2 mL of 1:10,000 anti-mouse-HRP in blocking buffer were added to the tube, spun at 1500 rpm for 2 min, then discarded. The solution was discarded, and the membranes were washed and processed as previously described.

*Sandwich VAIA Detection of eGFP-FLAG with anti-FLAG and anti-eGFP-HRP.* Membranes were prepared as previously described. Five serial dilutions of anti-FLAG (1:100, 1:1000, 1:10,000, 1:100,000, 1:1,000,000) were prepared and 1 µL of each was added in triplicate on each of the five columns within the grid. The membrane was sandwiched in filter paper and blocked as previously described. Next, 2 mL of 3 µM eGFP-FLAG in blocking buffer were added, and the tube was spun at 1500 rpm for 2 min. The solution was then discarded, and the membrane was washed as previously described. Next, 2 mL of 1:1000 anti-eGFP-HRP in blocking buffer were added to the tube and spun at 1500 rpm for 2 min, then discarded. The solution was discarded, and the membrane was washed, and the data were processed as previously described.

*Sandwich VAIA Detection of eGFP-FLAG with anti-FLAG and FLAG-Binding Phage.* The membrane was prepared and blocked as previously described. Next, 2 mL of 1 nM FLAG-binding phage in blocking buffer were added to the tube and spun at 1500 rpm for 2 min. The solution was then discarded, and the membrane washed as described above. Next, 2 mL of 1:1000 anti-M13-HRP in blocking buffer were added to the tube and spun at 1500 rpm for 2 min, then discarded. The solution was discarded, and the membrane was washed, and data processed as previously described.

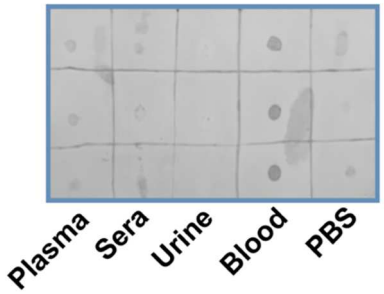


**Figure 3-8. Image of VAIA assay completed in a variety of biofluids.** Images were acquired under a light table with an iPhone 12 mini camera and imported into ImageJ for further analysis. For images shown in this manuscript, an additional adjustment of contrast was performed after data analysis.

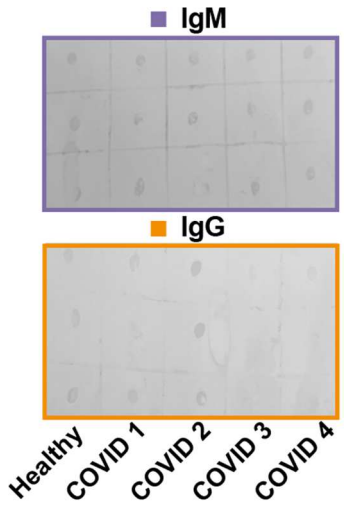


**Figure 3-9. Images of patient plasma VAIAs.** IgMs and IgGs were detected with anti-IgM-HRP or anti-IgG-HRP, respectively. Images were acquired under a light table with an iPhone 12 mini camera and imported into ImageJ for further analysis. For images shown in this manuscript, an additional adjustment of contrast was performed after data analysis.

*Direct VAIA Detection of HSA in Biofluids.* The membrane was prepared as previously described. Plasma, sera, urine, blood were diluted (1:100) in PBS and dotted on the membrane in triplicate. Additionally, PBS was dotted on the membrane as a negative control. An image of the membrane was acquired as before. The membrane was sandwiched in filter paper and blocked as previously described. Next, 2 mL of anti-HSA-HRP (Bethyl Laboratories, 1:1000) in blocking buffer were added to the tube and spun at 1500 rpm for 2 min. The solution was discarded, and the membrane was washed and imaged as described.

To account for the initial dark color of the diluted blood, the mean density values were calculated by subtracting the values before and after the assay (**Fig. 3-8**).

*Antibody Detection in COVID-19 Patient Plasma.* The membrane was prepared as previously described. Plasma from healthy patients and COVID-19 patients were diluted (1:100) in PBS and dotted on the membrane in triplicate. The membrane was sandwiched in filter paper and blocked as previously described. Next, 2 mL of anti-IgG-HRP (Sigma-Aldrich, 1:1000) or anti-IgM-HRP (Invitrogen, 1:1000) in blocking buffer were added to the tube and spun at 1500 rpm for 2 min. The solution was discarded, and the membrane was washed and imaged as described above (**Fig. 3-9**).

## 3.5 References


(1) Howitt, P.; Darzi, A.; Yang, G. Z.; Ashrafian, H.; Atun, R.; Barlow, J.; Blakemore, A.; Bull, A. M. J.; Car, J.; Conteh, L.; Cooke, G. S.; Ford, N.; Gregson, S. A. J.; Kerr, K.; King, D.; Kulendran, M.; Malkin, R. A.; Majeed, A.; Matlin, S.; Merrifield, R.; Penfold, H. A.; Reid, S. D.; Smith, P. C.; Stevens, M. M.; Templeton, M. R.; Vincent, C.; Wilson, E. Technologies for Global Health. *Lancet* **2012**, *380* (9840), 507–535. https://doi.org/10.1016/S0140-6736(12)61127-1.

(2) Gavazzi, G.; Herrmann, F.; Krause, K. H. Aging and Infectious Diseases in the Developing World. *Clin. Infect. Dis.* **2004**, *39* (1), 83–91. https://doi.org/10.1086/421559.

(3) Hendi, S. Bin; Malik, Z. A.; Khamis, A. H.; Al-Najjar, F. Y. A. High Diagnostic Accuracy of Automated Rapid Strep A Test Reduces Antibiotic Prescriptions for Children in the United Arab Emirates. *BMC Pediatr.* **2021**, *21* (1), 1–6. https://doi.org/10.1186/s12887-021-02516-3.

(4) Balish, A.; Garten, R.; Klimov, A.; Villanueva, J. Analytical Detection of Influenza A(H3N2)v and Other A Variant Viruses from the USA by Rapid Influenza Diagnostic Tests. *Influenza Other Respi. Viruses* **2013**, *7* (4), 491–496. https://doi.org/10.1111/irv.12017.

(5) Uyeki, T. M. Influenza Diagnosis and Treatment in Children: A Review of Studies on Clinically Useful Tests and Antiviral Treatment for Influenza. *Pediatr. Infect. Dis. J.* **2003**, *22* (2), 164–177. https://doi.org/10.1097/00006454-200302000-00015.

(6) Gnoth, C.; Johnson, S. Strips of Hope: Accuracy of Home Pregnancy Tests and New Developments. *Geburtshilfe Frauenheilkd.* **2014**, *74* (7), 661–669. https://doi.org/10.1055/s-0034-1368589.

(7) Selleck, M. J.; Senthil, M.; Wall, N. R. Making Meaningful Clinical Use of Biomarkers. *Biomark. Insights* **2017**, *12*, 1–7. https://doi.org/10.1177/1177271917715236.

(8) Falconar, A. K. I.; Romero-Vivas, C. M. E. A Simple, Inexpensive, Robust and Sensitive Dot-Blot Assay for Equal Detection of the Nonstructural-1 Glycoprotein of All Dengue Virus Serotypes. *Virol. J.* **2013**, *10*, 1–13. https://doi.org/10.1186/1743-422X-10-126.

(9) Marini, M.; Guglielmi, V.; Faulkner, G.; Piffer, S.; Tomelleri, G.; Vattemi, G. Immunoblot as a Potential Diagnostic Tool for Myofibrillar Myopathies. *Electrophoresis* **2015**, *36* (24), 3097–3100. https://doi.org/10.1002/elps.201500277.

(10) Esteban, J. I.; Tai, C. C.; Kay, J. W. D.; Shih, J. W. K.; Bodner, A. J.; Alter, H. J. Importance of Western Blot Analysis in Predicting Infectivity of Anti-Htlv-Iii/Lav Positive Blood. *Lancet* **1985**, *326* (8464), 1083–1086. https://doi.org/10.1016/S0140-6736(85)90683-X.

(11) CDC Laboratory Procedure Manual. *HIV Western Blot Confirmatory Test*; 2013.

(12) Montagnese, F.; Babačić, H.; Eichhorn, P.; Schoser, B. Evaluating the Diagnostic Utility of New Line

Immunoassays for Myositis Antibodies in Clinical Practice: A Retrospective Study. *J. Neurol.* **2019**, *266* (6), 1358–1366. https://doi.org/10.1007/s00415-019-09266-4.

(13) Harrell, J.; Rubio, X. B.; Nielson, C.; Hsu, S.; Motaparthi, K. Advances in the Diagnosis of Autoimmune Bullous Dermatoses. *Clin. Dermatol.* **2019**, *37* (6), 692–712. https://doi.org/10.1016/j.clindermatol.2019.09.004.

(14) Stott, D. I. Immunoblotting and Dot Blotting. *Journal of Immunological Methods*. 1989, pp 153–187. https://doi.org/10.1016/0022-1759(89)90394-3.

(15) Kurien, B. T.; Danda, D.; Bachmann, M.; Scofield, R. H. SDS PAGE to Immunoblot in One Hour. *Methods Mol. Biol.* **2015**, No. 1312, 449–454. https://doi.org/10.1007/978-1-4939-2694-7.

(16) Mai, J.; Xie, R. Zoom Plate ™ Dot Blot. *Nat. Methods Appl. Note* **2015**, 1–3.

(17) Wu, M.; Stockley, P. G.; Martin, W. J. An Improved Western Blotting Technique Effectively Reduces Background. *Electrophoresis* **2002**, *23* (15), 2373–2376. https://doi.org/10.1002/1522-2683(200208)23:15<2373::AID-ELPS2373>3.0.CO;2-W.

(18) Britton, J.; Dyer, R. P.; Majumdar, S.; Raston, C. L.; Weiss, G. A. Ten-Minute Protein Purification and Surface Tethering for Continuous-Flow Biocatalysis. *Angew. Chemie - Int. Ed.* **2017**, *56* (9), 2296–2301. https://doi.org/10.1002/anie.201610821.

(19) Totoiu, C. A.; Phillips, J. M.; Reese, A. T.; Majumdar, S.; Girguis, P. R.; Raston, C. L.; Weiss, G. A. Vortex Fluidics-Mediated DNA Rescue from Formalin-Fixed Museum Specimens. *PLoS One* **2020**, *15* (1), 1–13. https://doi.org/10.1371/journal.pone.0225807.

(20) Britton, J.; Smith, J. N.; Raston, C. L.; Weiss, G. A. Protein Folding Using a Vortex Fluidic Device. *Methods Mol. Biol.* **2017**, *1586*, 211–220. https://doi.org/10.1007/978-1-4939-6887-9_13.

(21) Luo, X.; Mohammed Al-Antaki, A. H.; Igder, A.; Stubbs, K. A.; Su, P.; Zhang, W.; Weiss, G. A.; Raston, C. L. Vortex Fluidic-Mediated Fabrication of Fast Gelated Silica Hydrogels with Embedded Laccase Nanoflowers for Real-Time Biosensing under Flow. *ACS Appl. Mater. Interfaces* **2020**, *12* (46), 51999–52007. https://doi.org/10.1021/acsami.0c15669.

(22) Ogata, A. F.; Edgar, J. M.; Majumdar, S.; Briggs, J. S.; Patterson, S. V.; Tan, M. X.; Kudlacek, S. T.; Schneider, C. A.; Weiss, G. A.; Penner, R. M. Virus-Enabled Biosensor for Human Serum Albumin. *Anal. Chem.* **2017**, acs.analchem.6b04840. https://doi.org/10.1021/acs.analchem.6b04840.

(23) Sen, S.; Sanders, E. C.; Gabriel, K. N.; Miller, B. M.; Isoda, H. M.; Salcedo, G. S.; Garrido, J. E.; Dyer, R. P.; Nakajima, R.; Jain, A.; Caldaruse, A.-M.; Santos, A. M.; Bhuvan, K.; Tifrea, D. F.; Ricks-Oddie, J. L.; Felgner, P. L.; Edwards, R. A.; Majumdar, S.; Weiss, G. A. Predicting COVID-19 Severity with a Specific Nucleocapsid Antibody plus Disease Risk Factor Score Authors. *mSphere* **2021**, 2020.10.15.341743.

(24) Lee, S.; Sung, D. B.; Kang, S.; Parameswaran, S.; Choi, J. H.; Lee, J. S.; Han, M. S. Development of Human Serum Albumin Selective Fluorescent Probe Using Thieno[3,2-b]Pyridine-5(4h)One Fluorophore Derivatives. *Sensors* **2019**, *19* (23). https://doi.org/10.3390/s19235298.

(25) Doumas, B. T.; Peters, T. Serum and Urine Albumin: A Progress Report on Their Measurement and Clinical Significance. *Clin. Chim. Acta* **1997**, *258* (1), 3–20. https://doi.org/10.1016/S0009-8981(96)06446-7.

(26) Choi, S.; Choi, E. Y.; Kim, D. J.; Kim, J. H.; Kim, T. S.; Oh, S. W. A Rapid, Simple Measurement of Human Albumin in Whole Blood Using a Fluorescence Immunoassay (I). *Clin. Chim. Acta* **2004**, *339* (1–2), 147–156. https://doi.org/10.1016/j.cccn.2003.10.002.

(27) Strassburg, C. P. Autoimmune Hepatitis. *Best Pract. Res. Clin. Gastroenterol.* **2010**, *24* (5), 667–682. https://doi.org/10.1016/j.bpg.2010.07.011.

(28) Phillips, A. C.; Carroll, D.; Drayson, M. T.; Batty, G. D. Raised Levels of Immunoglobulin G, A and M Are Associated with an Increased Risk of Total and Cause-Specific Mortality: The Vietnam Experience Study. *J. Epidemiol. Community Health* **2015**, *69* (2), 129–135. https://doi.org/10.1136/jech-2014-204345.

(29) Zhang, H.; Li, P.; Wu, D.; Xu, D.; Hou, Y.; Wang, Q.; Li, M.; Li, Y.; Zeng, X.; Zhang, F.; Shi, Q. Serum IgG Subclasses in Autoimmune Diseases. *Med. (United States)* **2015**, *94* (2), e387. https://doi.org/10.1097/MD.0000000000000387.

# CHAPTER 4

## Predicting COVID-19 Severity with a Specific Nucleocapsid Antibody plus Disease Risk Factor Score

Adapted with permission from *mSphere*.
DOI: 10.1128/mSphere.00203-21

### 4.1 Abstract

Effective methods for predicting COVID-19 disease trajectories are urgently needed. Here, ELISA and coronavirus antigen microarray (COVAM) analysis mapped antibody epitopes in the plasma of COVID-19 patients (n = 86) experiencing a wide-range of disease states. The experiments identified antibodies to a 21-residue epitope from nucleocapsid (termed Ep9) associated with severe disease, including admission to the ICU, requirement for ventilators, or death. Importantly, anti-Ep9 antibodies can be detected within six days post-symptom onset and sometimes within one day. Furthermore, anti-Ep9 antibodies correlate with various comorbidities and hallmarks of immune hyperactivity. We introduce a simple-to-calculate, disease risk factor score to quantitate each patient's comorbidities and age. For patients with anti-Ep9 antibodies, scores above 3.0 predict more severe disease outcomes with a 13.42 Likelihood Ratio (96.7% specificity). The results lay the groundwork for a new type of COVID-19 prognostic to allow early identification and triage of high-risk patients. Such information could guide more effective therapeutic intervention.

## 4.2 Introduction

The COVID-19 pandemic has triggered an ongoing global health crisis. More than 108.2 million confirmed cases and 2.3 million deaths have been reported worldwide as of February 16, 2021[1]. The virus that causes COVID-19, severe acute respiratory syndrome coronavirus (SARS-CoV-2), belongs to the same family of viruses responsible for respiratory illness linked to recent epidemics – severe acute respiratory syndrome (SARS-CoV-1 termed SARS here) in 2002-2003 and Middle East respiratory syndrome (MERS) in 2012[2]. The current and previous outbreaks suggest coronaviruses will remain viruses of concern for global health.

Many risk factors and comorbidities, including age, sex, hypertension, diabetes, and obesity, can influence COVID-19 patient outcomes [3]. Analysis of patient immune parameters has linked disease severity to elevated levels of biomarkers for inflammation (c-reactive protein and cardiac troponin I), organ damage (aspartate aminotransferase, abbreviated AST, and hypoalbuminemia), immune hyperactivity (IL-6 and IL-10), and clotting (D-dimer)[4]. Mortality in COVID-19 is often caused by multi-organ injury and severe pneumonia attributed to an excessive immune response, termed a cytokine storm[5]. Given the rapid and wide spectrum of COVID-19 disease progression, a more precise prognostic linking disease risk factors and specific immune responses can potentially predict disease trajectories and guide interventions.

One hypothesis to explain differences in severity of COVID-19 implicates weakly binding, non-neutralizing antibodies (Abs) to SARS-CoV-2 proteins[6]. However, the potential harm of these suboptimal Abs in COVID-19 patient outcomes remains ill-defined. Furthermore, a recent review on antibody-dependent enhancement of SARS-CoV-2 stated,

“At present, there are no known clinical findings, immunological assays or biomarkers that can differentiate any severe infection from immune-enhanced disease, whether by measuring antibodies, T cells or intrinsic host responses[7]." This conclusion inspired our study.

SARS-CoV-2 encodes four major structural proteins – spike (S), nucleocapsid (N), membrane (M), and envelope (E). The S, N, and M proteins from SARS elicit an Ab-based immune response[8,9]. The Ab response and its effects on disease progression in SARS-CoV-2 remain under investigation[10,11]. Bioinformatics has predicted >55 Ab binding epitope regions from SARS-CoV-2[12–17]. The epitopes for N, M or E proteins are less well-characterized than for S protein. Several studies have reported comprehensive epitope mapping of the antibody response to SARS-CoV-2[18–21]. Here, we sought to characterize epitopes from SARS-CoV-2 and their correlations with disease severity. ELISAs with phage-displayed epitopes (phage ELISAs) and coronavirus antigen microarray (COVAM) analysis [22] examined plasma samples from COVID-19 patients (n = 86). The results demonstrate that Abs to a specific epitope from N protein plus disease risk factors strongly correlate with COVID-19 disease severity.

**4.3 Results**

*Design and Production of Candidate Epitopes.* Twenty-one putative SARS-CoV-2 epitopes were predicted through bioinformatics [12–14] and structure-based analysis. The candidate epitopes span the S, N, M, or E proteins and are on average 34 amino acids in length (**Fig. 4-1**). These epitopes were phage-displayed as fragments of the full-length protein and were likely unstructured. Here, epitope refers to the predicted region of the antigenic protein recognized by the antibody's paratope. The structure of S protein bound to a neutralizing

antibody [23,24] provided the starting point for 12 of these antibody epitopes. Epitopes were designed to potentially isolate even suboptimal Abs binding to small portions of these structural proteins; such suboptimal Abs were hypothesized to provide insight into disease severity. After display of each potential epitope on the surface of phage, the quality of the epitopes was evaluated by PCR, DNA sequencing, and QC ELISA. A total of 18 phage-displayed, putative epitopes passed quality control PCR, and were selected for further study.

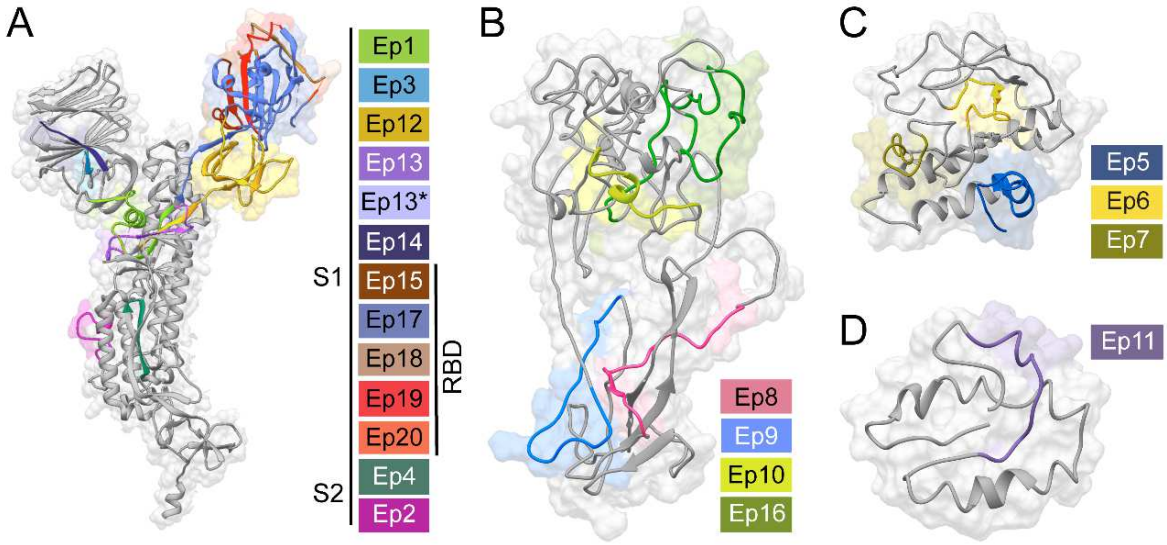


**Figure 4-1. Predicted SARS-CoV-2 epitopes examined by phage ELISA.** Structural models (gray) of the SARS-CoV-2 **A**) S, **B**) N, **C**) M, or **D**) E proteins illustrate our epitope design (colored). Sequence Ep13* has the mutation D614G, which increases the fitness of SARS-CoV-2[25,26]. The depicted structural models were derived from an S protein X-ray structure (PDB: 6VXX)[23] or computation modeling of N, M, and E proteins (Protein Gene Bank: QHD43423, QHD43419, and QHD43418, respectively)[52]. Sequences, sources, and rationale for selections can be found in the original publication.

*Mapping Epitope Binding to anti-SARS-CoV-2 Abs.* Plasma from COVID-19 patients was subjected to ELISAs with the phage-displayed SARS-CoV-2 epitopes (**Fig. 4-2A**). Unless otherwise indicated (e.g., healthy controls), plasma refers to samples from PCR-verified, COVID-19 patients. In this initial assay, plasma was pooled, diluted 100-fold, and coated on a microtiter plate (3 pools of n = 5 patients per pool). Nonspecific interactions were blocked (ChonBlock), and phage-displayed epitopes were added for ELISA. The resultant data were normalized by signal from the corresponding negative control (phage without a displayed

epitope). Seven candidate epitopes from the pooled patients were further investigated with a larger number of individual patient samples (n = 28) (**Fig. 4-2B**). The strongest, reproducible binding was observed for three epitopes from M (Ep6), N (Ep9), and S (Ep20) proteins. Additional COVID-19 plasma samples were profiled for binding to these three epitopes (n = 86 total) (**Fig. 4-2B**).

Only the Ep9 epitope from N protein demonstrated robust, statistically significant antibody binding in 27% of patients (n = 186) (**Fig. 4-2B**). Of these patients, 100 did not have corresponding health information and were not analyzed further in this report. To test non-phage displayed epitopes, dose-dependent binding to Ep9 fused to eGFP (eGFP-Ep9) or to full-length N protein demonstrates that αEp9 IgGs bind its antigen with $EC_{50}$ = 3.22 nM (95% CI = 2.49 to 4.14 nM). This experiment examines plasma samples with the highest IgG response against the N protein in the COVAM assay. Patients without αEp9 Abs have roughly the same level of binding to N protein as observed for αEp9 Abs binding to Ep9. However, such αEp9 Abs appear to add to N protein binding by antibodies; we observe approximately two-fold increase in apparent antibody binding levels for N protein if the patient also has αEp9 Abs (**Fig. 4-2C**). Therefore, the αEp9 response we report cannot solely be due to N protein antigenicity. In patients for whom longitudinal samples were available, the highest levels of αEp9 Abs were observed at days 1 to 14 post-symptom onset (n = 11) and were detectable within 6 days (**Fig. 4-2D**). In four of these patients, αEp9 Abs persisted after day 14.

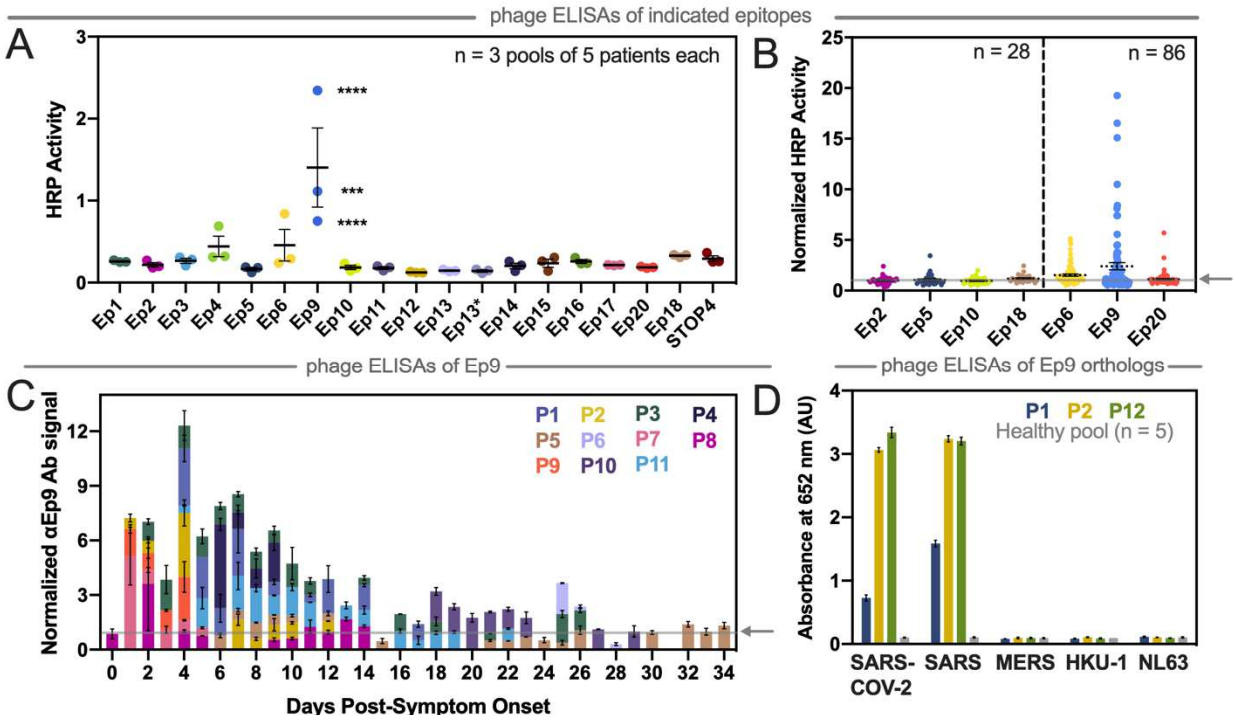


**Figure 4-2. Mapping COVID-19 patient antibody responses with phage-displayed SARS-CoV-2 epitopes. A)** This phage ELISA with the indicated epitopes (*x* axis) examined plasma pooled from patients (*n* = 3 pools of 5 patients each, 2 technical replicates). STOP4 is the phage negative control. **B)** The epitopes with the highest signals were then further examined by ELISA with plasma from individual patients (*n* as indicated). **C)** This ELISA measures dose-dependent binding of αN IgGs from plasma pooled from five αEp9-positive patients and five non-Ep9, αN-positive patients to eGFP-Ep9 (dashed line), eGFP negative control (eGFP-FLAG, dotted line), or full-length N protein (fl-N, solid line). The indicated concentrations of Ep9 or fl-N were immobilized on microtiter plates, and binding of pooled patient plasma (1:100) was detected using α-Fc IgG-HRP Abs (1:10,000). Pooled patients were matched by similar αN IgG binding signal in COVAM analysis (inset). Nonlinear lines of best fit for binding saturation are represented. Statistical comparisons of $B_{max}$, Hill slope, and $EC_{50}$ between groups determines that binding of αEp9 IgGs to fl-N or eGFP-Ep9 and that of non-Ep9, αN IgGs to fl-N are significantly different ($P < 0.0001$). Error bars represent ±SD. The data demonstrate that the $EC_{50}$ value of αEp9 Abs is equal to the cumulative $EC_{50}$ of all other αN Abs in patients lacking the αEp9 Abs. In the presence of the αEp9 Abs, the apparent binding levels of αN Abs against fl-N approximately double. **D)** With samples from individual patients (designated P# and by color) collected at the indicated times, αEp9 Abs were measured. The subset of patients shown here comprises all samples for which longitudinal data were available. **E)** Phage ELISA with samples from patients with strong αEp9 Ab responses (two from the longitudinal study and one from the patient population) examines cross-reactive binding to Ep9 or Ep9 orthologs from the indicated coronaviruses (*x* axis, 3 technical replicates). The arrow on the *y* axis and gray line (B and D) represents the negative control used for normalizing the data. Error bars represent SEM (A, B, C, and E) or range of two measurements (D).

*Cross-Reactivity of αEp9 Abs Against Orthologous Epitopes.* Next, the cross-reactivity of αEp9 Abs was examined with Ep9-orthologs from four phylogenetically related coronaviruses known to infect humans. Specifically, plasma with αEp9 Abs (n = 3) and pooled plasma from healthy individuals (n = 5) were assayed. The Ep9 epitopes from SARS-

CoV-2 and SARS have 90% amino acid sequence homology. Unsurprisingly, this high degree of similarity resulted in a cross-reactive Ep9 epitope, and a strong antibody response was observed to Ep9 epitopes from both viruses (**Fig. 4-2E**). The coronaviruses, MERS, HKU-1, and NL63 have 52%, 43%, and 8% sequence homology to SARS-CoV-2 Ep9, respectively. These more distantly related orthologs exhibited no cross-reactivity with the αEp9 Abs. Furthermore, no response was observed to Ep9 in pooled plasma from healthy individuals.

The protein microarray COVAM analysis is a high-throughput serological test for SARS-CoV-2 Ab cross-reactivity with a panel of 61 antigens from 23 strains of 10 respiratory tract infection-causing viruses [22]. In this assay, each antigen was printed onto microarrays, probed with human plasma, and analyzed with an ArrayCam imager. COVAM distinguishes between IgG and IgM Abs binding to the full-length N protein. Thus, the COVAM analysis complements the phage ELISA by expanding the scope of antigens surveyed and adding Ab serotype information. The ELISA and COVAM data both demonstrate that αEp9 Abs are highly specific for lineage B betacoronaviruses, and unlikely to be found in patients before their infection with SARS-CoV-2.

*More Severe Disease and Poorer Outcomes for αEp9 Patients.* Direct comparison of data with full-length N protein from COVAM and Ep9 phage ELISA (n = 40 patients assayed with both techniques) reveals five unique categories of patients **(Fig. 4-3A)**. To enable this comparison, raw data from each assay was normalized as a percentage of the negative control. Category 1 consists of patients without Abs to the N protein. The next categories include patients with IgMs (Category 2) or IgGs (Category 3) binding to N protein, but not Ep9, termed non-Ep9 αN Abs. Category 4 includes patients with αEp9 Abs (both IgMs and IgGs). Category 5 patients have exclusively IgG αEp9 Abs. The αEp9 Abs are only found in

patients with IgMs or IgGs against full-length N protein from the COVAM assay; the COVAM analysis thus independently corroborate the phage ELISAs **(Fig. 4-3A)**.

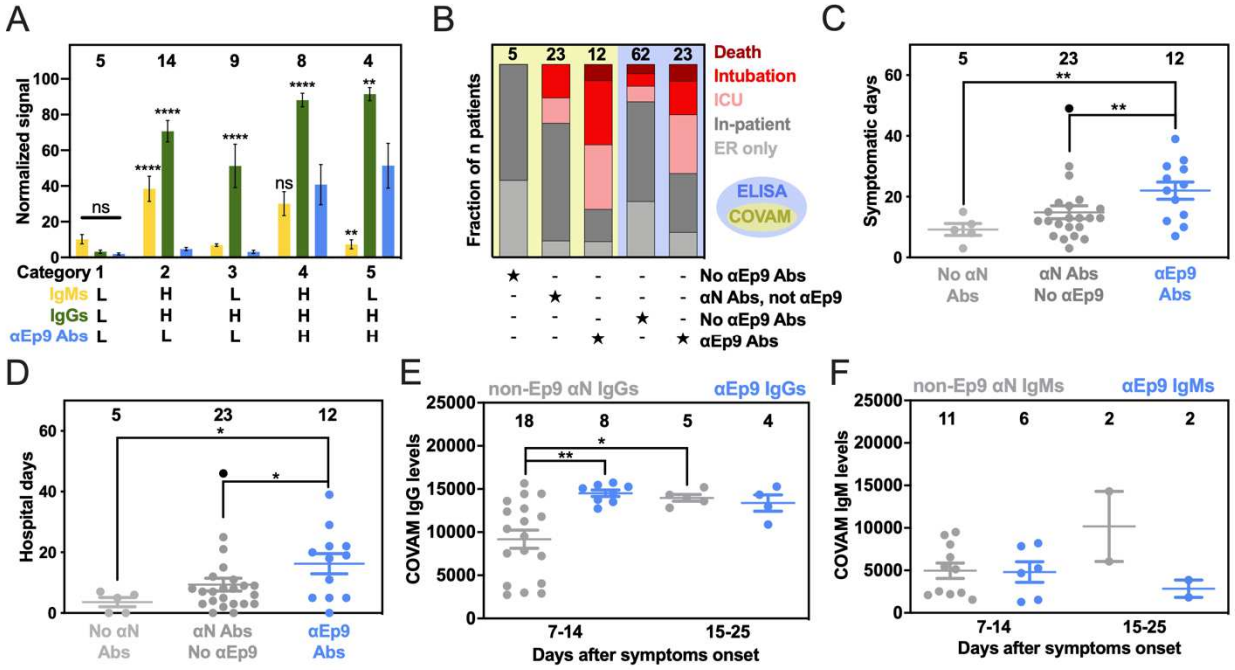


**Figure 4-3. Patients with αEp9 Abs have more severe disease. A)** Normalized and categorized data from measurements by COVAM (IgMs in yellow, IgGs in green) and Ep9 phage ELISA (blue). ANOVA comparing COVAM to ELISA with Dunnett's multiple comparisons yields p-values of **<0.01, ****<0.0001, or ns: not significant. **B)** Disease severity (color) binned by antibody response (COVAM in yellow, or ELISA in blue). Statistical analysis reveals significant differences between distributions of severe and non-severe disease comparing patient categories, p<0.01 and p<0.001 (Fisher's exact test) for COVAM and ELISA, respectively. Patients with αEp9 Abs are **C)** symptomatic for longer durations and **D)** spend more days in the hospital than those with other αN Abs or no αN Abs. ANOVA with Tukey's multiple comparisons yields p-values of *<0.05 and **<0.01. One outlier (black) (ROUT = 0.1%) was omitted from statistical calculations for panels C and D. **E)** The αN IgG appear at high levels early in the course of disease only for αEp9-positive patients, but are lower in non-Ep9, αN-positive patients. After >15 days post symptom onset, αN IgG levels increase for both groups of patients. **F)** However, IgM levels do not change significantly. Error bars depict SEM with the indicated number of patients (n, numbers above columns).

Interestingly, the patients with αEp9 Abs suffer more prolonged illness and worse clinical outcomes compared to patients with non-Ep9 αN Abs or no αN Abs. In this study, severe COVID-19 cases are defined as resulting in death or requiring admission to the ICU or intubation. The fraction of severe COVID-19 cases was 2.5 times higher in αEp9 Abs patients than non-Ep9 αN Abs patients (**Fig. 4-3B, yellow panel**); the differences in proportions of severe and non-severe αN-positive patients with or without αEp9 Abs are statistically

significant ($p<0.030$, Fisher's exact test). Patients without αN Abs (Category 1) had less severe symptoms. The αEp9 Abs patients also had longer durations of symptoms and hospital stays relative to non-Ep9 αN Abs and no αN Abs patients (**Figs. 4-3C** and **D**). A larger data set of patient plasma analyzed by phage ELISA confirmed this conclusion ($p<0.0013$, Fisher's exact test) (**Fig. 4-3B, blue panel**). Our data further demonstrates that asymptomatic COVID-19 patients (n = 3) also tested negative for αEp9 Abs. The data also reveals early seroconversion of αEp9 IgGs (**Fig. 4-3E**), but not αEp9 IgMs (**Fig. 4-3F**).

*Strong Correlation of Severity in Patients with αEp9 Abs and High DRFS.* We compared risk factors, clinical parameters, and disease outcomes among patients with αEp9 Abs (n = 23) (**Figs. 4-4A**). A *disease risk factor score* (DRFS) was developed to evaluate the relationship between clinical preconditions and disease severity in patients with αEp9 Abs. The DRFS quantifies a patient's age, sex, and pre-existing health conditions associated with COVID-19 disease severity and mortality. Risk factors include hypertension, diabetes, obesity, cancer, and chronic conditions of the following: cardiac, cerebrovascular, kidney, and pulmonary [25–28]. Using the *age score* from the Charlson Comorbidity Index [29] yields a patient's DRFS as:

**(eq. 4-1)** $$DRFS = \Sigma \text{ (\# of risk factors)} + \text{(age score)}$$

where each risk factor is valued as either 0 or 1 if absent or present, respectively. The DRFS of patients with αEp9 Abs strongly correlates with COVID-19 disease severity (Pearson's r = 0.72, p-value <0.0001, and $R^2$= 0.52) (**Fig. 4-4A**). The correlation in patients without αEp9 Abs is weak (r = 0.30, p-value = 0.089, $R^2$= 0.018) (**Fig. 4-4A**). Amongst patients with αEp9 Abs (n = 23), a DRFS ≧3 can determine disease severity with 92.3% sensitivity (1/13 false negatives) and 80% specificity (2/10 false positives) (**Fig. 4-4B**). In the entire study cohort

(n = 86), patients with αEp9 Abs and DRFS ≧3 (n = 11) have severe disease with a high degree of specificity (96.7%) and a sensitivity of 44%. Notably, DRFS predicts disease severity only for patients with αEp9 Abs (n = 23), and patients without such Abs (n = 63) had no correlation with disease outcomes.

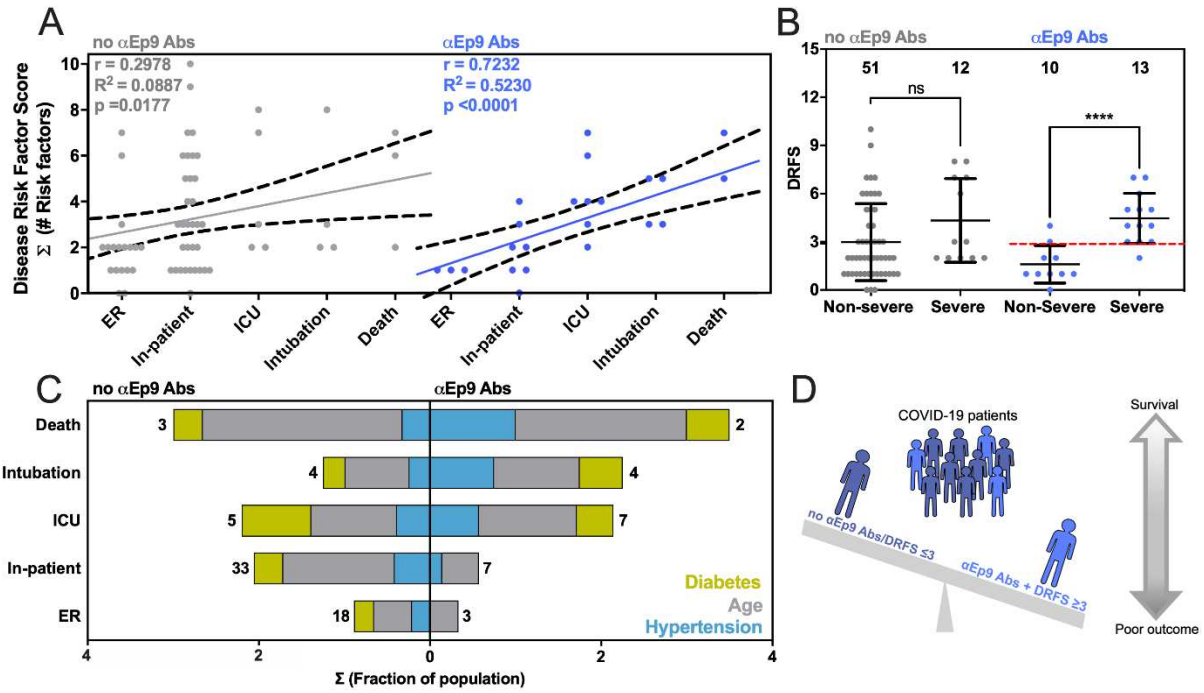


**Figure 4-4. Correlation between disease severity and risk factors in patients with αEp9 Abs. A)** The relationship between DRFS and disease severity of COVID-19 patients with αEp9 Abs (blue) or no αEp9 Abs (gray). Each data point represents one patient. The solid lines indicate linear regression fits with 95% confidence intervals (dotted lines), and Pearson's r-value as noted. **B)** Correlation of disease severity with DRFS in patients with αEp9 Abs. The data depicts a significant correlation between DRFS and disease severity in patients with αEp9 Abs (blue), but not in patients lacking αEp Abs (gray). In αEp9 patients, a DRFS threshold of 3.0 can predict severe disease (red). Two-tailed, parametric t-tests were conducted to compare non-severe and severe disease outcomes of patients with and without αEp9 Abs, where ****p<0.0001. The error bars represent SD with the indicated n. **C)** The color-indicated risk factors (diabetes, hypertension, and age score) are depicted on the x-axis as the fractions of patients in each disease severity category (y-axis). Numbers indicate total patients (n) without αEp9 Abs (left) or with αEp9 Abs (right). The prevalence of risk factors (colors) increases with disease severity in patients with αEp9 Abs, but not in patients without these Abs. **D)** Patients with αEp9 Abs and DRFS ≥3 are predisposed to increased COVID-19 severity and poorer outcomes.

Examining key contributors to high DRFS, the presence of αEp9 Abs correlates with more severe disease in patients who have hypertension, diabetes, or age >50 years. Such correlation is not observed for patients lacking αEp9 Abs (**Fig. 4-4C**). Such risk factors are

prevalent at roughly the same percentages in both populations of patients. Thus, these risk factors are particularly acute for patients with αEp9 Abs.

*Inflammatory Cytokine Levels and Tissue Damage Markers in αEp9 Patients.* COVID-19 patients can have elevated serum concentrations of >20 inflammatory cytokines and chemokines [30]. However, information on the cytokine levels and the association with tissue damage and worse COVID-19 outcomes have been inconsistent [30–32]. For patients with IL-6 concentrations measured in plasma, patients with (n = 8) or without (n = 11) αEp9 Abs were compared. Interestingly, the comparison uncovered a strong positive sigmoidal association between IL-6 and AST unique to patients with αEp9 Abs ($R^2$ = 0.968, Spearman's r = 1.0, p-value <0.0001, n = 8); correlation of IL-6 and AST in patients with αEp9 Abs remains strong even after removal of the data point at the highest IL-6 concentration. Conversely, a slight negative trend is observed in patients lacking αEp9 Abs (Spearman's r = -0.575, p-value= 0.0612, n = 13). Thus, the presence of αEp9 Abs can disambiguate the sometimes-contradictory association of IL-6 with disease severity.

**4.4 Discussion**

This study introduces a two-step test as a prognostic for predicting COVID-19 disease severity and its worst outcomes. Specifically, αEp9 Abs can effectively predict severe disease (specificity 83.6%). However, combining presence of αEp9 Abs with DRFS ≧3 provides much higher specificity (96.7%) for predicting severe disease. Previously, αN IgGs have been recognized as a focal site for an antibody response [18,19,21,33] and associated with disease severity and poor outcomes [11,33,34].

The present investigation expands on previous reports that recognize various regions of the RNA binding domain of N protein as focal sites for anti-SARS-CoV-2 antibody response.

For example, the phage display-based VirScan identified an epitope region spanning residues 141-196 and microarrays further isolated peptides including residues 134-171, 155-171, 153-190, and 153-171[18,19,21]. The above investigations, however, do not find correlations between any these epitopes and disease severity. Our results are confirmed by observations from a patient cohort in Singapore, which identify an epitope (residues 153-170) very similar to Ep9 (residues 152-172) and shows a correlation between antibody response against the epitope and pneumonia and the tissue damage markers (CRP and LDH) [20]. In our investigation, we examine in-depth patient clinical histories, test results, disease outcomes ranging from asymptomatic to fatal, and longer longitudinal profiling post-symptom onset, to determine the association of a larger subset of markers and risk factors. Such data allows calculation of the DRFS. Together with the presence of αEp9 Abs, patient DRFS allows early discrimination of severe from non-severe disease outcomes. Additionally, fine epitope mapping demonstrates that αEp9 Abs strongly and uniquely correlate with COVID-19 disease severity relative to other αN Abs.

We hypothesize that the underlying mechanism relating αEp9 Abs to increased disease severity involves an overzealous immune response. Specifically, we observe early seroconversion and strong early upregulation of αEp9 IgGs (**Fig. 4-3E**). Similar IgG observations have been correlated with poor viral neutralization and clearance, resulting in increased COVID-19 severity[10,34,35]. Also, high levels of IL-6 are observed for αEp9-positive patients with increased levels of the tissue damage marker AST; this correlation does not exist for patients lacking αEp9 Abs. The sensitivity to IL-6 concentration before AST-monitored organ damage suggests anti-IL-6 therapeutics could be an effective management in the early and rapidly progressive stages of respiratory distress for αEp9-positive patients

[30,36–40]. Since binding to N protein by αEp9 antibodies is unlikely to enhance uptake of SARS-CoV-2, an antibody-dependent enhancement mechanism could invoke antigen uptake by macrophages. This mechanism could stimulate complement activation and the cytokine storm observed here as elevated IL-6 response. Further investigation is required to determine the basis for increased disease severity in αEp9 patients.

The data demonstrate that αEp9 positive patients with DRFS ≥3 are 13.42 times (Likelihood Ratio) more likely to have severe COVID-19 disease symptoms within the study cohort (n = 86). The presence of αEp9 without DRFS is less effective as a prognostic (Likelihood Ratio of 3.17). Despite its high specificity (96.7%), the sensitivity of this two-step test is 44% (n = 86). However, this test could predict a subset of patients with a specific immune response (i.e., early IgG response and IL-6 dependent immune hyperactivity), and could suggest targeted treatment options (e.g., targeting IL-6 and its pathways).

Importantly, αEp9 Abs appear early in the course of disease. Thus, such a prognostic could outperform traditional markers for the cytokine storm such as IL-6, which appears 6-8 days after symptom onset [30,38]; all plasma collected from αEp9 positive patients (n = 7, **Fig. 4-2C**) between 1 to 6 days post-symptoms onset demonstrate detectable levels of αEp9 IgG (≥ 2 fold over negative control). Early detection of αEp9 Abs in patients could be used to triage and treat COVID-19 prior to the onset of its most severe symptoms; delayed treatments of IL-6 targeting drugs can decrease their efficacy or be counterproductive [30,36–41]. The αEp9 Ab biomarker could identify patients most likely to benefit from anti-IL-6 therapeutics and avoid ineffective treatments.

## 4.5 Conclusions

This study demonstrates the usefulness of fine epitope mapping, but the following limitations should be noted. Short linear epitopes, unlike conformational epitopes in larger domains, might not resemble the tertiary structure of an antigen. Post-translational modifications, such as glycosylation were omitted for the phage-displayed S protein epitopes; the COVAM antigens, however, are produced in baculovirus or HEK-293 cells, which could glycosylate the antigens. Our analysis is largely based upon a population of 86 COVID-19 patients and 5 healthy individuals, with the majority of Hispanic descent. The conclusions could be further strengthened with follow-up investigations in a larger population. Additionally, the population examined here only included three asymptomatic individuals, and additional testing is required to verify absence of αEp9 Abs in such patients. The sample size of patients with multiple antibody targets was too limited to allow correlation analysis; future investigations could examine associations between αEp9 and other Abs. Abs recognizing other SARS-CoV-2 structural proteins could also exhibit similar characteristics to αEp9 Abs.

Existing diagnostic platforms could readily be adapted to test for αEp9 Abs, and the DRFS calculation is quite simple to implement (e.g., assay with eGFP-Ep9 fusion demonstrated here). As shown here, αEp9 Abs do not recognize orthologous sequences from closely related coronaviruses, providing good specificity for αEp9 as a prognostic. Previous studies have shown that the high homology of N protein among related coronaviruses can lead to high false positive rates in serodiagnostics with full-length N antigen [42]. Thus, the two-step prognostic reported here could mitigate the worst outcomes of COVID-19, particularly for patients at high risk.

## 4.6 Materials and Methods

*Cloning Phagemids and eGFP Fusion Plasmids.* For phage display of epitopes, the pm1165a phagemid vector as previously described[43] was engineered to encode an N-terminal FLAG tag and a C-terminal fusion to the P8 coat protein of M13 phage. This template, termed FlagTemplate, was used for subcloning of SARS-CoV-2, SARS, MERS, HKU-1, and NL63 epitopes. A vector map of the FlagTemplate, cloning procedures, and a list of oligonucleotides for Q5 site-directed mutagenesis and Gibson assembly are available online.

Short (approximately 30 amino acids) putative epitopes for phage display and Escherichia coli expression as eGFP fusion peptides in the pET28 vector were cloned via Q5 site-directed mutagenesis according to the manufacturer's instructions. A vector map of the peptide with Ep9 fused to eGFP, termed eGFP-Ep9, is available online. For large epitopes (>500 bp), such as Ep17, Gibson assembly (New England Biolabs) was conducted in two PCR steps with the FlagTemplate or pCAGGS containing the SARS-CoV-2 S protein gene (BEI Resources) to generate the vectors and inserts, respectively. The Gibson assembly (2 µl) or KLD (kinase, ligase, DpnI) mix (5 µl) was transformed into Nova Blue E. coli competent cells, and transformants were plated on a carbenicillin-supplemented (50 µg/ml) agar plate before incubation at 37°C overnight. Five single colonies were selected to inoculate 4 ml of super optimal broth (2% wt/vol tryptone, 0.5% yeast extract, 8.56 mM NaCl, 2.5 mM KCl, 10 mM $MgCl_2$, 10 mM $MgSO_4$) in a 15-ml culture tube supplemented with carbenicillin (50 µg/ml). The seed cultures were incubated at 37°C with shaking at 225 rpm for 8 to 12 h. Phagemid DNA was isolated using the QIAprep spin miniprep kit according to the manufacturer's instructions. The successful subcloning of the open reading frame (ORF) encoding each epitope was verified via DNA sequencing (Genewiz). The full-length N protein

in a pLVX-EF1α-IRES-Puro plasmid was a generous gift from Rachel Martin of University of California, Irvine (UCI).

*Purification and Preparation of Phage.* Phage were propagated and purified using procedures previously described[44] with the following changes. A single colony was selected to inoculate 15 ml of yeast extract and tryptone media (2YT) (1.6% wt/vol tryptone, 1% wt/vol yeast extract, 0.5% wt/vol NaCl) and shaken at 37°C until the optical density at 600 nm ($OD_{600}$) reached 0.6. After incubation at 37°C for 45 min, 8 ml of the primary culture was used to inoculate 300 ml of 2YT supplemented with carbenicillin (50 μg/ml), kanamycin (20 μg/ml), and isopropyl-β-d thiogalactopyranoside (IPTG; 30 μM).

To precipitate the phage, the cultures were centrifuged at 10 krpm (15,300 × g) for 10 min at 4°C. The supernatant was decanted into a centrifuge tube containing 60 ml polyethylene glycol (PEG) 8000 (20%, wt/vol) and NaCl (2.5 M). The tube was inverted 10 times and stored on ice for 30 min followed by an additional centrifugation at 10 krpm (15,300 × g) for 20 min at 4°C. The supernatant was decanted, and tubes were centrifuged for an additional 4 min at 4 krpm (2,429 × g) at 4°C. The pellets were resuspended in PBS (10 mM phosphate, 137 mM NaCl, pH 7.2) with Tween 20 (0.05%, vol/vol) and glycerol (10%, vol/vol), separated into 1-ml aliquots, flash frozen with liquid nitrogen, and stored at −80°C. For binding assays via ELISA, the purified phage was thawed on ice, precipitated a second time as before. The quality of each phage preparation was routinely checked by quality control ELISA, termed QC ELISA, to a FLAG peptide fused to the N terminus of each epitope; additionally, PCR using Oligo69 and Oligo70 followed by DNA sequencing (Genewiz) was performed for every phage preparation. Such quality control allowed for identification of toxic clones; for example, C8 was apparently toxic to E. coli, and three protein epitopes

failed to express in E. coli for unknown reasons. The phage concentration was determined by absorbance at 260 nm using a coefficient of molar absorptivity of 0.003 $nM^{-1}$ $cm^{-1}$ and diluted to 40 nM in PBS.

*Expression and Purification of eGFP-Ep9 and N Protein.* A pET28c plasmid containing Ep9 fused to an N-terminal eGFP was transformed into BL21(DE3)* E. coli heat shock-competent cells. A single colony was transferred to LB medium (20 ml) supplemented with kanamycin (40 μg/ml) and incubated at 37°C for 18 h. An aliquot of the starter culture (2.5 ml) was transferred to LB medium with 1% glucose (250 ml LB in a 1-liter baffled flask). After reaching an $OD_{600}$ between 0.4 and 0.6, the culture was induced through addition of IPTG (0.5 mM) before incubation at 25°C for 18 h. The cells were centrifuged (15,300 × g) for 20 min at 4°C, and the cell pellet was resuspended in lysis buffer (25 mM Tris-HCl and 200 mM NaCl, pH 8.0, and supplemented with protease inhibitor cocktail) followed by sonication. The lysate was subjected to centrifugation (26,892 relative centrifugal force [rcf], 45 min, 4°C). The supernatant was incubated with charged nickel immobilized-metal affinity chromatography resin overnight on a rotary shaker (150 rpm at 4°C). The resin was equilibrated in a column and washed with wash buffer (20 mM imidazole in lysis buffer), and the purified protein was eluted using elution buffer (250 mM imidazole in lysis buffer). Elutions containing the purified protein were visualized using 10% or 12% SDS-PAGE (Bio-Rad Mini-Protean Tetra electrophoresis system) stained with Coomassie brilliant blue stain. The eluted fractions containing the purified eGFP-Ep9 were pooled, and buffer exchanged for 3 column volumes (20 ml) with lysis buffer without imidazole using a 10-kDa-cutoff microconcentrator (Vivaspin; Fisher Scientific). The protein concentration was determined by a bicinchoninic acid (BCA) assay or Bradford assay using the estimated molecular weight

(MW) (http://www.expasy.org). Like eGFP-Ep9, the full-length N protein was expressed in 250 ml LB with 1% glucose and induced with 0.25 mM IPTG at an OD600 of 0.8. Protein overexpression cultures were incubated at 16°C for 22 h. Lysis and purification were conducted as described above, using N protein lysis buffer (20 mM Tris-HCl, 300 mM NaCl, 5 mM $MgCl_2$, 5 mM β-mercaptoethanol [BME], 10% glycerol, pH 8.0). The purified full-length N protein was analyzed using 10% SDS-PAGE.

*Patient Sample Collection.* The UCI Experimental Tissue Resource (ETR) operates under a blanket IRB protocol (UCI no. 2012-8716) that gives ETR personnel "Honest Broker" status and enables the collection of any fluid or tissue remnant in excess of that needed for clinical diagnosis and distribution to investigators under the conditions of their own IRB approval. Patients undergoing COVID testing in the Emergency Department or on the inpatient service with confirmed COVID+ pharyngeal swabs were followed for their blood collections daily. Specimens collected originally for diagnostic purposes were processed and stored by the hospital laboratory in a manner compliant with College of American Pathologists (CAP) standards. EDTA-anticoagulated whole blood was stored for 2 days at 4°C after clinical diagnosis and released for research purposes. Plasma from heparin-anticoagulated blood was centrifuged immediately after collection and preserved at 4°C for 3 to 4 days before being released for research use. All COVID+ specimens were handled under biosafety level 2 (BSL-2) conditions, aliquoted into screw-cap cryovials, and stored at −80°C long term with constant temperature monitoring. Specimens were coded by the ETR with unique identifiers, and accompanying clinical information was stripped of protected health information such that investigators could receive specimens under a Non-Human Subjects Determination exemption from the UCI IRB. All samples from SARS-CoV-2-infected

patients were inactivated by incubation in a water bath at 56°C for 30 min[45], aliquoted (40 µl each), and stored at −80°C.

*Phage ELISA with Patient Plasma.* The phage-displayed SARS-CoV-2 epitopes were used in phage ELISAs with patient plasma samples diluted 100-fold in coating buffer (50 mM $Na_2CO_3$, pH 9.6). After incubation in a 96-well Nunc MaxiSorp flat-bottom microtiter plate with shaking at 150 rpm at 4°C for 12 to 18 h, plasma was aspirated by a plate washer (BioTek). Next, the plate was treated with 100 µl per well of ChonBlock blocking/sample dilution buffer (Chondrex, Inc.) for 1 h with shaking at 150 rpm at room temperature and washed three times with wash buffer (0.05% [vol/vol] Tween 20 in PBS). The epitope displaying phage and controls were diluted to 1 nM in ChonBlock blocking/sample dilution buffer, and 100 µl was added to each well before incubating for 2 h with shaking (150 rpm) at room temperature. The plate was then washed three times with wash buffer. The primary antibody, anti-M13-horseradish peroxidase (HRP) (Creative Diagnostics), was diluted 1:5,000 in ChonBlock secondary antibody buffer, and 100 µl was added per well; the plate was incubated for 1 h at 150 rpm and room temperature. Following three washes with wash buffer, 1-Step Ultra 3,3′,5,5′-tetramethylbenzidine (TMB)-ELISA substrate solution (100 µl per well; Thermo Scientific) was added. Absorbance of TMB substrate was measured twice at 652 nm by a UV-visible (UV-Vis) plate reader (BioTek) after 5 and 15 min of incubation.

*ELISA of eGFP-Ep9 and Full-Length N Protein with Plasma.* Various doses, with a maximum concentration of 1.7 µM, of eGFP-Ep9, eGFP-FLAG, or full-length N protein (fl-N) were diluted in PBS (pH 8.0) and then immobilized on a 96-well Nunc MaxiSorp flat-bottom microtiter plate before incubation on a shaker (150 rpm) at 4°C for 12 to 18 h. After incubation, unattached proteins were removed through aspiration using a plate washer

(BioTek) and wells were blocked with 100 µl ChonBlock blocking/sample dilution buffer (Chondrex, Inc.) for 30 min with shaking (150 rpm) at room temperature. The plate was then washed three times with wash buffer (0.05% [vol/vol] Tween 20 in PBS). Pooled plasma from five patients within each experimental group was diluted 100-fold in ChonBlock blocking/sample dilution buffer, and 100 µl was added to each well before incubating for 1 h with shaking (150 rpm) at room temperature. The plate was then washed three times with wash buffer. The detection antibody, IgG Fc goat anti-human–HRP (Invitrogen), was diluted 1:5000 in ChonBlock secondary antibody buffer, and 100 µl was added per well; the plate was incubated for 30 min at 150 rpm and room temperature. Following six washes with wash buffer, 1-Step Ultra TMB-ELISA substrate solution (100 µl per well; Thermo Scientific) was added. Absorbance of TMB substrate was measured twice at 652 nm by UV-Vis plate reader (BioTek) after 5 and 15 min of incubation.

*COVAM.* Serum coronavirus antigen microarray (COVAM) included 67 antigens across respiratory virus subtypes including 11 antigens from SARS-CoV-2 expressed in either baculovirus or HEK-293 cells as previously detailed.[22] These antigens were provided by Sino Biological U.S. Inc. as either catalog products or custom synthesis service products. The antigens were printed onto microarrays, probed with human sera, and analyzed as previously described.[46–48] Briefly, lyophilized antigens were reconstituted with sterile water to a concentration of 0.1 mg/ml protein in PBS, and printing buffer was added. Antigens were then printed onto Oncyte Avid nitrocellulose-coated slides (Grace Bio-Labs) using an OmniGrid 100 microarray printer (GeneMachines). The microarray slides were probed with human sera diluted 1:100 in 1× protein array blocking buffer (GVS Life Sciences, Sanford, ME) overnight at 4°C and washed with TTBS buffer (20 mM Tris-HCl, 150 mM NaCl, 0.05%

Tween 20 in double-distilled water (ddH2O) adjusted to pH 7.5 and filtered) three times for 5 min each. A mixture of human IgG and IgM secondary antibodies conjugated to quantum dot fluorophores Q800 and Q585, respectively, was applied to each of the microarray pads and incubated for 2 h at room temperature, and pads were then washed with TTBS three times for 5 min each and dried. The slides were imaged using an ArrayCam imager (Grace Bio-Labs) to measure background-subtracted median spot fluorescence. Nonspecific binding of secondary antibodies was subtracted using a saline control. The mean fluorescence of the 4 replicate spots for each antigen was used for analysis.

*Statistical Analysis.* The ELISA data were analyzed in GraphPad Prism 8. Since the total antibody content differs from person to person, the raw absorbance values for every patient sample were normalized and represented as the ratio compared to a negative control. Analysis of variance (ANOVA) with Dunnett's multiple-comparison test was performed to determine if values were statistically significant. Correlations between COVAM IgG/IgM and ELISA were determined by plotting normalized values on an xy graph and performing a nonparametric correlation analysis using a Spearman rank correlation coefficient test.

For data visualization of clinical patient data, trends in data were evaluated using Knime Analytics Platform software. GraphPad Prism was used to calculate column statistics including mean, standard deviation, standard error of the mean (SEM), P values, odds ratios, and likelihood ratios defined as sensitivity/(1 − specificity). ANOVA with Tukey's multiple-comparison test was used to evaluate antibody response and disease severity between patients with αEp9 Abs, non-Ep9 Abs, αN Abs, or non-αN Abs. Comparisons of patients with αEp9 Abs and non-αEp9 Abs were conducted using unpaired, two-tailed, parametric t tests. Contingency graphs were statistically evaluated using Fisher's exact test, for groups with

binary categorization, and the chi-squared test for groups with multiple categories. Different data sets were fitted with linear or nonlinear regression methods; the fit with the higher R2 value was chosen. Correlations between two clinical parameters (e.g., IL-6 and AST) were evaluated using the Pearson coefficient or Spearman coefficients (r) for linear or nonlinear regressions, respectively; r values between 1.0 and 0.7 were considered strong correlations, r values between 0.7 and 0.5 were considered moderate correlations, and values below 0.5 were considered weak correlations.[49] The significance of the correlation was evaluated based on a P value of $<0.05$.

**Table 4-1. Phage-displayed putative epitopes of SARS-CoV-2 and Ep9 orthologs.**

| Epitope | Protein | Residues* | Amino Acid Sequence | Ref |
|---|---|---|---|---|
| Ep1 | S | 287-317 | DAVDCALDPLSETKCTLKSFTVEKGIYQTSN | 13 |
| Ep2 | S | 802-819 | FSQILPDPSKPSKRSFIE | 13 |
| Ep3 | S | 15-30 | CVNLTTRTQLPPAYTN | 14 |
| Ep4 | S | 1056-1070 | APHGVVFLHVTYVPA | 12 |
| Ep5 | M | 1-24 | MADSNGTITVEELKKLLEQWNLVI | 13 |
| Ep6 | M | 132-151 | PLLESELVIGAVILRGHLRI | 13 |
| Ep7 | M | 97-111 | IASFRLFARTRSMWS | 15 |
| Ep8 | N | 41-61 | RPQGLPNNTASWFTALTQHGK | 13 |
| Ep9 | N | 152-172 | ANNAAIVLQLPQGTTLPKGFY | 13 |
| Ep10 | N | 264-278 | ATKAYNVTQAFGRRG | 12 |
| Ep11 | E | 52-66 | VKPSFYVYSRVKNLN | 12 |
| Ep12 | S | 524-598 | VCGPKKSTNLVKNKCVNFNFNGLTGTGVLTESNKKFL PFQQFGRDIADTTDAVRDPQTLEILDITPCSFGGVSV I | 13 |
| Ep13 | S | 601-640 | GTNTSNQVAVLYQDVNCTEVPVAIHADQLTPTWRVYS TGS | 13 |
| Ep13* | S | 601-640 | GTNTSNQVAVLYQGVNCTEVPVAIHADQLTPTWRVYS TGS | 25,26,52 |
| Ep14 | S | 61-76 | NVTWFHAIHVSGTNGT | 14 |
| Ep15 | S | 373-390 | SFSTFKCYGVSPTKLNDL | 14 |
| Ep16 | N | 354-400 | NKHIDAYKTFPPTEPKKDKKKKADETQALPQRQKKQQ TVTLLPAADL | 13 |
| Ep17 | S | 319-529 | RVQPTESIVRFPNITNLCPFGEVFNATRFASVYAWNR KRISNCVADYSVLYNSASFSTFKCYGVSPTKLNDLCF TNVYADSFVIRGDEVRQIAPGQTGKIADYNYKLPDDF TGCVIAWNSNNLDSKVGGNYNYLYRLFRKSNLKPFER DISTEIYQAGSTPCNGVEGFNCYFPLQSYGFQPTNGV GYQPYRVVVLSFELLHAPATVCGPKK | 23 |
| Ep18 | S | 488-507 | CYFPLQSYGFQPTNGVGYQP | 23 |
| Ep19 | S | 429-448 | FTGCVIAWMSNNLDSKVGGN | 23 |
| Ep20 | S | 448-466 | NYNYLYRLFRKSNLKPFER | 23 |
| Ep21 | S | 467-487 | DISTEIYQAGSTPCNGVEGFN | 23 |
| sEp9 | N | 153-173 | NNNAATVLQLPQGTTLPKGFY | |
| mEp9 | N | 141-161 | NNDSAIVTQFAPGTKLPKNFH | |
| hEp9 | N | 166-186 | TTQEAIPTRFPPGTILPQGYY | |
| nEp9 | N | 119-136 | NQKPLEPKFSIALPPELS | |

*Residue numbering from protein sequences deposited in GenBank. Specifically, the accession numbers were as follows: S protein (YP_009724390.1), M protein (YP_009724393.1), N protein (YP_009724397.2), and E protein (YP_009724392.1) from SARS-CoV-2 and N protein from SARS (NP_828855.1), MERS (YP_009047211.1), HKU-1 (YP_173242.1), or NL63 (TP_003771.1).

**Table 4-2. Demographics and clinical characteristics of COVID-19 patients.**

| Characteristics | No αEp9 Abs (n = 63) | αEp9 Abs (n = 23) | p-value |
|---|---|---|---|
| **Demographics** | | | |
| Age (± SD) | 49.75 (± 18.45) | 47.26 (± 18.45) | 0.5668 |
| Sex F:M (%) | 21:42 (44.4/66.7) | 10:13 (43.5/56.5) | 0.4502 |
| Ethnicity n, (%) Hispanic: Asian: Caucasian: Black: Other | 15 (65.2):4 (17.4): 3 (13.0): 1 (4.3): 0 (0) | 39 (61.9): 8 (12.7): 9 (14.3): 3 (4.8): 4 (6.3) | 0.7760 |
| BMI (± SD) | 28.9 (± 6.4) | 32.0 (± 7.9) | 0.0642 |
| **Preconditions, n (%)** | | | |
| Hypertension | 23 (36.5) | 10 (43.5) | 0.6203 |
| Diabetes | 21 (33.2) | 6 (26.1) | 0.6065 |
| CVD | 6 (9.5) | 2 (8.7) | 1.0000 |
| CAD | 6 (9.5) | 2 (8.7) | 1.0000 |
| CKD/ESRD | 6 (9.5) | 2 (8.7) | 1.0000 |
| Asthma/COPD | 8 (12.7) | 3 (13.0) | 1.0000 |
| Obesity | 24 (38.1) | 13 (56.5) | 0.1461 |
| Cancer | 2 (3.17) | 3 (13.0) | 0.1163 |
| **Symptoms, n (%)** | | | |
| Total Days of Symptoms | 9.8 (± 9.0) | 17 (± 10) | 0.0059** |
| Cough | 43 (68.3) | 15 (65.2) | 0.7997 |
| Dyspnea/SOB | 28 (44.4) | 11 (47.8) | 0.8108 |
| Myalgia/Fatigue | 17 (27.0) | 8 (34.8) | 0.5926 |
| Headache | 12 (19.0) | 2 (8.7) | 0.3349 |
| Chest Pain | 7 (11.1) | 3 (13.0) | 1.0000 |
| Anosmia | 4 (6.3) | 2 (8.7) | 0.6561 |
| Stroke-like Symptoms | 0 | 2 (8.7) | 0.0692 |
| Abdominal Pain | 3 (4.8) | 0 | 0.5611 |
| Pulmonary Symptoms^ (Pneumonia: Other: None) | 16 (25.4): 36 (52.4): 8 (12.7) | 13 (56.5): 7 (30.4): 1 (4.3) | 0.0421* |
| **Severity, n (%)** | | | |
| Asymptomatic | 3 | 0 | 0.5611 |
| Non-severe: Sever^^ | 51:12 (n, severity 19.0%) | 10:13 (n, severity 56.5%) | 0.0013** |
| Days in Hospital | 5.8 (± 8.0) | 11.0 (± 10.7) | 0.0183* |
| Days in ICU | 12.6 (± 13.2) n = 11 | 12.5 (± 6.9), n = 12 | 0.8004 |
| Days on Ventilator | 14.0 (± 4.0), n = 6 | 13.0 (± 5.4), n = 7 | 0.7934 |

Results are presented as mean ± SD or n and percentage of population. P-values for continuous variables are calculated using unpaired, two-tailed T-tests. P-values for categorical variables use Fisher's exact test for single value parameters, and Chi-squared test for multi-group variables. *, ** p-values < 0.05, 0.01, respectively.

^ Pulmonary symptoms are based on descriptive reports of X-ray and CT scans. "Other" pulmonary symptoms include, but are not limited to, atelectasis, pleural scarring, pleural effusion, pulmonary edema, mild peribronchial thickening.
^^ Non-severe include ER and in-patients only, severe includes patients in the ICU, on the ventilator or death.

BMI = body mass index, CVD = cardiovascular disease, CAD = coronary artery disease, CKD = chronic kidney disease, ESRD = end-stage renal disease, SOB = shortness of breath, COPD = chronic obstructive pulmonary disease.

## 4.7 References


(1) World Health Organization. *Coronavirus Disease (COVID-19)*; 2020. https://doi.org/10.1097/jcn.0000000000000710.

(2) Llanes, A.; Restrepo, C. M.; Caballero, Z.; Rajeev, S.; Kennedy, M. A.; Lleonart, R. Betacoronavirus Genomes: How Genomic Information Has Been Used to Deal with Past Outbreaks and the Covid-19 Pandemic. *Int. J. Mol. Sci.* **2020**, *21* (12), 1–28. https://doi.org/10.3390/ijms21124546.

(3) Richardson, S.; Hirsch, J. S.; Narasimhan, M.; Crawford, J. M.; McGinn, T.; Davidson, K. W.; Barnaby, D. P.; Becker, L. B.; Chelico, J. D.; Cohen, S. L.; Cookingham, J.; Coppa, K.; Diefenbach, M. A.; Dominello, A. J.; Duer-Hefele, J.; Falzon, L.; Gitlin, J.; Hajizadeh, N.; Harvin, T. G.; Hirschwerk, D. A.; Kim, E. J.; Kozel, Z. M.; Marrast, L. M.; Mogavero, J. N.; Osorio, G. A.; Qiu, M.; Zanos, T. P. Presenting Characteristics, Comorbidities, and Outcomes among 5700 Patients Hospitalized with COVID-19 in the New York City Area. *JAMA - J. Am. Med. Assoc.* **2020**, *323* (20), 2052–2059. https://doi.org/10.1001/jama.2020.6775.

(4) Gallo Marin, B.; Aghagoli, G.; Lavine, K.; Yang, L.; Siff, E. J.; Chiang, S. S.; Salazar-Mather, T. P.; Dumenco, L.; Savaria, M. C.; Aung, S. N.; Flanigan, T.; Michelow, I. C. Predictors of COVID-19 Severity: A Literature Review. *Rev. Med. Virol.* **2020**, No. June. https://doi.org/10.1002/rmv.2146.

(5) Song, P.; Li, W.; Xie, J.; Hou, Y.; You, C. Cytokine Storm Induced by SARS-CoV-2. *Clin. Chim. Acta* **2020**, *509* (June), 280–287. https://doi.org/10.1016/j.cca.2020.06.017.

(6) Iwasaki, A.; Yang, Y. The Potential Danger of Suboptimal Antibody Responses in COVID-19. *Nature Reviews Immunology*. Nature Research June 2020, pp 339–341. https://doi.org/10.1038/s41577-020-0321-6.

(7) Arvin, A. M.; Fink, K.; Schmid, M. A.; Cathcart, A.; Spreafico, R.; Havenar-Daughton, C.; Lanzavecchia, A.; Corti, D.; Virgin, H. W. A Perspective on Potential Antibody-Dependent Enhancement of SARS-CoV-2. *Nature* **2020**, *584* (7821), 353–363. https://doi.org/10.1038/s41586-020-2538-8.

(8) Huang, L. R.; Chiu, C. M.; Yeh, S. H.; Huang, W. H.; Hsueh, P. R.; Yang, W. Z.; Yang, J. Y.; Su, I. J.; Chang, S. C.; Chen, P. J. Evaluation of Antibody Responses against SARS Coronaviral Nucleocapsid or Spike Proteins by Immunoblotting or ELISA. *J. Med. Virol.* **2004**, *73* (3), 338–346. https://doi.org/10.1002/jmv.20096.

(9) He, Y.; Zhou, Y.; Siddiqui, P.; Niu, J.; Jiang, S. Identification of Immunodominant Epitopes on the Membrane Protein of the Severe Acute Respiratory Syndrome-Associated Coronavirus. *J. Clin. Microbiol.* **2005**, *43* (8), 3718–3726. https://doi.org/10.1128/JCM.43.8.3718-3726.2005.

(10) Long, Q. X.; Liu, B. Z.; Deng, H. J.; Wu, G. C.; Deng, K.; Chen, Y. K.; Liao, P.; Qiu, J. F.; Lin, Y.; Cai, X. F.; Wang, D. Q.; Hu, Y.; Ren, J. H.; Tang, N.; Xu, Y. Y.; Yu, L. H.; Mo, Z.; Gong, F.; Zhang, X. L.; Tian, W. G.; Hu, L.; Zhang, X. X.; Xiang, J. L.; Du, H. X.; Liu, H. W.; Lang, C. H.; Luo, X. H.; Wu, S. B.; Cui, X. P.; Zhou, Z.; Zhu, M. M.; Wang, J.; Xue, C. J.; Li, X. F.; Wang, L.; Li, Z. J.; Wang, K.; Niu, C. C.; Yang, Q. J.; Tang, X. J.; Zhang, Y.; Liu, X. M.; Li, J. J.; Zhang, D. C.; Zhang, F.; Liu, P.; Yuan, J.; Li, Q.; Hu, J. L.; Chen, J.; Huang, A. L. Antibody Responses to SARS-CoV-2 in Patients with COVID-19. *Nat. Med.* **2020**, *26* (6), 845–848. https://doi.org/10.1038/s41591-020-0897-1.

(11) Batra, M.; Tian, R.; Zhang, C.; Clarence, E.; Sofia Sacher, C.; Nestor Miranda, J.; Rafa De La Fuente, J. O.; Mathew, M.; Green, D.; Patel, S.; Virginia Perez Bastidas, M.; Haddadi, S.; Murthi, M.; Santiago Gonzalez, M.; Kambali, S.; M Santos, K. H.; Asif, H.; Modarresi, F.; Faghihi, M.; Mirsaeidi, M. Role of IgG against N-Protein of SARS-CoV2 in COVID19 Clinical Outcomes. *medRxiv* **2020**, 2020.09.23.20197251.

(12) Fast, E.; Altman, R.; Chen, B. Potential T-Cell and B-Cell Epitopes of 2019-NCoV. *bioRxiv* **2020**, *XXX* (Xx), 1–9. https://doi.org/10.1101/2020.02.19.955484.

(13) Grifoni, A.; Sidney, J.; Zhang, Y.; Scheuermann, R. H.; Peters, B.; Sette, A. A Sequence Homology and Bioinformatic Approach Can Predict Candidate Targets for Immune Responses to SARS-CoV-2. *Cell Host Microbe* **2020**, *27* (4), 671-680.e2. https://doi.org/10.1016/j.chom.2020.03.002.

(14) Baruah, V.; Bose, S. Immunoinformatics-Aided Identification of T Cell and B Cell Epitopes in the Surface Glycoprotein of 2019-NCoV. *J. Med. Virol.* **2020**, *92* (5). https://doi.org/10.1002/jmv.25698.

(15) Zheng, M.; Song, L. Novel Antibody Epitopes Dominate the Antigenicity of Spike Glycoprotein in SARS-CoV-2 Compared to SARS-CoV. *Cellular and Molecular Immunology*. Springer Nature May 2020, pp 536–538. https://doi.org/10.1038/s41423-020-0385-z.

(16) Tilocca, B.; Soggiu, A.; Sanguinetti, M.; Musella, V.; Britti, D.; Bonizzi, L.; Urbani, A.; Roncada, P. Comparative Computational Analysis of SARS-CoV-2 Nucleocapsid Protein Epitopes in Taxonomically Related Coronaviruses. *Microbes Infect.* **2020**, *22* (4–5), 188–194. https://doi.org/10.1016/j.micinf.2020.04.002.

(17) Rakib, A.; Sami, S. A.; Mimi, N. J.; Chowdhury, M. M.; Eva, T. A.; Nainu, F.; Paul, A.; Shahriar, A.; Tareq, A. M.; Emon, N. U.; Chakraborty, S.; Shil, S.; Mily, S. J.; Ben Hadda, T.; Almalki, F. A.; Emran, T. Bin. Immunoinformatics-Guided Design of an Epitope-Based Vaccine against Severe Acute Respiratory Syndrome Coronavirus 2 Spike Glycoprotein. *Comput. Biol. Med.* **2020**, *124* (May). https://doi.org/10.1016/j.compbiomed.2020.103967.

(18) Wang, L.; Candia, J.; Ma, L.; Zhao, Y.; Imberti, L.; Sottini, A.; Dobbs, K.; NIAID-NCI COVID Consortium; Lisco, A.; Sereti, I.; Su, H. C.; Notarangelo, L. D.; Wang, X. W. Serological Responses to Human Virome Define Clinical Outcomes of Italian Patients Infected with SARS-CoV-2. *medRxiv* **2020**.

(19) Zamecnik, C. R.; Rajan, J. V.; Yamauchi, K. A.; Mann, S. A.; Loudermilk, R. P.; Sowa, G. M.; Zorn, K. C.; Alvarenga, B. D.; Gaebler, C.; Caskey, M.; Stone, M.; Norris, P. J.; Gu, W.; Chiu, C. Y.; Ng, D.; Byrnes, J. R.; Zhou, X. X.; Wells, J. A.; Robbiani, D. F.; Nussenzweig, M. C.; DeRisi, J. L.; Wilson, M. R. *ReScan, a Multiplex Diagnostic Pipeline, Pans Human Sera for SARS-CoV-2 Antigens*; Elsevier Inc., 2020. https://doi.org/10.1016/j.xcrm.2020.100123.

(20) Naqiah Amrun, S.; Yi-Pin Lee, C.; Lee, B.; Fong, S.-W.; Edward Young, B.; Sin-Ling Chee, R.; Kim-Wah Yeo, N.; Torres-Ruesta, A.; Carissimo, G.; Meng Poh, C.; Wei Chang, Z.; Zirui Tay, M.; Chan, Y.-H.; I-Cheng Chen, M.; Guek-Hong Low, J.; Tambyah, P. A.; Kalimuddin, S.; Pada, S.; Tan, S.-Y.; Jin Sun, L.; Leo, Y.-S.; Lye, D. C.; Renia, L.; Ng, L. F. Linear B-Cell Epitopes in the Spike and Nucleocapsid Proteins as Markers of SARS-CoV-2 Exposure and Disease Severity. *EBioMedicine* **2020**, *58*, 102911. https://doi.org/10.1016/j.ebiom.2020.102911.

(21) Musicò, A.; Frigerio, R.; Mussida, A.; Barzon, L.; Sinigaglia, A.; Riccetti, S.; Gobbi, F.; Piubelli, C.; Bergamaschi, G.; Chiari, M.; Gori, A.; Cretich, M. SARS-CoV-2 Epitope Mapping on Microarrays Highlights Strong Immune-Response to n Protein Region. *Vaccines* **2021**, *9* (1), 1–11. https://doi.org/10.3390/vaccines9010035.

(22) Hedde, P. N.; Abram, T. J.; Jain, A.; Nakajima, R.; Ramiro de Assis, R.; Pearce, T.; Jasinskas, A.; Toosky, M. N.; Khan, S.; Felgner, P. L.; Gratton, E.; Zhao, W. A Modular Microarray Imaging System for Highly Specific COVID-19 Antibody Testing. *Lab Chip* **2020**, *20* (18), 3302–3309. https://doi.org/10.1039/d0lc00547a.

(23) Walls, A. C.; Park, Y. J.; Tortorici, M. A.; Wall, A.; McGuire, A. T.; Veesler, D. Structure, Function, and Antigenicity of the SARS-CoV-2 Spike Glycoprotein. *Cell* **2020**, *181* (2), 281-292.e6. https://doi.org/10.1016/j.cell.2020.02.058.

(24) Lan, J.; Ge, J.; Yu, J.; Shan, S.; Zhou, H.; Fan, S.; Zhang, Q.; Shi, X.; Wang, Q.; Zhang, L.; Wang, X. Structure of the SARS-CoV-2 Spike Receptor-Binding Domain Bound to the ACE2 Receptor. *Nature* **2020**, *581* (7807), 215–220. https://doi.org/10.1038/s41586-020-2180-5.

(25) Tian, W.; Jiang, W.; Yao, J.; Nicholson, C. J.; Li, R. H.; Sigurslid, H. H.; Wooster, L.; Rotter, J. I.; Guo, X.; Malhotra, R. Predictors of Mortality in Hospitalized COVID-19 Patients: A Systematic Review and Meta-Analysis. *J. Med. Virol.* **2020**, *92* (10), 1875–1883. https://doi.org/10.1002/jmv.26050.

(26) Simonnet, A.; Chetboun, M.; Poissy, J.; Raverdy, V.; Noulette, J.; Duhamel, A.; Labreuche, J.; Mathieu, D.; Pattou, F.; Jourdain, M.; Caizzo, R.; Caplan, M.; Cousin, N.; Duburcq, T.; Durand, A.; El kalioubie, A.; Favory, R.; Garcia, B.; Girardie, P.; Goutay, J.; Houard, M.; Jaillette, E.; Kostuj, N.; Ledoux, G.; Mathieu, D.; Moreau, A. S.; Niles, C.; Nseir, S.; Onimus, T.; Parmentier, E.; Préau, S.; Robriquet, L.; Rouze, A.; Six, S.; Verkindt, H. High Prevalence of Obesity in Severe Acute Respiratory Syndrome Coronavirus-2 (SARS-CoV-2) Requiring Invasive Mechanical Ventilation. *Obesity* **2020**, *28* (7), 1195–1199. https://doi.org/10.1002/oby.22831.

(27) Lee, L. Y. W.; Cazier, J. B.; Starkey, T.; Briggs, S. E. W.; Arnold, R.; Bisht, V.; Booth, S.; Campton, N. A.; Cheng, V. W. T.; Collins, G.; Curley, H. M.; Earwaker, P.; Fittall, M. W.; Gennatas, S.; Goel, A.; Hartley, S.; Hughes, D. J.; Kerr, D.; Lee, A. J. X.; Lee, R. J.; Lee, S. M.; Mckenzie, H.; Middleton, C. P.; Murugaesu, N.; Newsom-Davis, T.; Olsson-Brown, A. C.; Palles, C.; Powles, T.; Protheroe, E. A.; Purshouse, K.; Sharma-Oates, A.; Sivakumar, S.; Smith, A. J.; Topping, O.; Turnbull, C. D.; Várnai, C.; Briggs, A. D. M.; Middleton, G.; Kerr, R.; Gault, A.; Agnieszka, M.; Bedair, A.; Ghaus, A.; Akingboye, A.; Maynard, A.; Pawsey, A.; Mohamed, A. A.; Okines, A.; Massey, A.; Kwan, A.; Ferreira, A.; Angelakas, A.; Wu, A.; Tivey, A.; Armstrong, A.; Madhan, A.; Pillai, A.; Poon-King, A.; Kurec, B.; Usborne, C.; Dobeson, C.; Thirlwell, C.; Mitchell, C.; Sng, C.; Scrase, C.; Jingree, C.; Brunner, C.; Fuller, C.; Griffin, C.; Barrington, C.; Muller, D.; Ottaviani, D.; Gilbert, D.; Tacconi, E.; Copson, E.; Renninson, E.; Cattell, E.; Burke, E.; Smith, F.; Holt, F.; Soosaipillai, G.; Boyce, H.; Shaw, H.; Hollis, H.; Bowyer, H.; Anil, I.; Illingworth, J.; Gibson, J.; Bhosle, J.; Best, J.; Barrett, J.; Noble, J.; Sacco, J.; Chacko, J.; Chackathayil, J.; Banfill, K.; Feeney, L.; Horsley, L.; Cammaert, L.; Mukherjee, L.; Eastlake, L.; Devereaux, L.; Melcher, L.; Cook, L.; Teng, M.; Hewish, M.; Bhattacharyya, M.; Choudhury, M.; Baxter, M.; Scott-Brown, M.; Fittall, M.; Tilby, M.; Rowe, M.; Alihilali, M.; Galazi, M.; Yousaf, N.; Chopra, N.; Cox, N.; Chan, O.; Sheikh, O.; Ramage, P.; Greaves, P.; Leonard, P.; Hall, P. S.; Naksukpaiboon, P.; Corrie, P.; Peck, R.; Sharkey, R.; Bolton, R.; Sargent, R.; Jyothirmayi, R.; Goldstein, R.; Oakes, R.; Shotton, R.; Kanani, R.; Board, R.; Pettengell, R.; Claydon, R.; Moody, S.; Massalha, S.; Kathirgamakarthigeyan, S.; Dolly, S.; Derby, S.; Lowndes, S.; Benafif, S.; Eeckelaers, S.; Kingdon, S.; Ayers, S.; Brown, S.; Ellis, S.; Parikh, S.; Pugh, S.; Shamas, S.; Wyatt, S.; Grumett, S.; Lau, S.; Wong, Y. N. S.; McGrath, S.; Cornthwaite, S.; Hibbs, S.; Tillet, T.; Rabbi, T.; Robinson, T.; Roques, T.; Angelis, V.; Woodcock, V.; Brown, V.; Peng, Y. Y.; Drew, Y.; Hudson, Z. COVID-19 Prevalence and Mortality in Patients with Cancer and the Effect of Primary Tumour Subtype and Patient Demographics: A Prospective Cohort Study. *Lancet Oncol.* **2020**, 1309–1316. https://doi.org/10.1016/S1470-2045(20)30442-3.

(28) Zhang, L.; Sun, W.; Wang, Y.; Wang, X.; Liu, Y.; Zhao, S.; Long, D.; Chen, L.; Yu, L. Clinical Course and Mortality of Stroke Patients with Coronavirus Disease 2019 in Wuhan, China. *Stroke* **2020**, No. September, 2674–2682. https://doi.org/10.1161/STROKEAHA.120.030642.

(29) Charlson, M. E.; Pompei, P.; Ales, K. L.; MacKenzie, C. R. A New Method of Classifying Prognostic Comorbidity in Longitudinal Studies: Development and Validation. *J. Chronic Dis.* **1987**, *40* (5), 373–383. https://doi.org/10.1016/0021-9681(87)90171-8.

(30) Lu, L.; Zhang, H.; Zhan, M.; Jiang, J.; Yin, H.; Dauphars, D. J.; Li, S. Y.; Li, Y.; He, Y. W. Preventing Mortality in COVID-19 Patients: Which Cytokine to Target in a Raging Storm? *Front. Cell Dev. Biol.* **2020**, *8* (July), 1–10. https://doi.org/10.3389/fcell.2020.00677.

(31) Cummings, M. J.; Baldwin, M. R.; Abrams, D.; Jacobson, S. D.; Meyer, B. J.; Balough, E. M.; Aaron, J. G.; Claassen, J.; Rabbani, L. R. E.; Hastie, J.; Hochman, B. R.; Salazar-Schicchi, J.; Yip, N. H.; Brodie, D.; O'Donnell, M. R. Epidemiology, Clinical Course, and Outcomes of Critically Ill Adults with COVID-19 in New York City: A Prospective Cohort Study. *Lancet* **2020**, *395* (10239), 1763–1770. https://doi.org/10.1016/S0140-6736(20)31189-2.

(32) Yang, Y.; Shen, C.; Li, J.; Yuan, J.; Wei, J.; Huang, F.; Wang, F.; Li, G.; Li, Y.; Xing, L.; Peng, L.; Yang, M.; Cao, M.; Zheng, H.; Wu, W.; Zou, R.; Li, D.; Xu, Z.; Wang, H.; Zhang, M.; Zhang, Z.; Gao, G. F.; Jiang, C.; Liu, L.; Liu, Y. Plasma IP-10 and MCP-3 Levels Are Highly Associated with Disease Severity and Predict the Progression of COVID-19. *J. Allergy Clin. Immunol.* **2020**, *146* (1), 119-127.e4. https://doi.org/10.1016/j.jaci.2020.04.027.

(33) Shrock, E.; Fujimura, E.; Kula, T.; Timms, R. T.; Lee, I.-H.; Leng, Y.; Robinson, M. L.; Sie, B. M.; Li, M. Z.; Chen, Y.; Logue, J.; Zuiani, A.; McCulloch, D.; Lelis, F. J. N.; Henson, S.; Monaco, D. R.; Travers, M.; Habibi, S.; Clarke, W. A.; Caturegli, P.; Laeyendecker, O.; Piechocka-Trocha, A.; Li, J.; Khatri, A.; Chu, H. Y.; Villani, A.-C.; Kays, K.; Goldberg, M. B.; Hacohen, N.; Filbin, M. R.; Yu, X. G.; Walker, B. D.; Wesemann, D. R.; Larman, H. B.; Lederer, J. A.; Elledge, S. J. Viral Epitope Profiling of COVID-19 Patients Reveals Cross-Reactivity and Correlates of Severity. *Science (80-. ).* **2020**, *4250* (September). https://doi.org/10.1126/science.abd4250.

(34) Tan, W.; Lu, Y.; Zhang, J.; Wang, J.; Dan, Y.; Tan, Z.; He, X.; Qian, C.; Sun, Q.; Hu, Q.; Liu, H.; Ye, S.; Xiang, X.; Zhou, Y.; Zhang, W.; Guo, Y.; Wang, X.-H.; He, W.; Wan, X.; Sun, F.; Wei, Q.; Chen, C.; Pan, G.; Xia, J.; Mao,

Q.; Chen, Y.; Deng, G. Viral Kinetics and Antibody Responses in Patients with COVID-19. **2020**. https://doi.org/10.1101/2020.03.24.20042382.

(35) Jiang, H. wei; Li, Y.; Zhang, H. nan; Wang, W.; Yang, X.; Qi, H.; Li, H.; Men, D.; Zhou, J.; Tao, S. ce. SARS-CoV-2 Proteome Microarray for Global Profiling of COVID-19 Specific IgG and IgM Responses. *Nat. Commun.* **2020**, *11* (1). https://doi.org/10.1038/s41467-020-17488-8.

(36) Benucci, M.; Giannasi, G.; Cecchini, P.; Gobbi, F. L.; Damiani, A.; Grossi, V.; Infantino, M.; Manfredi, M. COVID-19 Pneumonia Treated with Sarilumab: A Clinical Series of Eight Patients. *J. Med. Virol.* **2020**, *92* (11), 2368–2370. https://doi.org/10.1002/jmv.26062.

(37) Kooistra, E. J.; Waalders, N. J. B.; Grondman, I.; Janssen, N. A. F.; de Nooijer, A. H.; Netea, M. G.; van de Veerdonk, F. L.; Ewalds, E.; van der Hoeven, J. G.; Kox, M.; Pickkers, P.; Kooistra, E. J.; Waalders, N. J. B.; Grondman, I.; Janssen, N. A. F.; de Nooijer, A. H.; Netea, M. G.; van de Veerdonk, F. L.; Ewalds, E.; van der Hoeven, J. G.; Kox, M.; Pickkers, P.; Hemelaar, P.; Beunders, R.; Bruse, N.; Frenzel, T.; Schouten, J.; Touw, H.; van der Velde, S.; van der Eng, H.; Roovers, N.; Klop-Riehl, M.; Gerretsen, J.; Claassen, W.; Heesakkers, H.; van Schaik, T.; Buijsse, L.; Joosten, L.; de Mast, Q.; Jaeger, M.; Kouijzer, I.; Dijkstra, H.; Lemmers, H.; van Crevel, R.; van de Maat, J.; Nijman, G.; Moorlag, S.; Taks, E.; Debisarun, P.; Wertheim, H.; Hopman, J.; Rahamat-Langendoen, J.; Bleeker-Rovers, C.; Koenen, H.; Fasse, E.; van Rijssen, E.; Kolkman, M.; van Cranenbroek, B.; Smeets, R.; Joosten, I. Anakinra Treatment in Critically Ill COVID-19 Patients: A Prospective Cohort Study. *Crit. Care* **2020**, *24* (1), 1–12. https://doi.org/10.1186/s13054-020-03364-w.

(38) Langer-Gould, A.; Smith, J. B.; Gonzales, E. G.; Castillo, R. D.; Garza Figueroa, J.; Ramanathan, A.; Li, B. H.; Gould, M. K. Early Identification of COVID-19 Cytokine Storm and Treatment with Anakinra or Tocilizumab. *Int. J. Infect. Dis.* **2020**, *99*, 291–297. https://doi.org/10.1016/j.ijid.2020.07.081.

(39) Castelnovo, L.; Tamburello, A.; Lurati, A.; Zaccara, E.; Marrazza, M. G.; Olivetti, M.; Mumoli, N.; Mastroiacovo, D.; Colombo, D.; Ricchiuti, E.; Paola, F.; Mazzone, A. Anti-IL6 Treatment of Serious COVID-19 Disease. *Medicine (Baltimore).* **2021**, *100* (1), 1–6.

(40) Salama, C.; Han, J.; Yau, L.; Reiss, W. G.; Kramer, B.; Neidhart, J. D.; Criner, G. J.; Kaplan-Lewis, E.; Baden, R.; Pandit, L.; Cameron, M. L.; Garcia-Diaz, J.; Chávez, V.; Mekebeb-Reuter, M.; Lima de Menezes, F.; Shah, R.; González-Lara, M. F.; Assman, B.; Freedman, J.; Mohan, S. V. Tocilizumab in Patients Hospitalized with Covid-19 Pneumonia. *N. Engl. J. Med.* **2021**, *384* (1), 20–30. https://doi.org/10.1056/nejmoa2030340.

(41) Veiga, V. C.; Prats, J. A. G. G.; Farias, D. L. C.; Rosa, R. G.; Dourado, L. K.; Zampieri, F. G.; Machado, F. R.; Lopes, R. D.; Berwanger, O.; Azevedo, L. C. P.; Avezum, Á.; Lisboa, T. C.; Rojas, S. S. O.; Coelho, J. C.; Leite, R. T.; Carvalho, J. C.; Andrade, L. E. C.; Sandes, A. F.; Pintão, M. C. T.; Castro, C. G.; Santos, S. V; de Almeida, T. M. L.; Costa, A. N.; Gebara, O. C. E.; de Freitas, F. G. R.; Pacheco, E. S.; Machado, D. J. B.; Martin, J.; Conceição, F. G.; Siqueira, S. R. R.; Damiani, L. P.; Ishihara, L. M.; Schneider, D.; de Souza, D.; Cavalcanti, A. B.; Scheinberg, P.; Coalition covid-19 Brazil VI Investigators. Effect of Tocilizumab on Clinical Outcomes at 15 Days in Patients with Severe or Critical Coronavirus Disease 2019: Randomised Controlled Trial. *BMJ* **2021**, *372*, n84. https://doi.org/10.1136/bmj.n84.

(42) Yamaoka, Y.; Jeremiah, S. S.; Miyakawa, K.; Saji, R.; Nishii, M.; Takeuchi, I.; Ryo, A. Whole Nucleocapsid Protein of Severe Acute Respiratory Syndrome Coronavirus 2 May Cause False-Positive Results in Serological Assays. *Clin. Infect. Dis.* **2020**. https://doi.org/10.1093/cid/ciaa637.

(43) Murase, K.; Morrison, K. L.; Tam, P. Y.; Stafford, R. L.; Jurnak, F.; Weiss, G. A. EF-Tu Binding Peptides Identified, Dissected, and Affinity Optimized by Phage Display. *Chem. Biol.* **2003**, *10* (2), 161–168. https://doi.org/10.1016/S1074-5521(03)00025-5.

(44) Bhasin, A.; Sanders, E. C.; Ziegler, J. M.; Briggs, J. S.; Drago, N. P.; Attar, A. M.; Santos, A. M.; True, M. Y.; Ogata, A. F.; Yoon, D. V.; Majumdar, S.; Wheat, A. J.; Patterson, S. V.; Weiss, G. A.; Penner, R. M. Virus Bioresistor (VBR) for Detection of Bladder Cancer Marker DJ-1 in Urine at 10 PM in One Minute. *Anal. Chem.* **2020**, *92* (9), 6654–6666. https://doi.org/10.1021/acs.analchem.0c00534.

(45) Pastorino, B.; Touret, F.; Gilles, M.; Lamballerie, X. De; Charrel, R. N. Heat Inactivation of Different Types of SARS-CoV-2 Samples: What Protocols for Biosafety, Molecular Detection and Serological Diagnostics?

*Viruses* **2020**, *12* (735), 1–8.

(46) Khan, S.; Jain, A.; Taghavian, O.; Nakajima, R.; Jasinskas, A.; Supnet, M.; Felgner, J.; Davies, J.; de Assis, R. R.; Jan, S.; Obiero, J.; Strahsburger, E.; Pone, E. J.; Liang, L.; Davies, D. H.; Felgner, P. L. Use of an Influenza Antigen Microarray to Measure the Breadth of Serum Antibodies across Virus Subtypes. *J. Vis. Exp.* **2019**, *2019* (149), 1–8. https://doi.org/10.3791/59973.

(47) Jain, A.; Taghavian, O.; Vallejo, D.; Dotsey, E.; Schwartz, D.; Bell, F. G.; Greef, C.; Davies1, D. H.; Grudzien, J.; Lee, A. P.; Felgner, P.; Liang, L. Evaluation of Quantum Dot Immunofluorescence and a Digital CMOS Imaging System as an Alternative to Conventional Organic Fluorescence Dyes and Laser Scanning for Quantifying Protein Microarrays. *Protemoics* **2016**, *16* (8), 1271–1279. https://doi.org/10.1002/pmic.201500375.Evaluation.

(48) Nakajima, R.; Supnet, M.; Jasinskas, A.; Jain, A.; Taghavian, O.; Obiero, J.; Milton, D. K.; Chen, W. H.; Grantham, M.; Webby, R.; Krammer, F.; Carter, D.; Felgner, P. L.; Davies, D. H. Protein Microarray Analysis of the Specificity and Cross-Reactivity of Influenza Virus Hemagglutinin-Specific Antibodies. *mSphere* **2018**, *3* (6), 1–15. https://doi.org/10.1128/msphere.00592-18.

(49) Mukaka, M. M. *Statistics Corner: A Guide to Appropriate Use of Correlation Coefficient in Medical Research*; 2012; Vol. 24.

(50) Baric, R. S. Emergence of a Highly Fit SARS-CoV-2 Variant. *N. Engl. J. Med.* **2020**, *383* (27), 2684–2686. https://doi.org/10.1056/nejmcibr2032888.

(51) Plante, J. A.; Liu, Y.; Liu, J.; Xia, H.; Johnson, B. A.; Lokugamage, K. G.; Zhang, X.; Muruato, A. E.; Zou, J.; Fontes-Garfias, C. R.; Mirchandani, D.; Scharton, D.; Bilello, J. P.; Ku, Z.; An, Z.; Kalveram, B.; Freiberg, A. N.; Menachery, V. D.; Xie, X.; Plante, K. S.; Weaver, S. C.; Shi, P. Y. Spike Mutation D614G Alters SARS-CoV-2 Fitness. *Nature* **2020**, 1–6. https://doi.org/10.1038/s41586-020-2895-3.

(52) Zheng, W.; Li, Y.; Zhang, C.; Pearce, R.; Mortuza, S. M.; Zhang, Y. Deep-Learning Contact-Map Guided Protein Structure Prediction in CASP13. *Proteins Struct. Funct. Bioinforma.* **2019**, *87* (12), 1149–1164. https://doi.org/10.1002/prot.25792.

# CHAPTER 5

## Evidence for Deleterious Original Antigenic Sin in SARS-CoV-2 Immune Response

### 5.1 Abstract

A previous report demonstrated the strong association between the presence of an antibody against a SARS-CoV-2 nucleocapsid epitope, termed Ep9, and COVID-19 disease severity. Patients with anti-Ep9 antibodies (Abs) had early IgG upregulation and cytokine-associated injury, which are the hallmarks of original antigenic sin (OAS). Thus, the immunological memory of an unknown previous infection was hypothesized to drive formation of suboptimal anti-Ep9 Abs in severe COVID-19 infections. This study identifies a putative original antigen capable of stimulating production of cross-reactive, anti-Ep9 Abs. From bioinformatics analysis, 21 potential "original" epitope regions were identified. Binding assays with patient blood samples directly show cross-reactivity between Abs binding to Ep9 and only one homologous potential antigen, a sequence derived from the neuraminidase protein of H3N2 Influenza A virus. This cross-reactive binding affinity is highly virus strain specific and sensitive to even single amino acid changes in epitope sequence. The neuraminidase protein is not present in the influenza vaccine, and the anti-Ep9 Abs likely resulted from the widespread influenza infection in 2014. Therefore, OAS from a previous infection could underlie some cases of COVID-19 disease severity and explain the diversity observed in disease outcomes.

## 5.2 Introduction

Original antigenic sin (OAS) occurs when the immune responses adapted for a primary (or "original") infection instead target a similar, but not identical, pathogen[1]. Since B-cells undergo affinity maturation post-primary infection, affinity-matured Abs from previous infections can sometimes outcompete naïve Abs with specificity for the new antigen [2]. The phenomenon has been observed for immune responses to dengue fever, influenza, respiratory syncytial virus and human immunodeficiency virus (HIV)[3,4]. OAS ideally accelerates pathogen clearance by targeting highly conserved antigens; however, suboptimal targeting by non-neutralizing Abs binding to the antigen can exacerbate disease conditions by either enhancing viral infection or hyperactivating the innate immune response[2]. The wide range of outcomes observed in SARS-CoV-2 infected individuals, from asymptomatic to fatal, has been hypothesized to result from a patient's unique immunological memory[1,5].

Reports of OAS in COVID-19 patient have largely focused on the phenomenon's beneficial or benign impacts on the immune response. For example, Abs from individuals naïve for SARS-CoV-2 infection, but exposed to other common human coronaviruses (hCoV), could cross-react with the spike protein and neutralize SARS-CoV-2 pseudotypes[6]. Another study of pre-pandemic-collected plasma found Abs that cross reacted with SARS-CoV-2 nucleocapsid (NP) and spike proteins, but did not confer protection against severe COVID-19 outcomes for the patients[7]. While higher rates of prior infection by cytomegalovirus and herpes simplex virus 1 have been observed for hospitalized COVID-19 patients compared to patients with milder symptoms, no Ab signature linking to a molecular mechanism has been shown [8].

Recently, our laboratory reported a strong association of severe COVID-19 disease outcomes with the presence of Abs binding specifically to a 21-mer peptide derived from SARS-CoV-2 NP, an epitope region termed Ep9. The patients, described as αEp9(+), comprised about 27% of the sampled, SARS-CoV-2-infected population (n = 186). The αEp9(+) patients (n = 34 used in this report due to sample availability) had high, early levels of αN IgGs, typically within the first week, compared to αEp9(-) patients; cytokine-related immune hyperactivity also appeared in the αEp9(+) individuals [9]. These two observations suggest an OAS-based mechanism for the disease severity observed in αEp9(+) patients. Here, we explore the epitope homology landscape and αEp9 Ab cross-reactivity to potentially identify the original antigen driving Ab-based immune response in αEp9(+) patients.

### 5.3 Results and Discussion

Assays measured levels of αEp9 IgGs and IgMs from αEp9(+) patients whose plasma was collected at various times post-symptom onset (PSO). Consistent with the hallmarks of OAS tracing a prior infection, αEp9 IgG levels appeared elevated as early as one day PSO in one patient and have similar levels in the patient population over >4 weeks (one-way ANOVA, p = 0.321) (**Fig. 5-2A**). Levels of αEp9 IgMs between patients at all stages of disease progression were also similar (one-way ANOVA, p = 0.613). The signals measured for αEp9 IgM levels were significantly lower than the equivalent αEp9 IgG levels (T-test, p = 0.0181) (**Fig. 5-2B**); this difference could reflect the lower IgM affinity, quantity, or both.

Searches for homologs to Ep9 in protein sequence and structural homology databases suggested candidate primary antigens or potential OAS epitopes. The Basic Local Alignment Sequence Tool (pBLAST) [10] and Vector Alignment Search Tool (VAST) [11], were used to

identify a structurally homologous region on the beta herpesvirus 6A, and 14 different proteins with Ep9 sequence homology spanning >7 residues. Additionally, Ep9-orthologous regions from six common human coronaviruses (SARS-CoV, MERS, OC43, HKU-1, NL63, 229E) were also chosen for production and assays (**Figs. 5-1 and Fig. 5-2A**). To expedite the binding measurements, the potential OAS epitope regions were subcloned into phagemid vectors and displayed as fusions to the M13 bacteriophage P8 coat protein. DNA sequencing and ELISA experiments demonstrated successful cloning and consistent phage display, respectively (**Fig. 5-1A**). Two of the 21 epitopes could not be displayed on phage and were omitted from subsequent investigations.

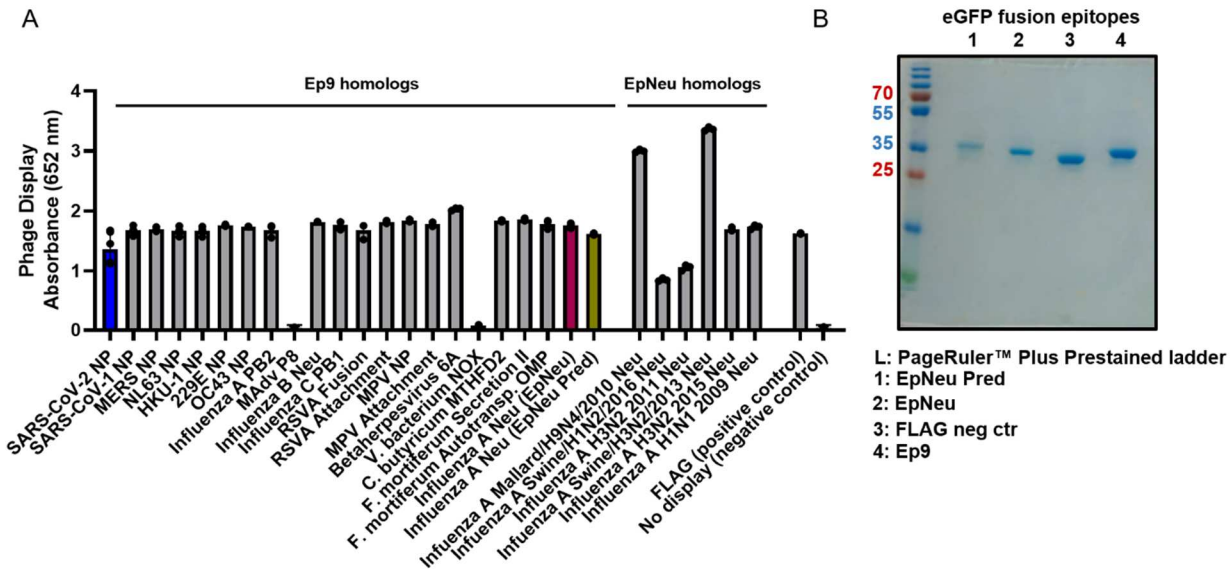


**Figure 5-1. Expression of phage-displayed and eGFP-fused potential OAS epitopes. A)** ELISA demonstrating the display of N-terminal FLAG-tagged potential epitopes fused to the N-terminus of the P8 coat protein. Immobilized αFLAG Abs in microtiter wells bind the displayed FLAG-tag and epitope, and binding is detected with αM-13-HRP Abs as usual. Phage with no epitope displayed provide the negative control. Epitopes for mastadenovirus protein (mAdV) P8 and *V. bacterium* NADH oxidoreductase (NOX) did not display. Error bars represent SD values. **B)** 10% SDS-PAGE gel stained with Coomassie Blue shows His-tag affinity-purified and buffer-exchanged eGFP-fused epitopes, EpPred, EpNeu, FLAG negative control and Ep9.

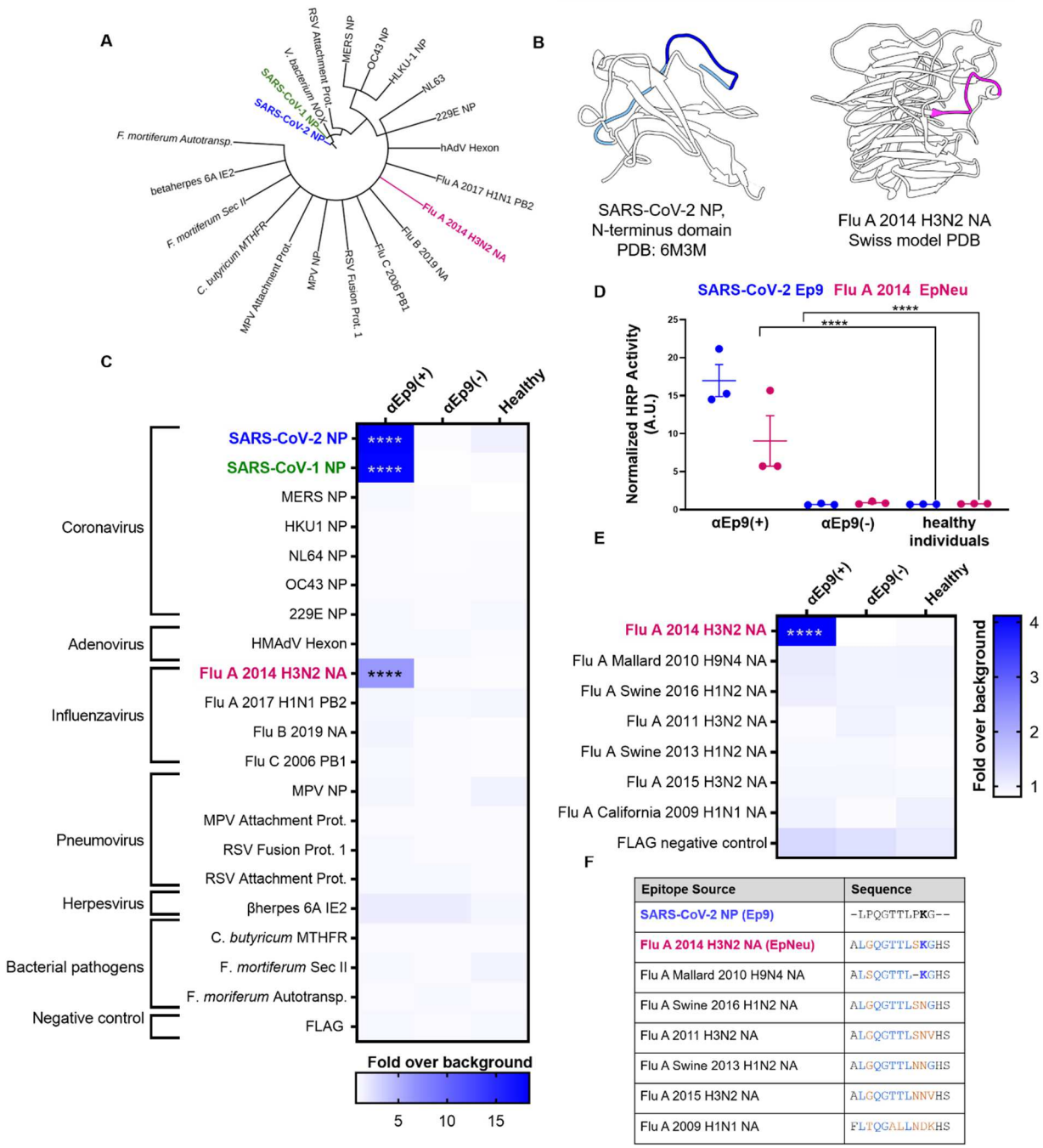


**Figure 5-2. Potential OAS epitopes for αEp9 Abs identified from bioinformatics and validated by phage ELISA.** **A)** Cladogram depicting sequence homology of proteins from different human pathogens to the Ep9 sequence. Sequence alignments used pBLAST [10] and VAST [11] software, and the cladogram was generated by iTOL [28]. **B)** Structures of SARS-CoV-2 NP RNA binding domain (PDB: 6M3M) and the Flu A 2014 H3N2 NA protein (modeled by SWISS-Model[15]). SARS-CoV-2 NP highlights Ep9 residues (light and dark blue) and the region homologous to EpNeu (dark blue). The depicted model of Flu A 2014 H3N2 NA highlights the EpNeu putative antigen (pink).

**C)** ELISAs examined binding of phage-displayed potential OAS epitopes to Abs from the pooled plasma of five αEp9(+) patients, or five αEp9(-) patients. Pooled plasma from healthy patients was used as the negative control. The colors of the heat map represent the mean binding signal normalized to the negative controls (phage without a displayed peptide) from three separate experiments with pools of plasma from different patient samples. Thus, a total of 15 αEp9(+) patients and 15 αEp9(-) patients were examined in this experiment. **D)** The data from panel C showing results from the individual pools (****p <0.0001 for a two-way ANOVA including the phage-displayed epitopes listed in panel C, *ad hoc* Tukey test). **E)** Using EpNeu as the search template, ELISAs examined the most homologous epitopes, with the data represented as described in panel C (****p <0.0001 for two-way ANOVA including all phage-displayed epitopes, *ad hoc* Dunnett's test, using healthy patients as the control). **F)** Amino acid sequence alignment of the closely related Flu A NA homologs of EpNeu from pBLAST [10]. Blue and orange residues represent conserved and mismatched amino acids, respectively, relative to Ep9. Bolded residues are important for epitope recognition by αEp9 Abs. Here, the term Flu refers to influenza.

The potential OAS epitopes to αEp9 Abs were tested by ELISA. To assess average response within a patient population, pooled plasma from five αEp9(+) and five αEp9(-) COVID-19 patients were coated onto ELISA plates, and tested for binding to the phage-displayed potential OAS epitopes. Pooled plasma from healthy individuals provided an additional negative control. Confirming previously reported results, SARS-COV-2 Ep9 along with a homologous epitope from SARS-CoV-1 (90% similarity) bound only to plasma from αEp9(+) patients [9]. SARS-CoV-1 is unlikely to be associated with OAS, as only 75 cases were reported in the United States during the 2003 pandemic[12]. However, the panel of potential epitopes revealed a candidate epitope from the neuraminidase (NA) protein of an H3N2 influenza A strain, which circulated in 2014 (A/Para/128982-IEC/2014, Accession No. AIX95025.1). From three separate experiments with pooled plasma, assaying a total of 15 αEp9(+) and 15 αEp9(-) patients, only αEp9(+) patient pools demonstrated significant binding to this specific NA epitope, termed EpNeu here. Pooled samples from αEp9(-) patients and healthy individuals (commercially purchased plasma) did not bind to EpNeu ($p<0.0001$, two-way ANOVA *ad hoc* Tukey test) (**Fig. 5-2C,D**). Surprisingly, SARS-CoV-2 Ep9 and EpNeu share only 38% amino acid sequence similarity, which is significantly less homology that other candidate epitope regions.

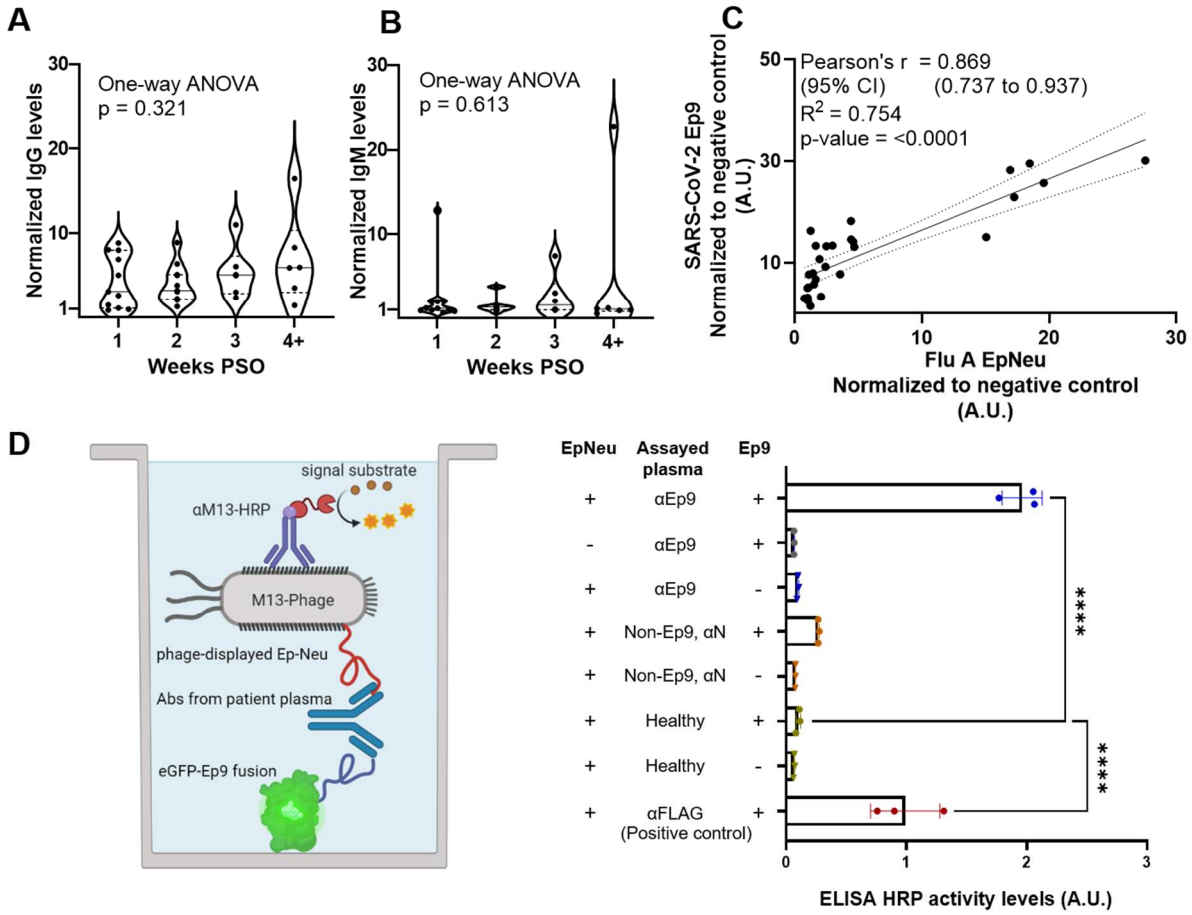


**Figure 5-3. Early upregulation of αEp9 IgGs and cross-reactive Ab binding to both Ep9 and EpNeu.** ELISA of αEp9 **A)** IgG and **B)** IgM levels in αEp9(+) patients (n = 34) for plasma collected at the indicated time periods post-symptom onset (PSO). Statistical analysis was conducted using one-way ANOVA, *ad hoc* Tukey test. The solid line represents the median value, and dashed lines represent quartiles. **C)** Comparing normalized levels of phage-displayed Ep9 and EpNeu binding to plasma-coated wells from individual αEp9(+) patients (n = 34). A strong correlation is observed, as shown by the depicted statistics. Individual points in panels A-C represent data from individual patients. **D)** A schematic diagram of the sandwich ELISA to examine cross-reactivity of αEp9 Abs. The assay tests for bivalent binding to both Ep9 and EpNeu. Pooled plasma from five αEp9(+) patients or five αEp9(-) patients with other αNP Abs was tested for bivalent binding to both eGFP-fused Ep9 and phage-displayed EpNeu. Healthy patient plasma was used as a negative control. For additional negative controls, phage-FLAG and eGFP-FLAG replaced Ep9 and EpNeu, respectively (****p <0.0001 one-way ANOVA, *ad hoc* Dunnett's test, with healthy plasma group in the presence of EpNeu and Ep9 as control). Error bars represent SD. Individual points on bar graph represent technical replicates.

To test whether the observed binding to H3N2 influenza A NA protein was strain specific, the EpNeu sequence was used as a template to search for homologs via pBLAST [10]. Closely aligned NA sequences isolated from human, avian and swine hosts in North America

were chosen for further analysis (**Fig. 5-2F**). These sequences were phage-displayed as before. Despite their close similarity to EpNeu (up to 92.3% similarity, with a difference of only one residue), none of the EpNeu homologs bound to Abs from αEp9(+) patients (Figure 5-2E). A single EpNeu amino acid substitution, K142N (numbering from full-length NA, Accession No. AID57909.1) occurs in an H1N2 swine flu from 2016; the single substitution dramatically decreased binding affinity. The epitope from H4N6 avian influenza A from 2010 omits residue S141, but includes the conserved K142, also greatly reduced binding to Abs from αEp9(+) patients. The H1N2 strain of swine flu from 2013 includes mutations S141N and K142N. This sequence entirely lacks binding to αEp9 Abs, as shown by comparison to αEp9(-) patients and healthy individuals (**Fig. 5-2E,F**). Therefore, we conclude that the presence of S141 and K142 are critical for αEp9 Abs binding.

Next, ELISAs were used to determine whether Ep9 and EpNeu epitopes bind to the same Abs. Assays of 34 αEp9(+) patients demonstrated a strong and highly significant correlation between levels of Abs binding to Ep9 and EpNeu epitopes in patient plasma, suggesting the two epitopes may bind to the same Abs (**Fig. 5-3C**). This cross-reactivity was confirmed by a sandwich-format assay requiring bivalent, simultaneous binding by Abs to Ep9 and EpNeu (**Fig. 5-3D**). In this assay, Ep9 was fused to the N-terminus of eGFP, and EpNeu was phage-displayed. The results demonstrated binding of Abs to both Ep9 and EpNeu epitopes in pooled plasma from αEp9(+) patients, but not in αEp9(-) patients with

other αNP Abs or healthy donors. Thus, we conclude that αEp9 Abs also recognize the EpNeu epitope region.

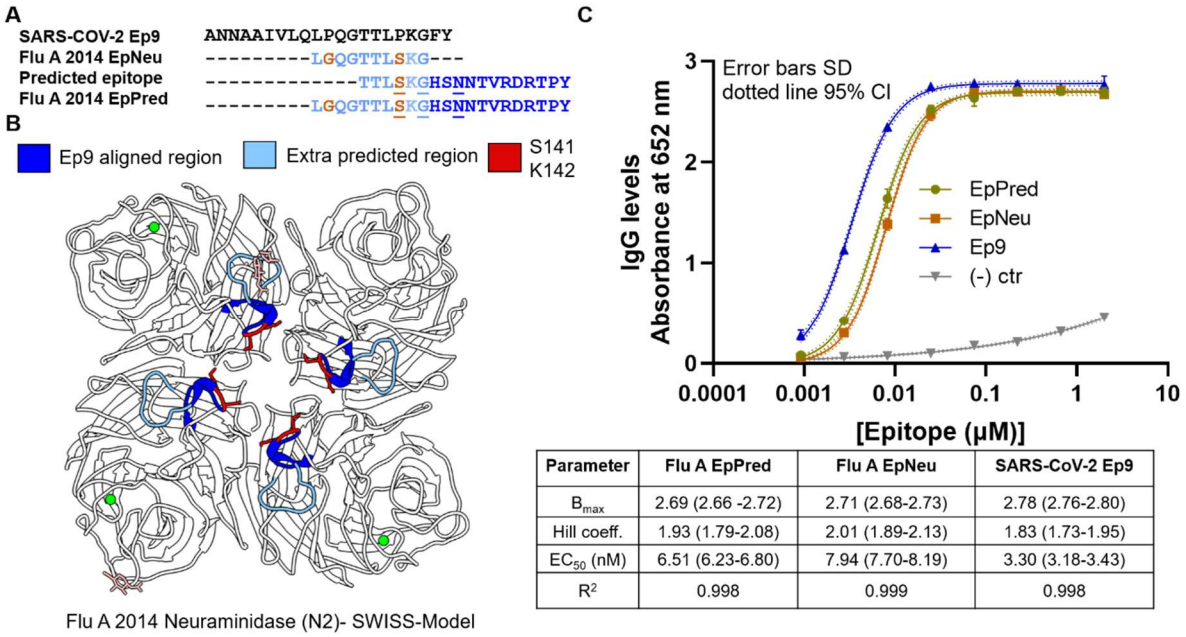


| Parameter | Flu A EpPred | Flu A EpNeu | SARS-CoV-2 Ep9 |
|---|---|---|---|
| $B_{max}$ | 2.69 (2.66 -2.72) | 2.71 (2.68-2.73) | 2.78 (2.76-2.80) |
| Hill coeff. | 1.93 (1.79-2.08) | 2.01 (1.89-2.13) | 1.83 (1.73-1.95) |
| $EC_{50}$ (nM) | 6.51 (6.23-6.80) | 7.94 (7.70-8.19) | 3.30 (3.18-3.43) |
| $R^2$ | 0.998 | 0.999 | 0.998 |

**Figure 5-4. Binding interactions of αEp9 Abs with the predicted EpNeu epitope. A)** Linear and structural B-cell epitope prediction tools Bepipred 2.0 and Discotope 2.0 suggested an extended, linear epitope region from the influenza A H3N2 2014 NA, including the eight residues of Ep9 Neu (light blue) with an additional ten, C-terminal residues (dark blue). This extended, predicted epitope is termed EpPred. Structural epitope predictions are underlined. Residues on EpNeu that are not aligned with Ep9 are depicted in orange. **B)** Structural model depicting the influenza A H3N2 2014 NA. The model was generated using SWISS-Model based on the NA structure from influenza A H3N2 Tanzania 2010 (PDB: 4GZS). The EpNeu region (light blue), the extended residues in EpPred (dark blue), and the residues S141 and K142 (red), which are important for αEp9 Ab recognition, are shown. **C)** Dose-dependent ELISA comparing binding of αEp9 Abs to Ep9, EpNeu and EpPred. Pooled plasma from five αEp9(+) patients and five αEp9(-) patients were tested in triplicates with varying doses of eGFP-fused epitopes. The data demonstrates the strongest interactions occurred between αEp9 Abs and Ep9 with an approximately 2-fold decrease in binding affinity with EpNeu. EpPred bound slightly stronger to αEp9 Abs than EpNeu; the difference in trend lines of EpNeu and EpPred are statistically significant ($p<0.0001$, Comparison of Fits). Trendlines represent non-linear regression fit with Hill slope analysis.

We then investigated whether EpNeu could present a viable antigen during the 2014 H3N2 (NCBI: txid1566483) infection. Linear epitope analysis of the whole NA protein using Bepipred 2.0 [13] predicted a candidate with eight residues from EpNeu, including S141 and K142 plus ten additional residues (146-155). This predicted epitope region, termed EpPred, includes the conserved catalytic residue D151 targeted for viral neutralization by the human

immune system [14] (**Fig. 5-4A**). Using a modelled structure of the 2014 H3N2 NA from Swiss-Model [15–18], the structural epitope prediction tool, Discotope 2.0 [19], also identified potential epitopes within EpPred (**Fig. 5-4A**).

EpPred was overexpressed as an eGFP-fusion protein (Figure 1-supplement 3B). Pooled plasma from five αEp9(+) patients was tested for Ab binding to EpPred, EpNeu, the SARS-CoV-2 Ep9 and a negative control. Ep9, derived from SARS-CoV-2, bound approximately two-fold better than EpNeu to αEp9 Abs (**Fig. 5-4C**). The increased binding strength of Ep9 must result from additional arounds of Ab affinity maturation post-primary infection [2]. EpPred modestly improved upon the binding of EpNeu to αEp9 Abs (**Fig. 5-4C**). Thus, αEp9 Abs likely target a larger epitope of H3N2 2014 NA beyond regions homologous to Ep9, though expression of NA is difficult [20]. The results support the hypothesis that the αEp9 Abs found in severe COVID-19 disease may have originated from a primary infection with H3N2 influenza A.

Unfortunately, patient histories only rarely include previous influenza infections, and such information was unavailable. The H3N2 2014 NA sequence was isolated from Para, Brazil, and the strain's spread in North America remains unknown; however, a severe outbreak of influenza was recorded in 2014[21], making high levels of spread likely. Specific secondary structures and neighboring non-linear epitope regions may also further strengthen epitope Ab interactions. Furthermore, the phage-displayed and bacterially overexpressed epitopes applied here do not include post-translational modifications.

### 5.4 Conclusions

This report offers a molecular mechanism for OAS underlying the high-rate of severe COVID-19 in αEp9(+) patients. Specifically, we demonstrate cross-reactive binding between

αEp9 Abs and a predicted NA epitope from a 2014 influenza A strain. Future studies could examine correlation between a country's rate of the H3N2 2014 influenza and severe COVID-19. Additionally, health systems might have recorded such primary infections in specific patients, which could also be searched for correlation. Examining epitope conservation and Ab cross-reactivity could predict OAS-based immune responses and disease outcomes in future infections. Identifying detrimental, benign or beneficial OAS pathways could also guide vaccine design for increased efficacy and reduced risk.

## 5.5 Materials and Methods

*Sequence and Structural Alignment Analysis* To identify possible sources of primary infection responsible for αEp9 Ab generation, sequence and structural alignment with Ep9 residues and the SARS-CoV-2 NP was conducted. Alignment of Ep9 sequence with the orthologs from other human coronaviruses (hCoVs) such as SARS-CoV, MERS, HKU-1, NL63, 229E and OC43 was conducted using the Benchling sequence alignment tool [22] (https://benchling.com). To explore a wider range of human host pathogens pBLAST[10] (https://blast.ncbi.nlm.nih.gov/Blast.cgi) was used to search for Ep9 homology in a database of non-redundant protein sequences; common human-host viruses were specified in the organism category. The queries were conducted with the blastp (protein-protein BLAST) program[10] with search parameters automatically adjusted for short input sequences. Alignments spanning >7 residues were included here. The Vector Alignment Search Tool (VAST)[11] (https://structure.ncbi.nlm.nih.gov/Structure/VAST/vast.shtml) was used to find structural alignment between SARS-CoV-2 Ep9 and proteins from other viral and bacterial human host pathogens. Alignment for NP from common hCoV were not further examined, as they had been included in sequence alignment analysis. The aligned sequences were sorted

by the number of aligned residues as well as root-mean square deviation (RMDS). The top 50 structurally aligned proteins were then examined for structural homology in the Ep9 epitope region. Regions of proteins that aligned with the Ep9 region were selected for subsequent analysis.

*Cloning.* Predicted OAS epitopes were subcloned for phage display using the pM1165a phagemid vector[23] with an N-terminal FLAG-tag and a C-terminal P8 M13-bacteriophage coat protein. OAS constructs were subcloned using the Q5 site-directed mutagenesis kit (New England Biolabs, Ipswich, MA) as per manufacturer's instructions. After cloning, cells were transformed into XL-1 Blue *E. coli* and spread on carbenicillin-supplemented (50 μg/ml) plates. Individual colonies were then inoculated into 5 ml cultures, and shaken overnight at 37 °C. The phagemid was isolated using the QIAprep spin miniprep kit (Qiagen, Germantown, MD) as per manufacturer's instructions. Cloned sequences were verified by Sanger sequencing (Genewiz, San Diego, CA).

*Phage Propagation and Purification.* The Ep9 homologs were expressed as N-terminal fusions to the P8 coat protein of M13 bacteriophage. Plasmids were transformed into SS320 *E. coli* and spread onto carbenicillin-supplemented (50 μg/ml) LB-agar plates before overnight incubation at 37 °C. A single colony was inoculated into a primary culture of 15 ml of 2YT supplemented with 50 μg/ml carbenicillin and 2.5 μg/ml of tetracycline, and incubated at 37 °C with shaking at 225 rpm until an optical density at 600 nm ($OD_{600}$) of 0.5 to 0.7 was reached. 30 μM IPTG and M13KO7 helper phage at an MOI 4.6 was added to the primary culture, and the culture was incubated for an additional 37 °C with shaking at 225 rpm for 45 min. 8 ml of the primary culture was then transferred to 300 ml of 2YT

supplemented with 50 μg/ml of carbenicillin and 20 μg/ml of kanamycin. The cultures were inoculated at 30 °C with shaking at 225 rpm for around 19 h.

The phage propagation culture was centrifuged at 9632 x *g* for 10 min at 4 °C. The supernatant, containing the phage, was transferred into a separate tubes pre-aliquoted with 1/5$^{th}$ volume of phage precipitation buffer (20% w/v PEG-8000 and 2.5 M NaCl), and incubated on ice for 30 min. The solution, containing precipitated phage, was centrifuged for 15 min at 4 °C, and the supernatant was discarded. The precipitated phage was centrifuged a second time at 1,541 x *g* for 4 min at 4 °C, and then dissolved in 20 ml of resuspension buffer (10 mM phosphate, 137 mM NaCl, pH 7.4 - 8.0 with Tween-20 0.05%, v/v and glycerol 10% v/v). The resuspended pellet solution was divided into 1 ml aliquots, which were flash frozen with liquid nitrogen for storage in -80 °C. Prior to use in ELISA binding assays, the aliquoted phage-displayed constructs were re-precipitated in 0.2 ml of phage precipitation buffer after incubation for 30 min on ice. Aliquots were centrifuged at 12298 x *g* for 20 min at 4 °C and the supernatant was discarded. The phage pellets were re-centrifuged at 1968 x *g* for 4 min at 4 °C, and then resuspended in 1 ml of 10 mM phosphate, 137 mM NaCl, pH 7.4.

*Expression and Purification of eGFP Fusion Peptides.* pET28c plasmids encoding eGFP fusions to C-terminal Ep9-FLAG, EpNeu-FLAG, EpPred-FLAG and FLAG (negative control) and N-terminal $His_6$ peptide epitopes, were transformed into BL21DE3 Star *E. coli* chemically competent cells. Transformants were spread on carbenicillin-supplemented (50 μg/ml) LB-agar plates and incubated at 37 °C overnight. Single colonies of each construct were selected to inoculate 25 ml LB media supplemented with carbenicillin (50 μg/ml). After incubation at 37 °C with shaking at 255 rpm overnight, 5 ml of seed cultures were used to inoculate 500 ml of LB media supplemented with carbenicillin (50 μg/ml). Expression cultures were

incubated at 37 °C with shaking at 225 rpm until an $OD_{600}$ of ~0.5 was reached. The cultures were induced with 0.5 mM IPTG and incubated at 25 °C for 18 h. The cells were pelleted by centrifugation at 9632 x *g* for 20 min and resuspended in Tris-HCl lysis buffer (20 mM Tris-HCl, 250 mM NaCl, pH 8). Cells were lysed by sonication and the insoluble fractions were pelleted by centrifugation at 24696 x *g*. The supernatant was affinity-purified using Profinity™ IMAC (BioRad, Hercules, CA) resin charged with nickel sulfate. The protein lysate was batch bound overnight to the IMAC resin and purified using gravity columns. Columns were washed with lysis buffer supplemented with 20 mM imidazole, and the elution fractions were collected from lysis buffer containing 250 mM imidazole. The elution fractions were then buffer-exchanged with lysis buffer lacking imidazole using Vivaspin® 20 Ultrafiltration Units (Sartorius, Goettingen, Germany) with a molecular weight cutoff of 10 kDa. The final buffer imidazole concentrations were calculated to be ~0.1 mM. Purified and buffer-exchanged protein fractions were then visualized using 10% SDS-PAGE with Coomassie dye staining.

*Patient Sample Collection.* Samples were collected as previously described [9]. Briefly, the UC Irvine Experimental Tissue Resource (ETR) operates under a blanket IRB protocol (UCI #2012-8716) which enables sample collection in excess of requirements for clinical diagnosis, and allows distribution to investigators. Plasma was collected from daily blood draws of COVID(+) patients, initially confirmed with pharyngeal swabs. After immediate centrifugation, plasma from heparin-anticoagulated blood was stored for 3-4 days at 4 °C prior to its release for research use. Personal health information was omitted and unique de-identifier codes were assigned to patients to comply with the Non-Human Subjects Determination exemption from the UCI IRB. At the research facility, SARS-CoV-2 virus in

plasma samples was inactivated through treatment by incubation in a 56 °C water bath for 30 min[24] prior to storage at -80 °C.

*Phage ELISAs.* As described in previous reports[9], pooled plasma from five αEp9(+) patients, five αEp9(-) patients, or healthy patients (Sigma-Aldrich, Saint Louis, MO) were separately prepared in coating buffer (50 mM $Na_2CO_3$, pH 9.6); the plasma was diluted 100-fold during this step. Plasma samples were then immobilized in 96 well microtiter plates by shaking the plasma solutions at 150 rpm at room temperature (RT) for 30 min. After aspiration and washing by plate washer (BioTek, Winooski, VT), each well was blocked with 100 µL of ChonBlock Blocking Buffer (CBB) (Chondrex, Inc., Woodinville, WA) for 30 mins, shaking at 150 rpm at RT. Wells were subsequently washed three times with PBS-T (0.05% v/v Tween-20 in PBS). Next, 1 nM phage-displayed candidate "original" epitopes and controls prepared in CBB was incubated in microtiter wells for 1 h at RT with shaking at 150 rpm. Unbound phage were aspirated and removed using three washes with PBS-T. The peroxidase-conjugated detection antibody, αM13-HRP (Creative Diagnostics, Shirley, NY), was diluted 1000-fold in Chonblock Secondary Antibody Dilution (Chondrex, Inc., Woodinville, WA) buffer; 100 µl of this solution was added to each well before incubation for 30 min at RT with shaking at 150 rpm. Following aspiration and three washes (100 µl each), 1-Step Ultra TMB-ELISA Substrate Solution (ThermoScientific, Carlsbad, CA) was added (100 µl per well). Absorbance of TMB substrate was measured twice at 652 nm by UV-Vis plate reader (BioTek Winooski, VT) after 5 and 15 min of incubation. The experiment was repeated three times using plasma from different αEp9(+) and αEp9(-) patients for each experiments, using a total of 15 patients for each group. Each experiment was conducted in technical duplicate.

*αEp9 IgG and IgM ELISA.* Plasma from 34 patients, previously tested for the presence of αEp9 Abs using phage ELISAs [9], were used to test levels of αEp9 IgGs and IgMs. 2 μM eGFP-Ep9 or eGFP-FLAG in PBS pH 8.0 were immobilized onto 96 well microtiter plates via overnight incubation with shaking at 150 rpm at 4 °C. Excess protein was aspirated and removed with three consecutive PBS-T washes. Wells were blocked by adding CBB (100 μl) before incubation at 30 min at RT with shaking at 150 rpm. Next, αEp9(+) patient plasma, diluted 1:100 in CBB (100 μl), was added to duplicate wells before incubation at RT for 1 h with shaking at 150 rpm. The solutions were discarded and sample wells were washed with PBS-T three times. αEp9 Abs binding to the potential epitopes was detected using horse radish peroxidase (HRP) conjugated αHuman Fc IgG (Thermo Fisher Scientific, Waltham MA) or αIgM μ-chain specific (Millipore Sigma, Temecula, CA) Abs diluted 1:5000 in ChonBlock Sample Antibody Dilution buffer. 100 μl of detection Abs were added to each sample well, and incubated for 30 min at RT with shaking at 150 rpm. Sample wells were aspirated and washed three times in PBS-T, and the binding signal was detected after addition of TMB substrate (100 μl per well).

*Bivalent Abs Binding ELISA.* eGFP-Ep9 or eGFP-FLAG was serially diluted (120 nM, 40 nM, 13 nM and 4 nM) in PBS pH 8.0, and added to the appropriate wells in 96 well microtiter plates, followed by shaking overnight at 150 rpm at 4 °C. Excess unbound protein was removed, and the plate was washed three times in PBS-T. Wells were then blocked in CBB and incubated for 30 min at RT. After blocking, pooled plasma (100 μl per well) from either five αEp9(+) patients, or five non-αEp9, αNP(+) patients, or healthy individuals was added to the appropriate wells. Plasma from pooled patients was diluted 100-fold in CBB. As a positive control αFLAG Ab was used as a 1:2000 dilution in CBB. Samples were incubated for

1 h at RT with 150 rpm shaking. The solution was removed by aspiration, and the plate and washed three times with PBS-T. Then 1 nM EpNeu displaying phage or the phage negative control with no epitopes displayed was diluted in CBB. 100 µl phage solution was added to microtiter wells and incubated for 30 min at RT with shaking at 150 rpm. After aspirating and washing off unbound phage, binding of phage-displayed EpNeu to plasma αEp9 Abs was visualized using αM13-HRP Ab diluted 1:10,000 in ChonBlock Sample Antibody Dilution buffer. Samples were incubated for 30 min at RT with 150 rpm shaking, and unbound Abs were removed through washing with PBS-T three times before addition of TMB substrate (100 µl). Experiments were conducted in technical triplicates and repeated three times with different αEp(+) and αEp(-) patient samples.

*Dose-Dependent ELISA.* Wells of microtiter plates were coated with serially diluted concentration of eGFP-Ep9, EpNeu and EpPred or eGFP-FLAG, and incubated overnight at 4 °C before blocking as described above. Next, pooled plasma (100 µl per well) from either five αEp9(+) patients, or five αEp9(-) patients, or healthy individuals at 1:100 total plasma dilution in CBB was added to the appropriate wells. Samples were incubated for 1 h at RT with shaking at 150 rpm. After incubation, unbound solution was removed, and the plates were washed three times with PBS-T. αEp9 IgG levels were detected by adding αFc IgG-HRP diluted 1:5000 in ChonBlock Sample Dilution buffer, followed by incubation for 30 min at RT with shaking at 150 rpm, followed by addition of TMB substrate (100 µl per well). Experiments were conducted in technical triplicates and repeated three times with different αEp(+) and αEp(-) patient samples.

*Linear B-cell Epitope Prediction.* Linear epitopes from the Influenza A/Para/128982-IEC/2014(H3N2) neuraminidase protein were predicted using the partial sequence with

Accession AIX95025.1 from the National Center for Biotechnology Information's GenBank and the linear B-cell epitope prediction tool, Bepipred 2.0 [13] (http://www.cbs.dtu.dk/services/BepiPred-2.0/). The prediction thresholds were set to 0.5. The specificity and sensitivity of epitope prediction at this threshold is 0.572 and 0.586, respectively.

*Structure-Based B-cell Epitope Prediction.* The structure of Influenza A/Para/128982-IEC/2014(H3N2) neuraminidase protein was modelled using Swiss-Model [15–18,25,26] (https://swissmodel.expasy.org/interactive). Using the ProMod3 3.2.0 tool [16], a structural model was generated based on the crystal structure (2.35Å, PDB 4GZS 1.A) of a homologous H3N2 neuraminidase with 96.39% sequence identity. Modelling methods and quality assessments are further detailed in the report below.

The structural model of Influenza A/Para/128982-IEC/2014(H3N2) neuraminidase was used to predict structure-based epitopes. Using the *in silico* online platform Discotope 2.0 [19] (http://www.cbs.dtu.dk/services/DiscoTope-2.0/), structure-based epitope propensity scores were calculated to predict likely B-cell epitope residues. The score of -3.7 was set as the threshold for epitope prediction, which estimates a specificity and sensitivity of 0.75 and 0.47, respectively (Figure 3 – supplement 1).

*Statistical Analysis.* The ELISA data were analyzed in GraphPad Prism 9 (https://www.graphpad.com). Since the ELISA assays of 21 potential OAS epitopes were conducted over several microtiter plates for repeated experiments, the raw absorbance values for every patient sample were normalized and represented as the ratio of phage negative control to the signal. For heatmaps, two-way Analysis of variance (ANOVA) with Tukey multiple comparisons tests were conducted for the entire dataset of epitopes. For

column comparisons of two groups, for example IgM levels and IgG levels in the αEp(+) patients, unpaired, two-tailed, parametric t-tests were applied. Additionally, for column comparisons between more than two groups, for example IgM or IgG levels groups by weeks PSO, One-way ANOVA with Tukey multiple comparisons tests were used. Where indicated, Dunnett's tests were performed to compare results to healthy Abs interactions to αEp9(+) patient results. Graphs represent SD error bars for technical replicates, defined as replicates of the same conditions in multiple wells of the same plate. Whereas error bars are shown as SEM when an experiment is repeated with different patient sample sets. Correlations between Ep9 and EpNeu levels in patients were determined by plotting normalized values on an XY graph and performing a linear Pearson's correlation coefficient test, where r-values between 1.0-0.7 were considered strong correlations, values between 0.7 and 0.5 were considered a moderate correlation, and values below 0.5 were considered a weak correlation[27]. The significance of the correlation was evaluated based on p-value <0.05.

## 5.6 References


(1) Fierz, W.; Walz, B. Antibody Dependent Enhancement Due to Original Antigenic Sin and the Development of SARS. *Front. Immunol.* **2020**, *11*, 1120. https://doi.org/10.3389/fimmu.2020.01120.

(2) Brown, E. L.; Essigmann, H. T. Original Antigenic Sin: The Downside of Immunological Memory and Implications for COVID-19. *mSphere* **2021**, *6* (2). https://doi.org/10.1128/mSphere.00056-21.

(3) Park, M. S.; Kim, J. Il; Park, S.; Lee, I.; Park, M. S. Original Antigenic Sin Response to RNA Viruses and Antiviral Immunity. *Immune Network*. Korean Association of Immunologists 2016, pp 261–270. https://doi.org/10.4110/in.2016.16.5.261.

(4) Welsh, R. M.; Fujinami, R. S. Pathogenic Epitopes, Heterologous Immunity and Vaccine Design. *Nat. Rev. Microbiol.* **2007**, *5* (7), 555–563. https://doi.org/10.1038/nrmicro1709.

(5) Kohler, H.; Nara, P. A Novel Hypothesis for Original Antigenic Sin in the Severe Disease of SARS-CoV-2 Infection. *Monoclonal Antibodies in Immunodiagnosis and Immunotherapy*. Mary Ann Liebert Inc. August 2020, pp 107–111. https://doi.org/10.1089/mab.2020.0029.

(6) Ng, K. W.; Faulkner, N.; Cornish, G. H.; Rosa, A.; Harvey, R.; Hussain, S.; Ulferts, R.; Earl, C.; Wrobel, A. G.; Benton, D. J.; Roustan, C.; Bolland, W.; Thompson, R.; Agua-Doce, A.; Hobson, P.; Heaney, J.; Rickman, H.; Paraskevopoulou, S.; Houlihan, C. F.; Thomson, K.; Sanchez, E.; Shin, G. Y.; Spyer, M. J.; Joshi, D.; O'Reilly, N.; Walker, P. A.; Kjaer, S.; Riddell, A.; Moore, C.; Jebson, B. R.; Wilkinson, M.; Marshall, L. R.; Rosser, E. C.; Radziszewska, A.; Peckham, H.; Ciurtin, C.; Wedderburn, L. R.; Beale, R.; Swanton, C.; Gandhi, S.; Stockinger, B.; McCauley, J.; Gamblin, S. J.; McCoy, L. E.; Cherepanov, P.; Nastouli, E.; Kassiotis, G. Preexisting and de Novo Humoral Immunity to SARS-CoV-2 in Humans. *Science (80-. ).* **2020**, *370* (6522), 1339–1343. https://doi.org/10.1126/science.abe1107.

(7) Anderson, E. M.; Goodwin, E. C.; Verma, A.; Arevalo, C. P.; Bolton, M. J.; Weirick, M. E.; Gouma, S.;

McAllister, C. M.; Christensen, S. R.; Weaver, J. E.; Hicks, P.; Manzoni, T. B.; Oniyide, O.; Ramage, H.; Mathew, D.; Baxter, A. E.; Oldridge, D. A.; Greenplate, A. R.; Wu, J. E.; Alanio, C.; D'Andrea, K.; Kuthuru, O.; Dougherty, J.; Pattekar, A.; Kim, J.; Han, N.; Apostolidis, S. A.; Huang, A. C.; Vella, L. A.; John Wherry, E.; Meyer, N. J.; Cherry, S.; Bates, P.; Rader, D. J.; Hensley, S. E.; Alam, Z.; Addison, M. M.; Byrne, K. T.; Chandra, A.; Descamps, H. C.; Kaminskiy, Y.; Hamilton, J. T.; Noll, J. H.; Omran, D. K.; Perkey, E.; Prager, E. M.; Pueschl, D.; Shah, J. B.; Shilan, J. S.; Vanderbeck, A. N. Seasonal Human Coronavirus Antibodies Are Boosted upon SARS-CoV-2 Infection but Not Associated with Protection. *medRxiv*. medRxiv November 2020, p 2020.11.06.20227215. https://doi.org/10.1101/2020.11.06.20227215.

(8) Shrock, E.; Fujimura, E.; Kula, T.; Timms, R. T.; Lee, I.-H.; Leng, Y.; Robinson, M. L.; Sie, B. M.; Li, M. Z.; Chen, Y.; Logue, J.; Zuiani, A.; McCulloch, D.; Lelis, F. J. N.; Henson, S.; Monaco, D. R.; Travers, M.; Habibi, S.; Clarke, W. A.; Caturegli, P.; Laeyendecker, O.; Piechocka-Trocha, A.; Li, J.; Khatri, A.; Chu, H. Y.; Villani, A.-C.; Kays, K.; Goldberg, M. B.; Hacohen, N.; Filbin, M. R.; Yu, X. G.; Walker, B. D.; Wesemann, D. R.; Larman, H. B.; Lederer, J. A.; Elledge, S. J. Viral Epitope Profiling of COVID-19 Patients Reveals Cross-Reactivity and Correlates of Severity. *Science (80-. ).* **2020**, *4250* (September). https://doi.org/10.1126/science.abd4250.

(9) Sen, S. R.; Sanders, E. C.; Gabriel, K. N.; Miller, B. M.; Isoda, H. M.; Salcedo, G. S.; Garrido, J. E.; Dyer, R. P.; Nakajima, R.; Jain, A.; Caldaruse, A.-M.; Santos, A. M.; Bhuvan, K.; Tifrea, D. F.; Ricks-Oddie, J. L.; Felgner, P. L.; Edwards, R. A.; Majumdar, S.; Weiss, G. A. Predicting COVID-19 Severity with a Specific Nucleocapsid Antibody plus Disease Risk Factor Score. *mSphere* **2021**, *6* (2), 2020.10.15.341743. https://doi.org/10.1128/mSphere.00203-21.

(10) Altschul, S. F.; Madden, T. L.; Schäffer, A. A.; Zhang, J.; Zhang, Z.; Miller, W.; Lipman, D. J. Gapped BLAST and PSI-BLAST: A New Generation of Protein Database Search Programs. *Nucleic Acids Research*. 1997. https://doi.org/10.1093/nar/25.17.3389.

(11) Madej, T.; Lanczycki, C. J.; Zhang, D.; Thiessen, P. A.; Geer, R. C.; Marchler-Bauer, A.; Bryant, S. H. MMDB and VAST+: Tracking Structural Similarities between Macromolecular Complexes. *Nucleic Acids Res.* **2014**, *42* (D1). https://doi.org/10.1093/nar/gkt1208.

(12) World Health Organization (WHO). WHO | Cumulative Number of Reported Probable Cases of Severe Acute Respiratory Syndrome (SARS).

(13) Jespersen, M. C.; Peters, B.; Nielsen, M.; Marcatili, P. BepiPred-2.0: Improving Sequence-Based B-Cell Epitope Prediction Using Conformational Epitopes. *Nucleic Acids Res.* **2017**. https://doi.org/10.1093/nar/gkx346.

(14) Gentles, L. E.; Wan, H.; Eichelberger, M. C.; Bloom, J. D. Antibody Neutralization of an Influenza Virus That Uses Neuraminidase for Receptor Binding. *bioRxiv*. bioRxiv May 2020, p 2020.05.08.084954. https://doi.org/10.1101/2020.05.08.084954.

(15) Waterhouse, A.; Bertoni, M.; Bienert, S.; Studer, G.; Tauriello, G.; Gumienny, R.; Heer, F. T.; De Beer, T. A. P.; Rempfer, C.; Bordoli, L.; Lepore, R.; Schwede, T. SWISS-MODEL: Homology Modelling of Protein Structures and Complexes. *Nucleic Acids Res.* **2018**. https://doi.org/10.1093/nar/gky427.

(16) Studer, G.; Tauriello, G.; Bienert, S.; Biasini, M.; Johner, N.; Schwede, T. ProMod3 - A Versatile Homology Modelling Toolbox. *PLoS Comput. Biol.* **2021**. https://doi.org/10.1371/JOURNAL.PCBI.1008667.

(17) Guex, N.; Peitsch, M. C.; Schwede, T. Automated Comparative Protein Structure Modeling with SWISS-MODEL and Swiss-PdbViewer: A Historical Perspective. *Electrophoresis* **2009**. https://doi.org/10.1002/elps.200900140.

(18) Bienert, S.; Waterhouse, A.; De Beer, T. A. P.; Tauriello, G.; Studer, G.; Bordoli, L.; Schwede, T. The SWISS-MODEL Repository-New Features and Functionality. *Nucleic Acids Res.* **2017**. https://doi.org/10.1093/nar/gkw1132.

(19) Kringelum, J. V.; Lundegaard, C.; Lund, O.; Nielsen, M. Reliable B Cell Epitope Predictions: Impacts of Method Development and Improved Benchmarking. *PLoS Comput. Biol.* **2012**, *8* (12). https://doi.org/10.1371/journal.pcbi.1002829.

(20) Lipničanová, S.; Chmelová, D.; Godány, A.; Ondrejovič, M.; Miertuš, S. Purification of Viral Neuraminidase from Inclusion Bodies Produced by Recombinant Escherichia Coli. *J. Biotechnol.* **2020**, *316*, 27–34. https://doi.org/10.1016/j.jbiotec.2020.04.005.

(21) Xie, H.; Wan, X. F.; Ye, Z.; Plant, E. P.; Zhao, Y.; Xu, Y.; Li, X.; Finch, C.; Zhao, N.; Kawano, T.; Zoueva, O.; Chiang, M. J.; Jing, X.; Lin, Z.; Zhang, A.; Zhu, Y. H3N2 Mismatch of 2014-15 Northern Hemisphere Influenza Vaccines and Head-to-Head Comparison between Human and Ferret Antisera Derived Antigenic Maps. *Sci. Rep.* **2015**, *5* (1), 1–10. https://doi.org/10.1038/srep15279.

(22) Benchling, I. Benchling [Biology Software].
(23) Levin, A. M. Exploring the Interaction between the Protein Kinase A Catalytic Subunit and Caveolin-1 Scaffolding Domain with Shotgun Scanning, Oligomer Complementation, NMR, and Docking. *Protein Sci.* **2006**. https://doi.org/10.1110/ps.051911706.
(24) Pastorino, B.; Touret, F.; Gilles, M.; Lamballerie, X. De; Charrel, R. N. Heat Inactivation of Different Types of SARS-CoV-2 Samples: What Protocols for Biosafety, Molecular Detection and Serological Diagnostics? *Viruses* **2020**, *12* (735), 1–8.
(25) Studer, G.; Rempfer, C.; Waterhouse, A. M.; Gumienny, R.; Haas, J.; Schwede, T. QMEANDisCo—Distance Constraints Applied on Model Quality Estimation. *Bioinformatics* **2020**. https://doi.org/10.1093/bioinformatics/btz828.
(26) Bertoni, M.; Kiefer, F.; Biasini, M.; Bordoli, L.; Schwede, T. Modeling Protein Quaternary Structure of Homo- and Hetero-Oligomers beyond Binary Interactions by Homology. *Sci. Rep.* **2017**. https://doi.org/10.1038/s41598-017-09654-8.
(27) Mukaka, M. M. *Statistics Corner: A Guide to Appropriate Use of Correlation Coefficient in Medical Research*; 2012; Vol. 24.
(28) Letunic, I.; Bork, P. Interactive Tree of Life (ITOL) v4: Recent Updates and New Developments. *Nucleic Acids Res.* **2019**, *47* (W1), W256–W259. https://doi.org/10.1093/nar/gkz239.

# CHAPTER 6

## Virus Bioresistor (VBR) for Detection of Bladder Cancer Marker DJ-1 in Urine at 10 pM in One Minute

Adapted with permission from *Analytical Chemistry.*
DOI: 10.1021/acs.analchem.0c00534

### 6.1 Abstract

DJ-1, a 20.7 kDa protein, is overexpressed in people who have bladder cancer (BC). Its elevated concentration in urine allows it to serve as a marker for BC. However, no biosensor for the detection of DJ-1 has been demonstrated. Here, we describe a virus bioresistor (VBR) capable of detecting DJ-1 in urine at a concentration of 10 pM in 1 min. The VBR consists of a pair of millimeter-scale gold electrodes that measure the electrical impedance of an ultrathin (≈ 150–200 nm), two-layer polymeric channel. The top layer of this channel (90–105 nm in thickness) consists of an electrodeposited virus-PEDOT (PEDOT is poly(3,4-ethylenedioxythiophene)) composite containing embedded M13 virus particles that are engineered to recognize and bind to the target protein of interest, DJ-1. The bottom layer consists of spin-coated PEDOT–PSS (poly(styrenesulfonate)). Together, these two layers constitute a current divider. We demonstrate here that reducing the thickness of the bottom PEDOT–PSS layer increases its resistance and concentrates the resistance drop of the channel in the top virus-PEDOT layer, thereby increasing the sensitivity of the VBR and enabling the detection of DJ-1. Large signal amplitudes coupled with the inherent simplicity of the VBR sensor design result in high signal-to-noise (S/N > 100) and excellent sensor-to-sensor reproducibility characterized by coefficients of variation in the range of 3–7% across the DJ-1 binding curve down to a concentration of 30 pM, near the 10 pM limit of detection (LOD), encompassing four orders of magnitude in concentration.

## 6.2 Introduction

Minimally invasive cancer screening using bodily fluids, so-called "liquid biopsies", may eventually eliminate the evaluation of suspected malignancies using surgery.[1] Liquid biopsies involve the detection in blood, urine, and other bodily fluids of nucleic acids, circulating tumor cells (in blood), or distinctive protein markers that signal the presence of a particular cancer. DJ-1, a 20.7 kDa protein, is elevated in the urine of people with bladder cancer (BC).[2,3] Presently, the measurement of DJ-1 in urine requires an enzyme-linked immunosorbent assay (ELISA), which is both slow and inconvenient. A biosensor for DJ-1 could accelerate its assessment for the detection of BC recurrence in patients who have undergone treatment for the disease. However, no biosensor for DJ-1 has been demonstrated to our knowledge. Here we demonstrate that a new type of biosensor, the virus bioresistor or VBR, that uses virus particles as receptors can be programmed to detect DJ-1 in human urine.

The VBR is a bioresistor contacted with two gold electrodes. The bioresistor consists of an electronically conductive channel composed of a layer of poly(3,4-ethylene dioxythiophene) (PEDOT) doped with virus particles. Recently,[4] we demonstrated the VBR concept for the detection of human serum albumin (HSA, 66.5 kDa) in high salt (160 mM NaCl) buffer. A limit-of-detection for HSA (LODHSA) of 7 nM was achieved in that study. However, a sub-1.0 nM LOD for protein markers is required to enable cancer surveillance in urine. Here we unlock higher sensitivity for VBRs simply by engineering the PEDOT channel to concentrate the impedance in an ultrathin (≈ 90 nm) virus-PEDOT composite layer. With this modification, a limit-of-detection of ($LOD_{DJ1}$) of 10 pM is achieved in urine (synthetic and human), coupled with a dynamic range of more than four orders of magnitude from 10 pM

to 300 nM. This performance is clinically relevant because it allows for the detection of elevated DJ-1 in the urine of patients who have bladder cancer (≈ 100 pM).[2,3,5,6] Importantly, the modifications to the VBR do not compromise either the speed or the simplicity of its operation. As before, the VBR operates in a dip-and-read modality and produces a stable, quantitative signal within 1.0 min. The sensing performance reported here also eclipses prior virus-based biosensors that we have studied over a period of 14 years in our laboratories.[7–12]

The mechanism by which the VBR transduces protein binding remains under investigation. A hypothesis presented here proposes that a target protein permeates the virus-PEDOT layer as it undergoes affinity-driven partitioning to virus particles entrained in this layer. As the volume fraction of electrically insulating proteins increases, the electrical conductivity of the resistor channel imparted by PEDOT is reduced, generating the VBR signal.

### 6.3 Results and Discussion

*VBR Fabrication and Characterization.* Starting with patterned gold electrodes on glass, VBRs are prepared in three steps. First, a PEDOT–PSS layer is deposited by spin-coating. Second, a poly(methyl methacrylate) or PMMA solution cell with adhesive backing is pressed onto the PEDOT–PSS layer. Third, this solution cell is used to electrodeposit a virus-PEDOT layer. This electrodeposition process applied the following protocol. The VBR cell is rinsed with PBS buffer and filled with an aqueous solution of EDOT (2.5 mM), LiClO4 (12.5 mM), and engineered M13 virus particles (8 nM). Using a mercurous sulfate reference electrode (MSE), and a platinum counter electrode, the virus-PEDOT composite layer is electrodeposited onto the PEDOT–PSS surface by scanning its potential (20 mV/s) from

+0.20 V to +0.80 V and back versus MSE in two cycles. Under these conditions, EDOT is oxidized, and the growth of EDOT oligomers proceeds until insoluble cationic PEDOT is precipitated as a film, together with charge-compensating $ClO^{4-}$ anions, onto the PEDOT–PSS electrode.[13] If M13 virus is present in the plating solution, virus particles are incorporated into the growing film, a process promoted by the high negative charge density of these particles. At neutral pH, each M13 virion is blanketed with ~6000 negative charges.[14] Previously, we have demonstrated that the electrodeposition of films from a plating solution containing M13 virus particles and EDOT produces a composite virus-PEDOT film that concentrates virus particles by a factor of 500 times relative to the M13 concentration in the plating solution.[15] As seen in the photograph of a VBR shown in, the resulting VBR "channel", consisting of a PEDOT–PSS bottom layer and a virus-PEDOT top layer, is transparent.

The VBR device architecture and polymeric channel resembles that of an organic electrochemical transistor (OECT).[16–20] The differences between these two types of devices are the following. (1) The VBR is a two-terminal device with no gate electrode. This simplifies its operation considerably, as the VBR measures the impedance of its channel at its rest potential in the analysis solution without the need for gate scans and the requirement for optimization of the gate potential prior to a measurement.[21] (2) The VBR measures an impedance frequency spectrum for the channel, typically across five orders of magnitude in frequency instead of the DC resistance of the channel, as is common practice with OECTs.[22,23] This impedance data set allows the channel impedance, $R_{VBR}$, which provides the VBR signal, to be cleanly separated from the solution impedance, $R_{soln}$, which is correlated with the salt concentration of the analysis solution. For bodily fluids such as urine, $R_{soln}$ has the potential to provide information relating to the hydration state of a patient. (3) VBRs use engineered

virus particles as receptors. Virus particles may be entrained in a PEDOT film by coelectrodeposition of the virus with the polymer as described above. A fourth difference may be the mechanism of signal generation, as described below.

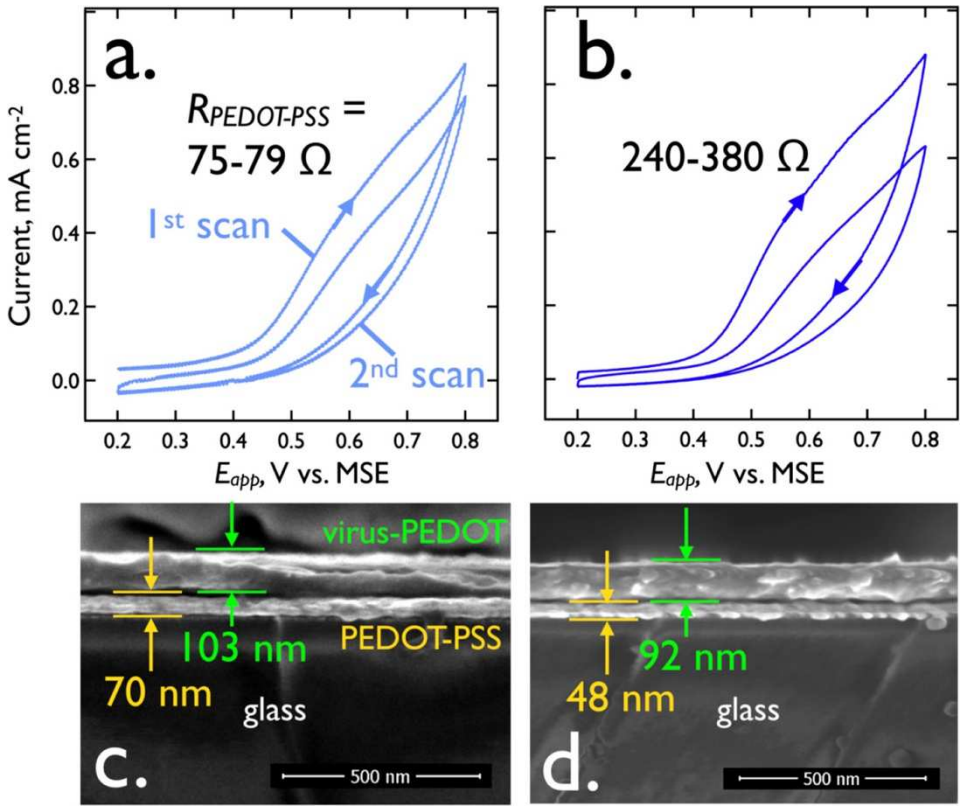


**Figure 6-1. Electrodeposition and SEM cross sections of virus-PEDOT bioaffinity layers.** **A)** Virus-PEDOT bioaffinity layer is electrodeposited on a PEDOT–PSS base layer using two voltametric scans, as shown. The plating solution is aqueous 2.5 mM EDOT and 12.5 mM $LiClO_4$, 8 nM virus, and the scan rate is 20 mV/s. The DC resistance, $R_{PEDOT-PSS}$, of the PEDOT–PSS layer here is 75–79 Ω. **B)** Same electrodeposition process for a thinner, PEDOT–PSS base layer with $R_{PEDOT-PSS}$ in the range from 240–380 Ω. **C,D)**. Cross-sectional SEM images of these two layers show that the more conductive PEDOT–PSS layer ($R_{PEDOT-PSS}$ = 75–79 Ω) is 70 nm (±3 nm) in thickness, whereas the less conductive PEDOT–PSS layer is 48 nm (±2 nm) in thickness. The electrodeposited virus-PEDOT layer is also somewhat thinner in panel d relative to panel c in accordance with the lower deposition currents observed for the second deposition scan.

The architecture and resultant properties of the VBR channel dictate its sensing performance. We focus attention here on the importance of the PEDOT–PSS layer thickness and electrical resistance. SEM cross-sectional images (**Fig 6-1C,D**) show that both polymer layers are tens of nanometers in total thickness. The thickness of the PEDOT–PSS bottom layer is influenced both by the presence of ethylene glycol (EG) in the deposition solution[24,25]

and the spin coater speed. The addition of EG is known to increase the conductivity of PEDOT–PSS by altering its morphology.[26,27] Relatively thick (70 (±3) nm) low resistance films were obtained using 3% (v/v) EG, while high resistance films (48 (±2) nm) were prepared using 1.5% (v/v) EG (**Fig. 6-1C,D**). The electrical resistance of these layers, RPEDOT–PSS, is = 75–79 Ω (thick) and 240–380 Ω (thin). The increased resistance of the PEDOT–PSS bottom layer has little effect on the thickness of the virus-PEDOT top layer electrodeposited on it, and the virus-PEDOT top layers have similar thicknesses of 92 (±4) nm (high PEDOT–PSS resistance) versus 103 (±4) nm (low resistance). As we demonstrate below, a reduction in thickness of the PEDOT–PSS layer, and an increase in its resistance, boosts the sensitivity of the VBR for the detection of HSA and DJ-1.

Electrodeposited virus-PEDOT and PEDOT-only films have a characteristic topography imparted by PEDOT crystallites protruding by up to a micron from the planar surface of the PEDOT film (**Fig. 6-2**). These "PEDOT stalagmites" are not related to virus particles as they are observed both in the absence (**Fig. 6-2A,B**) and presence (**Fig. 6-2C,D**) of added phage particles. PEDOT stalagmites have attributes of crystallites including a faceted appearance, as previously reported in the literature.[28,29] In virus-PEDOT films, entrained M13 virus particles appear as black filamentous objects against a gray PEDOT background (**Fig. 6-2C-E**). SEM examination of several samples shows that the virus concentration within the plane of the virus-PEDOT film is nonuniform with 10–30 $\mu m^2$ regions that are intensely black, indicating high virus concentrations, and other regions that

are gray with a relatively low virus concentration. The clustering of virus particles within the film is interesting and surprising, given the high negative charge density of these particles.

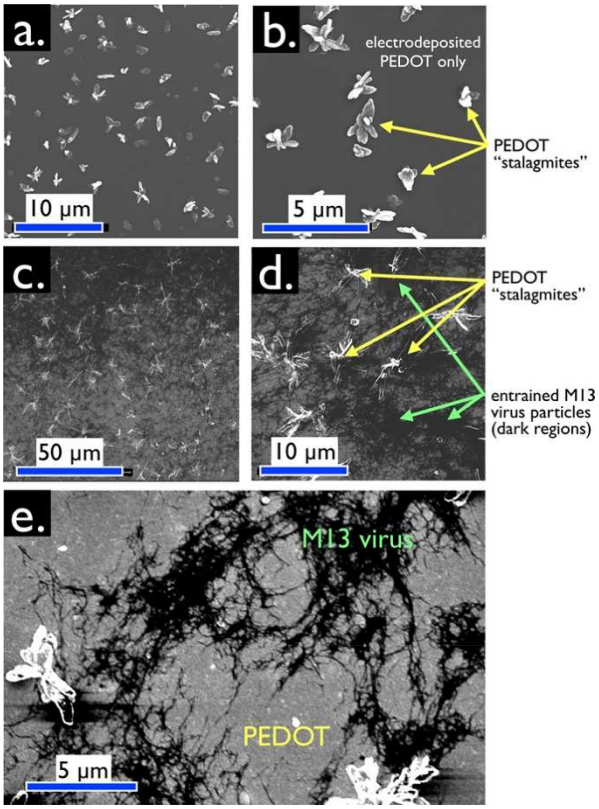


**Figure 6-2. Plane view SEM images.** Acquired with secondary electron detection (SED), of **A,B)** virus-free and **C,D,E)** virus-containing bioaffinity layers. **A,B)** Control *VBR* bioaffinity layer prepared by electrodeposition from a solution containing no virus particles. Micron scale protrusions from the surface of this film are characteristic of electrodeposited PEDOT. These protrusions are not seen at PEDOT–PSS films prepared by spin-coating. We refer to these structures as "PEDOT stalagmites". **C,D,E)** *VBR* bioaffinity layers containing M13 virus particles. Filamentous M13 virus particles comprise the dark regions of these images. Lighter gray regions contain no virus. PEDOT stalagmites are also observed. **E)** Enhanced contrast exposes tangles of M13, again distributed nonuniformly inside a virus-PEDOT bioaffinity layer.

*VBR Electrical Response and Signal.* As previously proposed, a simple equivalent circuit containing four circuit elements accounts for the measured frequency-dependent impedance of the VBR channel from DC to 40 kHz. In this circuit, the capacitance of the virus-PEDOT/solution interface is represented by a total capacitance, *C*. This capacitance provides coupling between the AC voltage signal applied to the channel and the analyte solution. Three resistors represent the resistance of the analyte solution ($R_{soln}$), the resistance of the

top polymer layer ($R_{PEDOT\text{-}virus}$), and the resistance of the bottom PEDOT–PSS layer ($R_{PEDOT\text{-}PSS}$).

The impedance response of a VBR is characterized by a semicircular Nyquist plot ($Z_{im}$ versus $Z_{re}$). A qualitative understanding of the VBR response is provided by examining its limiting behaviors at low and high frequencies across the range from 1.0 Hz to 40 kHz. At $f$ = 1.0 Hz, the capacitive reactance of the virus-PEDOT/solution interface, ($ZC = (2\pi fC)^{-1} \approx 6$ kΩ) is larger than $R_{VBR}$ (≈ 2.1–2.7 kΩ). Therefore, although $R_{soln}$ is small by comparison to $R_{VBR}$ (289–330 Ω), the value of $Z_C$ strongly attenuates the AC signal that accesses $R_{soln}$. In this limit, $R_{VBR}$ is approximated by the parallel combination of $R_{PEDOT\text{-}virus}$ and $R_{PEDOT\text{-}PSS}$ ($R_{VBR}$, eq 1):

**(Eq. 6-1)** $$R_{VBR} \approx \frac{(R_{PEDOT-PSS})(R_{PEDOT-virus})}{R_{PEDOT-PSS} + R_{PEDOT-virus}}$$

As shown below and previously, $R_{VBR}$ increases in the presence of a target protein that is bound by virus particles in the virus-PEDOT layer. The difference between $R_{VBR}$ in the presence and absence of this protein is the VBR signal, $\Delta R_{VBR}$. At the high frequency limit, f = 40 kHz, the capacitive reactance approaches zero ($Z_C = (2\pi fC)^{-1} \approx 0.15$ Ω), and the circuit of simplifies to three resistors in parallel:

**(Eq. 6-2)** $$R_{VBR} \approx \frac{(R_{PEDOT-PSS})(R_{PEDOT-virus})(R_{soln})}{R_{PEDOT-PSS}R_{PEDOT-virus} + R_{soln}R_{PEDOT-virus} + R_{soln}R_{PEDOT-PSS}}$$

At $f$ = 40 kHz, $R_{VBR}$ is much lower than at 1 Hz because the small resistor $R_{soln}$ is accessed in parallel to $R_{PEDOT\text{-}PSS}$ and $R_{virus\text{-}PEDOT}$. To a first approximation, the impedance at both of these frequency limits, 1.0 Hz and 40 kHz, is purely resistive but at intermediate frequencies, a significant capacitive component is introduced, producing the characteristic semicircular Nyquist plot that is observed.

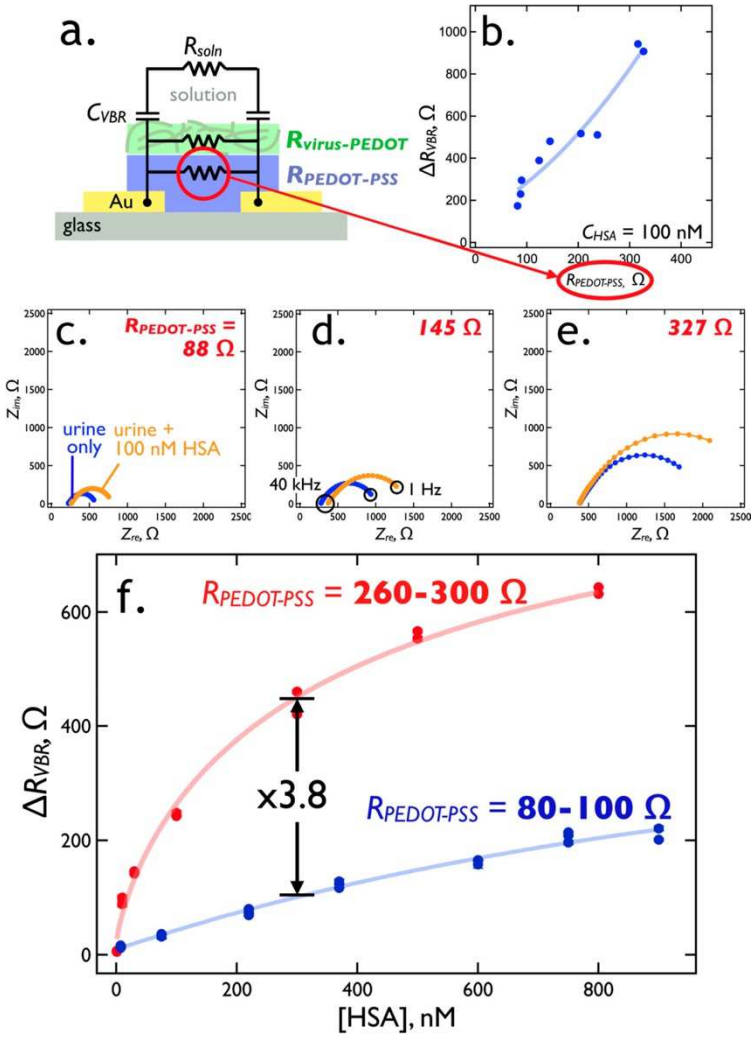


**Figure 6-3. $R_{PEDOT-PSS}$ tuning of the VBR sensitivity for HSA.** **A)** Equivalent circuit for the *VBR* places the electrical impedance of the virus-PEDOT layer, $R_{VBR}$, in parallel with that of the PEDOT–PSS bottom layer, $R_{PEDOT-PSS}$, forming a current divider. **B)** Increasing $R_{PEDOT-PSS}$ from 80 Ω to 300 Ω, by reducing the PEDOT–PSS layer thickness, forces current, *i*, through the virus-PEDOT measurement layer, increasing the signal for 100 nM HSA by a factor of 3 to 5 from 200 Ω to more than 900 Ω. **C,D,E)** Three Nyquist plots corresponding to three values of the resistor, $R_{PEDOT-PSS}$, as indicated. In each plot, impedances are plotted in the complex plane from 1 Hz (right) to 40 kHz (left). A shift in the low frequency $Z_{re}$ from synthetic urine only (blue trace) to 100 nM DJ-1 (orange trace) approximates the signal, $\Delta R_{VBR}$. **F)** $R_{VBR}$ versus [HSA] calibration plots for a series of 42 *VBR* sensors (21 in each plot) with $R_{PEDOT-PSS}$ values in the range from 80 to 100 Ω and 260 to 300 Ω. The higher $R_{PEDOT-PSS}$ devices produce 3–5-times more signal amplitude across the HSA binding curve.

The values of *C*, $R_{soln}$, and $R_{VBR}$ (encompassing $R_{PEDOT-virus}$ and $R_{PEDOT-PSS}$) are obtained by deconvolution of the complex impedance data set. How do $R_{VBR}$, $R_{soln}$, and C change in response to the concentration of a target protein? For DJ-1 concentrations from 0–100 nM, variations of $R_{soln}$ are constant within the error bars for this measurement and are

independent of DJ-1 concentration. The capacitance, $C$, approximated as a constant phase element (CPE, $Z_C \approx Z_{CPE} = \frac{1}{Q(\iota\omega)^n}$), varies weakly with the DJ-1 concentration. $R_{VBR}$ at low frequency, in contrast, is strongly correlated with the DJ-1 concentration and, as already indicated, $\Delta R_{VBR}$ is used to transduce the concentration of a target protein bound by entrained virus particles.

Since, as noted above, the VBR signal $\Delta R_{VBR}$ is best measured at low frequency, would it not be simpler to use the DC resistance of the VBR channel to derive signal? In practice, the DC measurement does work, but there are two reasons for measuring the frequency spectrum instead. (1) In DC sensing mode, one does not acquire the high frequency impedance (**Eq. 6-2**) that permits deconvolution (and measurement) of the solution resistance from the $\Delta R_{VBR}$ signal. (2) The reproducibility of the impedance at low frequency is better than for a DC measurement. That is, the signal-to-noise at low frequencies down to 1 Hz is higher than the noise at DC (data not shown).

*Tuning VBR Signal Amplitude Using $R_{PEDOT\text{-}PSS}$.* Eq 5-1 predicts that at low frequencies, increasing $R_{PEDOT–PSS}$ causes $R_{VBR}$ to converge on $R_{PEDOT\text{-}virus}$ (**Fig. 6-3A**). If $\Delta R_{VBR}$ is generated by the virus-PEDOT top-layer, then an increase in $R_{PEDOT–PSS}$ should increase VBR sensitivity. This expectation is confirmed by measurement of ΔRVBR for the protein human serum albumin, HSA, a 66.5 kDa protein that is a marker for renal failure. A plot of $\Delta R_{VBR}$ versus $R_{PEDOT–PSS}$ for [HSA] = 100 nM shows that increasing $R_{PEDOT–PSS}$ is from 70 Ω to 380 Ω by reducing thickness of this layer increases the $\Delta R_{VBR}$ from 40 Ω to more than 500 Ω (**Fig. 6-3B**).

Nyquist plots for three $R_{PEDOT-PSS}$ values (**Fig. 6-3C,D,E**) document the increase in sensitivity for three VBRs. It should be noted that $R_{PEDOT-PSS} \approx 300\ \Omega$ is a practical upper limit in our experiments. Attempts to further thin the PEDOT–PSS layer to achieve even higher sensitivities resulted in pronounced irreproducibility in both $R_{PEDOT-PSS}$ and measured $\Delta R_{VBR}$ values.

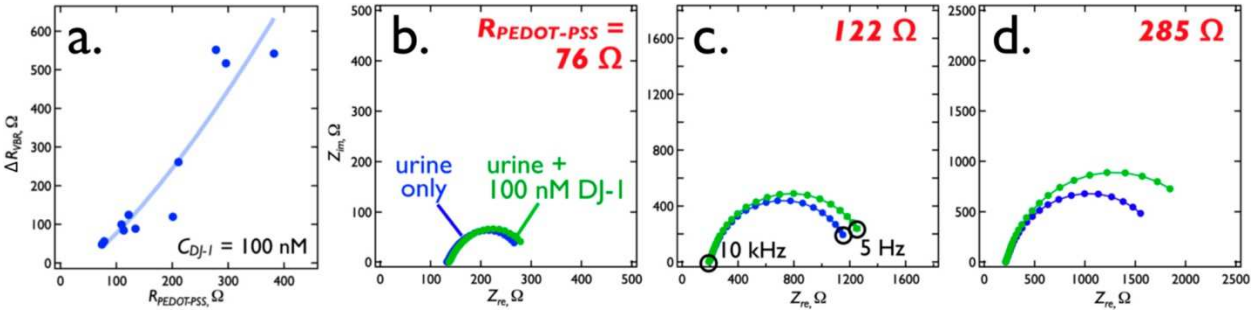


**Figure 6-4. $R_{PEDOT-PSS}$ tuning of the VBR sensitivity for DJ-1. A)** Increasing $R_{PEDOT-PSS}$ from 80 Ω to 300 Ω by reducing the PEDOT–PSS layer thickness increases the signal for 100 nM DJ-1 by a factor of ≈10 from 50 Ω to 550 Ω. **B,C,D)** Three Nyquist plots corresponding to three values of the resistor, $R_{PEDOT-PSS}$, as indicated. In each plot, impedances are plotted in the complex plane from 1 Hz (right) to 40 kHz (left). A shift in the low frequency $Z_{re}$ from synthetic urine only (blue trace) to 100 nM DJ-1 (green trace) approximates the signal, $\Delta R_{VBR}$.

Two calibration plots for HSA in PBS buffer solution acquired using VBRs compare the performance of high resistance PEDOT–PSS layers ($R_{PEDOT-PSS}$= 260–300 Ω) with low resistance PEDOT–PSS layers ($R_{PEDOT-PSS}$ = 80–100 Ω, Figure 6f). The $\Delta R_{VBR}$ signal for HSA increases by between 10× (at low concentrations) to 3× (at high concentrations) across the HSA concentration range encompassed by these data.

$R_{PEDOT-PSS}$ tuning of the VBR sensitivity also works for DJ-1–a bladder cancer marker that is significantly smaller than HSA (20.7 kDa versus 66.5 kDa). Again, a plot of $\Delta R_{VBR}$ versus $R_{PEDOT-PSS}$ for a concentration of DJ-1 of 100 nM in synthetic urine shows that increasing $R_{PEDOT-PSS}$ from 75 Ω to 300 Ω increases $\Delta R_{VBR}$ from 50 Ω to 550 Ω (**Fig. 6-4A**). Nyquist plots for three $R_{PEDOT-PSS}$ values (**Fig. 6-4B-D**) document the increase in sensitivity for three VBRs.

In looking more carefully at the DJ-1 sensing performance of VBRs with high resistance PEDOT–PSS layers ($R_{PEDOT-PSS} \approx 300\ \Omega$), Nyquist plots (**Fig. 6-5A–C**) show the accessible DJ-1 dynamic range extends from a limit-of-detection of 10 pM to 300 nM, a range of more than four orders of magnitude. A plot of $\Delta R_{VBR}$ versus DJ-1 concentration across this same range for a total of 35 VBR sensors (**Fig. 6-5D**) conforms to the Hill equation:[30]

**(Eq. 6-3)**
$$R_{VBR} \approx \Delta R_{VBR,0} + \frac{\Delta R_{VBR,lim} - \Delta R_{VBR,0}}{1 + (\frac{K_D}{[DJ-1]})^h}$$

A best fit of eq 3 to these data yields the following parameter values: $\Delta R_{VBR,lim} = 950 \pm 640\ \Omega$, $\Delta RVBR,0 = 50 \pm 140\ \Omega$, KD = 39 ± 170 nM, h = 0.3 ± 0.2, and R2 = 0.94. It should be noted that these data encompass measurements of DJ-1 in synthetic urine (21 sensors) and in pooled human urine (14 sensors). The measured value of h indicates strong negative cooperativity, meaning that the microscopic dissociation constant, $K_D$, is increased (the affinity interaction is reduced) as the fraction of binding sites occupied by the target protein increases.[30] This has the effect of stretching the binding curve across a wider range of DJ-1 concentration range, exceeding four orders of magnitude in the present case (**Fig. 6-5D**).

In principle, the absence of a gate and an applied gate potential referenced to an external reference electrode leaves open the possibility of potential drift of the channel that could drive doping and de-doping reactions of the PEDOT sensing layers, causing baseline drift of the sensor and degrading reproducibility of the concentration measurements. However, the data show that this "channel conductivity drift" is inconsequential on the time scale of 1–2 min required for carrying out VBR measurements of concentration. To this end, we made measurements of DJ-1 conducted in triplicate (for synthetic urine) and duplicate (for human urine) document the reproducibility of VBRs (**Fig. 6-5E**). Sensor-to-sensor

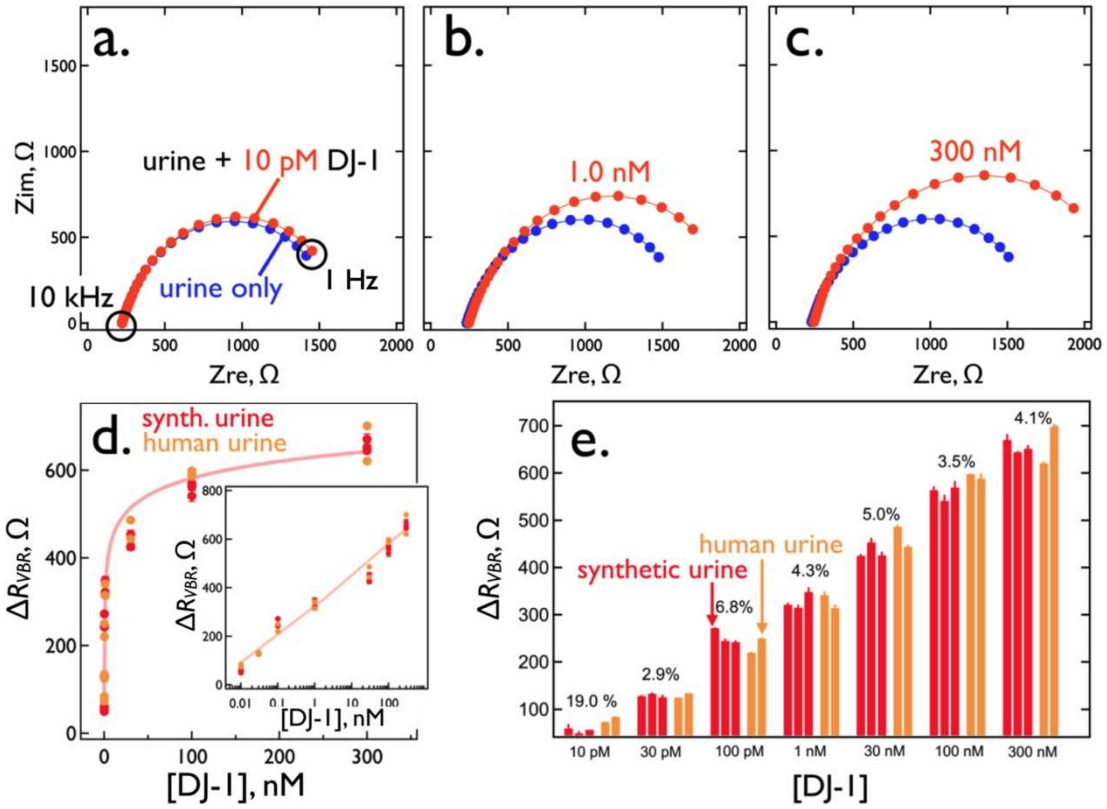


**Figure 6-5. DJ-1 sensing performance using VBRs with $R_{PEDOT-PSS}$= 280 to 300 Ω. A,B,C)** Nyquist plots for three DJ-1 concentrations of **A)** 10 pM, **B)** 1 nM, and **C)** 300 nM. Also shown (blue traces) are background Nyquist responses in synthetic urine only. **D)** Calibration curve for the detection of DJ-1 using the $R_{VBR}$ signal constructed using 21 individual measurements from the same number of *VBR*s, at seven concentrations. Values of $K_D$ and $h$ (the Hill exponent) obtained from a best fit of the experimental data to Eq. 5-2 are indicated. **E)** Bar plot for $\Delta R_{VBR}$ measurements acquired from 21 electrodes, illustrating the sensor-to-sensor reproducibility of these data. CoVs for these data, shown, are in the 2 to 8% range across 4 orders of magnitude in DJ-1 concentration.

coefficients-of-variation (CoV) vary from 2.9% (30 pM), to 4.1% (300 nM), extraordinarily low values. As expected, at the 10 pM LOD, a higher CoV of 19% is obtained. It should be noted that VBRs are effectively single use devices because the off-rate for bound DJ-1 after a single exposure is several hours (data not shown). This means that individual VBRs cannot be calibrated; every VBR sensor must respond to the same calibration curve placing a premium on the sensor-to-sensor reproducibility.

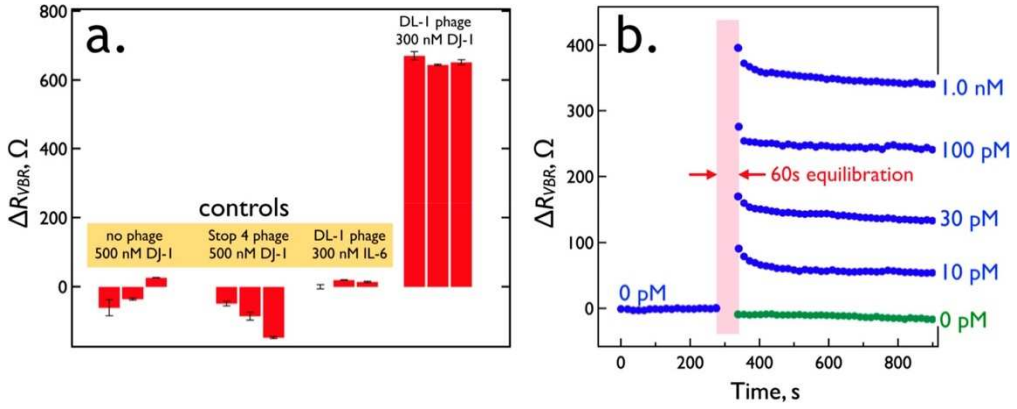


**Figure 6-6. VBR specificity and speed.** **A)** Three control experiments. At left is the response of three *VBR*s prepared with no phage exposed to 500 nM DJ-1. To the right of this is the response of three *VBR*s prepared with Stop-4 phage that has no displayed peptides on its surface. Finally, at right are shown the results of three VBRs containing DL1 phage (selected for the binding to DJ-1) upon exposure to IL-6, a protein of similar MW (20.9 kDa) and pI (6.2) to DJ-1 (20.7 kDa and pI of 6.7, respectively). **B)** Real-time *VBR* sensing data. Responses for five *VBR* sensors are shown for DJ-1 exposures of 0 pM (green trace), 10 pM, 30 pM, 100 pM, and 1.0 nM. These traces were obtained by first stabilizing sensors in synthetic urine for 9 min, measuring a $R_{VBR}$ baseline at 0.10 Hz, and then interrupting for 1.0 min while the synthetic urine was replaced with synthetic urine supplemented with DJ-1 at the specified concentration, after which $\Delta R_{VBR}$ signal was acquired.

Nonspecific adsorption at the unmodified virus-PEDOT surface of a VBR is negligible, contributing to the simplicity of VBR fabrication. Blocking, often accomplished by pre-equilibrating a bioaffinity layer with solutions of bovine serum albumin (BSA), casein,[31–33] or poly (ethylene glycol),[34] prior to exposure to a target protein, is not required. Three sets of negative controls (Figure 9a) for VBRs containing no phage, VBRs prepared using Stop-4 phage (which has no displayed peptides at its surface), and VBRs prepared using DJ-1 binding phage in the presence of interleukin 6 or IL-6 (a protein of similar size, 20.9 kDa, and

pI, 6.2 versus 6.7 for DJ-1) either produce no measurable signal or a small "negative" signal, corresponding to a negative value of $\Delta R_{VBR}$ (**Fig. 6-6A**).

Analysis speed and simplicity of operation are two requirements for biosensors that are used either at the point-of-care (PoC) or outside a care facility, at a point-of-need (PoN).[35,36] The VBR provides for detection of DJ-1 across a range of concentrations within one minute in a dip-and-read modality (**Fig. 6-6B**). Thus, the VBR is well-adapted to PoC and PoN applications.

The frequency-dependent signal-to-noise ratio (S/N) for the VBR (**Fig. 6-7A**) increases with decreasing frequency from 40 kHz to 1.0 Hz. In this measurement, noise is defined as the standard deviation of repetitive measurements (N = 3) for $\Delta R_{VBR}$ (the signal) at a defined concentration of target protein. At a DJ-1 concentration of 300 nM, S/N peaks at 150 at 1.0 Hz and decreases to 60 at 100 pM and 4 at 10 pM, the limit-of-detection. S/N ratios at 40 kHz, in contrast, are in the range from 2 to 14 for this range of DJ-1 concentration. Consistent with the equivalent circuit, increasing frequency reduces the impedance of the virus-PEDOT solution capacitance, $Z_C$, opening a low impedance path through the analyte solution, $R_{soln}$, and bypassing the signal-generating current path of the channel. It should be noted that the S/N versus frequency data sets (**Fig. 6-7A**) are themselves noisy. Repeated measurements of these data show that the sharp peaks and valleys seen in these traces are not reproduced. This means that there are temporal variations in the noise present in the VBR circuit. However, the trend of increasing S/N with decreasing frequency remains prominent in these data.

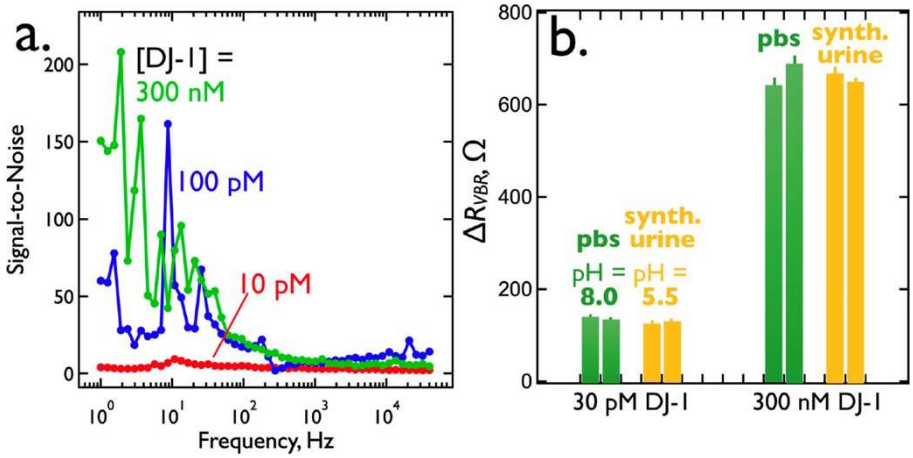


**Figure 6-7. Signal-to-noise (S/N) versus frequency for the detection of DJ-1.** Shown are three plots of *S/N* versus frequency measured for three *VBR*s immersed in three DJ-1-spiked synthetic urine solutions containing DJ-1 at the indicated concentrations. Noise is calculated as the standard deviation of three replicate measurements at each frequency. *S/N* consistently increases from high to low frequencies. **B)** Comparison of $\Delta R_{VBR}$ for the detection of DJ-1 in two electrolytes: synthetic urine (pH = 5.5) and PBS buffer (pH = 8.0). The charge state of DJ-1 (pI = 6.7) inverts across this pH difference, and is negatively charged at pH = 8.0 and positively charged at pH = 5.5. However, $\Delta R_{VBR}$ at two different concentrations are the same, despite changes in pH, within the reproducibility of these measurements.

*Proposed Mechanism for VBR Signal Generation.* The mechanism by which the VBR produces an impedance increase in the presence of target protein is of interest. This mechanism must account for three experimental observations: (1) $\Delta R_{VBR}$ is positive. In particular, the sign of the protein charge, positive or negative, has no influence on the signal. For example, DJ-1 (pI = 6.7) can be measured both at pH = 5.5 and at 8.0, corresponding to a positively charged protein, and a negatively charged protein, respectively (**Fig. 6-7B**). $\Delta R_{VBR}$ signal is unaffected by this charge inversion. (2) VBR signal is insensitive to the salt concentration of the test solution. Previously, we demonstrated this for the detection of 75 nM HSA in salt solutions ranging from 134 mM to 670 mM NaCl where no significant change in HSA signal was observed. Collectively, (1) and (2) imply that a charge gating mechanism, responsible for signal in field-effect transistors,[37] cannot be operating in VBRs. (3) The signal-to-noise ratio is strongly frequency dependent: S/N is high at low frequency (≈ 1 Hz) and near zero at high frequency (≈ 40 kHz) where it is also independent of the concentration

of a target protein. The implication is that the signal generating process does not require the transmission of AC signal through electrolyte. This includes electrolyte that is present in the voids within the porous virus-PEDOT signal-generating layer. Thus, $R_{VBR}$ decreases by just 24 Ω or 4% (against a background of 600 Ω) in protein-free aqueous NaCl as $C_{NaCl}$ is increased by a factor of 50 from 0.02 to 1.00 M.

A simple mechanism that may account for these observations is shown schematically in Figure 5-8. Here, just the virus-PEDOT layer is illustrated. The virus-PEDOT layer itself is semicrystalline, containing crystalline PEDOT-only domains surrounded by disordered domains that contain disordered PEDOT chains and, likely, most of the virus particles (**Fig. 6-8**). Electrical conduction within this layer occurs by two processes: (i) intrachain charge transport (via bipolarons) and (ii) interchain electron hopping (Figure 11a). Interchain hopping, in particular, can be disrupted by the partitioning of protein into this layer, promoted by the immunoaffinity partitioning of target protein by virus particles entrained in the virus-PEDOT film.[38]

This mechanism is analogous to that proposed for chemiresistive gas sensors that exploit a carbon/polymer composite chemiresistor.[39–43] In these systems, permeation of a carbon/polymer (insulating) composite by a molecule in the vapor phase causes an increase in the volume of the composite and a decrease in the volume fraction of the conducting carbon phase, leading to a reduction in the conductivity of the composite, a process that is described by percolation theory:[44,45]

**(Eq. 6-4)** $$\sigma = \sigma_0[V - V_c]^{\alpha}$$

where $\sigma_0$ is the conductivity of the composite in the absence of permeating vapor species, σ is the conductivity of the composite after exposure to this vapor, V is the volume

fraction of the conductive component of the composite, Vc is the volume fraction of the conductive phase at the percolation threshold, and α is a scaling exponent that depends only on the dimensionality of the percolation process (2-dimensional or 3-dimensional). Eq 5-4 is intended to model the conductivity at values of V near the percolation threshold, but more generally, it provides a signal transduction mechanism for chemiresistors in which the resistor is composed of a nonconductive and a conductive component and for which permeation of analyte(s) induces swelling of this system.

The mechanism depicted (**Fig. 6-8**) requires that target protein diffuses into the virus-PEDOT layer. Does this occur on the one-minute time-scale of signal generation, and if so, what mass loading of protein is obtained in this layer during this brief period? These questions can be addressed using quartz crystal microbalance (QCM) gravimetry. In this measurement, a two-layer PEDOT–PSS + virus-PEDOT bioaffinity layer is prepared on a QCM crystal coated with a thin photoresist layer. Exactly the same processes used for VBR fabrication (Figure 12a), involving the PVD deposition of gold electrodes, spin-coating of the PEDOT–PSS layer, and electrodeposition of the virus-PEDOT layer, are used for the preparation of these layers; for these experiments, the gold electrodes are not used to make electrical measurements.

Upon exposure to DJ-1 solutions, the resonant frequency, $f_R$, decreases within seconds and stabilizes within ~40–60 s (Figure 12b). Using the Sauerbrey equation,[46] the observed frequency change, $\Delta f$, can be translated into a mass change, $\Delta m$:

$$\Delta f = -\frac{f_R}{\rho_q d A}\Delta m \qquad \textbf{(Eq. 6-5)}$$

where $f_R$ is the resonant frequency of the quartz crystal oscillator in air, $\rho_q$ is the density of this crystal, $d$ is its thickness, and $A$ is the area of the gold electrodes deposited onto this crystal.

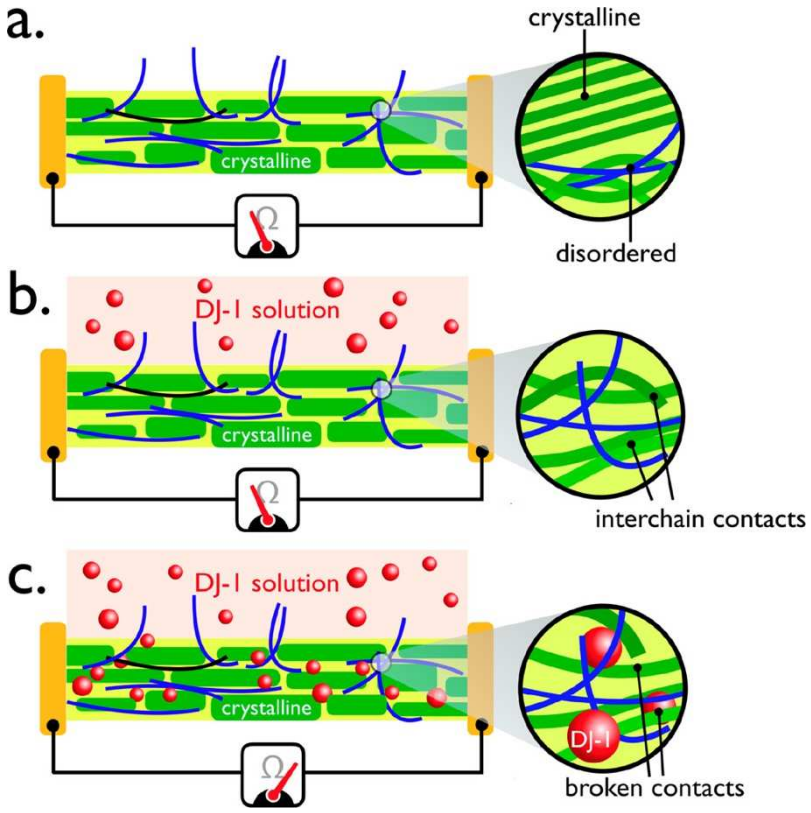


**Figure 6-8. Schematic representation of a hypothesized signal transduction mechanism for the VBR.** **A)** The virus-PEDOT layer shown here consists of semicrystalline PEDOT with virus particles that are concentrated within disordered regions of the PEDOT layer. **B)** When exposed to the DJ-1 protein solution, $\Delta R_{VBR}$ is initially zero, because an induction time is associated with the rate-limiting diffusion of the protein into the virus-PEDOT layer. **C)** Permeation of the virus-PEDOT layer by DJ-1 is associated with an increase in its resistance as the insulating protein interferes with conduction pathways within this layer.

A plot of $\Delta m$ versus DJ-1 concentration shows saturation behavior resembling the VBR calibration plot for DJ-1. The mass loading saturates at ~4 μg/cm$^2$, which corresponds to more than 1.0 monolayer of DJ-1 at the surface of the virus-PEDOT layer, even if this layer has significant roughness. For purposes of comparison, the mass of a hydrated protein monolayer has been measured using QCM for several proteins including RNAase (13.7 kDa, 300 ng/cm$^2$ on silica), bovine serum albumen (66.5 kDa, 150 ng/cm$^2$ on silica),[47] and human serum albumin (66.5 kDa, 230 ng/cm$^2$ on oxidized gold).[48] An estimate of the mass of a

closest packed DJ-1 monolayer can also be derived from the dimensions of this protein previously reported using single crystal X-ray diffraction.[49] The refined crystallographic data include 323 structural water molecules per DJ-1 protein, which should be considered a lower bound to the actual water content of this system. The mass of this monolayer is predicted to be 146 ng/cm$^2$.

The low end (146 ng/cm$^2$) and high end of these estimates (300 ng/cm$^2$) are indicated by dashed lines in Figure 12c. On the basis of these numbers, the ~4 μg/cm$^2$ plateau measured for DJ-1 corresponded to 13–27 equiv protein monolayers. These data are consistent with permeation of DJ-1 into the virus-PEDOT layer, and perhaps the PEDOT–PSS layer as well, on the one-minute time scale as required by the mechanism depicted in Figure 11.

Finally, it is useful to confirm that the diffusion coefficient, $D_{DJ\text{-}1}$, required for DJ-1 permeation by diffusion in one minute is physically realistic. $D_{DJ\text{-}1}$ can be estimated using the equation: $D_{DJ\text{-}1} = T^2/2t$ where $T$ is the total thickness of the two-layer channel (≈ 150–170 nm) and $t$ is the time required for diffusive permeation of DJ-1 (≈ 60 s), which we estimate as the time required for signal generation. The range of calculated $D_{DJ\text{-}1}$ values is (1.9–2.4) × $10^{-12}$ cm$^2$/s, which is approximately 5–6 orders of magnitude slower than the diffusion coefficient for proteins of this size ($D \approx 10^{-7}$–$10^{-6}$ cm$^2$/s)[50] in aqueous electrolyte solutions, qualitatively as expected. Potentially, the estimates of $T$, derived from SEM data (Figure 3), could be too low because these values pertain to dried films. However, doubling the estimate of $T$ (≈ 300–340 nm) produces $D_{DJ\text{-}1}$ values of (7.5–9.6) × $10^{-12}$ cm$^2$/s within an order of magnitude of the dried values.

## 6.4 Conclusions

The VBR is a biosensor that exploits direct electrical communication with virus particles to measure the concentration of protein biomarkers for cancer and disease. These virus particles, which are engineered to recognize and bind a target protein of interest, are entrained within an electrodeposited virus-PEDOT film. The electrical impedance of this film directly produces the signal required for protein quantitation, eliminating the need for any additional amplification. In addition, no reagents such as redox couples are required for these measurements.

Direct QCM measurement of the mass of the bioaffinity bilayer demonstrates that the equivalent of multiple (>10) monolayers of DJ-1 protein is able to diffuse into this layer from solution within one minute, a process that coincides temporally with the generation of the VBR impedance signal. The resulting QCM binding curve for DJ-1 resembles the binding curve measured by the VBR for this protein. On the basis of this observation as well as other evidence, a simple model is proposed for signal transduction involving the dilution of the PEDOT conductor by insulating protein molecules resulting in an increased resistance for this layer, a mechanism analogous to that operating in carbon/polymer chemiresistor gas sensors.

## 6.5 Materials and Methods

Gold electrodes were prepared by photolithography and physical vapor deposition. The following materials and reagents were purchased commercially and used as received: PMMA cells (Wainamics Inc., Fremont CA) and bare gold electrodes were oxygen plasma-cleaned (PDC-32G, Harrick Plasma). PEDOT–PSS (poly(3,4-ethylenedioxythiophene) polystyrenesulfonate) Heraeus Clevios PH1000 from Ossila; lithium perchlorate 99+%

purity from Acros organics; EDOT (3,4-ethylenedioxythiophene) from Sigma-Aldrich; ethylene glycol from Macron Fine Chemicals. Phosphate-buffered saline (PBS, 10× concentrate) from Sigma-Aldrich. 1× concentrate of the PBS yielded a phosphate-buffered saline solution at pH 7.4 with a sodium chloride concentration of 0.154 M and a phosphate buffer concentration of 0.01 M. The DJ-1 overexpression plasmid pET3a-His-DJ1 was a gift from Michael J. Fox Foundation, MJFF (Addgene plasmid #51488). DJ-1 was recombinantly overexpressed in *E. coli*. Interleukin 6 (IL-6) was purchased from Tonbo Bioscences. M13 phage library design and procedures for the selection of DJ-1 binders using this library are described in the Supporting Information, available online.

The affinity of engineered M13 virus particles for DJ-1 can be seen from the results of two enzyme-linked immunosorbent assay (ELISA) measurements (Figure 1). The ELISA measurement was conducted two ways: with DJ-1 adsorbed onto a 96-well plate, measuring the recognition of adsorbed DJ-1 by phage particles in solution (Figure 1a), and by adsorbing the phage particles on the plate and measuring the binding of DJ-1 to this virus layer (Figure 1b). The latter configuration, which yields a much higher apparent dissociation constant, K*d,app,* more closely resembles the operation of the VBR.

A.

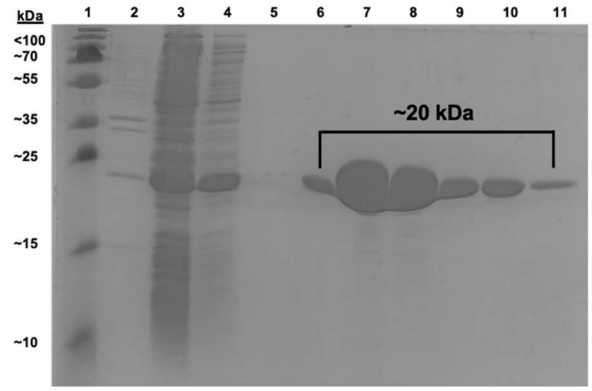


| Lane | Sample |
|---|---|
| 1 | PageRuler Plus Prestained Protein Ladder |
| 2 | *E. coli* cell pellet |
| 3 | Cell lysate |
| 4 | Wash 1 |
| 5 | Wash 2 |
| 6 | Elution 1 |
| 7 | Elution 2 |
| 8 | Elution 3 |
| 9 | Elution 4 |
| 10 | Elution 5 |
| 11 | Elution 6 |

B.

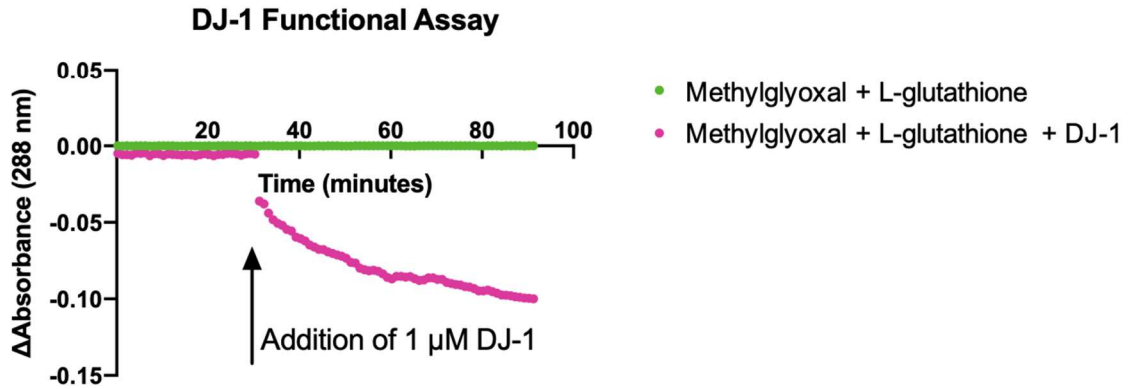


**Figure 6-9. SDS-PAGE analysis of purified DJ-1 after IMAC purification.** **A)** ImageJ analysis of similar gels quantified DJ-1 purity as >99% post-purification. **B)** DJ-1 enzyme activity assay. DJ-1 (1 μM) was added to 7.5 mM methylglyoxal and 7.5 mM L-glutathione. The decrease in absorbance at 268 nm over 90 min compared to the negative control indicates changes in hemithioacetal levels and therefore DJ-1 enzyme activity.

*Expression and Purification of DJ-1.* The plasmid pET3a-His-DJ1 was heat shock-transformed into BL21(DE3) *E. coli* cells and incubated overnight on an agar plate supplemented with carbenicillin (50 μg/mL). A single colony was selected and inoculated into 20 mL of LB media supplemented with carbenicillin (50 μg/mL) before incubation overnight at 37 °C with shaking at 225 rpm. A 5 mL aliquot of the overnight culture was transferred to 500 mL of LB media supplemented with carbenicillin (50 μg/mL) and shaken

at 225 rpm and 37 °C until OD600 reached 0.6. The culture was induced through addition of IPTG (1 mM) and was incubated at 30 °C with shaking at 225 rpm for 4 h.

Following bacterial overexpression, the culture was centrifuged at 6 krpm (4302 x g) for 30 min at 4 °C, and the supernatant was discarded. The resulting pellet was resuspended in 25 mL of lysis buffer (1X TBS, 10 mM 2-mercaptoethanol (BME), 1X Halt protease inhibitor cocktail, pH 7.5) and lysed by sonication. This lysed cell solution was centrifuged at 10 krpm (11952 x g) for 1 h at 4 °C. The protein was purified from the supernatant by immobilized metal affinity chromatography (IMAC) with $Ni^{2+}$-NTA resin (BioRad). The resultant eluted fractions were visualized by 12% acrylamide SDS-PAGE and ImageJ analysis (**Fig. 6-9A**). The appropriate eluted fractions were combined and stored at -20 °C in storage buffer (1X TBS, 10 mM BME, 50% glycerol, pH 7.5). DJ-1 enzyme activity was assayed by hemithioacetal consumption.2 Briefly, methylglyoxal (7.5 mM) and L-glutathione (7.5 mM) were mixed and preincubated for 30 min at room temperature in sodium phosphate (50 mM, pH 7.0) to form hemithioacetals. DJ-1 (1 μM), diluted in sodium phosphate (50 mM, pH 7.0), was then added to the reaction mixture. Changes in hemithioacetal levels were monitored over 90 min as a time-dependent change in the characteristic absorbance at 288 nm (**Fig. 6-9B**).

*Selection of DJ-1 Ligands.* Four rounds of phage-based selections identified four DJ-1 binding phage. In each round, 15 wells of a 96-well Nunc MaxiSorp microtiter plate were coated with DJ-1 (10 μg/mL) in PBS (pH 8.0, 100 μL per well) and incubated overnight at 4 °C with shaking at 150 rpm. This solution was discarded and a blocking solution containing 0.2% (w/v) nonfat milk in PBS (400 μL per well) were added to the wells, and the plate was incubated at room temperature at 150 rpm for 30 min. In sequential rounds, this blocking

step was performed with hen egg white lysozyme, ovalbumin, or a mixture of BSA and HSA to minimize selection of peptide ligands to blocking agents.

After washing three times with wash buffer (0.05% (v/v) TWEEN 20 in PBS, 300 µL per well), mega random peptide libraries (MRPLs) were diluted to a final concentration of 60 nM in binding buffer (0.2% (w/v) BSA, 0.05% (v/v) TWEEN 20 in PBS). The diluted libraries were added to the microtiter plate (100 µL per well) before incubation for 90 min with shaking at 150 rpm at room temperature. Next, the wells were washed to remove non-specific phage ligands. In each round of selections, the number of washes were increased by three to a maximum of 15.

The bound phage were eluted from the plate by adding 0.1 M HCl (100 µL per well) and sonicating the plate in a water bath for 10 min. The eluted phage solution was immediately neutralized by transferring to 1/3 volume of 1 M Tris-HCl (pH 8.0). A portion of the eluted phage solution was used to infect a 20 mL LB culture (supplemented with 5 µg/mL tetracycline) of log phage E. coli XL1 Blue cells. The cells were incubated with shaking at 225 rpm at 37 °C for 1 h. Next, the culture was further infected with M13KO7 helper phage (NEB) to achieve a multiplicity of infection of 4.6. After 45 min of incubation at 37 °C with shaking at 225 rpm, the culture was transferred to 200 mL of 2YT (16 g tryptone, 5 g NaCl, 10 g yeast extract in 1 L autoclaved water) supplemented with 50 µg/mL carbenicillin and 20 µg/mL kanamycin and incubated at 225 rpm at 37 °C for 16-18 h.

The cultures were centrifuged at 10 krpm (15300 x g) for 10 min. The supernatant was decanted into a tube containing 1/5 the final volume of 20% (w/v) PEG-8000 and 2.5 M NaCl. The tube was inverted 5 times and stored on ice for 30 min followed by an additional centrifugation at 10 krpm (15300 x g) for 15 min. The supernatant was decanted, and tubes

were centrifuged for an additional 4 min at 4 krpm (2429 x g). The pellets were resuspended in PBS and the precipitation steps were repeated. Phage concentrations were quantified by measuring absorbance at 268 nm measurements. Finally, the phage were diluted to 60 nM, flash frozen with 10% (w/v) glycerol, and stored at -80 °C.

After four rounds of selections, spot assays were performed on 96 selectants. Briefly, individual phage colonies were amplified in 96 deep well plates as before. After centrifugation at 3 krpm (1462 x g), the supernatants were assayed by phage-based ELISA (see Phage ELISA method) to assess binding to either DJ-1 or the blocking agent, casein. From these screens, four unique potential DJ-1 ligands were isolated and identified by Sanger sequencing. The peptides' specificity for DJ-1 was tested by additional screening for binding to a panel of proteins including BSA, HSA, ovalbumin, lysozyme, and E. coli supernatant. Two of the four potential ligands showed specificity for DJ-1. Ultimately, only one ligand was incorporated into the sensor design due to its significantly stronger apparent binding affinity than the other ligand, as measured by ELISA. This ligand is referred to as DJ-1 ligand one (DL1).

*Site-directed mutagenesis of DL1.* The phage displayed DL1 ligand included an amber stop codon (TAG). In an amber suppressor strain of E. coli such as XL1-Blue, glutamine will be incorporated at a low rate of occurrence.3 To reduce this inherent heterogeneity, Q5 Site-Directed Mutagenesis (NEB) was performed to replace the TAG stop codon with CAG, which encodes for glutamine. Sanger sequencing confirmed the successful introduction of the glutamine codon.

*Phage propagation and Purification.* The phagemid DNA was transformed into SS320 competent E. coli, and transformants were plated on a carbenicillin-supplemented (50

μg/mL) agar plate before incubation at 37 °C overnight. A single colony was selected to inoculate 25 mL of 2YT supplemented with 50 μg/mL carbenicillin and 2.5 μg/mL tetracycline. The culture was shaken at 37 °C until $OD_{600}$ reached 0.5; then, 30 μM IPTG and sufficient M13KO7 to achieve a multiplicity of infection of 4.6 was added. After an additional 45 min incubation, 8 mL of the culture was used to inoculate a 150 mL of 2YT supplemented with 50 μg/mL carbenicillin, 20 μg/mL kanamycin, and 30 μM IPTG. This culture was incubated at 30 °C with shaking at 225 rpm for 18 h.

The phage were precipitated as described above. The resulting phage pellets were resuspended in 1X PBS with 0.05% (v/v) TWEEN 20 and 10% (v/v) glycerol, separated into 1 mL aliquots, flash frozen with liquid nitrogen, and stored at -80 °C. To prepare for devices or ELISAs, the phage solution was thawed on ice, precipitated a second time, and diluted to 40 nM in either 12.5 mM $LiClO_4$ or PBS, respectively.

*Phage ELISA.* To characterize the apparent binding affinity of the selected phage, 5 μg/mL of DJ-1 in 50 mM $Na_2CO_3$ (pH 9.6, 100 μL per well) were added to a 96-well Nunc MaxiSorp microtiter plate. The plate was incubated at 4 °C with shaking at 225 overnight. The following day, the solution was discarded and a blocking solution of 0.2% (w/v) BSA in PBS (400 μL per well) was added to the coated wells. The plate was next incubated at room temperature for 30 min with shaking at 150 rpm. The coated wells were washed three times with wash buffer (300 μL per well), followed by the addition of either DL1 or negative control Stop4 phage serially diluted in binding buffer (100 μL per well). The plate was incubated for 60 min at room temperature and shaking at 150 rpm. Next, the plate was washed three times. Finally, a 1:5000 dilution of HRP/Anti-M13 monoclonal conjugate (GE Healthcare Life Sciences, 100 μL per well) were added, and the plate was incubated at room temperature

with shaking at 150 rpm for 30 min. After five additional washes with wash buffer and one PBS wash, 1-Step Ultra TMB-ELISA Substrate Solution (ThermoScientific, 100 µL per well) were added to each well. After 5 min, 2 M $H_2SO_4$ (100 µL) was added to every well and the absorbance at 450 nm was measured with an Epoch Microplate Spectrophotometer (BioTek). Data were analyzed with GraphPad Prism 8 and fit with a four-parameter logistic curve fit. The apparent dissociation constant (Kd, app) for the interaction between the phage-displayed DL1 and DJ-1 was calculated to be 14 pM (**Fig. 5-10A**).

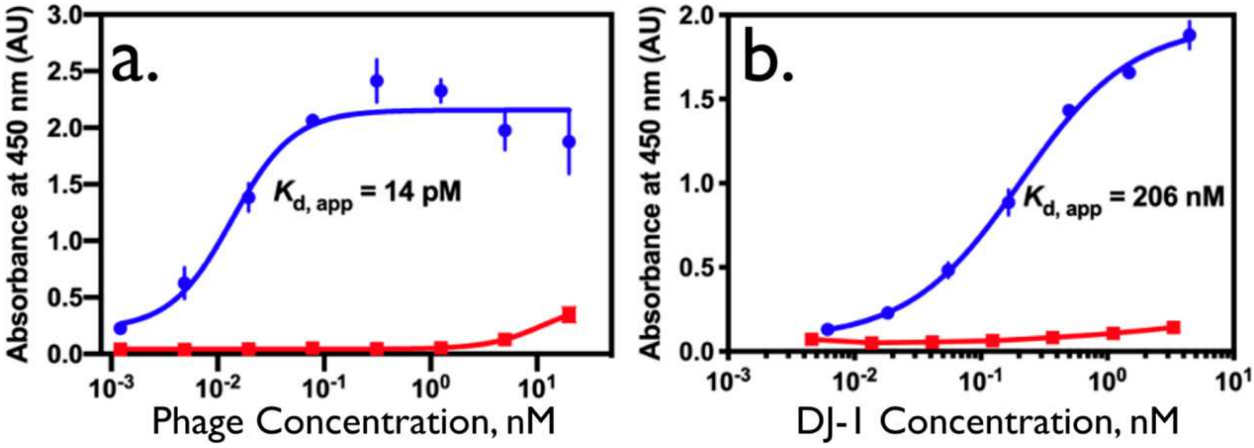


**Figure 6-10. Two ELISAs for M13 phage binding of DJ-1. A)** Phage ELISA of the DJ-1-binding phages DL-1 (blue) and a negative control Stop-4 phage (red). Here, DJ-1 is immobilized, and the DL-1 phage is detected. The data were fit with a four-parameter logistic curve fit ($R^2$ = 0.9230). Measurements were performed in triplicate; error bars represent the standard deviation of the mean. **B)** Sandwich ELISA of DJ-1. In this case, DL-1 phages (or the control Stop4 phage) are immobilized, and the DJ-1 protein is detected. This format mimics the function of the *VBR*. The data were fit as described above ($R^2$ = 0.9944). Measurements were performed in triplicate; error bars represent the standard deviation of the mean.

*DJ-1 Phage-Antibody Sandwich ELISA.* To simulate the DJ-1/DL1 interaction in the VBR format, 1 nM DL1 and Stop4 phages were bound to a 96-well microtiter plate as described above. The plate was treated identically to the indirect phage ELISA until the first binding step; DJ-1 dilutions were prepared and 100 µL of the diluted proteins were added to every well. The plate was incubated for 60 min at room temperature with shaking at 150 rpm. After washing three times, the primary antibody, PARK7/DJ-1 Antibody (LifeSpan

Biosciences, Inc.), was diluted to 1:1000 in binding buffer and 100 μL were added to each well. The plate was incubated again for 60 min at room temperature with shaking at 150 rpm, and washed three times. A secondary antibody, anti-rabbit IgG (Sigma-Aldrich), was diluted to 1:5000 in binding buffer and 100 μL were added to each well. The plate was incubated for 30 min and washed five times with wash buffer and once with PBS. Finally, the HRP activity was detected as described above and the Kd, app was determined to be 206 nM (**Fig. 6-10B**).

*VBR Fabrication.* The fabrication process for the VBRs is similar to that described previously with minor modifications. Briefly, gold-film electrodes were cleaned in an O2 plasma for 10 min immediately before use. Thick (≈ 70 nm) and thin (≈ 48 nm) PEDOT–PSS films were prepared as follows: thick PEDOT–PSS films were obtained by stirring a solution of 3% (v/v) ethylene glycol with PEDOT–PSS for 30 min. Thin PEDOT–PSS films were obtained by stirring a solution of 1.5% (v/v) ethylene glycol in PEDOT–PSS for 30 min. These solutions were spin-coated on the gold electrodes at 2500 rpm for 80 s and then heated for 1 h at 90 °C. A PMMA cell was then attached to the PEDOT–PSS film, and PEDOT–PSS coated gold electrodes were equilibrated in PBS for 30 min. Next, virus-PEDOT films were electropolymerized onto the PEDOT–PSS/gold-film electrodes using a platinum foil counter and MSE reference electrodes. Virus-PEDOT films were then electrodeposited onto the PEDOT–PSS film from aqueous solutions containing 8 nM M13 bacteriophage, 12.5 mM $LiClO_4$, and 2.5 mM EDOT by performing two voltammetric scans from 0.2 to 0.8 V versus MSE at a scan rate of 20 mV/s. A PARSTAT 2263 controlled by Electrochemistry PowerSuit 2.6 software was used for this deposition. All VBRs employed for sensing measurements

conformed to the screening parameters applied at each step of the fabrication process, as described in detail in the SI.

*Impedance Spectroscopy.* All solutions were prepared and equilibrated at room temperature (20 °C) prior to IS measurements. The VBR cell was first rinsed three times with PBS, after which impedance measurements were conducted as follows. Background IS measurement (in triplicate) was acquired in urine (synthetic or human) that contained no added protein, and a second impedance measurement (again in triplicate) was acquired in the same urine containing added DJ-1 or IL-6 at the indicated concentrations. The difference in $Z_{re}$ between these two measurements at each frequency is $\Delta R_{VBR}$. The two $R_{VBR}$ inputs to $\Delta R_{VBR}$ are obtained by fitting an impedance frequency spectrum that spans the range from 1 Hz to 40 kHz. All IS data were acquired using a Princeton Applied Research PARSTAT Model 2263 controlled by Electrochemistry PowerSuit 2.6 software. Fifty data points were acquired across a frequency range of 1 Hz to 40 kHz. The amplitude of the applied voltage was 10 mV for all IS measurements. VBRs are single use devices. A different VBR was therefore used for each measurement. Equivalent circuit fitting was accomplished using EIS Analyzer (ABC Chemistry). Minimization algorithm Powell (300 iterations) was used to generate values for each circuit element.

*Time Scan Experiment.* The time scan experiment was performed on four different VBRs for four concentrations of DJ-1 protein, 10 pM, 30 pM, 100 pM, and 1 nM. Each VBR was first equilibrated in synthetic urine for 9 min. A "pure" urine baseline $R_{VBR}$ was then acquired at $f$ = 0.1 Hz for 1.0 min. The synthetic urine was then removed from the PMMA cell and replaced with synthetic urine supplemented with DJ-1 protein at the specified

concentration, without disconnecting the *VBR* from the potentiostat. After a 1 min exposure to the test solution, $R_{VBR}$ was again recorded for 10 min.

*Control Experiments.* Three negative control experiments tested for signal specificity. In the first, a Stop-4 M13 virus, which has no displayed peptide binding moieties, was substituted for DJ-1-binding phage. The Stop-4 control VBRs were exposed to 500 nM DJ-1. Second, VBRs containing no phage were exposed to 500 nM DJ-1. Interleukin 6 (IL-6, 20.9 kDa, pI = 6.2), similar in size and pI to DJ-1, was used as a third control.

*SEM Analysis.* Scanning electron microscopy data were acquired using a FEI Magellan 400L XHR FE-SEM. An accelerating voltage of 2 keV was used for uncoated films and 10 keV for samples coated with 3 nm of iridium.

## 6.6 References


(1) Di Meo, A.; Bartlett, J.; Cheng, Y.; Pasic, M. D.; Yousef, G. M. Liquid Biopsy: A Step Forward towards Precision Medicine in Urologic Malignancies. *Mol. Cancer* **2017**, *16* (1), 1–14. https://doi.org/10.1186/s12943-017-0644-5.

(2) Kumar, P.; Nandi, S.; Tan, T. Z.; Ler, S. G.; Chia, K. S.; Lim, W.-Y.; Bütow, Z.; Vordos, D.; De laTaille, A.; Al-Haddawi, M.; Raida, M.; Beyer, B.; Ricci, E.; Colombel, M.; Chong, T. W.; Chiong, E.; Soo, R.; Park, M. K.; Ha, H. K.; Gunaratne, J.; Thiery, J. P. Highly Sensitive and Specific Novel Biomarkers for the Diagnosis of Transitional Bladder Carcinoma Prashant. *Oncotarget* **2015**, *6* (15), 13539–13549. https://doi.org/3.

(3) Soukup, V.; Capoun, O.; Pesl, M.; Vavrova, L.; Sobotka, K.; Levova, K.; Hanus, T.; Zima, T.; Kalousova, M. Title: The Significance of Calprotectin, CD147, APOA4 and DJ-1 in Non-Invasive Detection of Urinary Bladder Carcinoma. *Neoplasma* **2019**, *66* (6), 1019–1023.

(4) Bhasin, A.; Ogata, A. F.; Briggs, J. S.; Tam, P. Y.; Tan, M. X.; Weiss, G. A.; Penner, R. M. The Virus Bioresistor: Wiring Virus Particles for the Direct, Label-Free Detection of Target Proteins. *Nano Lett.* **2018**, *18* (6), 3623–3629. https://doi.org/10.1021/acs.nanolett.8b00723.

(5) Ku, J. Y.; Lee, C. H.; Lee, K.; Kim, K. H.; Baek, S. R.; Park, J. H.; Lee, J. Z.; Park, H. J.; Han, S. H.; Jeong, I. Y.; Kwon, M. J.; Ha, H. K.; Jean, P. T. Highly Sensitive and Specific Novel Biomarkers for the Diagnosis of Transitional Bladder Carcinoma. *Eur. Urol. Suppl.* **2017**, *16* (3), e1450–e1453. https://doi.org/10.1016/s1569-9056(17)30884-9.

(6) D'Costa, J. J.; Goldsmith, J. C.; Wilson, J. S.; Bryan, R. T.; Ward, D. G. A Systematic Review of the Diagnostic and Prognostic Value of Urinary Protein Biomarkers in Urothelial Bladder Cancer. *Bl. Cancer* **2016**, *2* (3), 301–317. https://doi.org/10.3233/BLC-160054.

(7) Yang, L. M. C.; Tam, P. Y.; Murray, B. J.; McIntire, T. M.; Overstreet, C. M.; Weiss, G. A.; Penner, R. M. Virus Electrodes for Universal Biodetection. *Anal. Chem.* **2006**, *78* (10), 3265–3270. https://doi.org/10.1021/ac052287u.

(8) Yang, L. M. C.; Diaz, J. E.; McIntire, T. M.; Weiss, G. A.; Penner, R. M. Covalent Virus Layer for Mass-Based Biosensing. *Anal. Chem.* **2008**, *80* (4), 933–943. https://doi.org/10.1021/ac071470f.

(9) Donavan, K. C.; Arter, J. A.; Pilolli, R.; Cio, N.; Weiss, G. A.; Penner, R. M.; Chimica, D.; Aldo, B. Virus - Poly(3,4-Ethylenedioxythiophene) Composite Films for Impedance-Based Biosensing. *Anal. Chem.* **2011**, *83*, 2420–2424.

(10) Arter, J. A.; Diaz, J. E.; Donavan, K. C.; Yuan, T.; Penner, R. M.; Weiss, G. A. Virus-Polymer Hybrid Nanowires Tailored to Detect Prostate-Specific Membrane Antigen. *Anal. Chem.* **2012**, *84* (6), 2776–2783. https://doi.org/10.1021/ac203143y.

(11) Mohan, K.; Donavan, K. C.; Arter, J. A.; Penner, R. M.; Weiss, G. A. Sub-Nanomolar Detection of Prostate-Specific Membrane Antigen in Synthetic Urine by Synergistic, Dual-Ligand Phage. *J. Am. Chem. Soc.* **2013**, *135* (20), 7761–7767. https://doi.org/10.1021/ja4028082.

(12) Ogata, A. F.; Edgar, J. M.; Majumdar, S.; Briggs, J. S.; Patterson, S. V.; Tan, M. X.; Kudlacek, S. T.; Schneider, C. A.; Weiss, G. A.; Penner, R. M. Virus-Enabled Biosensor for Human Serum Albumin. *Anal. Chem.* **2017**, *89* (2), 1373–1381. https://doi.org/10.1021/acs.analchem.6b04840.

(13) Seki, Y.; Takahashi, M.; Takashiri, M. Effects of Different Electrolytes and Film Thicknesses on Structural and Thermoelectric Properties of Electropolymerized Poly(3,4-Ethylenedioxythiophene) Films. *RSC Adv.* **2019**, *9* (28), 15957–15965. https://doi.org/10.1039/c9ra02310k.

(14) Purdy, K. R.; Fraden, S. Isotropic-Cholesteric Phase Transition of Filamentous Virus Suspensions as a Function of Rod Length and Charge. *Phys. Rev. E - Stat. Physics, Plasmas, Fluids, Relat. Interdiscip. Top.* **2004**, *70* (6), 8. https://doi.org/10.1103/PhysRevE.70.061703.

(15) Donavan, K. C.; Arter, J. A.; Weiss, G. A.; Penner, R. M. Virus-Poly(3,4-Ethylenedioxythiophene) Biocomposite Films. *Langmuir* **2012**, *28* (34), 12581–12587. https://doi.org/10.1021/la302473j.

(16) Kim, D. J.; Lee, N. E.; Park, J. S.; Park, I. J.; Kim, J. G.; Cho, H. J. Organic Electrochemical Transistor Based Immunosensor for Prostate Specific Antigen (PSA) Detection Using Gold Nanoparticles for Signal Amplification. *Biosens. Bioelectron.* **2010**, *25* (11), 2477–2482. https://doi.org/10.1016/j.bios.2010.04.013.

(17) Picca, R. A.; Manoli, K.; Macchia, E.; Sarcina, L.; Di Franco, C.; Cioffi, N.; Blasi, D.; Österbacka, R.; Torricelli, F.; Scamarcio, G.; Torsi, L. Ultimately Sensitive Organic Bioelectronic Transistor Sensors by Materials and Device Structure Design. *Adv. Funct. Mater.* **2020**, *30* (20), 1–23. https://doi.org/10.1002/adfm.201904513.

(18) Gentili, D.; D'Angelo, P.; Militano, F.; Mazzei, R.; Poerio, T.; Brucale, M.; Tarabella, G.; Bonetti, S.; Marasso, S. L.; Cocuzza, M.; Giorno, L.; Iannotta, S.; Cavallini, M. Integration of Organic Electrochemical Transistors and Immuno-Affinity Membranes for Label-Free Detection of Interleukin-6 in the Physiological Concentration Range through Antibody-Antigen Recognition. *J. Mater. Chem. B* **2018**, *6* (33), 5400–5406. https://doi.org/10.1039/c8tb01697f.

(19) Gualandi, I.; Tessarolo, M.; Mariani, F.; Cramer, T.; Tonelli, D.; Scavetta, E.; Fraboni, B. Nanoparticle Gated Semiconducting Polymer for a New Generation of Electrochemical Sensors. *Sensors Actuators, B Chem.* **2018**, *273* (March), 834–841. https://doi.org/10.1016/j.snb.2018.06.109.

(20) Kim, Y.; Lim, T.; Kim, C. H.; Yeo, C. S.; Seo, K.; Kim, S. M.; Kim, J.; Park, S. Y.; Ju, S.; Yoon, M. H. Organic Electrochemical Transistor-Based Channel Dimension-Independent Single-Strand Wearable Sweat Sensors. *NPG Asia Mater.* **2018**, *10* (11), 1086–1095. https://doi.org/10.1038/s41427-018-0097-3.

(21) Macchia, E.; Romele, P.; Manoli, K.; Ghittorelli, M.; Magliulo, M.; Kovács-Vajna, Z. M.; Torricelli, F.; Torsi, L. Ultra-Sensitive Protein Detection with Organic Electrochemical Transistors Printed on Plastic Substrates. *Flex. Print. Electron.* **2018**, *3* (3). https://doi.org/10.1088/2058-8585/aad0cb.

(22) Fu, Y.; Wang, N.; Yang, A.; Law, H. K. wai; Li, L.; Yan, F. Highly Sensitive Detection of Protein Biomarkers with Organic Electrochemical Transistors. *Adv. Mater.* **2017**, *29* (41), 1–7. https://doi.org/10.1002/adma.201703787.

(23) Gualandi, I.; Tonelli, D.; Mariani, F.; Scavetta, E.; Marzocchi, M.; Fraboni, B. Selective Detection of Dopamine with an All PEDOT:PSS Organic Electrochemical Transistor. *Sci. Rep.* **2016**, *6* (October), 1–10. https://doi.org/10.1038/srep35419.

(24) Zhang, F.; Johansson, M.; Andersson, M. R.; Hummelen, J. C.; Inganäs, O. Polymer Photovoltaic Cells with Conducting Polymer Anodes. *Adv. Mater.* **2002**, *14* (9), 662–665. https://doi.org/10.1002/1521-4095(20020503)14:9<662::AID-ADMA662>3.0.CO;2-N.

(25) Pasha, A.; Khasim, S.; Al-Hartomy, O. A.; Lakshmi, M.; Manjunatha, K. G. Highly Sensitive Ethylene Glycol-Doped PEDOT-PSS Organic Thin Films for LPG Sensing. *RSC Adv.* **2018**, *8* (32), 18074–18083. https://doi.org/10.1039/c8ra01061g.

(26) Thomas, J. P.; Zhao, L.; McGillivray, D.; Leung, K. T. High-Efficiency Hybrid Solar Cells by Nanostructural Modification in PEDOT:PSS with Co-Solvent Addition. *J. Mater. Chem. A* **2014**, *2* (7), 2383–2389. https://doi.org/10.1039/c3ta14590e.

(27) Ouyang, J.; Xu, Q.; Chu, C. W.; Yang, Y.; Li, G.; Shinar, J. On the Mechanism of Conductivity Enhancement

in Poly(3,4- Ethylenedioxythiophene):Poly(Styrene Sulfonate) Film through Solvent Treatment. *Polymer (Guildf).* **2004**, *45* (25), 8443–8450. https://doi.org/10.1016/j.polymer.2004.10.001.
(28) Poverenov, E.; Li, M.; Bitler, A.; Bendikov, M. Major Effect of Electropolymerization Solvent on Morphology and Electrochromic Properties of PEDOT Films. *Chem. Mater.* **2010**, *22* (13), 4019–4025. https://doi.org/10.1021/cm100561d.
(29) Włodarczyk, K.; Karczewski, J.; Jasiński, P. Influence of Electropolymerization Conditions on the Morphological and Electrical Properties of PEDOT Film. *Electrochim. Acta* **2015**, *176*, 156–161. https://doi.org/10.1016/j.electacta.2015.07.006.
(30) Kurganov, B. I.; Lobanov, A. V.; Borisov, I. A.; Reshetilov, A. N. Criterion for Hill Equation Validity for Description of Biosensor Calibration Curves. *Anal. Chim. Acta* **2001**, *427* (1), 11–19. https://doi.org/10.1016/S0003-2670(00)01167-3.
(31) Islam, F.; Haque, M. H.; Yadav, S.; Islam, M. N.; Gopalan, V.; Nguyen, N. T.; Lam, A. K.; Shiddiky, M. J. A. An Electrochemical Method for Sensitive and Rapid Detection of FAM134B Protein in Colon Cancer Samples. *Sci. Rep.* **2017**, *7* (1), 1–9. https://doi.org/10.1038/s41598-017-00206-8.
(32) Frey, B. L.; Jordan, C. E.; Corn, R. M.; Komguth, S. Control of the Specific Adsorption of Proteins onto Gold Surfaces with Poly(L-Lysine) Monolayers. *Anal. Chem.* **1995**, *67* (24), 4452–4457. https://doi.org/10.1021/ac00120a003.
(33) Pasinszki, T.; Krebsz, M.; Tung, T. T.; Losic, D. Carbon Nanomaterial Based Biosensors for Non-Invasive Detection of Cancer and Disease Biomarkers for Clinical Diagnosis. *Sensors (Switzerland)* **2017**, *17* (8), 1–32. https://doi.org/10.3390/s17081919.
(34) Ortiz-Aguayo, D.; del Valle, M. Label-Free Aptasensor for Lysozyme Detection Using Electrochemical Impedance Spectroscopy. *Sensors (Switzerland)* **2018**, *18* (2). https://doi.org/10.3390/s18020354.
(35) Roda, A.; Michelini, E.; Zangheri, M.; Di Fusco, M.; Calabria, D.; Simoni, P. Smartphone-Based Biosensors: A Critical Review and Perspectives. *TrAC - Trends Anal. Chem.* **2016**, *79*, 317–325. https://doi.org/10.1016/j.trac.2015.10.019.
(36) Brás, E. J. S.; Fortes, A. M.; Chu, V.; Fernandes, P.; Conde, J. P. Microfluidic Device for the Point of Need Detection of a Pathogen Infection Biomarker in Grapes. *Analyst* **2019**, *144* (16), 4871–4879. https://doi.org/10.1039/c9an01002e.
(37) Kaisti, M. Detection Principles of Biological and Chemical FET Sensors. *Biosens. Bioelectron.* **2017**, *98* (July), 437–448. https://doi.org/10.1016/j.bios.2017.07.010.
(38) Karr, L. J.; Shafer, S. G.; Harris, J. M.; Van Alstine, J. M.; Snyder, R. S. Immuno-Affinity Partition of Cells in Aqeuous Polymer Two-Phase Systems. *J. Chromatogr.* **1986**, *354*, 269–282.
(39) Field, C. R.; Yeom, J.; Salehi-Khojin, A.; Masel, R. I. Robust Fabrication of Selective and Reversible Polymer Coated Carbon Nanotube-Based Gas Sensors. *Sensors Actuators, B Chem.* **2010**, *148* (1), 315–322. https://doi.org/10.1016/j.snb.2010.05.026.
(40) Alizadeh, T.; Rezaloo, F. A New Chemiresistor Sensor Based on a Blend of Carbon Nanotube, Nano-Sized Molecularly Imprinted Polymer and Poly Methyl Methacrylate for the Selective and Sensitive Determination of Ethanol Vapor. *Sensors Actuators, B Chem.* **2013**, *176*, 28–37. https://doi.org/10.1016/j.snb.2012.08.049.
(41) Llobet, E. Gas Sensors Using Carbon Nanomaterials: A Review. *Sensors Actuators, B Chem.* **2013**, *179*, 32–45. https://doi.org/10.1016/j.snb.2012.11.014.
(42) Hangarter, C. M.; Chartuprayoon, N.; Hernández, S. C.; Choa, Y.; Myung, N. V. Hybridized Conducting Polymer Chemiresistive Nano-Sensors. *Nano Today* **2013**, *8* (1), 39–55. https://doi.org/10.1016/j.nantod.2012.12.005.
(43) Doleman, B. J.; Sanner, R. D.; Severin, E. J.; Grubbs, R. H.; Lewis, N. S. Use of Compatible Polymer Blends To Fabricate Arrays of Carbon Black-Polymer Composite Vapor Detectors. *Anal. Chem.* **1998**, *70*, 2560–2564.
(44) Lux, F. Models Proposed to Explain the Electrical Conductivity of Mixtures Made of Conductive and Insulating Materials. *J. Mater. Sci.* **1993**, *28* (2), 285–301. https://doi.org/10.1007/BF00357799.
(45) McLachlan, D. S.; Blaszkiewicz, M.; Newnham, R. E. Electrical Resistivity of Composites. *J. Am. Ceram. Soc.* **1990**, *73* (8), 2187–2203. https://doi.org/10.1111/j.1151-2916.1990.tb07576.x.
(46) Sauerbrey, G. Verwendung von Schwingquarzen Zur Wägung Dünner Schichten Und Zur Mikrowägung. *Zeitschrift für Phys.* **1959**, *155* (2), 206–222. https://doi.org/10.1007/BF01337937.
(47) Kondo, A.; Murakami, F.; Higashitani, K. Circular Dichroism Studies on Conformational Changes in Protein Molecules upon Adsorption on Ultrafine Polystyrene Particles. *Biotechnol. Bioeng.* **1992**, *40* (8),

889–894. https://doi.org/10.1016/0927-7765(93)80051-Y.
(48) Rodahl, M.; Höök, F.; Fredriksson, C.; Keller, C. A.; Krozer, A.; Brzezinski, P.; Voinova, M.; Kasemo, B. Simultaneous Frequency and Dissipation Factor QCM Measurements of Biomolecular Adsorption and Cell Adhesion. *Faraday Discuss.* **1997**, *107*, 229–246. https://doi.org/10.1039/a703137h.
(49) Honbou, K.; Suzuki, N. N.; Horiuchi, M.; Niki, T.; Taira, T.; Ariga, H.; Inagaki, F. The Crystal Structure of DJ-1, a Protein Related to Male Fertility and Parkinson's Disease. *J. Biol. Chem.* **2003**, *278* (33), 31380–31384. https://doi.org/10.1074/jbc.M305878200.
(50) Walters, R. R.; Graham, J. F.; Moore, R. M.; Anderson, D. J. Protein Diffusion Coefficient Measurements by Laminar Flow Analysis: Method and Applications. *Anal. Biochem.* **1984**, *140* (1), 190–195. https://doi.org/10.1016/0003-2697(84)90152-0.

# CHAPTER 7

## Viruses Masquerading as Antibodies in Biosensors: The Development of the Virus BioResistor

Adapted with permission from *Accounts of Chemical Research.*
DOI: 10.1021/acs.accounts.0c00474

### 7.1 Abstract

The 2018 Nobel Prize in Chemistry recognized in vitro evolution, including the development by George Smith and Gregory Winter of phage display, a technology for engineering the functional capabilities of antibodies into viruses. Such bacteriophages solve inherent problems with antibodies, including their high cost, thermal lability, and propensity to aggregate. While phage display accelerated the discovery of peptide and protein motifs for recognition and binding to proteins in a variety of applications, the development of biosensors using intact phage particles was largely unexplored in the early 2000s. Virus particles, 16.5 MDa in size and assembled from thousands of proteins, could not simply be substituted for antibodies in any existing biosensor architectures.

Incorporating viruses into biosensors required us to answer several questions: What process will allow the incorporation of viruses into a functional bioaffinity layer? How can the binding of a protein disease marker to a virus particle be electrically transduced to produce a signal? Will the variable salt concentration of a bodily fluid interfere with electrical transduction? A completely new biosensor architecture and a new scheme for electrical transduction of the binding of molecules to viruses were required.

This chapter describes the highlights of a research program launched in 2006 that answered these questions. These efforts culminated in 2018 in the invention of a biosensor specifically designed to interface with virus particles: The Virus BioResistor (VBR). The VBR is a resistor consisting of a conductive polymer matrix in which M13 virus particles are entrained. The electrical impedance of this resistor, measured across 4 orders of magnitude in frequency, simultaneously measures the concentration of a target protein and the ionic conductivity of the medium in which the resistor is immersed. Large signal amplitudes coupled with the inherent simplicity of the VBR sensor design result in high signal-to-noise ratio (S/N > 100) and excellent sensor-to-sensor reproducibility. Using this new device, we have measured the urinary bladder cancer biomarker nucleic acid deglycase (DJ-1) in urine samples. This optimized VBR is characterized by extremely low sensor-to-sensor coefficients of variation in the range of 3–7% across the DJ-1 binding curve down to a limit of quantitation of 30 pM, encompassing 4 orders of magnitude in concentration.

## 7.2 Introduction

In 2020, the most reliable techniques used by doctors for cancer surveillance are identical to practices from 20 years ago: colonoscopy (colon cancer), mammogram (breast cancer), and Pap smear (cervical cancer). Cancer surveillance involving the analysis of blood and urine for cancer markers—so-called liquid biopsies—are not part of an annual physical examination for most Americans because biosensors and laboratory assays that facilitate rapid, reliable, and affordable analyses for cancer markers do not yet exist.

We became interested in this problem in 2005.[1] Up to this time, most biosensors designed to detect the distinctive protein "biomarkers" produced by cancers used antibodies to recognize and bind these proteins. M13, a filamentous bacteriophage that infects Escherichia coli, was engineered to "display" Fv antibody fragments on its surface, providing an intriguing opportunity for the development of cheaper, more robust biosensors. The basic approach for the "display" of proteins on the M13 phage surface was invented by George Smith in 1985.[2,3] Subsequently, Jim Wells and co-workers introduced key and necessary improvements that enabled Greg Winter to display an antibody, or Fv, on the phage surface.[4,5] Our laboratories exploited these seminal contributions to extend phage display into biosensing applications.

M13 viruses are an attractive alternative to antibodies in biosensors for three main reasons: (1) the cost of engineered viruses is much lower; (2) the affinity of virus particles is similar (often with dissociation constants, KD, below 10–9 M); and (3) virus particles are quite robust and do not require refrigeration to maintain potency. In principle, biosensors based upon virus particles could be cheaper to manufacture and cheaper to distribute and store, especially in the resource challenged Third World. In this Account, we trace the

development over 14 years of a new biosensor, the Virus BioResistor (VBR),[6,7] designed specifically for rapid (60 s) point-of-need detection of cancer markers in urine using virus receptors.

### 7.3 Virus Biosensors That Resemble Antibody Biosensors

A generic biosensor has three components: (i) A bioaffinity layer equipped with receptors such as single-stranded DNA probes or antibodies to recognize and bind a target DNA or protein, respectively; (ii) a transducer that detects the binding of the target to the bioaffinity layer by means of a measurement of a property such as the mass of this layer or its optical or electrical response; and (iii) electronics that convert the raw transducer signal into a quantitative measure of the target concentration.

Bioaffinity layers for the detection of proteins have often exploited monolayers of antibodies conjugated to polymer or glass surfaces.[8] The first biosensors to exploit the Nobel Prize-winning phage-display technologies[2–5,8] were demonstrated in 2003 by a team at Auburn University lead by Valery Petrenko and Vitaly Vodyanoy.[9] In that work, M13 virus particles were immobilized by physisorption onto the surface of an acoustic wave sensor and used to measure the binding of β-galactosidase, a 465 kDa protein, at concentrations down to 0.60 nM. These experiments provided the first proof of concept that viruses could function as receptors in biosensors. However, physiosorbed virus layers,[9–11] were unstable in our measurements, compromising precision.

Li-Mei Yang, working with Juan Diaz and Phillip Tam, attempted to remedy the stability problem by preparing monolayers of M13 virus particles that were covalently bonded to a gold electrode surface (**Fig. 7-1**).[12,13] Her approach was first to electrochemically roughen a gold electrode and then to expose it to thioctic N-hydroxysuccinimide (NHS) ester

to form a thiol–Au-bonded self-assembled monolayer (SAM) and treat the SAM with a suspension of virus particles, thereby forming a covalent amide bond between free amines on the phage coat peptide and the activated carboxylate at the surface of the SAM. The final step was to plug any defects in this "covalent virus layer" (CVL) with bovine serum albumin (BSA) to minimize nonspecific adsorption (**Fig. 7-1A**). The CVL is complete after step 3. Steps 4–6 in **Fig. 7-1** illustrate the reversible binding of an antibody (p-Ab) by the CVL.

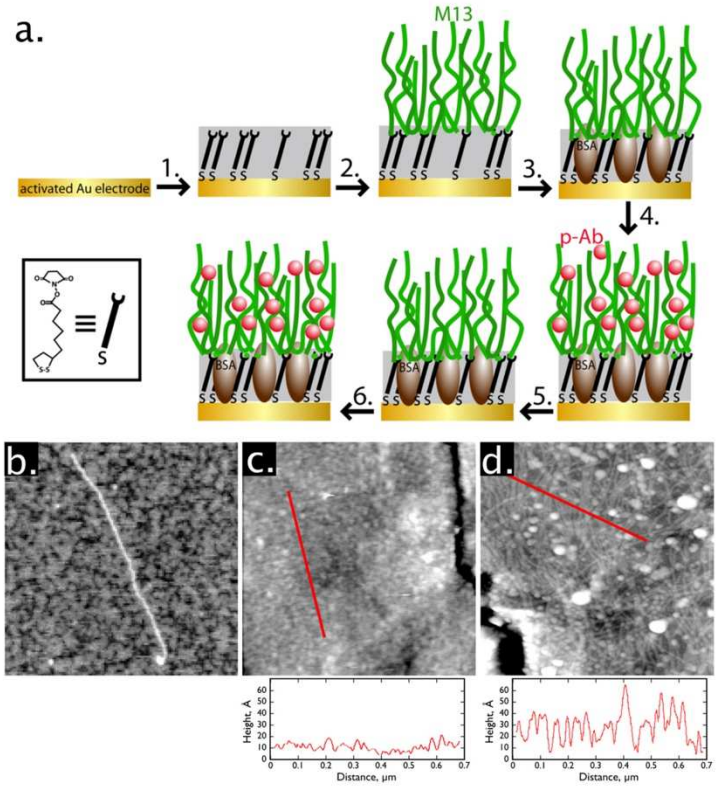


**Figure 7-1. The covalent virus layer (CVL).** **A)** Stepwise assembly (steps 1–3) and functionalization (steps 4–6) of the CVL. **B-D)** Noncontact mode AFM images (1 µm × 1 µm) of (b) a single M13 virion on mica, (c) a self-assembled monolayer (SAM) of N-hydroxysuccinimide thioctic ester (NHSTE) on gold after exposure to BSA with no virus particles attached to the surface, and **D)** a functional CVL consisting of a SAM of NHS-TE on gold that was reacted with M13 to produce covalent attachment and exposed to BSA (step 3 in (a)). Adapted from ref 13. Copyright 2008 American Chemical Society.

Atomic force microscopy (AFM) showed that the CVL consists of a close-packed monolayer of filamentous M13 virus particles (**Fig. 7-1B**). When many M13 virus are covalently bound to a surface, the densely packed "monolayer" of the virus resembles a shag

carpet (**Fig 7-1A**). The resulting CVL retains significant free volume, as evidenced by the fact that each phage particle is capable of binding 140 antibodies to the P8 major coat peptide (P8-Ab, 2700 copies/M13 virus) on average. In the vacuum of a scanning electron microscope, the water and ions supporting the "shag carpet" are removed, and filamentous virus particles collapsed onto the surface can be clearly seen (**Fig. 7-1D**).

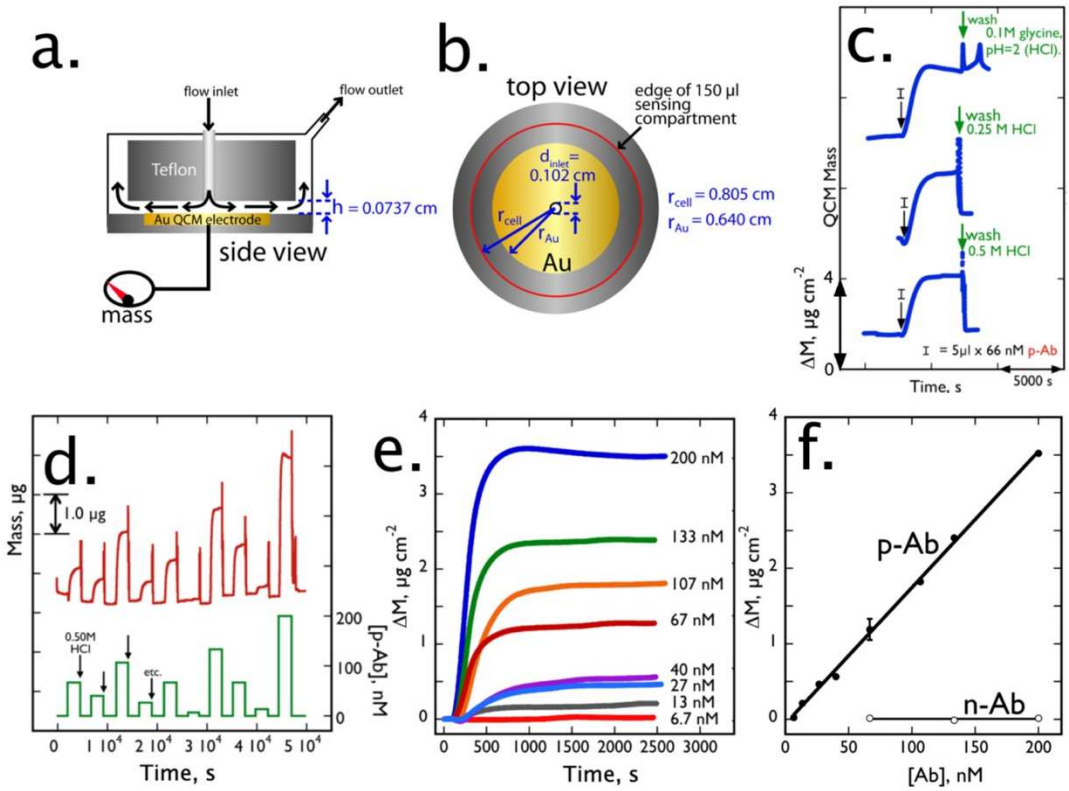


**Figure 7-2. QCM investigations of the CVL. A,B)** Schematic diagram of the QCM and flow cell. **C)** QCM evaluation of the efficacy of three wash solutions as indicated. **D)** Plot of mass vs time for the exposure of a CVL to doses of P8-Ab ranging in concentration from 6.6 to 200 nM. **E)** Same data as shown in **D)** but normalized to the same injection time to precisely show the relative heights of these transients. **F)** Plot of the maximum mass change versus P8-Ab concentration for the data shown in **D,E)**. The mass change was proportional to the concentration of injected P8-Ab ($R^2$ = 0.997) and yielded a sensitivity of 0.018 µg $cm^{-2}$ nM−1 and a limit of detection of 6.6 nM. Adapted from ref 13. Copyright 2008 American Chemical Society.

## 7.4 Mass-Based Signal Transduction of the CVL

The properties of the CVL for biosensing were first explored in 2008. Both mass-based biosensing, conducted by depositing the CVL on a gold quartz-crystal microbalance

(QCM) transducer, and electrochemical-based sensing[12] were evaluated. In these experiments, the response of a CVL-modified gold surface to P8-Ab was studied.

To measure the mass responses of a CVL during exposure to P8-Ab, the QCM crystal was mounted in a Teflon flow cell that provided for the radially symmetric delivery of solution to the circular QCM electrode surface (**Fig. 7-2A,B**). The increase in mass observed upon P8-Ab exposure (~3 μg/cm2) could be reversed by washing briefly with aqueous acid (**Fig. 7-2C**), enabling mass versus P8 antibody concentration, [P8-Ab], data to be acquired over a wide range of [P8-Ab] for a single CVL (**Fig. 7-2D-F**). These data were linear from 6.6 to 200 nM P8-Ab. A nonbinding antibody (n-Ab) control showed negligible nonspecific signal over this concentration range, establishing the limit of detection (LOD) for P8-Ab as 20 nM. This demonstrated that virus particles within the CVL were available for rapid binding of the antibody, suggesting that the CVL could function as a bioaffinity layer within a biosensor. Importantly, P8-Ab binding, while reversible, exhibited a very low off-rate of $<10-5\ s^{-1}$, indicating that reuse of the CVL would be a practical impossibility. The next question was whether the binding of a target antibody could be detected using the electrochemical response of these virus-modified electrodes instead of a QCM.

In addition to mass-based transduction using the QCM, the electrochemical response of the CVL to P8-Ab and n-Ab were investigated using electrochemical impedance spectroscopy (EIS). A goal in these experiments was to carry out direct detection of antibody binding to the CVL. "Direct" in this context meant that a redox couple such as $Fe(CN)_6^{4-/3-}$ was not added to the testing solution as in the "indirect" approach, in which blocking of the Faradaic electron transfer signals protein binding to an electrode surface.[14–19] Direct EIS

measurements, in contrast, probed changes to the non-Faradaic impedance of the CVL-modified gold electrode caused by antibody binding to the surface.

A conclusion of these experiments was that the highest signal-to-noise ratio (S/N ≈ 20) and best selectivity for P8-Ab binding to the CVL-modified electrode occurred at high frequencies in the range of 4–140 kHz. This was surprising because the shift in the real component of the impedance signal, $\Delta Z_{re}$, was the smallest in this frequency range, with $\Delta Z_{re}$ < 10 Ω at all P8-Ab concentrations. Selectivity for P8-Ab versus n-Ab was completely lost at lower frequencies, where $\Delta Z_{re}$ signals as large as 1 kΩ were observed. In contrast, prior work on EIS-detected indirect biosensors had emphasized the detection of target proteins at low frequencies, below 5 Hz in most cases. $Z_{re}$ is increased by binding of P8-Ab to the CVL because the bound, insulating P8-Ab molecules displace ionically conductive electrolyte from the free volume within the CVL layer. The LOD for P8-Ab in these experiments, limited by the low $\Delta Z_{re}$ signal amplitude, was 20 nM.

The conclusion from these experiments was that this CVL did not afford enough sensitivity to enable the detection of proteins at subnanomolar concentrations, as required for cancer screening. A fundamentally new method for preparing a virus-based bioaffinity layer was needed.

### 7.5 Virus-PEDOT Bioaffinity Layers

Inspiration for a new type of virus-based bioaffinity layer arrived from an unexpected direction. In the 2010 time frame, the Penner group had been investigating the thermoelectric properties of nanowires composed of the electronically conductive organic polymer poly(3,4-ethylenedioxythiophene) (PEDOT).[20] These PEDOT nanowires were prepared using lithographically patterned nanowire electrodeposition (LPNE).[21,22]

Could PEDOT act as a host for M13 virus particles? This idea was interesting for two reasons: First, the electronic conductivity of PEDOT provided a means by which the biosensor signal from M13 particles could be directly transmitted to an external circuit. Second, PEDOT is positively charged as synthesized, with one positive charge for each four or five EDOT residues. During electropolymerization (**Fig. 7-3A**), EDOT is oxidized to a cation radical, and radical coupling occurs near the electrode surface until the resulting oligomers lose solubility and, with anions from the solution to balance the positive charge, precipitate onto the electrode. M13 virus particles have a net negative charge near 6000 as a consequence of three ionizable moieties (Glu2, Asp4, and Asp5) on the 2700-copy P8 major coat protein near its exposed N-terminus.[23] Our hypothesis was that the polymerization of positively charged PEDOT in the presence of negatively charged M13 would electrostatically promote the incorporation of M13 particles within the polymer matrix.

To test this hypothesis, virus–PEDOT biocomposite films were prepared by electropolymerization of EDOT in aqueous electrolytes containing just 12 mM $LiClO_4$ and nanomolar concentrations of M13 virus particles.[24] In these experiments, it was observed that as the virus concentration was increased from 3 to 15 nM the EDOT electropolymerization current peak was depressed relative to that of the virus-free control. This observation suggested that the virus particles either interfered with, or participated in, EDOT polymerization. QCM gravimetry (**Fig. 7-3B**) showed that the mass of the resulting films was augmented when virus particles were present in the EDOT polymerization solution. The excess mass relative to pure PEDOT films (**Fig. 7-3C**) was attributed to the incorporation of virus particles into the growing PEDOT film. This observation directly

demonstrated that virus particles could be incorporated into these electrodeposited PEDOT films as predicted by the reaction shown in Fig. 6-3a.

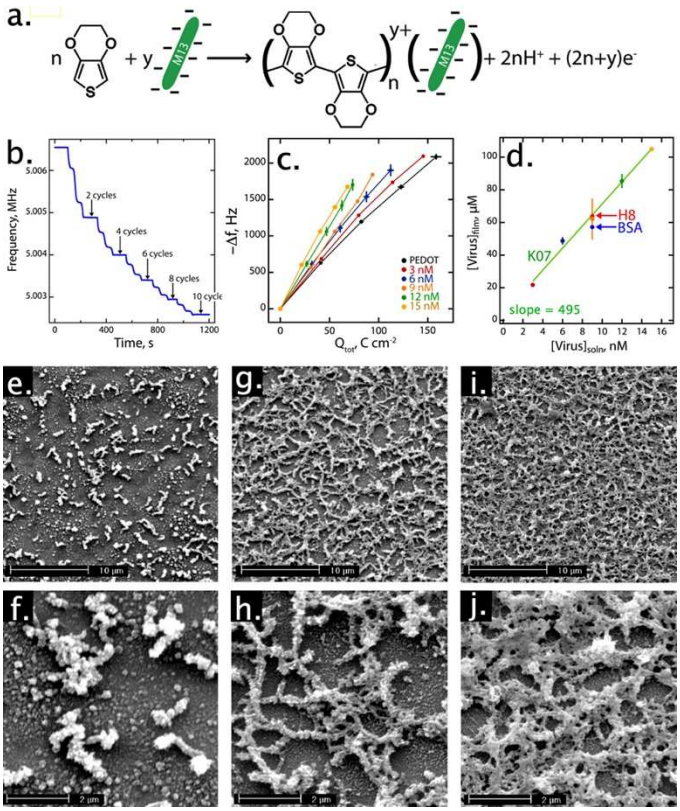


**Figure 7-3. Electrodeposition of a virus–PEDOT bioaffinity layer.** **A)** Virus–PEDOT electrodeposition reaction. **B)** QCM analysis of virus–PEDOT electrodeposition, with increased mass loading shown as a decrease in frequency. **C)** Frequency change vs deposition charge, $Q_{tot}$, for QCM measurements. **D)** Calibration curve showing the linear correlation of the virus concentration within the PEDOT film (vertical axis) vs the concentration of virus in solution. **E-J)** Topography of virus–PEDOT films imaged by scanning electron microscopy. Films were prepared from solutions containing virus particles at three concentrations: (e, f) $[virus]_{soln}$ = 3 nM; (g, h) $[virus]_{soln}$ = 9 nM; (i, j) $[virus]_{soln}$ = 15 nM. Adapted from ref 2. Copyright 2012 American Chemical Society.

How efficient is the virus incorporation into these films during electropolymerization? The QCM data in Fig. 6-3C provided the answer: The difference in mass (the vertical axis) at a particular deposition charge $Q_{tot}$ could be attributed to virus incorporated into the virus–PEDOT composite film. This analysis showed that concentration of M13 in the virus–PEDOT film prepared by electrodeposition was directly proportional to the M13 concentration in the polymerization solution (**Fig. 7-3D**), and the slope of this line

was an astonishing ~500. These experiments demonstrated that the reaction shown in Figure 3a provided for highly efficient incorporation of virus into a growing PEDOT film. Scanning electron microscopy (SEM) images of electrodeposited virus–PEDOT composite films showed a striking transformation as virus was incorporated into the plating solution (**Fig. 7-3E-J**). In these images, bundles of virus particles are seen protruding from the surface of the virus–PEDOT films, and as expected, the density of these virus particles is correlated with the concentration of virus in the deposition solution.

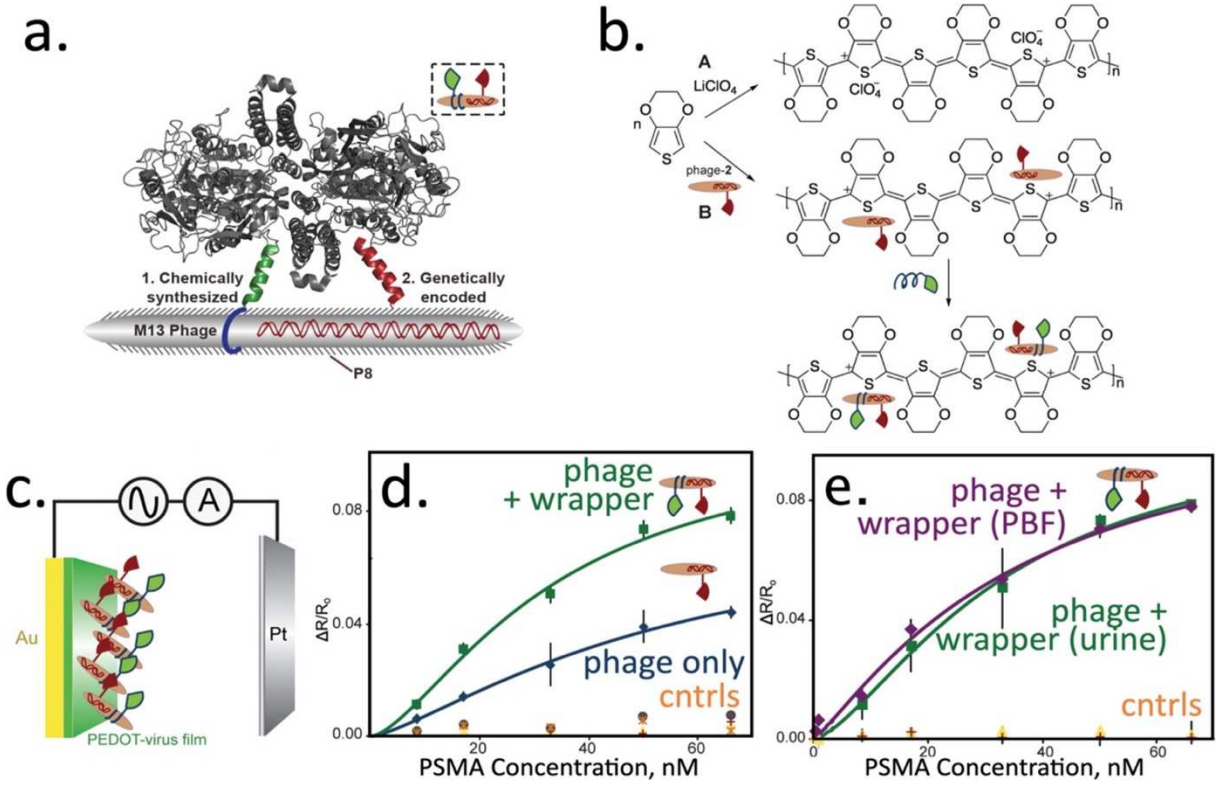


**Figure 7-4. PSMA detection in synthetic urine.** **A)** Schematic diagram of bidentate binding to PSMA by KCS-1 (green) and genetically encoded peptide (red). Simultaneous binding by these two ligands provides a higher apparent affinity for PSMA. **B)** Polymerization reactions of EDOT in the presence of (top) LiClO4 or (center) PSMA-binding phage and (bottom) PSMA-binding phage and exposure to the wrapper KCS-1 (green). **C)** Schematic diagram of the biosensing experiment. **D)** ΔR/R0 of the film increases with the PSMA concentration. **E)** Comparison of PSMA detection in synthetic urine (green) with detection in PBS buffer (purple). Adapted from ref 31. Copyright 2013 American Chemical Society.

What would be the best way to exploit this new virus–PEDOT material in a biosensor? Our initial answer to this question was to prepare arrays of nanowires composed of virus–PEDOT.[25,26] These were prepared using LPNE[21,22,27] in conjunction with the same

electrodeposition protocol employed for virus–PEDOT films described above. The resulting virus–PEDOT nanowires, deposited onto glass surfaces, were linear, millimeters in length, ~300 nm in width, and 60 nm in height. SEM, AFM, and fluorescence microscopy confirmed the incorporation of M13 into the conducting PEDOT nanowire arrays, and further fluorescence studies also demonstrated that the viruses remained intact and fully functional for binding to analytes.

Biosensing experiments were conducted by measuring the DC resistance of a virus–PEDOT nanowire array, rather than the frequency-dependent impedance of these arrays as in previous studies, and P8-Ab and the n-Ab control were compared. A P8-Ab concentration-dependent increase in resistance was observed, culminating in a 40% increase in response to exposure to 99 nM buffered P8-Ab solutions. An LOD for P8-Ab of 20 nM was established for these nanowire arrays. n-Ab showed no measurable signal.

Arrays of virus–PEDOT nanowires were also employed for the detection of prostate-specific membrane antigen (PSMA), a promising urine-borne cancer marker for prostate cancer.[28,29] PSMA is a 750 residue, 100 kDa glycoprotein that is overexpressed as a homodimer on the surface of prostate cancer cells. These studies exploited virus particles engineered to display the PSMA-binding epitope PSMA-3 (amino acid sequence SECVEVFQNSCDW). In spite of this change to the virus, the virus–PEDOT electrodeposition was unaffected because this process was completely modular with respect to the phage incorporation. In spite of the smaller size of PSMA relative to antibodies (100 vs 155 kDa), similar detection metrics were achieved in this study, which culminated in a PSMA LOD of 66 nM in high-salt (~160 mM) PBS buffer solutions and a linear response up to 150 nM PSMA.

The disappointing conclusion of these two studies was that arrays of virus–PEDOT nanowires performed approximately as well as the EIS-transduced CVL-modified gold electrodes. A more direct comparison of virus–PEDOT with the CVL was needed in experiments that exploited conventional electrodes and EIS, and this was our next step.

Compared with virus–PEDOT nanowires, a simpler approach was to coat a virus–PEDOT film onto a gold electrode. The response of such electrodes was studied using EIS for the detection of PSMA[30,31] and, separately, P8-Ab.[32] P8-Ab detection at virus–PEDOT electrodes showed a much higher S/N, ranging from 17 to 30, at high frequencies in the 100 Hz–10 kHz range. At 1 kHz, a LOD for P8-Ab of 6 nM was achieved, and quantitation of P8-Ab up to 65 nM was possible. This represented a 65% reduction in LOD for P8-Ab compared with the identical experiment conducted using CVL-modified gold electrodes.

An even better result was obtained for the detection of PSMA using a new paradigm: synergistic dual ligand phage. The hypothesis tested in that work was that two peptide binders would be better than one. In other words, the sensitivity to PSMA could be improved by incorporating a second peptide binder for PSMA (called KCS-1) onto an engineered phage (phage-2) that already displayed a peptide binder for the protein (**Fig. 7-4A**). This was accomplished by conjugating a positively charged oligolysine tether to the polypeptide and then permitting it to self-assemble by electrostatic attraction onto the negatively charged phage after electrodeposition of the virus–PEDOT bioaffinity layer **(Fig. 7-4B)**. The addition of the second ligand, KCS-1, significantly increased the affinity of the virus for PSMA in ELISA measurements (data not shown) and for electrochemical measurements **(Fig. 7-4D)**. This enhanced sensitivity afforded a PSMA LOD of 100 pM in buffer and in synthetic urine solutions **(Fig. 7-4E)** for these dual ligand systems.

## 7.6 The Virus BioResistor

All of the virus-based biosensors investigated in our laboratories up to 2015 were laboratory experiments in the sense that the electrochemical measurements were conducted using three-electrode cells incorporating separate reference, counter, and working (sensor) electrodes.[33] A portable, miniaturizable, and commercializable electrochemical sensor architecture—in which the necessary electrodes were incorporated into a single monolithic sensor body—had not been demonstrated.

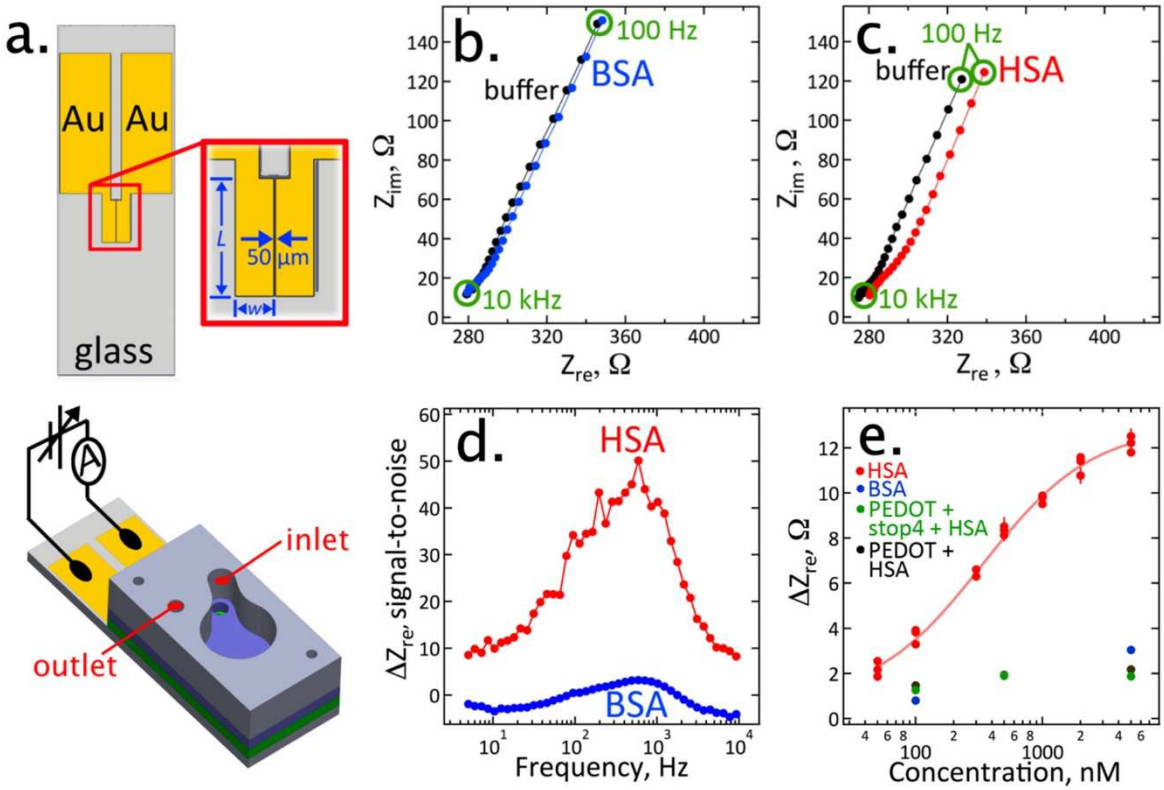


**Figure 7-5. Two-sided biosensor: a monolithic biosensor for HSA** **A)** Engineering diagram of the two-electrode virus– PEDOT biosensor. **B,C)** Nyquist plots ($Z_{im}$ vs $Z_{re}$) for a control protein (BSA) and HSA. **D)** Signal-to-noise ratio vs frequency plot for HSA and BSA. **E)** $\Delta R_{re}$ vs HSA concentration calibration curve. Controls for BSA and off-virus binding are also shown. Adapted from ref 34. Copyright 2016 American Chemical Society.

This advance occurred in 2016 with the demonstration by Alana Ogata, Ming Tan, and others that two virus–PEDOT-modified gold electrodes without reference or counter electrodes (**Fig. 7-5A**) could function as a biosensor for human serum albumin (HSA).[34] Prior

work on PSMA had demonstrated that the signal generated by a virus–PEDOT-modified gold electrode was concentrated in the resistive component of the impedance, $Z_{re}$, instead of the capacitive component, $Z_{im}$. The hypothesis explored in the 2017 "two-sided" sensor architecture (**Fig. 7-5B**) was that arranging two virus–PEDOT bioaffinity layers electrically in series would double the impedance signal produced by the biosensor.

In spite of its simplicity, the two-sided virus–PEDOT biosensor reliably distinguished HSA from BSA—proteins of identical size with 76% sequence homology. This demonstrated that the inherent selectivity of the engineered virus could be recovered with this device **(Fig. 7-5b,c)**. At an optimized detection frequency of 340 Hz **(Fig. 7-5d)**, the two-sided sensor produced a prompt increase in $Z_{re}$ within 5 s and a stable $Z_{re}$ signal within 15 min. HSA concentrations in the range from 100 nM to 5 μM were detectable **(Fig. 7-5e)**. These single-use biosensors demonstrated excellent sensor-to-sensor reproducibility characterized by a coefficient of variation of 2–8% across the entire concentration range. Two-sided virus–PEDOT sensors in synthetic urine demonstrated a concentration-dependent response to HSA similar to PBS buffer.

This performance provided reason for optimism, but the two-sided virus–PEDOT biosensor had two serious deficiencies. First, its 100 nM LOD for HSA was insufficient to measure cancer markers in urine at subnanomolar concentrations. The two-sided sensor simply did not produce enough signal—a maximum of signal of 12 Ω against a 100–200 Ω background **(Fig. 7-5e)**. Second, the two-sided biosensor required that current be carried through the test solution between the two electrodes, thus convoluting the resistance change due to binding of the target protein with the resistance of the solution. Since urine and other bodily fluids have highly variable ionic conductivities, this imposed a barrier to the clinical

use of this biosensor. In order to provide reliable results for highly variable single patient samples, a biosensor architecture that decoupled target binding from ionic conduction was required. In spite of these two issues, the two-sided virus–PEDOT biosensor was the progenitor of the VBR.

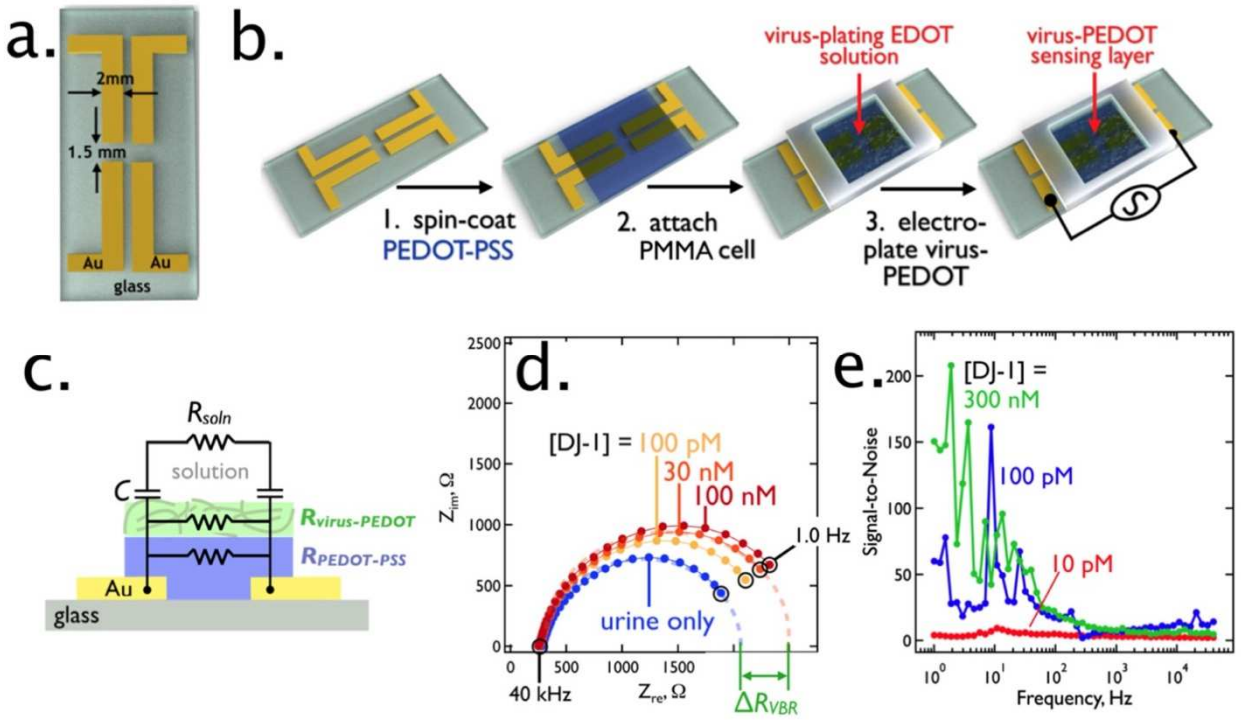


**Figure 7-6. The Virus BioResistor.** **A)** The VBR is constructed on a 10 mm glass chip with patterned gold electrodes. **B)** Three processing steps provide for the deposition of a PEDOT–PSS layer by spin-coating from solution (step 1), the attachment of a PMMA cell (step 2), and the electrodeposition of a virus–PEDOT layer (step 3). **C)** The electrical response of the VBR is modeled by three parallel resistors and a solution/channel capacitance. **D)** This circuit produces a semicircular Nyquist plot for which the high-frequency impedance (40 kHz) approximates the solution resistance (Zre ≈ Rsoln) and the low-frequency impedance is dominated by the parallel resistance imposed by the two film resistors, Zre ≈ ZVBR. ZVBR increases with the concentration of target protein present in the solution phase. **E)** The VBR circuit maximizes the signal-to-noise ratio at low frequencies, and S/N can exceed 100 at high protein concentrations. Adapted from ref 4. Copyright 2020 American Chemical Society.

Alana Ogata and Apurva Bhasin collaborated to invent the VBR in 2017 and, since then, to fully realize its capabilities.[6,7] The extension of the two-sided biosensor to the VBR is almost trivial: The virus–PEDOT bioaffinity layer was extended across the gap between the two gold electrodes. Since the virus–PEDOT layer is electrodeposited, this modification

required that a conductor be deposited across this gap first. A spin-coated PEDOT layer was used for this purpose, and the virus–PEDOT layer was electrodeposited on top of it (**Fig. 7-6A,B**). We refer to this two-layer construct connecting the gold electrodes as the VBR "channel". This elaboration of the two-sided biosensor dramatically alters its properties.

When the two gold electrodes are directly connected via the channel, an internal circuit is generated for the VBR (**Fig. 7-6C**) in which the resistance of the channel is arranged in parallel with the series capacitance and the resistance of the solution. This circuit produces a distinctive semicircular Nyquist plot ($Z_{im}$ vs $Z_{re}$ as a function of frequency) that can be modeled with the following two equations:

**(Eq. 7-1)**
$$Z_{im} = \frac{\omega C_{VBR} {R_{VBR}}^2}{1 + \omega^2 {C_{VBR}}^2 (R_{soln} + R_{VBR})^2}$$

**(Eq. 7-2)**
$$Z_{re} = \frac{R_{VBR}[1 + \omega^2 {C_{VBR}}^2 R_{soln}(R_{soln} + R_{VBR})]}{1 + \omega^2 {C_{VBR}}^2 (R_{soln} + R_{VBR})^2}$$

In contrast, the Nyquist plot for a two-sided biosensor produces a linear plot (**Fig. 7-5C**). The response of three VBRs to the protein DJ-1, a 20 kDa bladder cancer (BC) biomarker,[35,36] shows an increase in the diameter for the semicircle (**Fig. 7-6D**). This increase in diameter is produced by a shift in the low-frequency $Z_{re}$ to higher values, while the high-frequency edge of the semicircle is unchanged. This shift in the low-frequency $Z_{re}$ is correlated with the concentration of the target protein. One consequence of this circuit, shown in the signal-to-noise ratio versus frequency plot (**Fig. 7-6E**), is that the S/N is maximized at low frequency (~1 Hz) and is negligible above 100 Hz. The high-frequency edge of the semicircle measures the solution resistance, $R_{soln}$. We have demonstrated that these two resistors, $R_{VBR}$ and $R_{soln}$, are orthogonal, allowing the value of $R_{VBR}$ to be accurately measured independent of the value of $R_{soln}$. This means that the ionic resistance of the test

solution does not interfere with accurate measurement of the concentration of the target protein—a critically important capability for clinical measurements.

The mechanism by which the VBR operates remains under investigation, but a working hypothesis is summarized by **Fig. 7-7e,f**. Evidence suggests that affinity-driven diffusion of the target protein into the virus–PEDOT layer produces an increase in its low-frequency impedance. This impedance increase may be caused by disruption of the interchain electrical contacts between PEDOT chains in this material. Further experimentation, now underway, will be required to either refute or confirm this hypothesis.

How do the VBR architecture and capabilities compare with those of other biosensors? The closest relative of the VBR is the organic electrochemical transistor (OECT).[37–39] OECTs generally have a reference electrode, in addition to source and drain electrodes, and a semiconducting polymer film channel, similar to the VBR. The device is immersed in an electrolyte solution, the source and drain are bridged by the polymer, and the reference electrode is placed in the same electrolyte solution. Biasing one of the electrodes at a set potential changes the doping level of the polymer, inducing a large conductivity change. At the same time, the potential at another electrode is swept, and the current at the third electrode is measured. This allows small changes in the doping level of the film to be measured with great accuracy. By conjugation of a biorecognition element to the polymer film, low LODs (1 nM) and high specificity have been achieved for label-free detection of proteins.[40]

While OECTs can achieve detection of many analytes, these devices have limitations when it comes to clinical biomolecular sensing. High-ionic-strength solutions cause Debye

screening and prevent low LODs.[41] The doping level of the polymer is dependent on the ions in the solution, which can cause issues when ion detection is not desired.

## 7.7 Summary and Outlook

The VBR is noteworthy for its extreme simplicity, for its use of virus particles in place of antibodies as receptors, and because its performance for the detection of some cancer markers directly on bodily fluids can be adequate for the early detection of cancer. The 14-year story of its development, recounted here, includes both dead ends (two-sided biosensors) and near failures (nanowires). That it now exists is a testament to the power of perseverance in science.

A future goal is to create arrays of VBRs in which each VBR element contains a different M13 virus particle capable of detecting a different cancer or disease marker. Such a proteomic panel might provide a multidimensional picture containing information on disease progression and tumor grade.

## 7.8 References


(1) Yang, L. M. C.; Tam, P. Y.; Murray, B. J.; McIntire, T. M.; Overstreet, C. M.; Weiss, G. A.; Penner, R. M. Virus Electrodes for Universal Biodetection. *Anal. Chem.* **2006**, *78* (10), 3265–3270. https://doi.org/10.1021/ac052287u.

(2) Smith, G. P.; Petrenko, V. A. Phage Display. *Chem. Rev.* **1997**, *97* (2), 391–410. https://doi.org/10.1021/cr960065d.

(3) Smith, G. P. Phage Display: Simple Evolution in a Petri Dish (Nobel Lecture). *Angew. Chemie - Int. Ed.* **2019**, *58* (41), 14428–14437. https://doi.org/10.1002/anie.201908308.

(4) Winter, G.; Milstein, C. Man-Made Antibodies. *Nature* **1991**, *349*, 293–299.

(5) Marks, J. D.; Hoogenboom, H. R.; Bonnert, T. P.; McCafferty, J.; Griffiths, A. D.; Winter, G. By-Passing Immunization. Human Antibodies from V-Gene Libraries Displayed on Phage. *J. Mol. Biol.* **1991**, *222* (3), 581–597. https://doi.org/10.1016/0022-2836(91)90498-U.

(6) Bhasin, A.; Ogata, A. F.; Briggs, J. S.; Tam, P. Y.; Tan, M. X.; Weiss, G. A.; Penner, R. M. The Virus Bioresistor: Wiring Virus Particles for the Direct, Label-Free Detection of Target Proteins. *Nano Lett.* **2018**, *18* (6), 3623–3629. https://doi.org/10.1021/acs.nanolett.8b00723.

(7) Bhasin, A.; Sanders, E. C.; Ziegler, J. M.; Briggs, J. S.; Drago, N. P.; Attar, A. M.; Santos, A. M.; True, M. Y.; Ogata, A. F.; Yoon, D. V.; Majumdar, S.; Wheat, A. J.; Patterson, S. V.; Weiss, G. A.; Penner, R. M. Virus Bioresistor (VBR) for Detection of Bladder Cancer Marker DJ-1 in Urine at 10 PM in One Minute. *Anal. Chem.* **2020**. https://doi.org/10.1021/acs.analchem.0c00534.

(8) Li, Z.; Chen, G. Y. Current Conjugation Methods for Immunosensors. *Nanomaterials* **2018**, *8* (5), 1–11. https://doi.org/10.3390/nano8050278.

(9) Petrenko, V. A.; Vodyanoy, V. J. Phage Display for Detection of Biological Threat Agents. *J. Microbiol.*

*Methods* **2003**, *53* (2), 253–262. https://doi.org/10.1016/S0167-7012(03)00029-0.
(10) Petrenko, V. A. Landscape Phage as a Molecular Recognition Interface for Detection Devices. *Microelectronics J.* **2008**, *39* (2), 202–207. https://doi.org/10.1016/j.mejo.2006.11.007.
(11) Nanduri, V.; Sorokulova, I. B.; Samoylov, A. M.; Simonian, A. L.; Petrenko, V. A.; Vodyanoy, V. Phage as a Molecular Recognition Element in Biosensors Immobilized by Physical Adsorption. *Biosens. Bioelectron.* **2007**, *22* (6), 986–992. https://doi.org/10.1016/j.bios.2006.03.025.
(12) Yang, L. M. C.; Diaz, J. E.; McIntire, T. M.; Weiss, G. A.; Penner, R. M. Direct Electrical Transduction of Antibody Binding to a Covalent Virus Layer Using Electrochemical Impedance. *Anal. Chem.* **2008**, *80* (15), 5695–5705. https://doi.org/10.1021/ac8008109.
(13) Yang, L. M. C.; Diaz, J. E.; McIntire, T. M.; Weiss, G. A.; Penner, R. M. Covalent Virus Layer for Mass-Based Biosensing. *Anal. Chem.* **2008**, *80* (4), 933–943. https://doi.org/10.1021/ac071470f.
(14) Zhang, S.; Huang, F.; Liu, B.; Ding, J.; Xu, X.; Kong, J. A Sensitive Impedance Immunosensor Based on Functionalized Gold Nanoparticle-Protein Composite Films for Probing Apolipoprotein A-I. *Talanta* **2007**, *71* (2), 874–881. https://doi.org/10.1016/j.talanta.2006.05.081.
(15) Yan, F.; Sadik, O. A. Enzyme-Modulated Cleavage of DsDNA for Supramolecular Design of Biosensors the Serial Assembly Was First Achieved by Linearizing Enzyme . This Was Followed by a Bisulfite-Catalyzed Trans-. *Anal. Chem.* **2001**, *73* (21), 6121–6129.
(16) Yan, F.; Sadik, O. A. Enzyme-Modulated Cleavage of DsDNA for Studying Interfacial Biomolecular Interactions. *J. Am. Chem. Soc.* **2001**, *123* (46), 11335–11340. https://doi.org/10.1021/ja005719l.
(17) Ruan, C.; Yang, L.; Li, Y. Immunobiosensor Chips for Detection of Escherichia Coli O157:H7 Using Electrochemical Impedance Spectroscopy. *Anal. Chem.* **2002**, *74* (18), 4814–4820. https://doi.org/10.1021/ac025647b.
(18) Liu, J.; Tian, S.; Neilsen, P. E.; Knoll, W. In Situ Hybridization of PNA/DNA Studied Label-Free by Electrochemical Impedance Spectroscopy. *Chem. Commun.* **2005**, No. 23, 2969–2971. https://doi.org/10.1039/b419425j.
(19) Yang, L.; Li, Y.; Erf, G. F. Interdigitated Array Microelectrode-Based Electrochemical Impedance Immunosensor for Detection of Escherichia Coli O157:H7. *Anal. Chem.* **2004**, *76* (4), 1107–1113. https://doi.org/10.1021/ac0352575.
(20) Taggart, D. K.; Yang, Y.; Kung, S. C.; McIntire, T. M.; Penner, R. M. Enhanced Thermoelectric Metrics in Ultra-Long Electrodeposited PEDOT Nanowires. *Nano Lett.* **2011**, *11* (1), 125–131. https://doi.org/10.1021/nl103003d.
(21) Xiang, C.; Kung, S. C.; Taggart, D. K.; Yang, F.; Thompson, M. A.; Güell, A. G.; Yang, Y.; Penner, R. M. Lithographically Patterned Nanowire Electrodeposition: A Method for Patterning Electrically Continuous Metal Nanowires on Dielectrics. *ACS Nano* **2008**, *2* (9), 1939–1949. https://doi.org/10.1021/nn800394k.
(22) Xiang, C.; Yang, Y.; Penner, R. M. Cheating the Diffraction Limit: Electrodeposited Nanowires Patterned by Photolithography. *Chem. Commun.* **2009**, No. 8, 859–873. https://doi.org/10.1039/b815603d.
(23) Lamboy, J. A.; Arter, J. A.; Knopp, K. A.; Der, D.; Overstreet, C. M.; Palermo, E. F.; Urakami, H.; Yu, T. Bin; Tezgel, O.; Tew, G. N.; Guan, Z.; Kuroda, K.; Weiss, G. A. Phage Wrapping with Cationic Polymers Eliminates Nonspecific Binding between M13 Phage and High p/ Target Proteins. *J. Am. Chem. Soc.* **2009**, *131* (45), 16454–16460. https://doi.org/10.1021/ja9050873.
(24) Donavan, K. C.; Arter, J. A.; Weiss, G. A.; Penner, R. M. Virus-Poly(3,4-Ethylenedioxythiophene) Biocomposite Films. *Langmuir* **2012**, *28* (34), 12581–12587. https://doi.org/10.1021/la302473j.
(25) Arter, J. A.; Taggart, D. K.; McIntire, T. M.; Penner, R. M.; Weiss, G. A. Virus-PEDOT Nanowires for Biosensing. *Nano Lett.* **2010**, *10* (12), 4858–4862. https://doi.org/10.1021/nl1025826.
(26) Arter, J. A.; Diaz, J. E.; Donavan, K. C.; Yuan, T.; Penner, R. M.; Weiss, G. A. Virus-Polymer Hybrid Nanowires Tailored to Detect Prostate-Specific Membrane Antigen. *Anal. Chem.* **2012**, *84* (6), 2776–2783. https://doi.org/10.1021/ac203143y.
(27) Menke, E. J.; Thompson, M. A.; Xiang, C.; Yang, L. C.; Penner, R. M. Lithographically Patterned Nanowire Electrodeposition. *Nat. Mater.* **2006**, *5* (11), 914–919. https://doi.org/10.1038/nmat1759.
(28) Chang, S. S. Overview of Prostate-Specific Membrane Antigen. *Rev. Urol.* **2004**, *6*, S13–S18.
(29) O'Keefe, D. S.; Bacich, D. J.; Heston, W. D. W. Comparative Analysis of Prostate-Specific Membrane Antigen (PSMA) Versus a Prostate-Specific Membrane Antigen-Like Gene. *Prostate* **2004**, *58* (2), 200–210. https://doi.org/10.1002/pros.10319.
(30) Diaz, J. E.; Yang, L. C.; Lamboy, J. A.; Penner, R. M.; Weiss, G. A. *Specific Membrane Antigen*; Rasooly, A.,

Herold, K. E., Eds.; Humana Press, 2009; Vol. 504. https://doi.org/10.1007/978-1-60327-569-9.
(31) Mohan, K.; Donavan, K. C.; Arter, J. A.; Penner, R. M.; Weiss, G. A. Sub-Nanomolar Detection of Prostate-Specific Membrane Antigen in Synthetic Urine by Synergistic, Dual-Ligand Phage. *J. Am. Chem. Soc.* **2013**, *135* (20), 7761–7767. https://doi.org/10.1021/ja4028082.
(32) Donavan, K. C.; Arter, J. A.; Pilolli, R.; Cio, N.; Weiss, G. A.; Penner, R. M.; Chimica, D.; Aldo, B. Virus - Poly(3,4-Ethylenedioxythiophene) Composite Films for Impedance-Based Biosensing. *Anal. Chem.* **2011**, *83*, 2420–2424.
(33) Mohan, K.; Penner, R. M.; Weiss, G. A. Biosensing with Virus Electrode Hybrids. *Curr. Protoc. Chem. Biol.* **2015**, *7* (2), 53–72.
(34) Ogata, A. F.; Edgar, J. M.; Majumdar, S.; Briggs, J. S.; Patterson, S. V.; Tan, M. X.; Kudlacek, S. T.; Schneider, C. A.; Weiss, G. A.; Penner, R. M. Virus-Enabled Biosensor for Human Serum Albumin. *Anal. Chem.* **2017**, acs.analchem.6b04840. https://doi.org/10.1021/acs.analchem.6b04840.
(35) Tan, W. S.; Tan, W. P.; Tan, M. Y.; Khetrapal, P.; Dong, L.; deWinter, P.; Feber, A.; Kelly, J. D. Novel Urinary Biomarkers for the Detection of Bladder Cancer: A Systematic Review. *Cancer Treat. Rev.* **2018**, *69* (January), 39–52. https://doi.org/10.1016/j.ctrv.2018.05.012.
(36) Kumar, P.; Nandi, S.; Tan, T. Z.; Ler, S. G.; Chia, K. S.; Lim, W.-Y.; Bütow, Z.; Vordos, D.; De laTaille, A.; Al-Haddawi, M.; Raida, M.; Beyer, B.; Ricci, E.; Colombel, M.; Chong, T. W.; Chiong, E.; Soo, R.; Park, M. K.; Ha, H. K.; Gunaratne, J.; Thiery, J. P. Highly Sensitive and Specific Novel Biomarkers for the Diagnosis of Transitional Bladder Carcinoma Prashant. *Oncotarget* **2015**, *6* (15), 13539–13549. https://doi.org/3.
(37) Rivnay, J.; Inal, S.; Salleo, A.; Owens, R. M.; Berggren, M.; Malliaras, G. G. Organic Electrochemical Transistors. *Nat. Rev. Mater.* **2018**, *3*. https://doi.org/10.1038/natrevmats.2017.86.
(38) Wang, N.; Yang, A.; Fu, Y.; Li, Y.; Yan, F. Functionalized Organic Thin Film Transistors for Biosensing. *Acc. Chem. Res.* **2019**. https://doi.org/10.1021/acs.accounts.8b00448.
(39) Lin, P.; Yan, F.; Chan, H. L. W. Ion-Sensitive Properties of Organic Electrochemical Transistors. *ACS Appl. Mater. Interfaces* **2010**, *2* (6), 1637–1641. https://doi.org/10.1021/am100154e.
(40) Li, H.; Shi, W.; Song, J.; Jang, H. J.; Dailey, J.; Yu, J.; Katz, H. E. Chemical and Biomolecule Sensing with Organic Field-Effect Transistors. *Chem. Rev.* **2019**, *119* (1), 3–35. https://doi.org/10.1021/acs.chemrev.8b00016.
(41) Gao, N.; Zhou, W.; Jiang, X.; Hong, G.; Fu, T. M.; Lieber, C. M. General Strategy for Biodetection in High Ionic Strength Solutions Using Transistor-Based Nanoelectronic Sensors. *Nano Lett.* **2015**, *15* (3), 2143–2148. https://doi.org/10.1021/acs.nanolett.5b00133.

# CHAPTER 8

## Electrochemical Biosensing of Glycated Human Serum Albumin

Adapted with permission from *ACS Applied Materials & Interfaces.*
DOI: 10.1021/acsami.8b16071

### 8.1 Abstract

A polymer-based electrode capable of specific detection of human serum albumin, and its glycated derivatives, is described. The sensor is constructed from a glass microscope slide coated with a synthesized, polythiophene film bearing a protected, iminodiacetic acid motif. The electrode surface is then further elaborated to a functional biosensor through deprotection of the iminodiacetic acid, followed by metal-affinity immobilization of a specific and high-affinity, albumin ligand. Albumin was then quantified in buffer and synthetic urine via electrochemical impedance spectroscopy. Glycated albumin was next bound to a boronic acid-modified, single- cysteine dihydrofolate reductase variant to quantify glycation ratios by square wave voltammetry. The platform offers high sensitivity, specificity, and reproducibility in an inexpensive arrangement. The detection limits exceed the requirements for intermediate-term glycemic control monitoring in diabetes patients at 5 and 1 nM for albumin and its glycated forms, respectively.

## 8.2 Introduction

Human serum albumin (HSA) is a useful disease biomarker.[1] In healthy adults, the concentration of HSA in blood is 500-800 μM and <0.3 μM in urine.[2,3] Elevated urine HSA concentrations (0.3-3 μM) indicate renal failure or kidney damage, often associated with hypertension and diabetes mellitus (DM).[4–6] Glycation is the nonenzymatic, post-translational addition of carbohydrates to proteins.[7–9] Glycated HSA (gHSA) is typically modified at the free amines of its N-terminus and lysine side chains.[10,11] Healthy adults exhibit blood serum gHSA levels of 11-16% (as a proportion of total HSA), whereas DM patients present with levels of 20- 30%.[2] Thus, gHSA has emerged as an important, intermediate-term glycemic control marker and can report average blood glucose concentrations over the 2-3 week lifetime of HSA in blood.[12–15]

Standard methods for HSA quantification are either antibody-based (immunonephelometry, immunoturbidity, enzyme-linked immunosorbent assays, immunoelectrophoresis, and radio- and chemiluminescent immunoassays) or employ HSA-specific fluorogenic dyes.[16–22] gHSA detection and quantification typically involves automated analyzers, such as the Lucica GA-L (Asahi Kasei Pharma, Japan). This and similar instruments use proteolytic digestion and a colorimetric assay to detect glycated amino acids.[23–26] Extensive innovation has been reported over the past decade in the detection of HSA and gHSA, and improved luminescence methods[27–35] dominate the literature. Advanced materials could offer flexibility and tenability, which is difficult to achieve with conventional luminescence-based assays.

We report a modified poly-ethylenedioxythiophene (PEDOT) electrode capable of detecting and quantifying both HSA and gHSA in a single sample. The high synthetic

tractability of this organic polymer has facilitated the creation of a diverse repertoire of functional derivatives for sensing applications.[36–40] The device reported here employs a C-terminal, His6- tagged GFP construct immobilized on a PEDOT surface via formation of a ternary complex with copper(II), and an iminodiacetic acid (IDA) motif present within the PEDOT film **(Fig. 8-1a)**.[41] Previously, we described electrodeposited phage-PEDOT films for biosensing.[42,43] Here, the phage-derived peptide is fused to GFP (DCPIYCEDGYCLRKCVDLYR) which binds with equal apparent affinities for both HSA and gHSA. This affinity reagent (hereinafter referred to as αHSA) was acquired via recombinant protein expression. The PEDOT-Cu-αHSA-HSA quaternary complex generates distinctive electrochemical impedance spectra (EIS), allowing total HSA + gHSA concentrations to be quantified **(Fig. 8-1b)**.

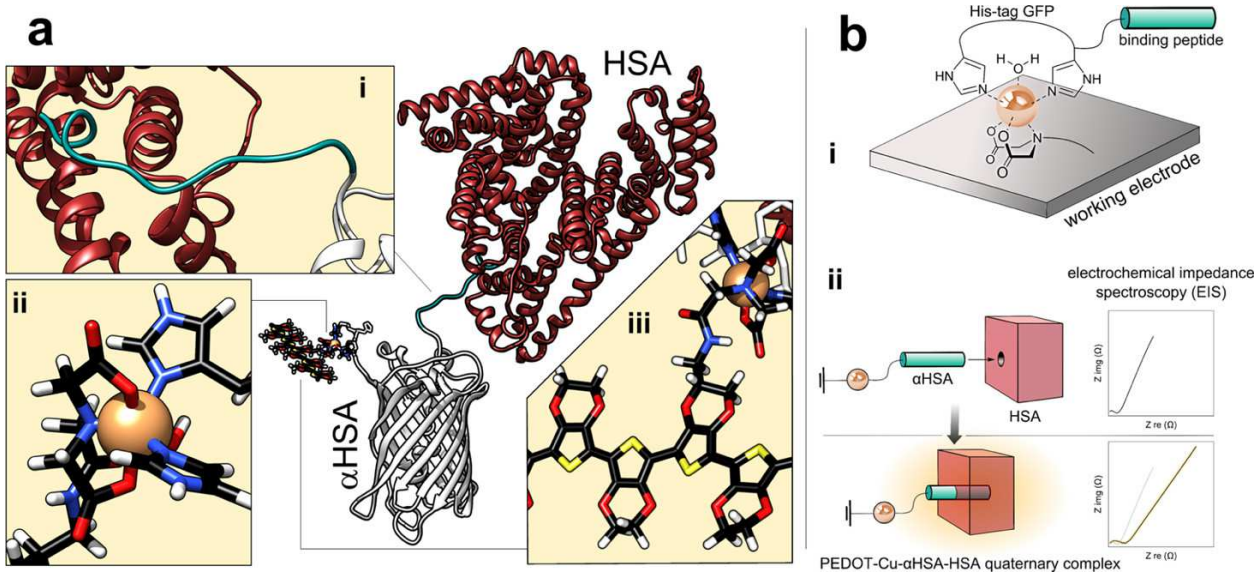


**Figure 8-1. Schematic of the reported biosensor. A)** (i) HSA-binding peptide of αHSA is depicted as a green-colored random coil. (ii) Immobilized Cu(II)–His6 complex. Coordinating IDA and His ligands are depicted as rounded sticks bound to copper(II) (orange). (iii) Copolymer of EDOT and EDOT–IDA. **B)** Simplified illustration of the sensor, including (i) device architecture, and (ii) EIS sensing.

The HSA-gHSA ratio was determined utilizing a boronate-tagged, engineered variant of the redox enzyme, dihydrofolate reductase (DHFR), as an electrochemical reporter (**Fig. 8-2**). The boronate affinity-tag associates selectively with the carbohydrate components of

gHSA.[16,44] The gHSA-immobilized DHFR reporter catalyzes a 2e- reduction of dihydrofolic acid to tetrahydrofolic acid with reduced nicotinamide adenine dinucleotide phosphate (NADPH) as the reducing agent. Under an applied potential, the tetrahydrofolic acid is oxidized, and its electrons are passed to the PEDOT electrode for detection (**Fig. 8-2B**). Thus, an exquisitely sensitive, switchable-mode sensor capable of dual quantification of total HSA, and gHSA ratios is realized.

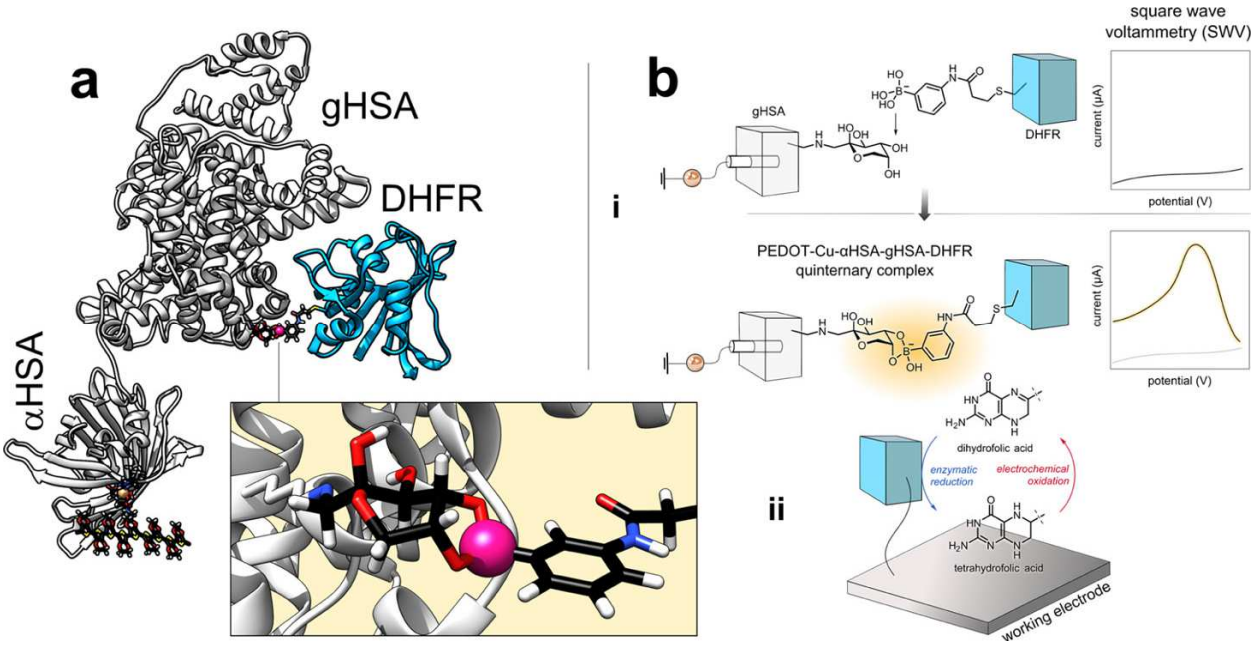


**Figure 8-2. Schematic representation of gHSA quantification. A)** DHFR (blue ribbon) associates with surface carbohydrates on gHSA via its boronate affinity tag. The surface-exposed fructosamine residue and phenyl boronic ester (pink) are depicted as sticks. **B)** (i) gHSA-sensing complex is detected electrochemically via SWV via (ii) redox cycling of dihydrofolic acid/tetrahydrofolic acid.

## 8.3 Results and Discussion

The PEDOT electrode was constructed from a 95:5 mixture of EDOT and an EDOT derivative bearing an anhydride-protected IDA motif (EDOT-pIDA). A surprisingly stable anhydride, the EDOT-pIDA monomer was synthesized in one step from existing literature compounds. The mixture was copolymerized onto a glass surface pretreated with nitrocellulose adhesive (collodion) and $Fe(ClO_4)_3$ as the requisite polymerization oxidant.

Protection of IDA as its anhydride prevents chelation of Fe(III) during this step. After thorough washing of the polymer surface, the essential IDA motif was liberated via base-catalyzed hydrolysis of the anhydride to yield PEDOT-IDA. Six rounds of iterative copolymerization with 95:5 EDOT-EDOT-pIDA mixtures resulted in optimal device performance. Interrogation of the PEDOT-pIDA electrode by scanning electron microscopy (SEM) and atomic force microscopy (AFM) revealed a moderately rough surface, and therefore a large effective sensing surface area. The ternary PEDOT-Cu–αHSA complex formed spontaneously at ambient temperatures after sequential treatment with aqueous CuSO4, then buffered αHSA solution.

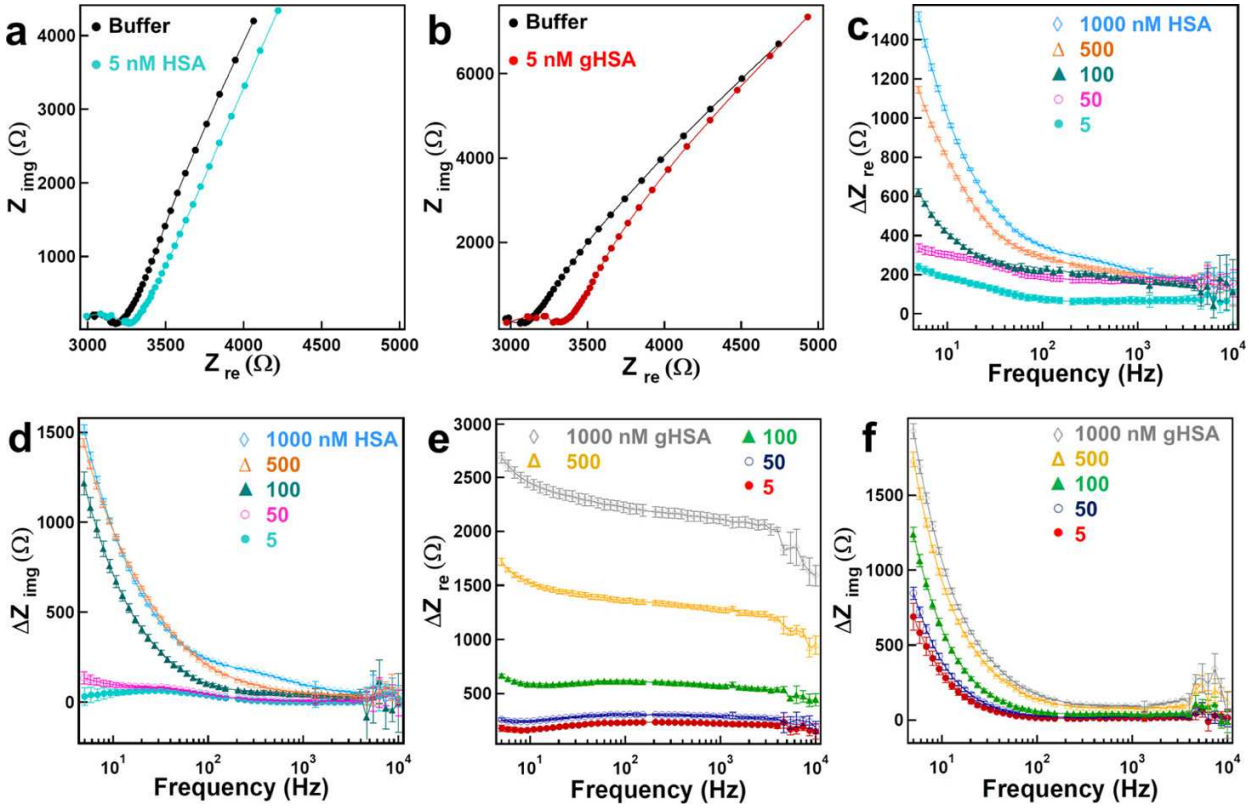


**Figure 8-3. EIS detection of HSA and gHSA. A,B)** Nyquist plots for PEDOT–IDA biosensors in solutions of buffer (black) and 5 nM HSA (blue) or gHSA (red). (c–f) $\Delta Z_{re}$ and $\Delta Z_{im}$ plots vs frequency for PEDOT–IDA biosensors exposed to varying concentrations of HSA **C,D)** and gHSA **E,F)** where $\Delta Z$ is defined as $Z_{HSA} - Z_{buffer}$. Error bars are defined as a propagated error from the standard deviation, ±1σ, for five consecutive EIS measurements.

For each concentration of HSA, three independent devices were used to perform five replicate measurements (**Fig. 8-4A**). The coefficients of variation (COVs) ranged from 2.9 to 15%, commensurate with existing FDA-approved bioanalytical methods. These COV values include the idiosyncrasies associated with fabrication at the hands of two experimentalists. In the future, print manufacturing could further lower device COVs. The calculated limit of quantification and limit of detection (LOD) (10σ and 3σ, where σ is the standard deviation of the blank)[45] are 1.0 and 0.13 nM, respectively, for HSA detection by these devices. In practice, the lowest consistently measurable HSA concentration was 5.0 nM (**Fig. 8-3A,B**), which is lower than the LOD (7 mg/mL, 105 nM) obtained by a point-of-care system that quantifies albumin.

At the highest protein concentrations examined here, gHSA consistently provided higher levels of impedance than HSA, despite both analytes exhibiting similar apparent binding affinities for αHSA. At lower concentrations, impedance levels for the two analytes did not markedly vary. This behavior was observed in samples prepared both in synthetic urine and in buffer (**Fig. 8-4B**). Bohli reported a different device configuration applying an immunosensor to detect gHSA. This device results in decreased impedance, an effect opposite to our device, which the authors attribute to the electric charge differences of HSA and gHSA.[46]

HSA binding to the PEDOT surface in our device increases the measured impedance (**Fig. 8-3**). This observation is consistent with a sensing mechanism in which electrolyte-filled channels within the PEDOT film become blocked by immobilized HSA. Channel blocking would be expected to increase the ionic resistance, and hence Zre, while also

increasing $Z_{im}$. In **eq 8-1**, $Z_{im}$ is the imaginary impedance, ω is the frequency of the alternating current, and C is the current amplitude.

$$\textbf{(Eq. 8-1)} \quad Z_{im} = (\omega C)^{-1}$$

In this mechanism, C decreases as water (ε = 79) within channels is displaced by bound protein with a range of hydrophobic and hydrophilic functionalities (ε ≈ 4-20). In previous reports, we have proposed this mechanism to account for the resistance increase induced by HSA binding at phage-PEDOT composite films.[47] Glycation presents additional steric bulk, further impeding such ion transport and decreasing $Z_{re}$ and $Z_{im}$. Collectively, the results support the proposed impedance-based sensing mechanism.

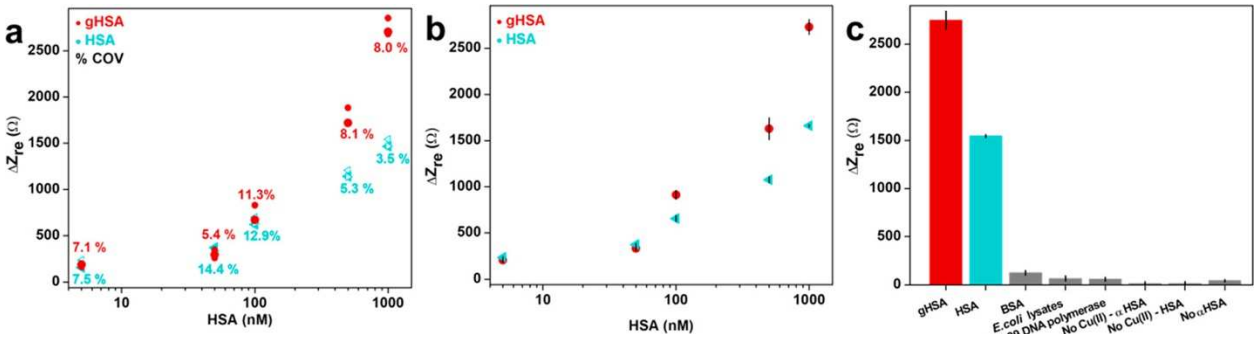


**Figure 8-4. Detection of HSA and gHSA by electrochemical impedance spectroscopy.** Calibration plot of $\Delta Z_{re}$ vs HSA concentrations for independent PEDOT–IDA biosensors exposed to the indicated concentrations of gHSA or HSA in **A)** PBS (three independent devices for each concentration with 5 measurements each with the indicated % COVs) or **B)** synthetic urine (one device for each concentration with 5 measurements each). Each data point represents the average obtained from five measurements on one device; error bars indicate standard deviations. **C)** Control experiments confirm specific detection of gHSA and HSA and demonstrate the necessity of each component in the quaternary sensing complex for the device function. Proteins were tested at concentrations of 1000 nM.

Six negative controls defined the biosensor and individual component responses to nonspecific binding (**Fig. 8-4C**). First, nonspecific binding examined biosensor response to bovine serum albumin (BSA, a close homolog of HSA), a mixture of proteins from Escherichia coli lysates, and an unrelated, high pI protein, phi29 DNA polymerase. Next, two different electrodes investigated the individual components of the biosensors as follows: a copper(II)-

free PEDOT-IDA electrode evaluated nonspecific binding of αHSA and HSA to PEDOT-IDA, and an electrode without αHSA examined nonspecific binding of HSA to the PEDOT-Cu(II) complex. These controls had low signal-to-noise ratios and generated impedance signals <10% of the positive controls.

The αHSA electrode recognizes both HSA and gHSA equally well, but sandwich capture of gHSA allows discrimination of the two proteins. In this scheme, the boronic acid, conjugated to the DHFR reporter, forms covalent bonds with vicinal diols present on the glycated protein (**Fig. 8-2**). The single-cysteine variant of DHFR used here was expressed in *E. coli* to avoid glycosylation, thus abrogating problems associated with self-dimerization and aggregation. Guided by a previous mutagenesis study,[48] we examined numerous mutant DHFR candidates, and the variant reported here (N37C/C85A/C152S) exhibits no loss of activity compared to wild-type DHFR. The DHFR variant was labeled using a thiol-ene click reaction between the C37 thiol of DHFR and the alkene of 3-acrylamidophenylboronic acid (3-APBA). This step is described in detail in the Materials and Methods section.

Binding of boronic acid-labeled DHFR to gHSA was detected by square-wave voltammetry (SWV) measurements. The THF produced through enzymatic catalysis is oxidized by the αHSA electrode, generating a peak potential (Ep) near +0.3 V versus MSE. The potential was scanned in phosphate-buffered saline (PBS) (pH 7.4) from −0.6 to −0.8 V with a step potential of 5 mV, an amplitude of 25 mV, and a frequency of 20 Hz. The obtained total current peak is proportional to the concentration of gHSA in the range of 1-1000 nM (**Fig. 8-5A**). The corresponding calibration plot of the SWV response versus gHSA concentration presents a logarithmic regression (**Fig. 8-5B**). The lowest measurable gHSA

concentration by the proposed biosensor is 1 nM, which is lower than the LOD obtained by the Lucica GA-L assay (7.9 μM).

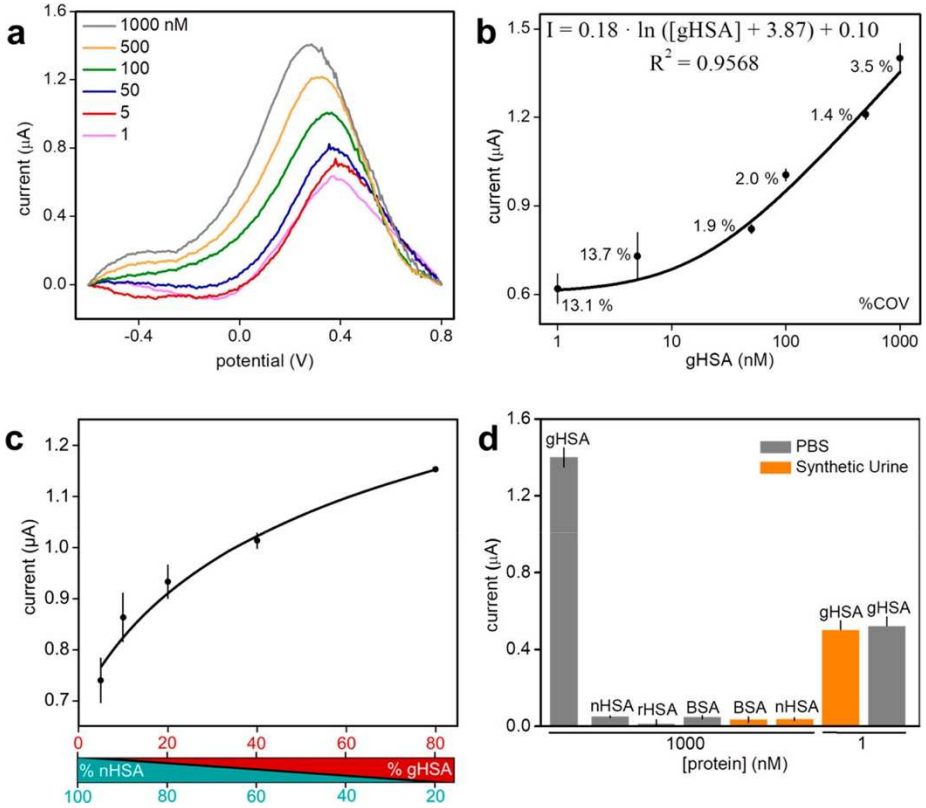


**Figure 8-5. gHSA quantification**. **A)** Square wave voltammetry with the indicated gHSA concentrations. **B)** Calibration plot of current vs gHSA concentration for 18 independent PEDOT–IDA biosensors exposed to the indicated concentrations of gHSA before incubation with boronic acid-labeled DHFR, NADPH, and dihydrofolic acid. The percentages indicate COVs for three devices. The logarithmic equation represents the curve fit to the depicted data. **C)** Current vs proportion of gHSA in gHSA + HSA mixtures after detection via SWV with boronic acid labeled DHFR (three independent biosensors at each concentration, total [nHSA + gHSA] is 500 nM in all cases). **D)** Control experiments verify specific binding of gHSA, nHSA isolated from healthy humans, rHSA, which also lacks glycation, and BSA to PEDOT–IDA biosensor and boronic acid-labeled DHFR in PBS (gray) and synthetic urine (orange).

HSA glycation ratios can be determined with this device. Mixtures of gHSA and its non- glycated counterpart [non-gHSA (nHSA)] were prepared such that the total gHSA + nHSA concentration was fixed at 500 nM. A significant increase in the current response with increasing gHSA ratios was observed in the range of 5 to 80% (**Fig. 8-5C**). HSA obtained from recombinant expression in bacteria [recombinant HSA (rHSA)] and BSA were used to evaluate nonspecific binding by boronic acid labeled-DHFR in PBS and synthetic urine (**Fig.**

**8-5D**). These controls generated a low signal of <8% the total current obtained from gHSA at the same concentrations.

## 8.4 Conclusions

In summary, this chapter focuses on development of key elements for robust sensor fabrication. The reported sensors exhibit exceptional reproducibility, within tolerances for FDA- approved medical diagnostics. Sensor-to-sensor reproducibility is very high, despite the lack of sophisticated manufacturing techniques. COVs of 1.4–15% were obtained across the 1–1000 nM HSA concentration range. The biosensor utilizes a boronate-tagged DHFR enzyme for SWV signal amplification, which allowed gHSA to be discriminated at proportions of total HSA as low as 5%. Our design is readily amenable to large-scale manufacture of both the polymer electrode, and the protein-based sensing components. The modularity of our design lends itself to rapid development of alternative sensors with different specificities, which can be achieved through substitution of αHSA with other His6-tagged ligands. Further development could establish sensors for point-of-care, at-home, or lab-based gHSA monitoring.

## 8.5 Materials and Methods

*General Experimental Methods.* Three different HSAs have been used in this work: (i) a lyophilized powder, fatty acid-free, globulin-free HSA with no carbohydrate content with a purity of >99.0% (Sigma-Millipore), (ii) a lyophilized powder, in vitro gHSA with 3 mol hexose (as fructosamine) per mol albumin (Sigma-Millipore), and (iii) a recombinant HSA from recombinant *S. cerevisiae* fermentation, manufactured without the use of animal- or human-derived materials (Novozymes). The synthetic urine was Surine Negative Urine

Control pH 6.9 (Sigma-Millipore), a nonbiological mixture commonly used as a negative reference standard for laboratory urine tests.

High-resolution mass spectra (HRMS) were obtained by electrospray ionization on a Waters (Micromass) LCT Premier equipped with a time-of-flight mass analyzer. Proton ($^{1}H$, 500 MHz) and carbon ($^{13}C$, 125 MHz) nuclear magnetic resonance (NMR) spectra were obtained on a Bruker instrument equipped with a switchable BBFO probe. NMR samples were prepared in CDCl3 and DMSO-d6, and residual protonated solvent was used as an internal chemical shift standard. 1H and 13C assignments were determined using HSQC and 10 Hz optimized HMBC 2D-NMR analyses. Fourier-transform infrared spectra were obtained as neat samples on a Jasco 4700 attenuated total reflectance instrument using a diamond-coated zinc selenide sample accessory. Flash chromatography was carried out on silica gel 60 according to the procedure of Still et al.53 Analytical thin-layer chromatography (TLC) was conducted on aluminium-backed 2 mm thick silica gel 60 GF254 and chromatograms were visualized under a UV lamp (254 and 365 nm), or by chemical staining with ceric ammonium molybdate (Hanessian's Stain) or $KMnO_4$.

*Synthesis of Chloromethyl EDOT, Azidomethyl EDOT, Nitrilotriacetic Acid Anhydride, and EDOT-pIDA*. In the interest of brevity, the syntheses of these materials can be found online at: doi: 10.1021/acsami.8b16071.

*Biosensor Fabrication and Characterization.* A 46 × 27 × 1 mm glass microscope slide was spin-coated with 0.5 M Fe(ClO4)3 and 3% w/v nitrocellulose in 1:1 EtOH/Et2O [iron(III) perchlorate in collodion, 150 μL] at 3500 rpm for 30 s. Then, 62.7 mM EDOT and 3.3 mM EDOT–pIDA in n-BuOH (150 μL) was spin-coated directly onto the collodion/Fe(III) film at 3500 rpm. The successful polymerization of the first PEDOT–pIDA layer can be confirmed

visually through a color change of the film from yellow to dark blue. The next five consecutive layers were deposited by alternating between spin coats of 0.5 M $Fe(ClO_4)_3$ in n-BuOH (150 μL), then 62.7 mM EDOT and 3.3 mM EDOT–pIDA in n-BuOH (150 μL). The slides were then placed in a polystyrene Petri dish with the PEDOT–pIDA face-up and cured overnight at rt. The mature films were then washed under a stream of EtOH for 30 s, air-dried, then fitted with a poly(methyl methacrylate) 100 μL capacity flow cell. The resulting device is bench stable, and no loss of performance was observed after storage for periods up to 30 days in air at rt. Hydrolysis of the IDA anhydride group is performed immediately prior to measurements.

Prior to measurements, the flow cell reservoir was first rinsed with 0.5 M aq EDTA (20 μL), then 4 M aq NaOH (20 μL), which causes hydrolysis of the anhydride protecting groups, and then 10 mM PBS (pH 7.4, 100 μL). Each rinse solution was left to stand without agitation for 2 min and then carefully removed by a pipette. The reservoir was then charged with 100 mM aq $CuSO_4$ (20 μL), incubated for 30 min at rt without agitation, and then the solution was removed by a pipette. The reservoir was rinsed with 10 mM PBS (pH 7.4, 3 × 100 μL), charged with 1 $\mu g \cdot mL^{-1}$ αHSA in 10 mM PBS (pH 7.2, 20 μL), and incubated for a further 30 min. The αHSA solution was removed by a pipette and the reservoir was rinsed with 10 mM PBS (pH 7.4, 3 × 100 μL), providing a clean bioaffinity layer ready for electrochemical biosensing experiments. The surface morphology of the PEDOT–pIDA was examined by SEM and AFM. The final thickness of collodion–PEDOT–pIDA layers was ~830 nm. The root mean square (rms) surface roughness of a single layer of PEDOT–pIDA was 5 nm; rms surface roughness of six layers of PEDOT–pIDA was 8 nm. Electrode surfaces were further characterized by contact angle analysis. A single drop (50 μL) of distilled water was

placed directly on the electrode surface and photographed with a DSLR camera (Nikon D60) equipped with a 60 mm macro lens. The water contact angle obtained for the nitrocellulose-coated glass surface was 15°. Contact angles increase with successive spin-coats of 95:5 PEDOT/PEDOT– pIDA; measured water contact angles were 50°, 65°, and 70° for surfaces with two, four, and six film layers, respectively. The increasing hydrophobicity of the surface is commensurate with increased coverage of the hydrophilic nitrocellulose by the film. The formation of the ternary sensing complex on the PEDOT–IDA films was characterized by impedance spectroscopy to illustrate changes in conductivity during the electrode assembly.

*Electrochemical Impedance Spectroscopy.* Electrochemical impedance and square wave voltammetry were performed using a PalmSens3 controlled by PS-Trace 4.8 software (PalmSens BV, Houten, Netherlands). All electrochemical data were processed on GNU Octave, Igor Pro and OriginLab Pro 8 software. The impedance-frequency properties of the binding of αHSA to HSA and gHSA were evaluated using a two-electrode system. The working electrode (PEDOT–Cu–αHSA bioaffinity layer) was connected to the input of a PalmSens3 potentiostat using a piece of copper tape fixed at its edge, and an alligator pin as electric contacts. The counter electrode (platinum foil) was connected to the output using an alligator pin and was inserted in the flow cell reservoir containing 100 μL of the sample. The frequency was scanned from 5 to 10 000 Hz with a 0.01 V alternating voltage. EIS was recorded and processed into an impedance difference (ΔZre), described as: $\Delta Z = Z_{HSA} - Z_{buffer}$, where ZHSA and $Z_{buffer}$ are the measured impedances before and after incubation with HSA for 5 min.

*Boronic Acid Modification of DHFR.* The boronic acid-labeled DHFR used to discriminate gHSA from HSA was obtained via a thiolene reaction. A solution of 10 mM 3-

APBA and 20 μM N37C/C85A/C152S DHFR in 10 mM PBS (pH 7.4, 500 μL) was incubated on a shaker (5 rpm) at 4 °C for 10 h. The suspension was then transferred to a 5 kDa Amicon Ultra-0.5 mL centrifugal filter and centrifuged at 12 000 rpm and 4–5 °C for 10 min. The concentrate (15 μL) was diluted with 10 mM PBS (pH 7.4, 485 μL) and centrifuged a second time under the same conditions. Eight additional rounds of dilution/ultrafiltration were performed (total ultrafiltration steps = 10), which provides a high level of confidence that any unreacted 3-APBA remaining in the sample, if any, is negligible. The ultrafiltered and purified boronic acid labeled- DHFR was re-suspended in 10 mM PBS (pH 7.4), up to a final concentration of 5 nM. This stock was stored at 4 °C for later use in the biosensing experiments.

*Square Wave Voltammetry.* The sensor was incubated with HSA and gHSA for 5 min before binding of boronate-labeled DHFR to surface-immobilized gHSA was assessed by SWV. A solution of 5 nM boronic acid labeled DHFR (10 μL) was added to the flow cell reservoir and incubated for 10 min and then washed with 10 mM PBS (pH 7.4, 3 × 100 μL). A solution of 5 μM dihydrofolic acid and 5 μM NADPH in 10 mM PBS (pH 7.4, 100 μL) was then added to the reservoir (DHFR substrate and cofactor, respectively), and the SWV signal was measured immediately (**Figs. 8-2 and 8-5**). The oxidation of tetrahydrofolic acid on PEDOT–IDA was detected at an applied potential of +0.3 V versus MSE. The potential was scanned in PBS (pH 7.4) from −0.6 to −0.8 V with a step potential of 5 mV, an amplitude of 25 mV, and a frequency of 20 Hz, and a baseline correction of the obtained voltammograms was performed using OriginLab Pro 8 software.

## 8.6 References

(1) Fanali, G.; Di Masi, A.; Trezza, V.; Marino, M.; Fasano, M.; Ascenzi, P. Human Serum Albumin: From Bench to Bedside. *Mol. Aspects Med.* **2012**, *33* (3), 209–290. https://doi.org/10.1016/j.mam.2011.12.002.

(2) Anguizola, J.; Matsuda, R.; Barnaby, O. S.; Hoy, K. S.; Wa, C.; DeBolt, E.; Koke, M.; Hage, D. S. Review: Glycation of Human Serum Albumin. *Clin. Chim. Acta* **2013**, *425*, 64–76. https://doi.org/10.1016/j.cca.2013.07.013.

(3) Jones, C. A.; Francis, M. E.; Eberhardt, M. S.; Chavers, B.; Coresh, J.; Engelgau, M.; Kusek, J. W.; Byrd-Holt, D.; Venkat Narayan, K. M.; Herman, W. H.; Jones, C. P.; Salive, M.; Agodoa, L. Y. Microalbuminuria in the US Population: Third National Health and Nutrition Examination Survey. *Am. J. Kidney Dis.* **2002**, *39* (3), 445–459. https://doi.org/10.1053/ajkd.2002.31388.

(4) Cravedi, P.; Ruggenenti, P.; Remuzzi, G. Proteinuria Should Be Used as a Surrogate in CKD. *Nat. Rev. Nephrol.* **2012**, *8* (5), 301–306. https://doi.org/10.1038/nrneph.2012.42.

(5) Sarafidis, P. A.; Bakris, G. L. Microalbuminuria and Chronic Kidney Disease as Risk Factors for Cardiovascular Disease. *Nephrol. Dial. Transplant.* **2006**, *21* (9), 2366–2374. https://doi.org/10.1093/ndt/gfl309.

(6) Koulouris, S.; Lekatsas, I.; Karabinos, I.; Ioannidis, G.; Katostaras, T.; Kranidis, A.; Triantafillou, K.; Thalassinos, N.; Anthopoulos, L. Microalbuminuria: A Strong Predictor of 3-Year Adverse Prognosis in Nondiabetic Patients with Acute Myocardial Infarction. *Am. Heart J.* **2005**, *149* (5), 840–845. https://doi.org/10.1016/j.ahj.2004.07.031.

(7) Neelofar, K.; Ahmad, J. An Overview of in Vitro and in Vivo Glycation of Albumin: A Potential Disease Marker in Diabetes Mellitus. *Glycoconj. J.* **2017**, *34* (5), 575–584. https://doi.org/10.1007/s10719-017-9789-0.

(8) Singh, R.; Barden, A.; Mori, T.; Beilin, L. Advanced Glycation End-Products: A Review. *Diabetologia* **2001**, *44* (2), 129–146. https://doi.org/10.1007/s001250051591.

(9) Hodge, J. E.; Rist, C. E. The Amadori Rearrangement under New Conditions and Its Significance for Non-Enzymatic Browning Reactions. *J. Am. Chem. Soc.* **1953**, *75* (2), 316–322. https://doi.org/10.1021/ja01098a019.

(10) Mendez, D. L.; Jensen, R. A.; McElroy, L. A.; Pena, J. M.; Esquerra, R. M. The Effect of Non-Enzymatic Glycation on the Unfolding of Human Serum Albumin. *Arch. Biochem. Biophys.* **2005**, *444* (2), 92–99. https://doi.org/10.1016/j.abb.2005.10.019.

(11) Vernon Roohk, H.; Zaidi, A. R. A Review of Glycated Albumin as an Intermediate Glycation Index for Controlling Diabetes. *J. Diabetes Sci. Technol.* **2008**, *2* (6), 1114–1121. https://doi.org/10.1177/193229680800200620.

(12) Ueda, Y.; Matsumoto, H. Recent Topics in Chemical and Clinical Research on Glycated Albumin. *J. Diabetes Sci. Technol.* **2015**, *9* (2), 177–182. https://doi.org/10.1177/1932296814567225.

(13) Gan, T.; Liu, X.; Xu, G. Glycated Albumin Versus HbA1c in the Evaluation of Glycemic Control in Patients With Diabetes and CKD. *Kidney Int. Reports* **2018**, *3* (3), 542–554. https://doi.org/10.1016/j.ekir.2017.11.009.

(14) Wu, W. C.; Ma, W. Y.; Wei, J. N.; Yu, T. Y.; Lin, M. S.; Shih, S. R.; Hua, C. H.; Liao, Y. J.; Chuang, L. M.; Li, H. Y. Serum Glycated Albumin to Guide the Diagnosis of Diabetes Mellitus. *PLoS One* **2016**, *11* (1), 1–14. https://doi.org/10.1371/journal.pone.0146780.

(15) Arasteh, A.; Farahi, S.; Habibi-Rezaei, M.; Moosavi-Movahedi, A. A. Glycated Albumin: An Overview of the In Vitro Models of an In Vivo Potential Disease Marker. *J. Diabetes Metab. Disord.* **2014**, *13* (1), 1–9. https://doi.org/10.1186/2251-6581-13-49.

(16) Kumar, D.; Banerjee, D. Methods of Albumin Estimation in Clinical Biochemistry: Past, Present, and Future. *Clin. Chim. Acta* **2017**, *469* (August 2016), 150–160. https://doi.org/10.1016/j.cca.2017.04.007.

(17) Aoyagi, S.; Iwata, T.; Miyasaka, T.; Sakai, K. Determination of Human Serum Albumin by Chemiluminescence Immunoassay with Luminol Using a Platinum-Immobilized Flow-Cell. *Anal. Chim. Acta* **2001**, *436* (1), 103–108. https://doi.org/10.1016/S0003-2670(01)00886-8.

(18) Choi, S.; Choi, E. Y.; Kim, H. S.; Oh, S. W. On-Site Quantification of Human Urinary Albumin by a Fluoresence Immunoassay. *Clin. Chem.* **2004**, *50* (6), 1052–1055.

(19) Comper, W. D.; Jerums, G.; Osicka, T. M. Differences in Urinary Albumin Detected by Four Immunoassays and High-Performance Liquid Chromatography. *Clin. Biochem.* **2004**, *37* (2), 105–111. https://doi.org/10.1016/j.clinbiochem.2003.10.008.

(20) Marre, M.; Claudel, J. P.; Ciret, P.; Luis, N.; Suarez, L.; Passa, P. Laser Immunonephelometry for Routine Quantification of Urinary Albumin Excretion. *Clin. Chem.* **1987**, *2* (1), 209–213.

(21) Thakkar, H.; Newman, D. J.; Holownia, P.; Davey, C. L.; Wang, C. C.; Lloyd, J.; Craig, A. R.; Price, C. P. Development and Validation of a Particle-Enhanced Turbidimetric Inhibition Assay for Urine Albumin

on the Dade Aca Analyzer. *Clin. Chem.* **997**, *43* (1), 109–113.
(22) Watts, G. F.; Bennett, J. E.; Rowe, D. J.; Morris, R. W.; Gatling, W.; Shaw, K. M.; Polak, A. Assessment of Immunochemical Methods for Determining Low Concentrations of Albumin in Urine. *Clin. Chem.* **1986**, *32*, 1544–1548.
(23) Kohzuma, T.; Koga, M. Lucica™ GA-L Glycated Albumin Assay Kit: A New Diagnostic Test for Diabetes Mellitus. *Mol. Diagnosis Ther.* **2010**, *14* (1), 49–51. https://doi.org/10.1007/BF03256353.
(24) Ferri, S.; Kim, S.; Tsugawa, W.; Sode, K. Review of Fructosyl Amino Acid Oxidase Engineering Research: A Glimpse into the Future of Hemoglobin A1c Biosensing. *J. Diabetes Sci. Technol.* **2009**, *3* (3), 585–592. https://doi.org/10.1177/193229680900300324.
(25) Abidin, D.; Liu, L.; Dou, C.; Datta, A.; Yuan, C. An Improved Enzymatic Assay for Glycated Serum Protein. *Anal. Methods* **2013**, *5* (10), 2461–2469. https://doi.org/10.1039/c3ay40165k.
(26) Paleari, R.; Bonetti, G.; Callà, C.; Carta, M.; Ceriotti, F.; Di Gaetano, N.; Ferri, M.; Guerra, E.; Lavalle, G.; Cascio, C. Lo; Martino, F. G.; Montagnana, M.; Moretti, M.; Santini, G.; Scribano, D.; Testa, R.; Vero, A.; Mosca, A. Multicenter Evaluation of an Enzymatic Method for Glycated Albumin. *Clin. Chim. Acta* **2017**, *469* (March), 81–86. https://doi.org/10.1016/j.cca.2017.03.028.
(27) Zheng, D. J.; Xu, J.; Su, M. M.; Sun, Z. G.; Jiao, Q. C.; Yang, Y. S.; Zhu, H. L. A Small, Steady, Rapid and Selective TICT Based Fluorescent HSA Sensor for Pre-Clinical Diagnosis. *Sensors Actuators, B Chem.* **2018**, *271* (February), 82–89. https://doi.org/10.1016/j.snb.2018.05.037.
(28) Xu, Y.; Zhang, M.; Li, B.; Wang, W.; Wang, B.; Yang, Y.; Zhu, H. A Fluorescence Probe Acted on Site I Binding for Human Serum Albumin. *Talanta* **2018**, *185* (April), 568–572. https://doi.org/10.1016/j.talanta.2018.04.029.
(29) Singh, P.; Mittal, L. S.; Kaur, S.; Kaur, S.; Bhargava, G.; Kumar, S. Self-Assembled Small Molecule Based Fluorescent Detection of Serum Albumin Proteins: Clinical Detection and Cell Imaging. *Sensors Actuators, B Chem.* **2018**, *255*, 478–489. https://doi.org/10.1016/j.snb.2017.08.072.
(30) Samanta, S.; Halder, S.; Das, G. Twisted-Intramolecular-Charge-Transfer-Based Turn-On Fluorogenic Nanoprobe for Real-Time Detection of Serum Albumin in Physiological Conditions. *Anal. Chem.* **2018**, *90* (12), 7561–7568. https://doi.org/10.1021/acs.analchem.8b01181.
(31) Luo, Z.; Liu, B.; Zhu, K.; Huang, Y.; Pan, C.; Wang, B.; Wang, L. An Environment-Sensitive Fluorescent Probe for Quantification of Human Serum Albumin: Design, Sensing Mechanism, and Its Application in Clinical Diagnosis of Hypoalbuminemia. *Dye. Pigment.* **2018**, *152* (February), 60–66. https://doi.org/10.1016/j.dyepig.2018.01.033.
(32) Liu, C.; Yang, W.; Gao, Q.; Du, J.; Luo, H.; Liu, Y.; Yang, C. Differential Recognition and Quantification of HSA and BSA Based on Two Red-NIR Fluorescent Probes. *J. Lumin.* **2018**, *197* (December 2017), 193–199. https://doi.org/10.1016/j.jlumin.2018.01.021.
(33) Li, P.; Wang, Y.; Zhang, S.; Xu, L.; Wang, G.; Cui, J. An Ultrasensitive Rapid-Response Fluorescent Probe for Highly Selective Detection of HSA. *Tetrahedron Lett.* **2018**, *59* (14), 1390–1393. https://doi.org/10.1016/j.tetlet.2018.02.065.
(34) Huang, C.; Ran, G.; Zhao, Y.; Wang, C.; Song, Q. Synthesis and Application of a Water-Soluble Phosphorescent Iridium Complex as Turn-on Sensing Material for Human Serum Albumin. *Dalt. Trans.* **2018**, *47* (7), 2330–2336. https://doi.org/10.1039/c7dt04676f.
(35) Guo, Y.; Chen, Y.; Zhu, X.; Pan, Z.; Zhang, X.; Wang, J.; Fu, N. Self-Assembled Nanosensor Based on Squaraine Dye for Specific Recognition and Detection of Human Serum Albumin. *Sensors Actuators, B Chem.* **2018**, *255*, 977–985. https://doi.org/10.1016/j.snb.2017.08.132.
(36) Groenendaal, L.; Jonas, F.; Freitag, D.; Pielartzik, H.; Reynolds, J. R. Poly(3,4-Ethylenedioxythiophene) and Its Derivatives: Past, Present, and Future. *Adv. Mater.* **2000**, *12* (7), 481–494. https://doi.org/10.1002/(SICI)1521-4095(200004)12:7<481::AID-ADMA481>3.0.CO;2-C.
(37) Huang, P. C.; Shen, M. Y.; Yu, H. H.; Wei, S. C.; Luo, S. C. Surface Engineering of Phenylboronic Acid-Functionalized Poly(3,4-Ethylenedioxythiophene) for Fast Responsive and Sensitive Glucose Monitoring. *ACS Appl. Bio Mater.* **2018**, *1* (1), 160–167. https://doi.org/10.1021/acsabm.8b00060.
(38) Hai, W.; Goda, T.; Takeuchi, H.; Yamaoka, S.; Horiguchi, Y.; Matsumoto, A.; Miyahara, Y. Specific Recognition of Human Influenza Virus with PEDOT Bearing Sialic Acid-Terminated Trisaccharides. *ACS Appl. Mater. Interfaces* **2017**, *9* (16), 14162–14170. https://doi.org/10.1021/acsami.7b02523.
(39) Wei, B.; Liu, J.; Ouyang, L.; Kuo, C. C.; Martin, D. C. Significant Enhancement of PEDOT Thin Film Adhesion to Inorganic Solid Substrates with EDOT-Acid. *ACS Appl. Mater. Interfaces* **2015**, *7* (28), 15388–15394. https://doi.org/10.1021/acsami.5b03350.

(40) Chen, C. H.; Luo, S. C. Tuning Charge and Morphology for the Efficient Detection of Dopamine under the Interferences of Uric Acid, Ascorbic Acid, and Protein Adsorption. *ACS Appl. Mater. Interfaces* **2015**, *7* (39), 21931–21938. https://doi.org/10.1021/acsami.5b06526.

(41) Ley, C.; Holtmann, D.; Mangold, K. M.; Schrader, J. Immobilization of Histidine-Tagged Proteins on Electrodes. *Colloids Surfaces B Biointerfaces* **2011**, *88* (2), 539–551. https://doi.org/10.1016/j.colsurfb.2011.07.044.

(42) Ogata, A. F.; Edgar, J. M.; Majumdar, S.; Briggs, J. S.; Patterson, S. V.; Tan, M. X.; Kudlacek, S. T.; Schneider, C. A.; Weiss, G. A.; Penner, R. M. Virus-Enabled Biosensor for Human Serum Albumin. *Anal. Chem.* **2017**, acs.analchem.6b04840. https://doi.org/10.1021/acs.analchem.6b04840.

(43) Mohan, K.; Donavan, K. C.; Arter, J. A.; Penner, R. M.; Weiss, G. A. Sub-Nanomolar Detection of Prostate-Specific Membrane Antigen in Synthetic Urine by Synergistic, Dual-Ligand Phage. *J. Am. Chem. Soc.* **2013**, *135* (20), 7761–7767. https://doi.org/10.1021/ja4028082.

(44) Wang, X.; Xia, N.; Liu, L. Boronic Acid-Based Approach for Separation and Immobilization of Glycoproteins and Its Application in Sensing. *Int. J. Mol. Sci.* **2013**, *14* (10), 20890–20912. https://doi.org/10.3390/ijms141020890.

(45) McNaught, A. D.; Wilkinson, A. *Compendium of Chemical Terminology. The Gold Book*, 2nd Editio.; Blackwell Scientific Publications, 1997.

(46) Bohli, N.; Meilhac, O.; Rondeau, P.; Gueffrache, S.; Mora, L.; Abdelghani, A. A Facile Route to Glycated Albumin Detection. *Talanta* **2018**, *184* (March), 507–512. https://doi.org/10.1016/j.talanta.2018.03.027.

(47) Yang, L. M. C.; Diaz, J. E.; McIntire, T. M.; Weiss, G. A.; Penner, R. M. Direct Electrical Transduction of Antibody Binding to a Covalent Virus Layer Using Electrochemical Impedance. *Anal. Chem.* **2008**, *80* (15), 5695–5705. https://doi.org/10.1021/ac8008109.

(48) Antikainen, N. M.; Smiley, R. D.; Benkovic, S. J.; Hammes, G. G. Conformation Coupled Enzyme Catalysis: Single-Molecule and Transient Kinetics Investigation of Dihydrofolate Reductase. *Biochemistry* **2005**, *44* (51), 16835–16843. https://doi.org/10.1021/bi051378i.

# CHAPTER 9

## Conclusions & Summary

Filamentous bacteriophage technology has advanced greatly from the first examples of phage display by Smith in 1985 to a powerful tool that has yielded 9 FDA approved antibody drugs and countless affinity reagents that otherwise may have remained a mystery. This dissertation covers the utility of conventional phage display in epitope mapping, biosensing, and novel assay development.

In chapter 4 phage display allowed identification of a population of COVID-19 antibodies strongly correlated to disease severity when taken with a disease risk-factor score. Similarly, in chapter 5, phage display provided the initial platform to probe the potential origin of these antibodies, which led to new findings to support the original antigenic sin hypothesis. These findings have significant implications for human health in light of the COVID-19 pandemic and could lead to a better immunological understanding of why certain populations produce certain antibodies.

Conventional phage display selections gave rise to the DJ-1 binding phage DL1Φ, which is highlighted several times throughout this dissertation. In chapter 6, DL1Φ was incorporated in a virus bioresistor capable of detecting 10 pM DJ-1. DL1Φ's utility was further exemplified in chapter 2, in which this dissertation presented a novel phage display "sandwich" selection technique. Furthermore, the DL1 peptide retained its strong binding interaction with DJ-1 even as a biotin-conjugated peptide bound to streptavidin.

Phage is well-represented in biopanning via phage display selections, but, as discussed in chapter 1, the inherent biophysical properties of phage should not be overlooked in future research. From a biomaterials perspective, a simple to purify and

produce, well-characterized, monodisperse material that can be surface-modified via basic molecular biology methodology is extremely desirable. Furthermore, the electrostatic, piezoelectric, and liquid crystalline properties of phage provide ample opportunity to incorporate phage into hybrid materials for applications such as biosensing, as discussed in chapter 6, chapter 7, and chapter 8. The future of phage biotechnology is bright, with seemingly endless applications in chemistry, biology, and engineering.